MULTIAXIAL FAILURE CRITERIA FOR CELLULAR MATERIALS

by

THANASIS C. TRIANTAFILLOU

Diploma in Civil Engineering, University of Patras, Greece
(1985)

M.Sc. in Civil Engineering, Massachusetts Institute of Technology
(1987)

SUBMITTED IN PARTIAL FULFILLMENT OF
THE REQUIREMENTS FOR THE DEGREE OF

DOCTOR OF PHILOSOPHY IN CIVIL ENGINEERING

at the

MASSACHUSETTS INSTITUTE OF TECHNOLOGY

April 1989

(c) Massachusetts Institute of Technology 1989

Signature of Author _____
Department of Civil Engineering
April 18, 1989

Certified by _____
Lorna J. Gibson
Thesis Supervisor

Accepted by _____
Ole S. Madsen
Chairman, Departmental Committee on Graduate Students

MASSACHUSETTS INSTITUTE
OF TECHNOLOGY

JUN 0 1 1989

LIBRARIES

ABSTRACT

MULTIAXIAL FAILURE CRITERIA FOR CELLULAR MATERIALS

by

THANASIS C. TRIANTAFILLOU

Submitted to the Department of Civil Engineering on May 2, 1989 in partial fulfillment of the requirements for the degree of Doctor of Philosophy in Civil Engineering.

Materials with a cellular structure are increasingly used in engineering. Proper design requires an understanding of the response of the materials under complex stress states. The behavior of cellular solids under multiaxial loads has, up until now, hardly been studied at all: no comprehensive attempt to establish multiaxial failure criteria exists. In this study, we attempt to do this.

The mechanical behavior of cellular materials is primarily governed by bending and axial deformations of their cell walls. Bending deformation dominates when the material is loaded uniaxially; but it can be entirely suppressed under a uniform (hydrostatic) stress state, in which case cell wall stretching controls the behavior.

We first model the elastic buckling, plastic yield, and brittle collapse of two-dimensional hexagonal honeycomb-like structures under in-plane stresses to develop equations describing their failure surfaces. In the absense of shear stresses, the failure envelopes for plastic or brittle materials are extremely elongated along the axis of equal biaxial stress. For the tensile fracture of brittle honeycombs a maximum principal stress criterion (based on linear elastic fracture mechanics) is employed, resulting in a box-like cutoff in the tension-tension quadrant. The elastic buckling envelope which, too, is almost box-like, acts as a cutoff in the compressive quadrant.

We next examine three-dimensional cellular materials. The failure criteria obtained for isotropic plastic and brittle materials are functions of both the mean stress and the deviatoric stress. While they require a limited number of parameters to be defined, they are by no means the result of curve fitting procedures. The failure surfaces follow the results obtained for honeycombs: when plotted in the principal stress space, they are extremely elongated along the hydrostatic axis. They are truncated by an almost box-like elastic buckling surface in the compressive octant; for brittle materials, the failure surface is also truncated by a box-like cutoff in the tensile octant corresponding to a maximum principal stress criterion. Failure criteria have also been developed for materials with hollow, porous cell walls such as some foamed ceramics. By appropriately distorting the failure surfaces criteria for axisymmetric and orthotropic

foams are also developed.

The failure criteria are compared with the results of an extensive experimental program that included uniaxial, biaxial, and triaxial (axisymmetric) testing of elastomeric, elastic-plastic, and elastic-brittle cellular solids. A novel experimental technique was developed for testing cylindrical specimens of materials with a continuous porosity under radial tensile stresses and axial compressive or tensile stresses; this technique is, remarkably, capable of producing hydrostatic tension in open-cell foams. The overall agreement between the tests and the models is satisfactory.

A constitutive model for isotropic elastic-perfectly plastic foams is developed based on the plastic yield failure criterion and the associated flow rule. The model can be implemented using a finite element technique. It is useful for describing the post-yield behavior of cellular materials, of particular relevance in designing protective padding and packaging for absorbing the energy of impacts. It can also be used to estimate the post-yield behavior of structural sandwich panels with foam cores.

Thesis Supervisor: Lorna Gibson

Title: Winslow Associate Professor of Civil Engineering

"...Δόσε – κηρύττω – στὸ ἔργον σου ὅλην τὴν δύναμί σου,
ὅλην τὴν μέριμνα..."

Κ. Π. Καβάφης
(Νέοι τῆς Σιδῶνος, 400 μ.Χ.)

To my parents Christo and Voula

ACKNOWLEDGEMENTS

I wish to express my deep gratitude to Professor Lorna Gibson, my thesis supervisor, for her guidance, constant encouragement, and her valuable advice during the course of this research. But more than that it is her personal warmth that has made working with her such a valuable experience to me.

I would like to express my sincere appreciation to Professors O. Buyukozturk and H. Einstein, Dr. J. Germaine, and Professor V. Li, members of my thesis committee, for the valuable suggestions and stimulating discussions we have had.

Appreciation is extended to Professors M. Ashby and J. Connor for their enlightening discussions.

I am also grateful to Philippe Bellwald for offering invaluable advice in the experimental work.

I was also able to discuss many of my ideas with other research students in the Civil and Mechanical Engineering Departments: I am thankful to them for their comments and suggestions.

The technicians of the Department provided valuable technical assistance. I would like to thank A. Rudolph for his advice and assistance in the design and fabrication of some parts of the test apparatus, and S. Rudolph for help with scanning electron microscopy.

The National Science Foundation Solid Mechanics Program (Grant No. MSM 8603821) supported financially this study, for which I am grateful.

And last but certainly not least, I would like to express my gratitude to Athena for her support and encouragement, and to my parents for their everlasting love.

TABLE OF CONTENTS

LIST OF TABLES

LIST OF FIGURES

LIST OF SYMBOLS

I. ENGLISH CHARACTERS

a = one half the crack length [mm]

A = area [mm^2]

b = depth of honeycomb cell [mm] or

= length of each side of the triangular holes in cellular ceramics [mm]

c = depth of neutral axis [mm] or

= core thickness of a sandwich beam [cm]

C_i, C'_j = constants, i=1,...,6, j=1,2 [-]

C_{11}, C_{12}, C_{44} = elements of the elastic constitutive matrix [MPa]

C_{ijmn} = ijmn element of constitutive matrix [MPa]

$[C^e]$ = elastic constitutive matrix [MPa]

$[C^{ep}]$ = elastic-plastic constitutive matrix [MPa]

d = diameter of cell walls in cellular ceramics [mm] or

- denotes increment or

= distance between the crack tips of notched cylinders [mm] or

= opening of jig used for testing of honeycombs [mm]

d_e = external diameter of rubber silicone impregnated cylinders [mm]

d_i = internal diameter of rubber silicone impregnated cylinders [mm]

d_{max} = maximum opening of jig used for testing of honeycombs [mm]

d_{min} = minimum opening of jig used for testing of honeycombs [mm]

D = diameter of notched cylinders [mm]

e_{ij} = deviatoric strain tensor, i,j=x,y,z [-]

E_s = Young's modulus of cell wall material [MPa]

E^* = Young's modulus of cellular material [MPa]

f, f_i = functions of the stress tensor, i=1,...,5 [-]

F = force [N]

F_i = force acting at point i, i=A,B [N]

F_p = peak force [N]

F_{crit} = Euler's buckling load [N]

g = plastic potential function [-]

G = shear modulus [MPa]

G^* = shear modulus of cellular material [MPa]

h = height of polyhedral cells [mm] or

= length of vertical members in honeycombs [mm] or

= height of cylindrical specimens [mm]

I = moment of inertia [mm^4]

I, II - denote fracture modes [-]

I, II, III - denote plastic or brittle collapse modes for honeycombs [-]

I_a, II_a, III_a - denote failure modes associated with tensile rupture of cell walls [-]

I_b, II_b, III_b - denote failure modes associated with compressive crushing of cell walls [-]

I^e, II^e, III^e - denote failure modes associated with elastic buckling of cell walls [-]

I^{ep}, II^{ep}, III^{ep} - denote failure modes associated with elastoplastic interactions [-]

I_i = i^{th} invariant of the stress tensor, i=1,2,3 [$(MPa)^i$]

J_j = j^{th} invariant of the deviatoric stress tensor, j=1,2,3 [$(MPa)^j$]

K = bulk modulus [MPa]

K_I = mode I stress intensity factor [$N/mm^{3/2}$]

K^* = bulk modulus of cellular material [MPa]

K^*_{IC} = mode I fracture toughness of cellular materials [$N/mm^{3/2}$]

$K^*_{IC,i}$ = mode I fracture toughness of honeycombs loaded in the i direction, i=x,y [$N/mm^{3/2}$]

l = edge length of polyhedral cells [mm] or

= length of inclined members in honeycombs [mm] or

= length of specimens [cm] or

= length of a simply supported sandwich beam [m]

l_i = cell size in direction i, i=x,y,z [mm]

l_1, l_2 = honeycomb specimen dimensions [mm]

$\bar{l}$ = mean intercept length [mm]

$\bar{l}_i$ = average cell size or mean intercept length in direction i, i=x,y,z [mm]

M = bending moment [Nm]

M_f = bending moment associated with fracture [Nm]

M_i = bending moment at the ends of member i, i=1,2,3 [Nm]

M_j = bending moment acting at point j, j=A,B [Nm]

M_p = fully plastic moment of cell walls [Nm]

M_{ij} = bending moment at end i of member ij, i=A,K, j=A,C,K [Nm]

n = end constraint factor [-]

n_i = end constraint factor for loading in the i direction, i=x,y,z [-]

N_l = number of intersections in a given length [-]

p = macroporosity of cellular ceramics [%]

p_i = internal pressure [MPa]

p_s = porosity of cell walls [%]

p^*_{el} = elastic collapse hydrostatic pressure [MPa]

P = load [N]

P_i = axial force along the inclined members in honeycombs [N]

P_v = axial force along the vertical members in honeycombs [N]

P_1 = axial force along the members of family 1 [N]

P_{ij} = force along member i in the direction j, i=1,2,3, j=x,y,z [N]

Q_i = shear force in the inclined members of honeycombs [N]

r = distance from crack tip [mm] or

= thickness of rubber silicone impregnated wall [mm] or

= elastic portion of the incremental strain [-]

R_{ij} = shape anisotropy ratio, i,j=x,y,z [-]

s_i = deviatoric stress in principal direction i, i=1,2,3 [MPa]

s_{ij} = deviatoric stress tensor, i,j=x,y,z [MPa]

S_{ijkl} = ijkl element of compliance tensor [m^2/N]

t = cell wall thickness [mm] or

= thickness of a package [mm] or

	=	face thickness of a sandwich beam [mm]
T, T_1	=	temperature [°C]
u, u_m	=	square root of axial force divided by the Euler buckling load, m=i,v [-]
U	=	kinetic energy [J]
W	=	energy absorbed per unit volume [J]
X	-	denotes direction X
Y	-	denotes direction Y
Z	-	denotes direction Z
$1a^p, 1b^p$	-	denote plastic collapse modes (geometrically similar to mode 1) [-]
$1a^{ep}, 1b^{ep}$	-	denote elastoplastic interactions for buckling mode 1 [-]
2^p	-	denotes plastic collapse modes (geometrically similar to mode 2) [-]
2^{ep}	-	denotes elastoplastic interaction for buckling mode 2 [-]

II. GREEK CHARACTERS

α, β	=	angles of rotation [degrees]	or
	=	constants [-]	
γ	=	constant [-]	
γ_{ij}	=	shear strain, i,j=x,y,z [-]	
δ_{ij}	=	Kronecker delta [-]	
Δ	-	denotes increment	
ε	=	normal strain [-]	
ε_D	=	densification strain [-]	
ε_i	=	normal strain in direction i, i=x,y [-]	
ε_v	=	dilatation [-]	
ε_{ij}	=	strain tensor, i,j=x,y,z [MPa]	
$\dot{\varepsilon}, \dot{\varepsilon}_1$	=	strain rate [sec^{-1}]	
ε^e_{ij}	=	elastic strain tensor, i,j=x,y,z [MPa]	
ε^p_{ij}	=	plastic strain tensor, i,j=x,y,z [MPa]	

ε^*_y = collapse strain in direction Y [-]

$\{\varepsilon\}$ = strain vector [-]

$\{\varepsilon\}_n$ = strain vector at the end of the nth loading increment [-]

θ = angle between the inclined and the horizontal members in honeycombs [degrees] or

= angle measured on a deviatoric plane [degrees]

λ = constant [-]

$\lambda_C, \lambda_F, \lambda_P$ = structure load factors [-]

ξ = distance measured on a deviatoric plane [MPa]

ξ_o = the value of ξ at ρ=0 [MPa]

ρ = distance measured on the hydrostatic axis [MPa]

ρ_o = the value of ρ at ξ=0 [MPa]

ρ_s = density of cell wall material [kg/m^3]

ρ^* = density of cellular material [kg/m^3]

ρ^o_s = density of cell wall material at zero porosity [kg/m^3]

σ = stress [MPa]

σ_a, σ_A = axial stress [MPa]

σ_i = normal stress in direction i, i=x,y,z [MPa]

σ_j = stress in principal direction j, j=1,2,3 [MPa]

σ_m = mean stress [MPa]

σ_p = peak stress [MPa]

σ_R = radial stress [MPa]

σ_{cs} = compressive strength of cell wall material [MPa]

σ_{fs} = modulus of rupture of cell wall material [MPa]

σ_{ij} = stress tensor, i,j=x,y,z [MPa]

σ_{ts} = tensile strength of cell wall material [MPa]

σ_{ys} = yield stress of cell wall material [MPa]

σ_{loc} = local stress field [MPa]

σ^*_{cr} = uniaxial brittle crushing stress of isotropic material [MPa]

$(\sigma^*_{cr})_i$ = brittle crushing stress in direction i, i=x,y,z [MPa]

σ^*_{el} = uniaxial elastic collapse stress of isotropic material [MPa]

$(\sigma^*_{el})_i$ = elastic collapse stress in direction i, i=x,y,z [MPa]

σ^*_{fr} = uniaxial tensile fracture stress of isotropic material [MPa]

$(\sigma^*_{fr})_i$ = tensile fracture stress in direction i, i=x,y,z [MPa]

σ^o_{fs} = modulus of rupture of cell wall material at zero porosity [MPa]

$(\sigma^*_h)_c$ = hydrostatic compressive crushing strength [MPa]

$(\sigma^*_h)_{pl}$ = hydrostatic plastic collapse strength [MPa]

$(\sigma^*_h)_t$ = hydrostatic tensile fracture strength [MPa]

σ^*_{pl} = uniaxial plastic collapse stress of isotropic material [MPa]

$(\sigma^*_{pl})_i$ = plastic collapse stress in direction i, i=x,y,z [MPa]

$(\sigma^*_{pl})^t_i$ = tensile yield stress in direction i, i=x,y,z [MPa]

σ^*_y = uniaxial collapse stress in direction Y [MPa]

$\{\sigma\}$ = stress vector [MPa]

$\{\sigma\}_n$ = stress vector at the end of the nth loading increment [MPa]

$\{\sigma\}'_{n+1}$ = trial stress vector at the end of the (n+1)th loading increment [-]

Σ_x, Σ_y = elastic buckling stress parameters [MPa]

τ_{ij} = shear stress, i,j=x,y,z [MPa]

$(\tau^*_{cr})_{ij}$ = crushing shear strength for orthotropic materials, i,j=x,y,z [MPa]

τ^*_{pl} = plastic shear strength for isotropic materials [MPa]

$(\tau^*_{pl})_{ij}$ = plastic shear strength for orthotropic materials, i,j=x,y,z [MPa]

ϕ, ψ = flexibility coefficients, functions of u [-]

φ_y, Φ_y = elastic buckling parameters [-]

CHAPTER I

INTRODUCTION

1.1 General

Cellular materials are made up of an interconnected network of solid struts or plates which form the edges and faces of *cells*. Typical structures are shown in Fig. 1.1. Figure 1.1a illustrates a two-dimensional array of hexagonal polygons; such two-dimensional cellular materials are called *honeycombs*. More commonly, the cells are polyhedra which pack to fill space; such three-dimensional cellular materials are called *foams*. If the solid of which the foam is made is contained in the cell edges only, the material is *open-celled* (Fig. 1.1b), while if the faces are solid, too, it is *closed-celled* (Fig. 1.1c). Depending on the nature of the cell wall material, cellular materials are characterized as *elastomeric* (e.g., rubbers), *elastic-plastic* (e.g., rigid polymers, metals), and *elastic-brittle* (e.g., ceramics, cements). The most important feature of a cellular material is its relative density, ρ^*/ρ_s, i.e., the bulk material density, ρ^*, divided by that of the solid from which the cell walls are made, ρ_s. As the relative density increases, the pore space shrinks; above about 0.3 the cell edges become thick relative to their length and the strut and plate model of the structure no longer applies. In this work we are concerned with relative densities of less than 0.3.

Almost any material can be foamed: polymers are the most common, but metals, ceramics, glasses, cement, and even composites can be fabricated into cells. Descriptions of the foaming processes can be found in Suh and Skochdopole (1980), Neville (1981), and Gibson and Ashby (1988). Foaming extends the range of properties available to the engineer significantly; those for the density, the thermal conductivity, the Young's modulus, and the compressive strength are shown in Fig. 1.2. The low densities permit the design of light structural components. The low thermal conductivity allows cheap

and reliable thermal insulation. The low stiffness makes foams ideal for cushioning applications. And finally, the low strengths and large compressive strains make them attractive for energy absorbing applications.

The largest application for polymeric and glass foams is in *thermal insulation*. Modern buildings and transport systems (refrigerated trucks, railway cars, and ships) all take advantage of the low thermal conductivity of expanded plastic foams. When fire hazard is a consideration, glass foams can be used instead. Another major use of man-made cellular solids is in *packaging*. Foams are particularly well suited to absorb the energy of impacts without generating high stresses. In marine *buoyancy* applications closed-cell foams are used extensively as supports for floating structures and as flotation in boats. Finally, cellular materials are used in other smaller areas of application including filters, water-repellant membranes, and antistatic shields.

The *structural* use of natural cellular materials is old: wood is probably the world's most widely used structural material. Today man-made foams and honeycombs are also used in applications in which they perform a truly structural function. The most obvious example is their use in *sandwich panels*, structural members made up of two stiff, strong faces separated by a lightweight core. Sandwich construction was first developed in the aircraft industry for flooring, tail and wing components, helicopter rotor blades, and components of space vehicles. The automobile industry is beginning to use the concepts developed by the aircraft industry for sandwich construction in the cars of the future. Sandwich panels are also used in modern sports equipment (in the decks and hulls of racing yachts, for instance). Sandwich roof, floor, and wall panels for housing construction are gaining increasing popularity because of their low weight and the ease with which they can be prefabricated (Nicholls, 1976; American Plywood Association, 1986; Winter Panel Corp.; Hexacomb Honeycomb Corp.). Other construction applications include portable buildings, fold-up bridges, and construction in remote areas. Illustrative examples of the use of cellular materials in sandwich panels are given in Fig. 1.3. Cellular materials in the form of large honeycombs are also now used for reinforcing earth, to confine and stabilize cohesionless or unstable soils in the construction of roads and retaining walls and to control erosion.

A promising, novel, cellular material from the structural engineer's standpoint is the so-called *aerated* or *cellular concrete*. It is produced by introducing gas bubbles into the plastic mix of cement and sand to give a material with cells between 0.1 mm and 1 mm in size (Neville, 1981). Densities as low as 200 kg/m^3 have been obtained. Currently, it is largely used for partitions for thermal insulation and for fireproofing as it offers better fire resistance than ordinary concrete (Valore, 1956). Structurally, it is mostly in the form of high-pressure steam-cured blocks of precast members but it can also be used for floor construction (Short and Kinniburgh, 1961). The use of this material as the core in sandwich panels is an area of future investigation, and according to the writer's opinion, it will result in light, stiff, strong (if appropriately reinforced), and rather cheap structural members. Aerated concrete can be modeled as a closed-cell foam.

When cellular materials are used in critical load-bearing applications, their response to *multiaxial* stresses becomes important. In designing lightweight sandwich structures, or in critical packaging applications, the engineer requires precise information about the way in which the foam will behave under complex stress states. The design of a sandwich plate, for instance, requires knowledge of the material behavior under 2 normal stresses acting in the plane of the plate and 2 shear stresses in the planes orthogonal to the plane of the plate. Multiaxial stress states also exist in foamed packages of complex geometry under impact; the critical peak stress generated on the packaged object depends on the combination of stresses causing failure of the foam. In their use as insulation, too, large temperature changes subject foams to biaxial tension or compression. The combination of stresses giving failure is given by the failure criterion; the goal of this thesis is to establish failure criteria for cellular materials which can be used in engineering design.

At this point it is helpful to develop a familiarity with the structure of cellular materials. Most honeycombs have prismatic hexagonal cells, although honeycombs with square or triangular cells can be made, too. In three dimensions a greater variety of cell shapes is possible: Figure 1.4 shows most of those that have been suggested as idealizations for the cells in foams (Jones and Fesman, 1965; Harding, 1967; Chan and Nakamura, 1969; Menges and Knipschild, 1975; Barma et al., 1978). Only the

triangular, rhombic, and hexagonal prisms and the rhombic dodecahedron and tetrakaidecahedron pack to fill space. The others, the tetrahedron, the icosahedron, and the pentagonal dodecahedron, do not pack properly unless distorted. Most foams, of course, are not regular packings of identical units but contain cells of different sizes and shapes with different numbers of faces and edges. In general, cellular materials are anisotropic; this is usually due to the anisotropy in cell shape although it sometimes (as in the case of wood) is also partially due to the anisotropy of the cell wall. The *principal cell dimensions* are obtained by measuring the mean cell diameters parallel to the principal directions, $\bar{l}_x$, $\bar{l}_y$, and $\bar{l}_z$. The *shape anisotropy ratios* $R_{xy}=\bar{l}_x/\bar{l}_y$ and $R_{xz}=\bar{l}_x/\bar{l}_z$ (where $\bar{l}_x$ is the largest principal dimension) give the degree of anisotropy of the material (see Huber and Gibson, 1988, for instance). Many foams are axisymmetric due to the rise of the foam in one preferred direction during processing, giving $R_{xy}=R_{xz}$ and $R_{yz}=1$.

1.2 Literature Review

Models for the mechanical behavior of cellular materials seek to identify and analyze the mechanisms by which the cell walls deform and fail under load. Early models for the uniaxial elastic behavior assumed that the cell walls carried axial loading only (Gent and Thomas, 1959, 1963; Lederman, 1971). This assumption leads to a conclusion which is inconsistent with experimental data: that the elastic properties vary linearly with the density. Later studies recognized the more important contributions of cell wall bending to the mechanical properties (Ko, 1965; Patel and Finnie, 1969, 1970; Menges and Knipschild, 1975; Abd El-Sayed et al., 1979; Gibson et al., 1982; Gibson and Ashby, 1982; Warren and Kraynik, 1987, 1988). The complete set of four elastic constants describing the in-plane, linear elastic response of honeycombs, calculated from the cell wall bending model, agree well with test results (Gibson et al., 1982). The modeling of the linear elastic behavior of foams is more complicated and, so far, less successful. The approach of Gibson and Ashby (1982, 1988) which extends the honeycomb analysis using dimensional arguments is the most complete to date, but it is

not capable of predicting the complete elastic modulus tensor from first principles. This gap is filled in the present study.

In uniaxial compression, cells fail by elastic buckling, plastic yielding or brittle crushing (Gent and Thomas, 1959; Matonis, 1964; Chan and Nakamura, 1969; Patel and Finnie, 1970; Rusch, 1970; Menges and Knipschild, 1975; Thornton and Magee, 1975; Barma et al., 1978; Morgan et al., 1981; Gibson et al., 1982; Gibson and Ashby, 1982; Ashby, 1983; Maiti et al., 1984a, b; Kurauchi et al., 1984). Elastic buckling gives large recoverable strains, while yielding and brittle crushing, of course, are irrecoverable. For honeycombs, with their regular, repeating geometry, an exact analysis is possible, and its results have been confirmed by experiments on elastomeric and elastic-plastic honeycombs with a wide range of geometries (Gibson et al., 1982; Klintworth and Stronge, 1988). Dimensional arguments can again be used to extend the analysis to the uniaxial collapse of foams, for all three mechanisms (Gibson and Ashby, 1982, 1988).

In uniaxial tension elastic buckling is, of course, not possible; elastomeric honeycombs and foams fail by cell wall rupture at large strains (Gent and Thomas, 1959). Cellular solids made from materials that yield plastically show a yield stress in tension caused, like that in compression, by plastic bending of the cell walls. Brittle materials fracture suddenly by fast crack propagation (Maiti et al., 1984b; Kurauchi et al., 1984).

Some attention has also been directed at modeling anisotropy in cellular materials. The mechanical properties of simple honeycomb-like materials made up of an array of prismatic hexagonal cells can be related to the cell geometry, the volume fraction of solids, and the cell wall properties in an exact way (Abd El-Sayed et al., 1979; Gibson et al., 1982). The degree of anisotropy in the mechanical properties can then easily be found in terms of the cell geometry. The complicated geometry of foams makes it more difficult to model them. Harrigan and Mann (1984) have shown that the shape of the cells can be characterized by an anisotropy tensor. Many attempts to describe the anisotropy in Young's modulus have, following the work of Gent and Thomas (1959, 1963), assumed that it is related to the uniaxial deformation of the cell walls (Kanakkanatt, 1973; Mehta and Colombo, 1976; Cunningham, 1981; Hilyard, 1982);

this neglects the important contribution of cell wall bending. This has been accounted for by Huber and Gibson (1988) who analyze the effect of shape anisotropy on material properties in a systematic manner. In their study, Huber and Gibson (1988) derived relationships for the elastic moduli, the elastic, plastic, and brittle collapse stresses, and the fracture toughness ratios for both axisymmetric and orthotropic materials, and successfully compared them with measurements of cell shape and mechanical properties.

Studies of the failure of cellular materials under multiaxial loads are much more limited. Klintworth and Stronge (1988) have recently identified and analyzed the elastic in-plane buckling modes of metal hexagonal honeycombs in which the vertical cell walls are rigid, assuming that each buckling mode is completely described by the deformation of a single hexagonal cell. They have also analyzed the plastic collapse of the same materials, subjected to a general, in-plane state of stress, accounting for large deformations. In addition, Klintworth and Stronge (1988) analyzed the interaction between plastic collapse and elastic buckling for modes which are geometrically similar; they concluded that this interaction can be estimated using a simple formula proposed by Merchant (1954).

The picture for the mechanical behavior of three-dimensional cellular solids under multiaxial loads is more confused. Shaw and Sata (1966) measured the combination of stresses required to cause failure of a polystyrene foam which yields plastically under several loading conditions. Their results suggest that failure is governed by the maximum principal stress. At first sight, this is an unusual result: plastic solids, when fully dense, fail in a way described approximately by the von Mises or the Tresca yield criterion, both of which involve more than one principal stresses. The later, more extensive, results from biaxial tests of Patel and Finnie (1969) and of Zaslawsky (1973) largely support Shaw and Sata's conclusion: all suggest a rectangular failure envelope for foams. Both Patel and Finnie (1969) and Zaslawsky (1973) used rigid polyurethane foams for their tests, which yield plastically in compression, but which may be brittle in tension. The failure envelope for biaxial states of stress suggested from the above studies is illustrated in Fig. 1.5.

The elastic buckling collapse of isotropic foams under a multiaxial stress state

(σ_x, σ_y, and σ_z) was modeled by Zhang (1987) by analyzing the elastic buckling of four struts in space which meet in at equal angles of 108° (assuming a pentagonal dodecahedral cell). The problem is complicated by the fact that the buckling mode may change with stress state. Zhang (1987), assuming a single buckling mode, found that the failure envelope in stress space is nearly box-like in the compressive octant; he calculated that the collapse strength of elastomeric foams loaded hydrostatically is 0.83 times the uniaxial collapse strength. Furthermore, Zhang (1989) tested a flexible polyethylene foam axisymmetrically with radial compression and axial tension and compression. His results are shown in Fig. 1.6. His findings are largely supported by data obtained by Shercliff (1988) in a recent study of flexible polyester foams. In this study, both the uniaxial buckling stresses and the hydrostatic pressures required to cause buckling were measured. For five different materials ranging in relative density from 0.01 to 0.05, the ratio of the two was more or less constant, with an average value 0.83 and a standard deviation 0.08. Shercliff's results are summarized in Table 1.1.

Table 1.1 Shercliff's hydrostatic compression results.

Material	Density (kg/m^3)	p^*_{el} [1] (KPa)	σ^*_{el} [1] (KPa)	p^*_{el}/σ^*_{el}
Flexible	14.3	-0.70	-0.82	0.85
polyurethane	21.8	-2.13	-2.77	0.77
(open-cell)	28.0	-2.14	-2.56	0.84
	41.5	-2.46	-3.09	0.80
	51.6	-2.34	-2.50	0.94
			Average:	0.83

1. Hydrostatic pressure.
2. Uniaxial elastic collapse stress.

In summary, only a limited effort has been made to date to establish the multiaxial behavior of cellular materials. It is this gap that the present study intends to fill.

References

Abd El-Sayed, F. K., Jones, R. and Burgess, I. W. (1979) A Theoretical Approach to the Deformation of Honeycomb Based Composite Materials, *Composites*, **10**, 209.

American Plywood Association (1986) *Design and Fabrication of Plywood Sandwich Panels*, Supplement 4.

Ashby, M. F. (1983) The Mechanical Properties of Cellular Solids, *Met. Trans.*, **14A**, 1755.

Barma, P., Rhodes, M. B. and Salovey, R. (1978) Mechanical Properties of Particulate-Filled Polyurethane Foams, *J. Appl. Phys.*, **49**, 4985.

Chan, R. and Nakamura, M. (1969) Mechanical Properties of Plastic Foams, *J. Cell. Plastics*, **5**, 112.

Cunningham, A. (1981) Modulus Anisotropy of Low-Density Cellular Plastics: An Aggregate Model, *Polymer*, **22**, 882.

Gent, A. N. and Thomas, A. G. (1959) The Deformation of Foamed Elastic Materials, *J. Appl. Polymer Sci.*, **1**, 107.

Gent, A. N. and Thomas, A. G. (1963) Mechanics of Foamed Elastic Materials, *Rubber Chem. Technol.*, **36**, 597.

Gibson, L. J., Ashby, M. F., Schajer, G. S. and Robertson, C. I. (1982) The Mechanics of Two-Dimensional Cellular Materials, *Proc. R. Soc. Lond.*, **A382**, 25.

Gibson, L. J. and Ashby, M. F. (1982) The Mechanics of Three-Dimensional Cellular Materials, *Proc. Roy. Soc.*, **A382**, 43.

Gibson, L. J. and Ashby, M. F. (1988) *Cellular Solids: Structure and Properties*, Pergamon, Oxford.

Harding, R. H. (1967) in *Resinography of Cellular Plastics*, ASTM Publ. STP-414.

Harrigan, T. P. and Mann, R. W. (1984) Characterization of Microstructural Anisotropy in Orthotropic Materials Using a Second Rank Tensor, . *Mater. Sci.*, **19**, 761.

Hexacomb Honeycomb Corp. *Hexacomb Panel Systems.*

Hilyard, N. C. (ed.) (1982) *Mechanics of Cellular Plastics*, MacMillan Publishing Co., Inc., New York.

Huber, A. T. and Gibson, L. J. (1988) Anisotropy of Foams, *J. Mater. Sci.*, **23**, 3031.

Jones, R. E. and Fesman, A. (1965) Air Flow Measurement and Its Relations to Cell Structure, Physical Properties, and Processibility for Flexible Urethane Foam, *J. Cell. Plast.*, **1**, 200.

Kanakkanatt, S. V. (1973) Mechanical Anisotropy of Open-Cell Foams, *J. Cell. Plast.*, **9**, 50.

Klintworth, J. and Stronge, W. (1988) Elasto-Plastic Yield Limits and Deformation Laws for Transversely Crushed Honeycombs, *Int. J. Mech. Sci.*, **30**, 273.

Ko, W. L. (1965) Deformations of Foamed Elastomers, *J. Cell. Plastics*, **1**, 45.

Kurauchi, T., Sato N., Kamigaito, O. and Komatsu, N. (1984) Mechanism of High Energy Absorption by Foamed Materials-Foamed Rigid Polyurethane and Foamed Glass, *J. Mat. Sci.*, **19**, 871.

Lager, J. R. and June, R. R. (1968) Design, Analysis, Fabrication and Test of a Boron Composite Beam, *J. Composite Mater.*, **2**, 128.

Lederman, J. M. (1971) The Prediction of the Tensile Properties of Flexible Foams, *J. Appl. Polymer Sci.*, **15**, 693.

Maiti, S. K., Gibson, L. J. and Ashby, M. F. (1984a) Deformation and Energy Absorption Diagrams for Cellular Materials, *Acta Metal.*, **32**, 1963.

Maiti, S. K., Ashby, M. F. and Gibson, L. J. (1984b) Fracture Toughness of Brittle Cellular Solids, *Scripta Metal.*, **18**, 213.

Matonis, V. A. (1964) Elastic Behavior of Low Density Figid Foams in Structural Applications, *Soc. Plast. Eng. J.*, **20**, 1024.

McCullough, R. L. (1971) *Concepts of Fiber-Reinforced Plastics*, Marcel Dekker, Inc., New York.

Mehta, B. S. and Colombo, E. A. (1976) Mechanical Properties of Foamed Thermoplastics, *J. Cell. Plast.*, **12**, 59.

Menges, G. and Knipschild, F. (1975) Estimation of Mechanical Properties for Rigid Polyurethane Foams, *Polymer Eng. Sci.*, **15**, 23.

Merchant, W. (1954) The Failure Load of Rigid Jointed Frameworks as Influenced by Stability, *Struct. Engr.* **32**, 185.

Morgan, J. S., Wood, J. L. and Bradt, R. C. (1981) Cell Size Effects on the Strength of Foamed Glass, *Mat. Sci. Eng.*, **47**, 37.

Neville, A. M. (1981) *Properties of Concrete*, 3rd edn., Pitman, London.

Nicholls, R. (1976) *Composite Construction Materials Handbook*, Prentice-Hall, Inc.,

New Jersey.

Patel, M. R. (1969) The Deformation and Fracture of Rigid Cellular Plastics Under Multiaxial Stress, Ph.D. Thesis, University of California at Berkeley, U.S.A.

Patel, M. R. and Finnie, I. (1969) The Deformation and Fracture of Rigid Cellular Plastics Under Multiaxial Stress, Lawrence Livermore Laboratory Report UCRL-13420.

Patel, M. R. and Finnie, I. (1970) Structural Features and Mechanical Properties of Rigid Cellular Plastics, *J. Materials*, **5**, 909.

Rusch, K. C. (1970) Load-Compression Behavior of Brittle Foams, *J. Appl. Polymer Sci.*, **14**, 1263.

Shaw, M. C. and Sata, T. (1966) The Plastic Behavior of Cellular Materials, *Int. J. Mech. Sci.*, **8**, 469.

Shercliff, T. (1988) Response of Cellular Solids to Multiaxial Loading, Cambridge University Engineering Department Report, Cambridge, U.K.

Short, A. and Kinniburgh, W. (1961) The Structural Use of Aerated Concrete, *The Struct. E.*, **39**(1), 1.

Suh, K. W. and Skochdopole, R. E. (1980) Foamed Plastics, in *Encyclopedia of Chemical Technology*, **2**, 3rd edn., John Wiley & Sons, Inc., New York.

Thornton, P. H. and Magee, C. L. (1975) The Deformation of Aluminum Foams, *Met. Trans.*, **6A**, 1253.

Valore, R. C. (1956) Insulating Concretes, *J. Amer. Concr. Inst.*, **53**, 509.

Warren, W. E. and Kraynic, A. M. (1987) Foam Mechanics: The Linear Elastic Response of Two-Dimensional Spatially Periodic Cellular Materials, *Mechanics of Materials*, **6**, 27.

Warren, W. E. and Kraynic, A. M. (1988) The Linear Elastic Properties of Open-Cell Foams, *J. Appl. Mech.*, **55**, 341.

Winter Panel Corp. *Structural Panels.*

Zaslawsky, M. (1973) Multiaxial-Stress Studies on Rigid Polyurethane Foam, *Exp. Mech.*, **2**, 70.

Zhang, J. (1987) Mechanics of Cellular Materials, CPGS Thesis, Cambridge University Engineering Department, Cambridge, U.K.

Zhang, J. (1989) Ph.D. Thesis, Cambridge University Engineering Department, Cambridge, U.K.

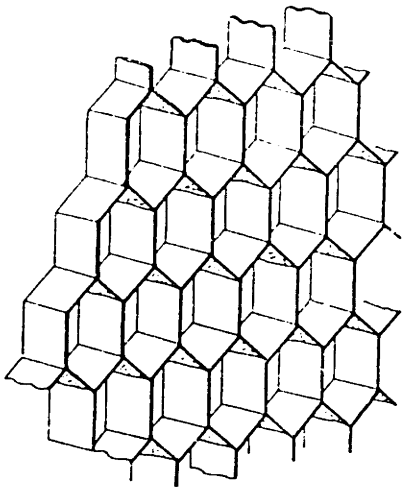

(a)

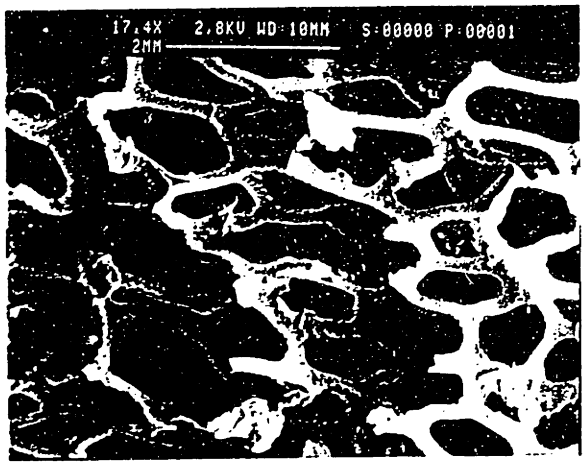

(b)

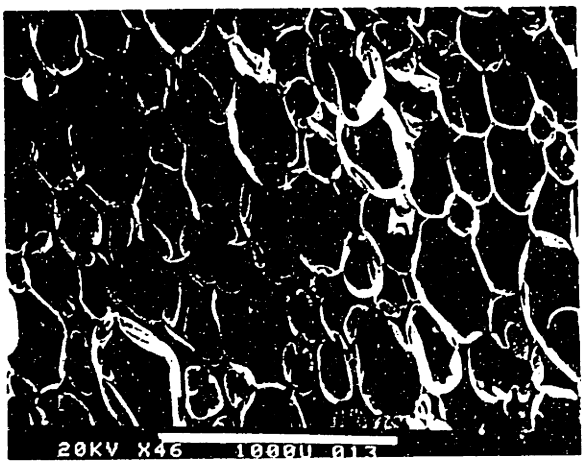

(c)

Fig. 1.1 Examples of cellular materials: (a) honeycomb; (b) open-cell foam; (c) closed-cell foam.

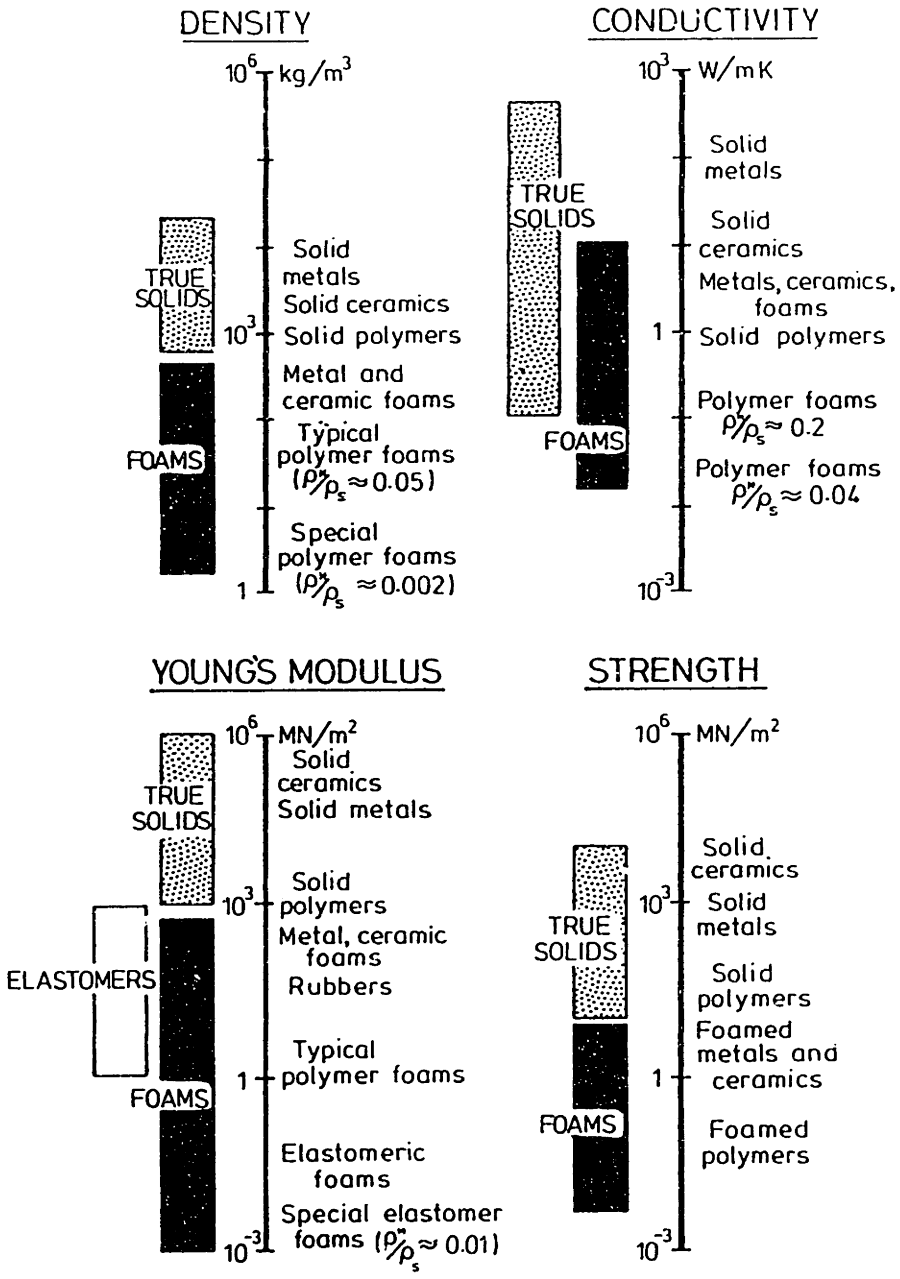

Fig. 1.2 The range of properties available to the engineer through foaming (after Gibson and Ashby, 1988).

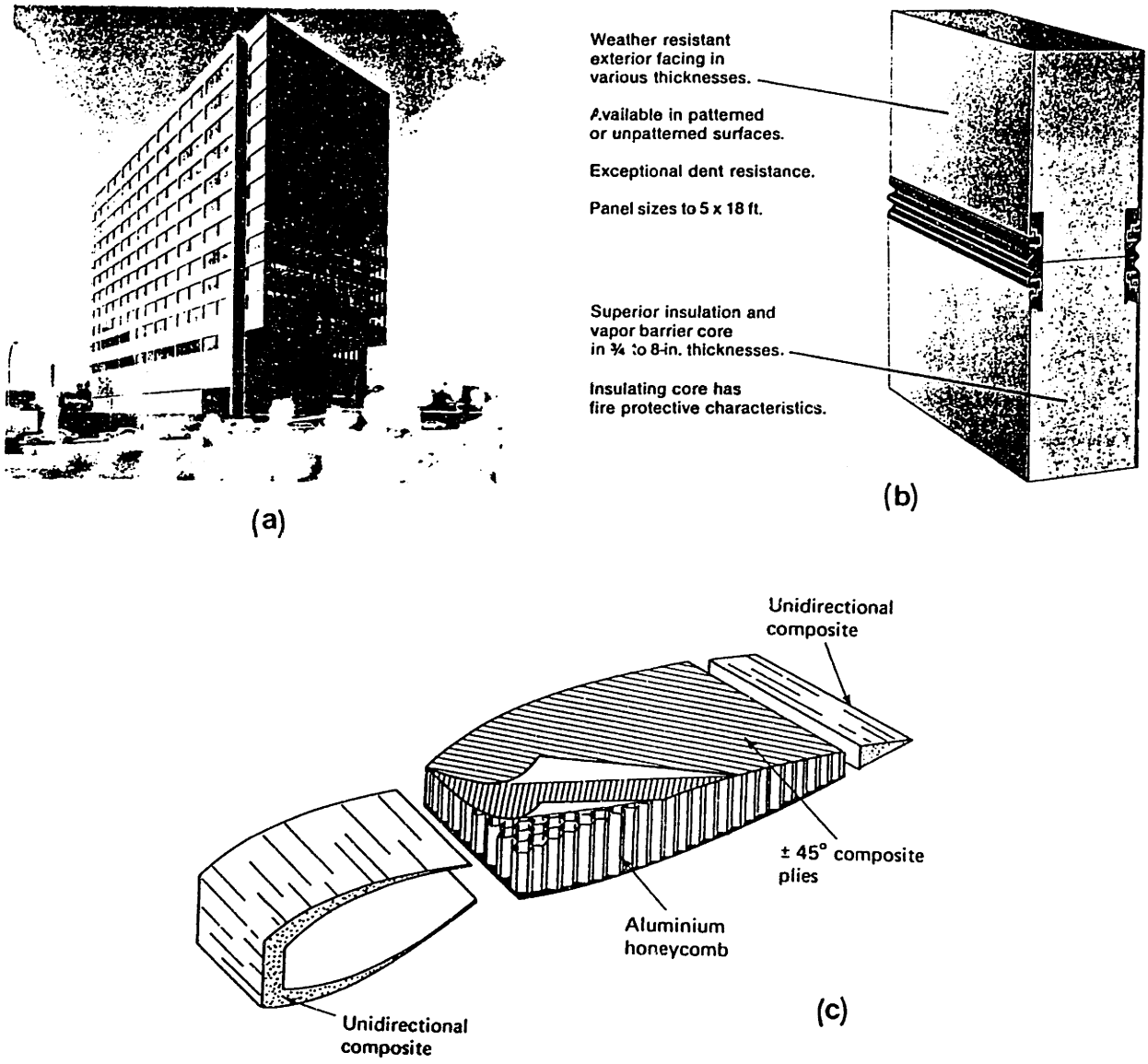

Fig. 1.3 Examples of sandwich construction: (a) and (b) wall panels in buildings (after Nicholls, 1976); (c) composite helicopter rotor blade (after McCullough, 1971); (d) roof to wall panel detail (after Winter Panel Corp.); (e) composite floor beam (after Lager and June, 1968); (f) construction with floor and wall sandwich panels.

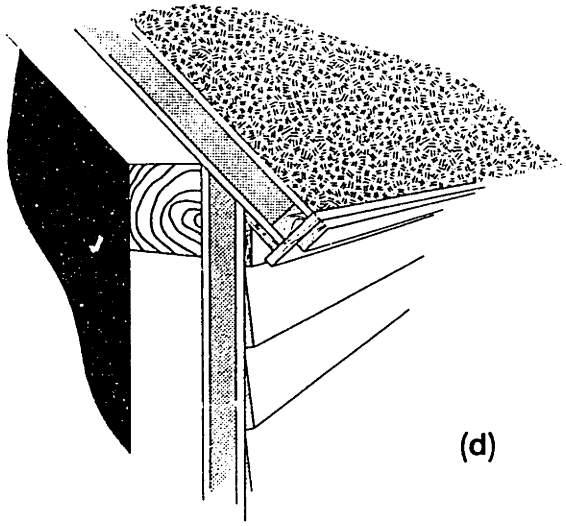

(d)

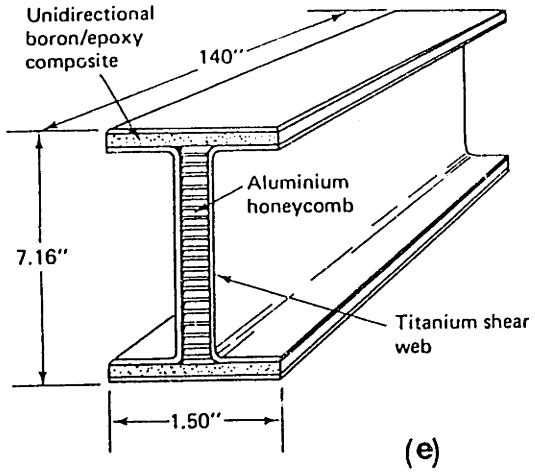

(e)

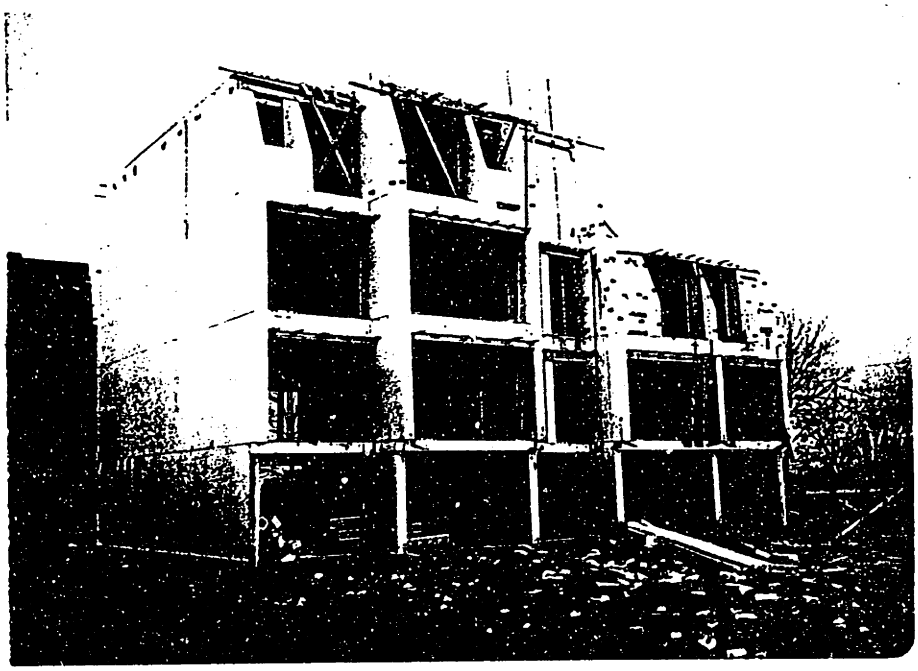

(f)

Fig. 1.3 cont'd.

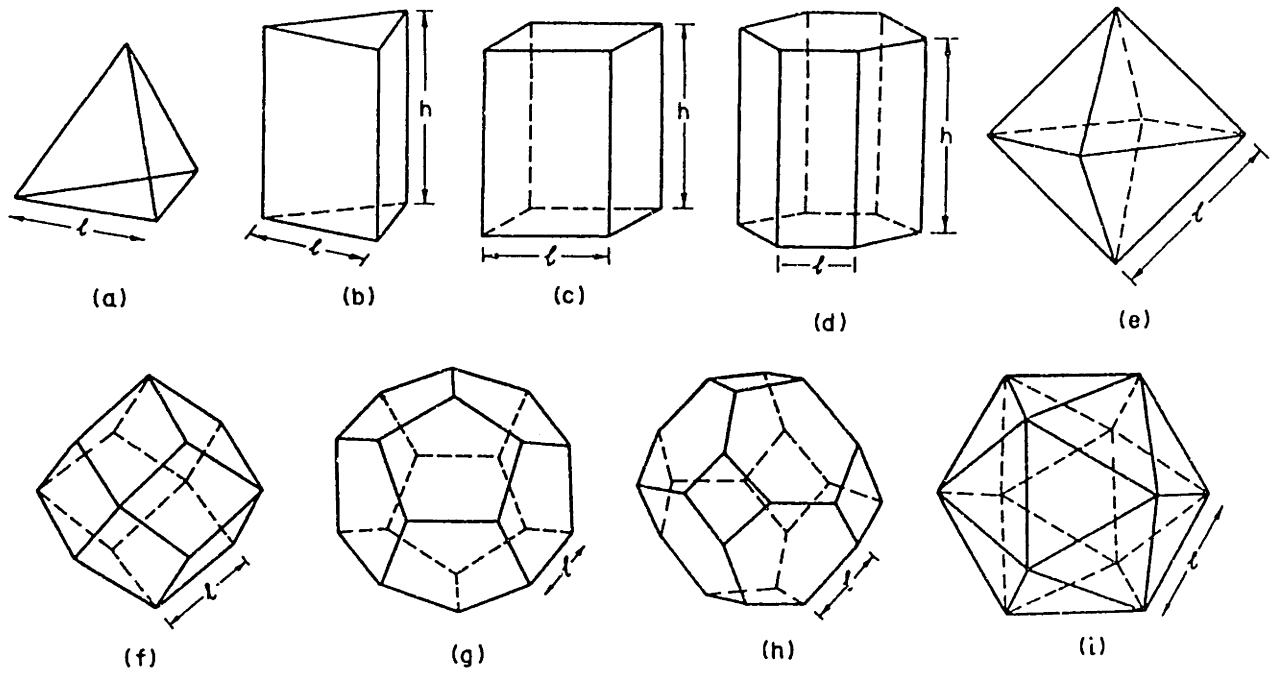

Fig. 1.4 Three-dimensional polyhedral cells: (a) tetrahedron, (b) triangular prism, (c) rectangular prism, (d) hexagonal prism, (e) octahedron, (f) rhombic dodecahedron, (g) pentagonal dodecahedron, (h) tetrakaidecahedron, (i) icosahedron (after Gibson and Ashby, 1988).

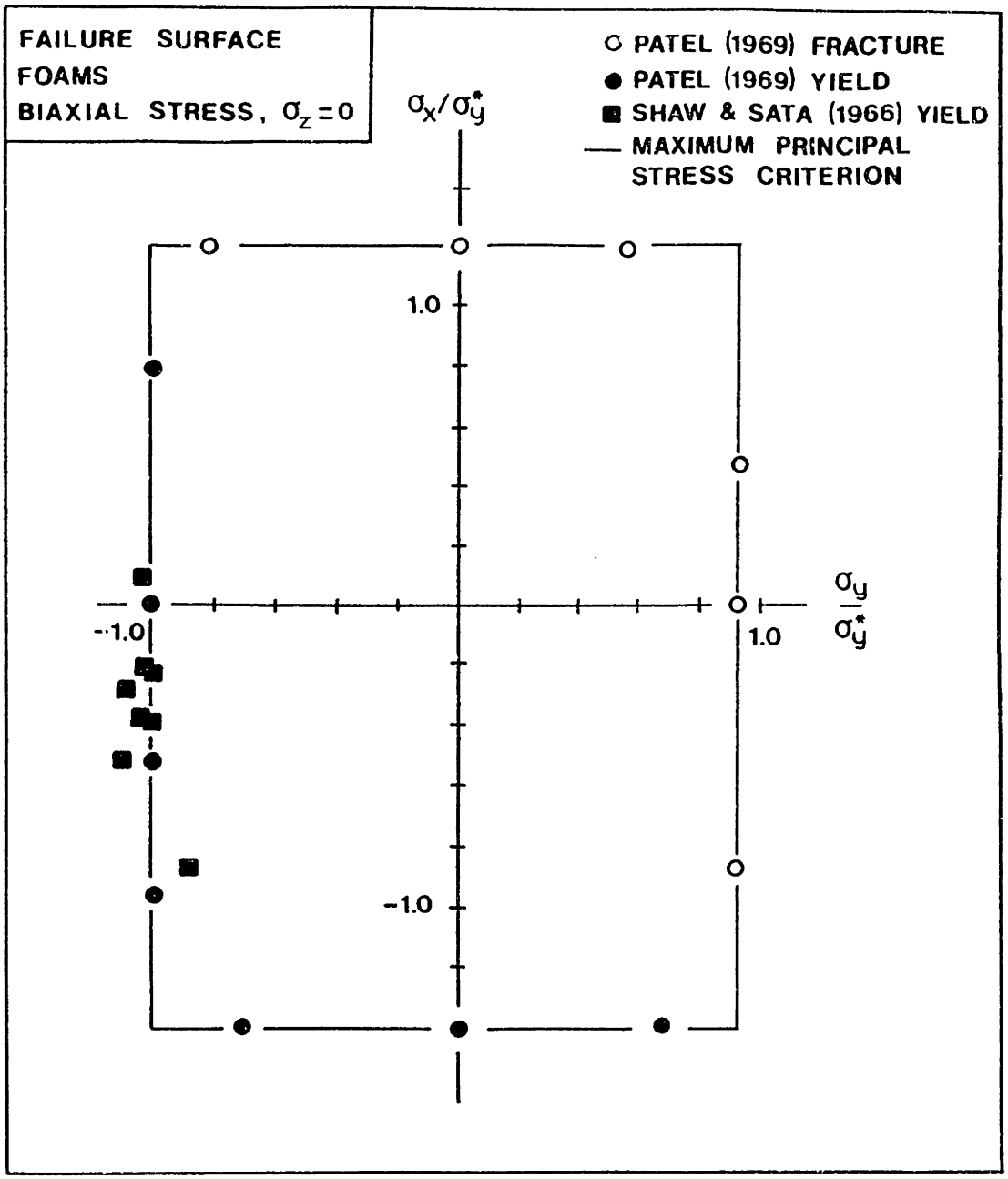

Fig. 1.5 Data for the failure of foams under biaxial loading. The data suggest that failure is described by a maximum principal stress criterion. σ_x, σ_y, and σ_z are the normal stresses acting parallel to the principal material directions; σ_y^* is the strength of the material in the direction Y.

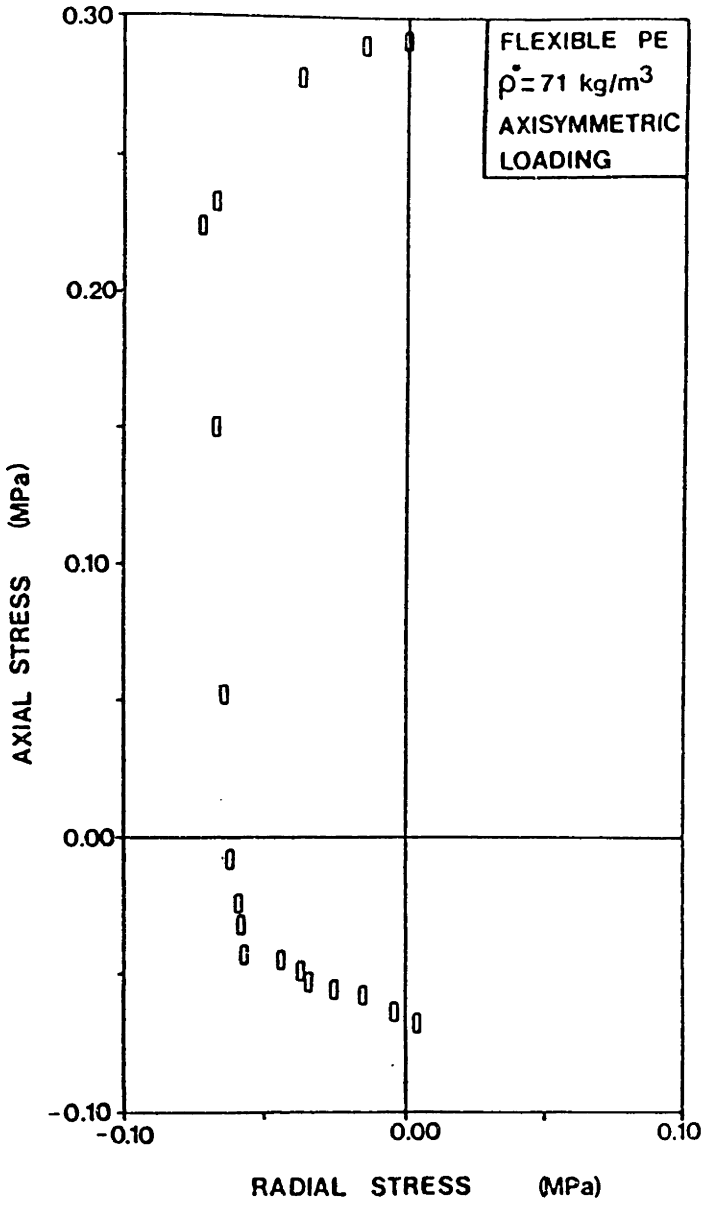

Fig. 1.6 Zhang's data (1989) for the failure of flexible polyethylene foam (ρ^*=71 kg/m^3). The material failed by elastic buckling and plastic collapse of the cell walls in uniaxial compression and tension, respectively.

CHAPTER II

OVERVIEW

2.1 Objectives of the Study

The present study is the first integrated attempt to model and measure the behavior of cellular materials under multiaxial stress states. The work is divided into two parts: the analytical and the experimental. The first part deals with the development of multiaxial failure criteria for both isotropic and anisotropic elastomeric, elastic-plastic, and elastic-brittle two-dimensional honeycombs and three-dimensional foams. The second part is devoted to the experimental validation of the analysis.

The main objectives of this study are:

(1) The development of criteria for the failure of honeycombs under in-plane stresses and for foams under a general state of stress by elastic buckling, plastic collapse, and brittle failure.

(2) The development of constitutive equations for isotropic elastic-plastic foams within the framework of classical plasticity theory.

(3) Comparison of the failure criteria with experimental data from uniaxial, biaxial, and triaxial tests.

(4) Application of the failure criteria to the design of structural sandwich panels and of protective packaging.

The failure criteria are first developed for isotropic materials; the results are then extended to axisymmetric and orthotropic materials.

The methodology of this study is based on the current understanding of the behavior of cellular materials under multiaxial loads. The key element of this behavior is that when the materials are loaded *uniformly*, they respond to the externally applied stresses by axial stretching of the cell walls; any deviation from the uniform stress state

causes cell wall bending. Depending on the nature of the cell wall material, initial bending can be followed by elastic buckling (if it is elastomeric), by formation of plastic hinges (if it is elastic-plastic), and by fracture (if it is elastic-brittle). Therefore, one recognizes the need for developing separate models, each one corresponding to a particular failure mechanism.

The procedures followed in the present study are constrained by the following conditions: (1) the materials experience small strains until they reach their failure point; (2) their microstructure can be idealized as an array of linear members which respond to remote suresses by undergoing axial and bending deformations, i.e., the contribution of shear deformations and shear stresses in the cell walls to the overall material behavior is neglected.

2.2 Overview of the Study

The methodology followed in this study has much in common with structural analysis procedures. The cell walls can be thought of as structural elements subjected to forces and moments as a result of the externally applied stresses. The combination of these forces and moments required to cause failure can be calculated knowing the properties of the cell wall material. These ideas, along with linear elastic fracture mechanics concepts (applicable to the determination of tension cutoffs for brittle materials), are the important features of the analysis presented in this work.

Chapter III describes the development of failure criteria for honeycombs under in-plane stresses. The uniaxial behavior of elastomeric honeycombs is reviewed first. Then, the combination of stresses required to cause elastic collapse of the honeycomb structure subjected to biaxial compression is calculated; it results in the elastic buckling envelope. Subsequently, after a brief overview of the uniaxial behavior of elastic-plastic honeycombs, the failure criterion for these materials is obtained as a function of the in-plane stresses σ_x, σ_y, and τ_{xy}. Furthermore, the uniaxial tensile strengths of elastic-brittle honeycombs are obtained using fracture mechanics methodologies, and the criterion for the brittle collapse of these materials is obtained again in terms of the in-plane

stresses. The appendix at the end of the chapter describes the interaction of elastic buckling and plastic collapse modes.

Chapter IV deals with the failure of three-dimensional foams. The failure envelope proposed by Zhang (1987) for the elastic buckling of isotropic foams under three-dimensional compressive stresses is presented and extended to describe the collapse of orthotropic foams. This is followed by a review of the uniaxial behavior and the development of the failure criterion for elastic-plastic foams, both isotropic and orthotropic, under a general state of stress. Elastic-brittle cellular materials are treated in the same manner: their uniaxial behavior is reviewed first, and the multiaxial failure criterion for isotropic and orthotropic materials is developed next. Finally, a model is described for the failure of elastic-brittle foams containing porous cell walls, subjected to uniaxial and general multiaxial stresses; both isotropic and orthotropic materials are considered. The second appendix of the chapter describes how one can use the multiaxial failure criterion for isotropic elastic-plastic foams along with the classical plasticity theory assuming an associated flow rule, to derive the post-yield constitutive relationships for this class of materials.

The experimental procedure followed in this study is described in Chapter V. The properties of the materials tested are given first. Then, a brief description of the technique followed for the microstructural characterization of the materials is presented (scanning electron microscopy). A novel testing method was developed for biaxial testing of honeycombs based on the idea of the equivalence of biaxial normal stresses and uniaxial strain conditions in plane stress problems. This method was employed in the biaxial compressive testing of elastomeric honeycombs. The experimental program for foams involved uniaxial, biaxial, and triaxial (axisymmetric) tests with several combinations of normal stresses; it is described in detail in Chapter V. Furthermore, the chapter presents the finite element calculations which were carried out in order to evaluate the stress state in cylindrical specimens loaded axisymmetrically with tensile stresses applied radially (a new technique developed here). Finally, Chapter V discusses possible sources of errors in the experimental procedure.

The experimental findings of this study are given in Chapter VI: data for the

microstructural characterization of the materials tested, the uniaxial and biaxial buckling of elastomeric honeycombs, and the collapse of elastomeric, elastic-plastic, and elastic-brittle foams under uniaxial, biaxial, and axisymmetric loading conditions. Typical load-deformation curves for all the loading cases are included. The most important observations related to the materials response under uniaxial and multiaxial loads are described. The data are plotted in stress space to obtain the experimental failure surfaces. The theoretical failure surfaces developed in Chapters III and IV are also shown on the same plots, allowing a direct comparison of the analysis with test results. Finally, the analytical models, based on both the extensive test results obtained in this work and on test results obtained in previous studies (Shaw and Sata, 1966; Patel, 1969; Zhang, 1989), are evaluated.

In Chapter VII applications of the multiaxial failure criterion for elastic-plastic foams in engineering design are presented. A complete constitutive model is described first, and its implementation using finite element analysis is briefly discussed. Then, the predictions of the plastic collapse criterion for the failure of the core material in structural sandwich panels are compared against previous models and test results (Triantafillou and Gibson, 1987). The agreement is found to be good. Lastly, the use of the failure criterion in the selection of the optimum material in packaging applications is discussed.

Chapter VIII summarizes the main findings that have come out of this research work. The main conclusions drawn from both the analytical and the experimental results are discussed, as well as new ideas to have come out of the work. Finally, a description of additional work suggested by this study, and new research directions are presented.

References

Patel, M. R. (1969) The Deformation and Fracture of Rigid Cellular Plastics Under Multiaxial Stress, Ph.D. Thesis, University of California at Berkeley, U.S.A.

Shaw, M. C. and Sata, T. (1966) The Plastic Behavior of Cellular Materials, *Int. J. Mech. Sci.*, **8**, 469.

Triantafillou, T. and Gibson, L. J. (1987) Failure Mode Maps for Foam Core Sandwich Beams, *Mat. Sci. Eng.*, **95**, 37.

Zhang, J. (1987) Mechanics of Cellular Materials, CPGS Thesis, Cambridge University Engineering Department, Cambridge, U.K.

CHAPTER III

IN-PLANE FAILURE CRITERIA FOR TWO-DIMENSIONAL CELLULAR MATERIALS

3.1 Introduction and Synopsis

A honeycomb is loaded *in-plane* when the applied stresses act in the X-Y plane shown in Fig. 3.1. The in-plane stiffnesses and strengths are the lowest because the cell walls respond to external loads by bending, and subsequent buckling, yielding, or fracturing. The *out-of-plane* stiffnesses and strengths (those in the Z direction of Fig. 3.1) are much larger since they require the axial deformation of the cell walls. In this chapter we study the in-plane strength of hexagonal honeycombs, by far the commonest kind.

Figure 3.2 shows uniaxial compressive and tensile stress-strain curves for elastomeric (rubber), elastic-plastic (metal), and elastic-brittle (ceramic) honeycombs. In compression, a linear regime is followed by a plateau leading into a final regime of steeply rising stress (Gibson and Ashby, 1988). On first loading, the cell walls *bend*, resulting in linear elasticity (assuming that the cell wall material is itself linear-elastic). When a critical stress is reached the cell walls begin to collapse. In elastomeric materials collapse is by the *elastic buckling* of the cell walls; deformation is recoverable on unloading. In materials with a plastic yield point collapse is due to formation of *plastic hinges* in the cell walls at sections where the bending moment is maximum. In brittle materials collapse is caused by *brittle crushing* of the cell walls. At high strains opposing cell walls touch or their broken fragments pack together, giving the final rising portion of the stress-strain curve called *densification.* Tensile deformation is different (Fig. 3.2). The cell wall members initially bend, giving linear-elastic deformation as in compression. But beyond the linear elastic regime, the tensile behavior deviates from the

compressive. Elastomeric honeycombs subjected to a tensile load do not buckle; instead, the cell walls continue to bend, rotating towards the tensile axis and increasing the stiffness. Elastic-plastic honeycombs form plastic hinges in the cell walls, as in compression; only the geometry change introduces a difference, pushing the tensile curve above the compressive one. Elastic-brittle honeycombs fail suddenly in tension, by the propagation of a crack at a stress less than the compressive strength. Fracture is controlled by the largest defect which propagates and can be studied using methods of fracture mechanics.

We model a two-dimensional cellular solid, or honeycomb, as an array of hexagonal cells (Fig. 3.3). The cell edges have lengths h and l, a thickness t, and a depth b. The angle between the horizontal and the inclined members is θ. Anisotropy is included by allowing the cells to have edges which differ in length ($h \neq l$) and which meet at an angle which is treated as variable. The solid material of which the cell wall is made has a density ρ_s and a Young's modulus E_s; if it is elastic-plastic it has a yield strength, σ_{ys}, while if it is brittle it has a modulus of rupture, σ_{fs} and a compressive strength, σ_{cs}.

In this chapter we review the uniaxial behavior of honeycombs, and then develop failure criteria for in-plane states of stress. In the case of elastomeric honeycombs we consider the action of two compressive principal stresses which coincide with the axes of symmetry of the honeycomb, resulting in *biaxial buckling*, while in the cases of elastic-plastic and elastic-brittle honeycombs we consider a general in-plane state of stress.

The ideas developed here are relevant to the study of the failure of much more geometrically complex foams under multiaxial loads, described in the next chapter.

3.2 Failure of Elastomeric 2D Cellular Solids

It has been experimentally observed (Gibson, 1981; Gibson and Ashby, 1988; Triantafillou et al., 1989) that an elastic honeycomb buckles in two modes (Fig. 3.4). Uniaxial compression in the Y direction, and biaxial compression with $\sigma_y > \sigma_x$ produce mode 1 (Fig. 3.4a); biaxial compression with $\sigma_y < \sigma_x$ produces mode 2 (Fig. 3.4b). Repeating units making up both modes are shown in Fig. 3.5; note that mode 1 requires

three members to completely describe it while mode 2 requires four. Mode 1 has been analyzed for both uniaxial and biaxial loading (Gibson et al., 1982, and Zhang, 1987). In both analyses, and that which follows for mode 2, t/l, t/h and the deflections of the members are assumed to be small; these assumptions, realistic for practical applications (U.S. Dept. of Defense, 1974; Hexcel TSB124, 1984), allow the use of classical beam-column theory (Timoshenko and Gere, 1961).

(a) Uniaxial Loading

When a honeycomb is loaded in the X or the Y direction, it initially deforms in a linear-elastic way, by cell wall bending (Patel and Finnie, 1970; Abd El-Sayed et al., 1979; Gibson et al., 1982; Warren and Kraynik, 1987). For loading in the Y direction, at some critical value of the remote stress σ_y the cell walls buckle in mode 1 (Figs 3.4a, 3.5a). Elastic collapse occurs when

$$\sigma_y = (\sigma^*_{el})_y = - \frac{n^2 \pi^2 t^3 E_s}{24 l h^2 \cos\theta} \qquad (3.1)$$

with n describing the rotational stiffness of the node where three cell walls meet (Gibson et al., 1982). Typical values of n are: n=0.686 for h/l=1; n=0.760 for h/l=1.5; n=0.806 for h/l=2.

Note that buckling is not observed when elastomeric honeycombs are compressed in the X direction; in this case the loads simply cause bending.

(b) Biaxial Loading

Guided by the results on the buckling of gridworks (Timoshenko and Gere, 1961; Renton, 1964; Wah, 1965; Forman and Hutchinson, 1970), the following formula has been proposed for the buckling of honeycombs subjected to a biaxial state of stress (Gibson and Ashby, 1988):

$$\sigma_x + \sigma_y = -\frac{n^2\pi^2 t^3 E_s}{24\, l h^2 \cos\theta} \tag{3.2}$$

with σ_x and σ_y positive when tensile. This equation appears to be too conservative when σ_x and σ_y are of similar magnitude; in addition, it predicts a finite buckling strength for loading in the X direction: $(\sigma^*_{el})_x$ is, in reality, infinite.

The buckling mode of Fig. 3.4a, in which all joints rotate through the same angle α (Fig. 3.5a), was assumed by Zhang (1987) to be valid for any combination of σ_x and σ_y. Using the slope-deflection theorem (Timoshenko and Gere, 1961) and the equilibrium of moments at each joint, Zhang was able to obtain the failure criterion for isotropic (h=l, θ=30°) elastomeric honeycombs as follows

$$\tan\left(\frac{l}{2t}\sqrt{\frac{-12\sqrt{3}\, l\sigma_y}{E_s t}}\right)\tan\left(\frac{l}{2t}\sqrt{\frac{-3\sqrt{3}\, l(3\sigma_x+\sigma_y)}{E_s t}}\right)$$

$$-\sqrt{\frac{3\sigma_x+\sigma_y}{\sigma_y}} = 0 \tag{3.3}$$

which reduces to equation (3.1) for a uniaxial stress, σ_y.

Klintworth and Stronge (1988) have recently identified (Fig. 3.6a) and analyzed the elastic buckling modes of metal honeycombs in which the cell walls parallel to the Y direction are rigid, assuming that each buckling mode is completely described by the deformation of a single hexagonal cell (which is the case in Fig. 3.4a, but is not in Fig. 3.4b). No elastic buckling mode involving more than a single cell was observed.

Next, we analyze the buckling of honeycombs subjected to stresses σ_x and σ_y, assuming that the collapse configuration is as shown in Figs 3.4b, 3.5b (mode 2). Consider the deformation of the unit cell shown in Fig. 3.7a. It is subjected to remote stresses σ_x and σ_y, positive when tensile, negative when compressive. Our primary concern here is the case of compressive stress. The forces and moments acting on the cell walls are shown in Fig. 3.7b. They can be calculated by assuming linear behavior as

follows:

$$P_{1x} = -P_{2x} = \sigma_x b(h + l\sin\theta)$$

$$P_{1y} = P_{2y} = \sigma_y bl\cos\theta \tag{3.4}$$

$$P_{3x} = 0; \qquad P_{3y} = 2\sigma_y bl\cos\theta$$

$$M_1 = -M_2 = \frac{1}{2}\sigma_x bl(h + l\sin\theta)\sin\theta - \frac{1}{2}\sigma_y bl^2\cos^2\theta \tag{3.5}$$

$$M_3 = 0$$

Then, the compressive axial forces along the inclined members, P_i, and along the vertical members, P_v, can be written as:

$$P_i = -\left(P_{1x}\cos\theta + P_{1y}\sin\theta\right) = -\sigma_x b(h + l\sin\theta)\cos\theta - \sigma_y bl\sin\theta\cos\theta \tag{3.6}$$

$$P_v = -2\sigma_y bl\cos\theta$$

The deformed shape for mode 2 is completely described by repetition of the configuration of four members shown in Fig. 3.5b. When buckling occurs, the rotation of node A is α while that of node B is zero since the member EB does not deform.

The moments and rotations of each member are related by the slope-deflection theorem (Timoshenko and Gere, 1961). From Fig. 3.8a one writes

$$\alpha - \beta = \frac{M_{AK}l}{3E_sI}\psi(u_i) + \frac{M_{KA}l}{6E_sI}\phi(u_i) \tag{3.7}$$

$$\beta = \frac{M_{KA}l}{3E_sI}\psi(u_i) + \frac{M_{AK}l}{6E_sI}\phi(u_i) \tag{3.8}$$

for members AB or AD. I is the moment of inertia and is equal to $bt^3/12$, and $\psi(u_i)$ and $\phi(u_i)$ are defined below. Moreover, for member AC (Fig. 3.8b) we obtain:

$$\alpha = \frac{M_{AC}h}{3E_sI}\psi(u_v) + \frac{M_{AC}h}{6E_sI}\phi(u_v) \tag{3.9}$$

The flexibility coefficients $\psi(u)$ and $\phi(u)$ are defined as

$$\psi(u) = \frac{3}{2u}\left(\frac{1}{2u} - \frac{1}{\tan 2u}\right); \qquad \phi(u) = \frac{3}{u}\left(\frac{1}{\sin 2u} - \frac{1}{2u}\right) \tag{3.10}$$

with $u=u_i$ and $u=u_v$, for the inclined and the vertical members, respectively. Finally, u_i and u_v are defined as

$$u_i = \sqrt{\frac{P_i l^2}{4E_sI}}, \qquad u_v = \sqrt{\frac{P_v h^2}{4E_sI}} \tag{3.11}$$

Force and moment equilibrium at node A result in the following equations:

$$Q_i = \frac{M_{AK} - M_{KA} + P_i\beta l}{l} = 0 \tag{3.12}$$

$$2M_{AK} + M_{AC} = 0 \tag{3.13}$$

Finally, appropriate combination of equations (3.7)-(3.10), (3.12), and (3.13), results in the following expression:

$$2u_i\tan u_v + u_v\tan 2u_i = 0 \tag{3.14}$$

with

$$u_i = l\sqrt{\frac{-3[\sigma_x(h + l\sin\theta)\cos\theta + \sigma_y l\sin\theta\cos\theta]}{E_s t^3}} \tag{3.15}$$

$$u_v = h\sqrt{\frac{-6\sigma_y l\cos\theta}{E_s t^3}} \tag{3.16}$$

Equation (3.14) is the *failure criterion* for in-plane mode 2 biaxial buckling of honeycombs, (Figs 3.4b, 3.5b). For isotropic honeycombs (h=l, θ=30°), it simplifies to

$$\sqrt{\frac{3\sigma_x + \sigma_y}{\sigma_y}} + \frac{\tan\left(l\sqrt{\frac{-3\sqrt{3}(3\sigma_x + \sigma_y)l}{E_s t^3}}\right)}{\tan\left(l\sqrt{\frac{-3\sqrt{3}\sigma_y l}{E_s t^3}}\right)} = 0 \tag{3.17}$$

Figure 3.9 shows the interaction of mode 1 (eqn. (3.3)) and mode 2 (eqn. (3.17)) for an isotropic honeycomb. Notice that in this figure, the applied stresses are normalized with respect to the uniaxial buckling strength, $(\sigma^*_{el})_y$, given by eqn. (3.1). Simple compression in the X direction does not cause buckling; the honeycomb folds up in a stable way. That is why the very end of the mode 2 curve is shown as a broken line. An analysis based on large deformations would result in a curve asymptotic to the horizontal axis. The figure documents the way in which the buckling mode switches, at the point $\sigma_x=\sigma_y$, from mode 1 to mode 2, and shows the very large difference in σ^*_{el} that this produces. The analytical predictions in Fig. 3.9 are compared with results of tests on elastomeric honeycombs in Chapter 6.

3.3 Failure of Elastic-Plastic 2D Cellular Solids

Metals and many polymers are elastic-plastic solids. Honeycombs made of them collapse plastically when the bending moment in the cell walls reaches the fully plastic

moment.

The uniaxial behavior of elastic-plastic honeycombs is completely understood and has been successfully analyzed (Abd El-Sayed et al., 1979; Gibson et al., 1982). Previous studies have correctly identified that plastic collapse due to formation of *plastic hinges* is the mechanism which governs failure. Some aspects of the behavior of honeycombs subjected to general in-plane stresses have been recently analyzed and verified (Gibson and Ashby, 1988; Klintworth and Stronge, 1988).

In this section we review the results of the above studies and present a general methodology for the analysis of the plastic collapse in honeycombs.

(a) Uniaxial Behavior

Consider loading in the X direction first (Fig. 3.10a). The collapse stress, $(\sigma^*_{pl})_x$, can be found by applying the upper and lower bound theorems of limit analysis (Horne, 1963; Massonnet and Save, 1965) to the structure shown in Fig. 3.10b. Gibson et al. (1982) have shown that

$$(\sigma^*_{pl})_x = \left(\frac{t}{l}\right)^2 \frac{1}{2((h/l) + \sin\theta)} \sigma_{ys} \tag{3.18}$$

where σ_{ys} is the yield stress of the cell-wall material. Plastic collapse in the Y direction is treated in the same way. In this case, limit analysis is applied to the structure of Fig. 3.10c. The plastic collapse stress is

$$(\sigma^*_{pl})_y = \left(\frac{t}{l}\right)^2 \frac{1}{2\cos^2\theta} \sigma_{ys} \tag{3.19}$$

In both cases, plastic hinges form in the inclined walls. In simple shear in the X-Y plane, plastic hinges form in the vertical walls (Fig. 3.10d); the shear strength is:

$$(\tau^*_{pl})_{xy} = \frac{1}{4}\left(\frac{t}{l}\right)^2 \frac{1}{(h/l)\cos\theta}\sigma_{ys} \qquad (3.20)$$

The central idea in the analysis of the uniaxial response of honeycombs is that the cell walls initially respond to loading by bending. Plastic failure occurs by formation of zones of yielding in the cell walls, or plastic hinges.

(b) Biaxial Behavior

General in-plane loading affects the plastic collapse of a honeycomb structure by producing significant axial as well as bending stresses in the cell walls (Gibson and Ashby, 1988; Klintworth and Stronge, 1988). Certain combinations of the stresses cancel the bending moments (e.g., $\sigma_x=\sigma_y$, $\tau_{xy}=0$ for an isotropic honeycomb), thus suppressing the formation of plastic hinges entirely. Then, plastic collapse requires the axial yielding of the cell walls, at a stress level that may be 10 to 100 times larger than the uniaxial strengths. The combination of σ_x, σ_y, and τ_{xy} which causes plastic collapse, plotted on axes of σ_x, σ_y, and τ_{xy}, is a closed surface called the *yield surface* for the honeycomb.

The most comprehensive study on the plastic collapse of honeycombs is that of Klintworth and Stronge (1988). They have analyzed honeycombs with rigid vertical walls subjected to a general, in-plane state of stress, accounting for large deformations; the collapse modes they considered are shown in Fig. 3.6b. They calculated an *upper-bound* to the collapse stress by equating the external work with the dissipated work at the plastic hinges for kinematically-admissible modes of collapse. In addition, Klintworth and Stronge (1988) analyzed the interaction between plastic collapse and elastic buckling for modes which are geometrically similar; they concluded that this interaction can be estimated with sufficient accuracy using a simple formula proposed by Merchant (1954). To model cell behavior at large deformations, their analysis accounts for the evolution of the cell geometry. In the present work we adopt a limit analysis (Gibson and Ashby, 1988) slightly different from theirs and assume that deformations

are small. A further assumption is that plastic collapse occurs *uniformly*, implying that the behavior of a group of cells may be deduced from that of a single representative cell.

The unit cell of a honeycomb is shown in Fig. 3.11a. The remote stresses σ_x, σ_y, and τ_{xy} produce forces and moments on the two inclined members as well as on the vertical member of the unit cell (Fig. 3.11b). They can be calculated as follows:

$$\begin{aligned}
P_{1x} &= \sigma_x b(h + l\sin\theta) + \tau_{xy} bl\cos\theta \\
P_{1y} &= \sigma_y bl\cos\theta + \tau_{xy} b(h + l\sin\theta) \\
P_{2x} &= -\sigma_x b(h + l\sin\theta) + \tau_{xy} bl\cos\theta \\
P_{2y} &= \sigma_y bl\cos\theta - \tau_{xy} b(h + l\sin\theta) \\
P_{3x} &= 2\tau_{xy} bl\cos\theta \\
P_{3y} &= 2\sigma_y bl\cos\theta
\end{aligned} \tag{3.21}$$

$$\begin{aligned}
M_1 &= \frac{1}{2}\left(P_{1x} l\sin\theta - P_{1y} l\cos\theta\right) = \\
&= \frac{1}{2} bl\left[\sigma_x(h + l\sin\theta)\sin\theta - \sigma_y l\cos^2\theta - \tau_{xy} h\cos\theta\right]
\end{aligned} \tag{3.22a}$$

$$\begin{aligned}
M_2 &= \frac{1}{2}\left(P_{2x} l\sin\theta + P_{2y} l\cos\theta\right) = \\
&= \frac{1}{2} bl\left[-\sigma_x(h + l\sin\theta)\sin\theta + \sigma_y l\cos^2\theta - \tau_{xy} h\cos\theta\right]
\end{aligned} \tag{3.22b}$$

$$M_3 = \frac{1}{2} P_{3x} h = \tau_{xy} blh\cos\theta \tag{3.22c}$$

The whole honeycomb structure is made up of a repetition of the three members marked 1, 2, and 3 in Fig. 3.11b. Provided deformations are small, the contribution of the axial load to the bending moment can be neglected. The bending moments vary linearly along the length of a member and are maximum and of opposite sign at its ends. The axial

force diagram shows a constant axial force within each cell wall. These observations lead to the conclusion that there are three modes of plastic collapse, depending on which member fails. The collapse modes are shown in Fig. 3.11c and are characterized as modes I, II, and III. Note that they are different from those analyzed by Klintworth and Stronge (1988) in that the vertical walls are flexible and bend under shear stresses.

The collapse criterion for mode I is obtained next. The axial stress in the inclined members of family 1, σ_a, is:

$$\sigma_a = \frac{P_{1x}\cos\theta + P_{1y}\sin\theta}{bt} \tag{3.23}$$

The maximum moment, M_1, tending to bend the cell walls is given by equation (3.22a). When the combination of σ_x, σ_y, and τ_{xy} is such that M_1 is positive, then it has the direction shown in Fig. 3.11b. When σ_x, σ_y, and τ_{xy} result in a negative value for M_1, the moment changes sign. Both cases must be considered to obtain the complete failure surface.

Failure occurs when the cell wall has yielded across its entire section. The stress distribution required to do this is shown in Fig. 3.12. The depth of the neutral axis is found by equating forces above and below the neutral axis; it is:

$$c = \frac{t}{2}\left(\frac{\sigma_{ys} + \sigma_a}{\sigma_{ys}}\right) \tag{3.24}$$

The plastic moment required to cause the formation of a plastic hinge is then given by the force, F, times the moment arm, t/2:

$$M_p = \frac{Ft}{2} = (\sigma_{ys} - \sigma_a)\frac{bct}{2}$$

or

$$M_p = \frac{\sigma_{ys} bt^2}{4}\left[1 - \left(\frac{\sigma_a}{\sigma_{ys}}\right)^2\right] \tag{3.25}$$

Failure occurs when the moment, M_1, equals the plastic moment, M_p. Remembering that the applied moment may be either positive or negative, depending on the magnitudes and signs of σ_x, σ_y, and τ_{xy}, we find:

$$\pm\left[\frac{\sigma_x\left(\frac{h}{l}+\sin\theta\right)\sin\theta-\sigma_y\cos^2\theta-\tau_{xy}\frac{h}{l}\cos\theta}{(t/l)^2}\right]$$

$$=\frac{\sigma_{ys}}{2}\left\{1-\left[\frac{\sigma_x\left(\frac{h}{l}+\sin\theta\right)\cos\theta+\sigma_y\sin\theta\cos\theta+\tau_{xy}\left(1+\frac{h}{l}\sin\theta\right)}{\sigma_{ys}(t/l)}\right]^2\right\} \qquad (3.26)$$

This equation defines the failure surface for plastic yield in a general in-plane state of stress, according to mode I collapse.

The collapse surface for mode II can be obtained using the same procedure. The only difference here is in the expression for the axial stress, σ_a, and the maximum bending moment, M_2. Thus we have:

$$\sigma_a=\frac{P_{2y}\sin\theta-P_{2x}\cos\theta}{bt} \qquad (3.27)$$

where M_2 is given by equation (3.22b). Failure occurs when M_2 equals the plastic moment, M_p. The result is:

$$\pm\left[\frac{\sigma_x\left(\frac{h}{l}+\sin\theta\right)\sin\theta-\sigma_y\cos^2\theta+\tau_{xy}\frac{h}{l}\cos\theta}{(t/l)^2}\right]$$

$$=\frac{\sigma_{ys}}{2}\left\{1-\left[\frac{\sigma_x\left(\frac{h}{l}+\sin\theta\right)\cos\theta+\sigma_y\sin\theta\cos\theta-\tau_{xy}\left(1+\frac{h}{l}\sin\theta\right)}{\sigma_{ys}(t/l)}\right]^2\right\} \qquad (3.28)$$

This equation defines the failure criterion for plastic collapse according to mode II.

The failure criterion for mode III yielding can be derived in a similar manner. The axial stress is given as

$$\sigma_a = \frac{P_{3y}}{bt} \tag{3.29}$$

while the maximum bending moment is defined by equation (3.22c). The result is:

$$\pm \frac{\tau_{xy}\frac{h}{l}\cos\theta}{(t/l)^2} = \frac{\sigma_{ys}}{4}\left\{1-\left[\frac{2\sigma_y\cos\theta}{\sigma_{ys}(t/l)}\right]^2\right\} \tag{3.30}$$

The overall collapse surface in stress space consists of intersecting surfaces which are associated with particular collapse modes. Vertices on the collapse surface represent hybrid collapse modes. Post-collapse plastic strain increments are normal to the relevant collapse surfaces, according to the classical formulation of the plasticity theory (Drucker, 1960; Kachanov, 1974). It is of interest to notice that the collapse surface corresponding to mode II is the mirror image of that corresponding to mode I, with respect to the plane $\tau_{xy}=0$ (compare equations (3.26) and (3.28)). This is not unexpected if we notice the symmetry of the honeycomb structure with respect to the vertical axis, Y.

Let us now consider the loading case with $\tau_{xy}=0$. In the absense of the in-plane shear stresses, modes I and II occur simultaneously; when collapse is caused by failure of inclined members, all the inclined members fail at the same instant, by formation of plastic hinges at their ends. For a certain combination of the stresses σ_x and σ_y, the bending moments acting on the members cancel and only axial stresses remain. The combination of σ_x and σ_y for which this occurs is given by setting $M_1=0$ (eqn. (3.22a)) or:

$$P_{1x}l\sin\theta - P_{1y}l\cos\theta = 0$$

or
$$\frac{\sigma_x}{\sigma_y} = \frac{\cos^2\theta}{\left(\frac{h}{l} + \sin\theta\right)\sin\theta} \tag{3.31}$$

For regular hexagonal cells, this ratio is 1, corresponding to equal biaxial stress. The ratio of applied stresses for which the inclined members are loaded in pure bending (that is, when the axial stresses cancel) is given by setting σ_a=0 (eqn. (3.23)):

$$P_{1x}\cos\theta + P_{1y}\sin\theta = 0$$

or
$$\frac{\sigma_x}{\sigma_y} = -\frac{\sin\theta}{\left(\frac{h}{l} + \sin\theta\right)} \tag{3.32}$$

For regular hexagonal cells, this ratio is -1/3.

Figure 3.13 shows the intersection of the plastic collapse surfaces with the planes τ_{xy}=0 (Fig. 3.13a), σ_y=0 (Fig. 3.13b), and σ_x=0 (Fig. 3.13c), for a honeycomb with regular hexagonal cells and t/l=0.1. In Fig. 3.13a, the failure envelope is the intersection of two ellipses. The extreme point on the failure envelope corresponds to pure axial stresses in the cell walls; the strength of the honeycomb in this case is many times higher than the uniaxial strength.

As a final remark, we shall add that the plastic collapse surface is sometimes truncated in the compressive regime by elastic buckling of the cell walls, which was studied in the previous section for τ_{xy}=0 (equations (3.3) and (3.17) for regular hexagonal cells). This is illustrated in Fig. 3.14.

In general, elastic buckling and plastic collapse interact if their modes are geometrically similar. The failure equation in this case is the superposition of two equations: one describing the elastic buckling, and another one describing the plastic collapse (Merchant, 1954; Horne, 1963). Elasto-plastic interactions may become important when the relative density ratio is very low, in which case the honeycomb structure is slender; they are discussed in Appendix 3A.

3.4 Failure of Elastic-Brittle 2D Cellular Solids

Honeycombs made of ceramic or glass, or of brittle plastics, fail in a brittle manner. In compression, the cells suffer progressive crushing which initiates when the tensile stress on the surface of a cell wall exceeds its *modulus of rupture*, (or, more unlikely, when the compressive stress on the surface of the cell wall exceeds its compressive or *crushing strength*). In tension, the honeycomb fails by fast brittle fracture, and the problem is best approached by the methods of fracture mechanics.

The uniaxial behavior of elastic-brittle honeycombs is well understood and has been analyzed by Gibson and Ashby (1988). The method of analyzing the behavior of brittle honeycombs subjected to general in-plane stresses is analogous to that for elastic-plastic honeycombs. In this section we review the basic results of the uniaxial behavior, refine the analysis, and present a general procedure for the analysis of the brittle failure of honeycombs subjected to a general in-plane state of stress.

(a) Uniaxial Behavior

Compressive Loading

As in the case of elastic-plastic honeycombs, a remote stress σ_x or σ_y or τ_{xy} (Fig. 3.15) applies bending moments to the cell walls. The cell wall material has a modulus of rupture, σ_{fs}, (defined as the maximum surface tensile stress in a bent beam at the instant at which it fractures) which is much lower than its compressive strength, σ_{cs}. This is a typical observation for brittle materials (e.g., McClintock and Argon, 1966). Consider loading in the X direction first (Fig. 3.15b). The crushing collapse stress, $(\sigma^*_{cr})_x$, has been shown to be (Gibson and Ashby, 1988)

$$(\sigma^*_{cr})_x = \left(\frac{t}{l}\right)^2 \frac{1}{3\left(\frac{h}{l} + \sin\theta\right)\sin\theta}\sigma_{fs} \tag{3.33}$$

Crushing in the Y direction (Fig. 3.15c) occurs at a stress level which is (Gibson and

Ashby, 1988)

$$(\sigma^*_{cr})_y = \left(\frac{t}{l}\right)^2 \frac{1}{3\cos^2\theta}\sigma_{fs} \tag{3.34}$$

Tensile Loading

Tensile fracture is different. If, in a brittle honeycomb loaded to near its fracture stress, one cell wall fails, the stress on the neighbouring walls increases and they will fail too. The failed cluster is like a macroscopic crack; the stress concentration at its periphery causes further walls to fail, and fracture propagates across the section. Furthermore, a macroscopic crack can exist in a honeycomb even before the application of external loads. Consider the honeycomb containing a crack as shown in Figs 3.16a and 3.17a. When subjected to tensile stresses, the cell walls at first bend elastically. The load is transmitted through the structure as a set of discrete forces and moments acting on each of the cell walls. The average force and moment on a given cell wall can be calculated from the stress field of the equivalent linear-elastic continuum (notice that the honeycomb is linear-elastic to fracture). The discrete problem can be solved by taking the solution to the continuous problem (just as done at the atomic level by replacing discrete interatomic forces by continuous elastic properties (Malvern, 1969)), and using it to calculate the forces and moments on the discrete cell walls (Ashby, 1983). When the combination of forces and moments is sufficient to fracture the cell wall just ahead of the crack tip, the crack advances. This condition defines the *fracture toughness* of the honeycomb, K^*_{IC}, which we calculate next. Our discussion here is restricted to mode I fracture.

Consider first loading in the X direction. A crack of length a in an elastic solid lying normal to a remote tensile stress σ_x creates a singular local stress field σ_{loc} (Griffith, 1924; Hertzberg, 1983; Ewalds and Wanhill, 1984) of

$$\sigma_{loc} = \frac{\sigma_x\sqrt{\pi a}}{\sqrt{2\pi r}} \tag{3.35}$$

at a distance r from its tips (Fig. 3.16b). Consider the first unbroken cell wall (labelled A in Fig. 3.16), which we take to be half the cell width, (h+lsinθ)/2, beyond the crack tip. The force on it is

$$F_A = \int_0^{(h+l\sin\theta)/2} \sigma_{loc}\, b\, dr = \sigma_x b\sqrt{a}\,(h + l\sin\theta)^{1/2} \tag{3.36}$$

and the bending moment is

$$M_A = \int_0^{(h+l\sin\theta)/2} \sigma_{loc}\, b\left(\frac{h + l\sin\theta}{2} - r\right)dr = \sigma_x \frac{b}{3}\sqrt{a}\,(h + l\sin\theta)^{3/2} \tag{3.37}$$

When the tensile stress at the extreme fiber of the cell wall, which is produced by the force F_A and the moment M_A, equals σ_{fs}, the wall fails and the crack advances. That occurs when

$$\frac{F_A \cos\theta}{bt} + \frac{6M_A}{bt^2} = \sigma_{fs} \tag{3.38}$$

Assembling these results gives the tensile fracture strength for loading in the X direction:

$$(\sigma^*_{fr})_x = \frac{1}{2\left(\frac{h}{l} + \sin\theta\right)^{3/2} + \frac{t}{l}\left(\frac{h}{l} + \sin\theta\right)^{1/2}\cos\theta}\sqrt{\frac{l}{a}}\left(\frac{t}{l}\right)^2\sigma_{fs}$$

$$\approx \frac{1}{2\left(\frac{h}{l} + \sin\theta\right)^{3/2}}\sqrt{\frac{l}{a}}\left(\frac{t}{l}\right)^2\sigma_{fs} \tag{3.39}$$

The last approximation is justifiable for small t/l ratios (in the order of 1/10), which is

typically the case in honeycomb structures.

Subsequently, consider loading in the Y direction (Fig. 3.17). The analysis is quite similar to that performed above. The first unbroken cell wall (labelled B in Fig. 3.17) is taken to be half the cell width, $2l\cos\theta/2$, beyond the crack tip. The force on it is

$$F_B = \int_0^{l\cos\theta} \sigma_{loc}\, b\, dr = \sqrt{2}\,\sigma_y b\sqrt{a}\,(l\cos\theta)^{1/2} \tag{3.40}$$

and the bending moment is

$$M_B = \int_0^{l\cos\theta} \sigma_{loc}\, b(l\cos\theta - r)\, dr = \sigma_y \frac{2\sqrt{2}\,b}{3}\sqrt{a}\,(l\cos\theta)^{3/2} \tag{3.41}$$

Failure of the cell wall occurs when

$$\frac{F_B}{bt} + \frac{6M_B}{bt^2} = \sigma_{fs} \tag{3.42}$$

Combining the results, we obtain the tensile fracture strength for loading in the Y direction:

$$(\sigma^*_{fr})_y = \frac{1}{4\sqrt{2}\cos^{3/2}\theta + \frac{t}{l}\sqrt{2}\cos^{1/2}\theta}\sqrt{\frac{l}{a}}\left(\frac{t}{l}\right)^2\sigma_{fs}$$

$$\approx \frac{1}{4\sqrt{2}\cos^{3/2}\theta}\sqrt{\frac{l}{a}}\left(\frac{t}{l}\right)^2\sigma_{fs} \tag{3.43}$$

Rephrasing our results in fracture mechanics terminology, we have shown that tensile fracture will occur in direction X when

$$\sigma_x\sqrt{\pi a} = K^*_{IC,x} = \frac{\sqrt{\pi l}}{2\left(\frac{h}{l} + \sin\theta\right)^{3/2}}\left(\frac{t}{l}\right)^2\sigma_{fs} \qquad (3.44)$$

and in direction Y when

$$\sigma_y\sqrt{\pi a} = K^*_{IC,y} = \frac{\sqrt{\pi l}}{4\sqrt{2}\cos^{3/2}\theta}\left(\frac{t}{l}\right)^2\sigma_{fs} \qquad (3.45)$$

A continuum mechanics approach to the solution of fracture problems in brittle honeycombs is justified only when the largest macroscopic crack found in the honeycomb structure is several times the cell size. When this is not the case, a discrete analysis is required instead. The procedure for performing such an analysis is summarized here. The honeycomb is idealized as a plane frame and each of the cell walls is treated as a beam element of it. The nodes of the frame structure are associated with the intersections of inclined and vertical cell walls, while additional nodes are assigned to the free ends of the broken cell walls surrounding the crack. The externally applied stresses (σ_x or σ_y) are substituted by equivalent forces acting at the outer nodes of the structure, and the response of the frame is calculated by performing a structural analysis by using, for instance, a finite element program. The result of the analysis yields the axial force and bending moment diagram for each member. From these, the maximum tensile stress developed in the cell wall next to the crack tip is calculated. By equating this stress to σ_{fs}, the modulus of rupture of the cell wall material, we calculate the value of the remote stress σ_x or σ_y corresponding to crack propagation; this is the uniaxial strength of the material.

The modulus of rupture of a brittle material depends on the largest flaw that may exist near the surface (Ashby and Jones, 1986). Assuming that linear elastic fracture mechanics is valid, the modulus of rupture is, in approximation, inversely proportional to the square root of the largest flaw. The statistics of the problem have been handled by Weibull (1951). The cell walls of a brittle honeycomb will show a dispersion of rupture

strengths because of the dispersion of flaw sizes. Therefore, an analysis based on a unit cell, such as the one presented above, would be only approximate, since it assumes that all the cell walls are characterized by the same modulus of rupture.

In the above analyses, we have considered only one location of the crack for each loading direction. For other crack locations, one simply has to follow the procedure described above. Keeping the results of the uniaxial behavior of brittle honeycombs in mind, we now proceed to the analysis of the in-plane behavior under a general state of stress.

(b) Biaxial Behavior

General in-plane loading of brittle materials results in both bending and axial loading of the cell walls (Gibson and Ashby, 1988). Certain combinations of the stresses may cancel the bending moments. Then, the axial load in the cell walls leads to collapse stresses several times larger than the uniaxial strengths. The combination of σ_x, σ_y, and τ_{xy}, which cause collapse in brittle honeycombs, is a closed surface called the *fracture surface*. The usual assumptions made before are considered here too: collapse occurs uniformly, implying that the behavior of a group of cells may be deduced from that of a single cell; deformations are small; and the thickness to length ratio of the cell walls is considered less than 1/5 so that shear deformations can be neglected.

The analysis is analogous to that presented for the elastic-plastic honeycombs. Only the failure criterion is different: here, failure occurs when the extreme tensile fiber stress in a cell wall exceeds the modulus of rupture of the cell wall material, σ_{fs} (or, sometimes, as we will see later, when the extreme compressive fiber stress exceeds the crushing strength, σ_{cs}).

The members of a unit cell (Fig. 3.11a) are subjected to forces and moments (Fig. 3.11b) which result from the remote stresses, σ_x, σ_y, and τ_{xy}. They are calculated from eqns (3.21) and (3.22). Following the reasoning presented in the analysis of the elastic-plastic honeycombs, three failure modes are identified for the collapse of brittle honeycombs (modes I, II, and III), depending on which set of cell wall members fails

first. This is illustrated in Fig. 3.11c.

The collapse criterion for mode I is obtained next. The axial stress in the inclined members of family 1, σ_a, is given by eqn. (3.23), while the maximum moment, M_1, tending to bend these members is given by eqn. (3.22a). Failure occurs when the cell wall ruptures. The stress distribution required to do this is shown in Fig. 3.18. The bending stress at failure, σ_{fs}-σ_a, is related to the applied moment M_1 by:

$$\sigma_{fs} - \sigma_a = \frac{M_1 t}{2I} \tag{3.46}$$

where $I=bt^3/12$ is the moment of inertia of the cell wall and the bending moment may be either positive or negative, depending on the magnitudes and signs of σ_x, σ_y, and τ_{xy}. Substituting for M_1 and σ_a, we obtain:

$$\pm\left\{\frac{3\left[\sigma_x\left(\frac{h}{l}+\sin\theta\right)\sin\theta-\sigma_y\cos^2\theta-\tau_{xy}\frac{h}{l}\cos\theta\right]}{(t/l)^2}\right\}$$

$$+\frac{\sigma_x\left(\frac{h}{l}+\sin\theta\right)\cos\theta+\sigma_y\sin\theta\cos\theta+\tau_{xy}\left(1+\frac{h}{l}\sin\theta\right)}{(t/l)}=\sigma_{fs} \tag{3.47}$$

This equation is the failure criterion and defines the fracture surface for collapse of brittle honeycombs according to mode I.

The collapse surface for mode II is obtained in an analogous manner. Here, the axial stress σ_a is given by eqn. (3.27), and the maximum bending moment, M_2, is given by eqn. (3.22b). Failure occurs when

$$\sigma_{fs} - \sigma_a = \frac{M_2 t}{2I} \tag{3.48}$$

The resulting equation for the failure surface is

$$\pm\left\{\frac{3\left[\sigma_x\left(\frac{h}{l}+\sin\theta\right)\sin\theta-\sigma_y\cos^2\theta+\tau_{xy}\frac{h}{l}\cos\theta\right]}{(t/l)^2}\right\}$$

$$+\frac{\sigma_x\left(\frac{h}{l}+\sin\theta\right)\cos\theta+\sigma_y\sin\theta\cos\theta-\tau_{xy}\left(1+\frac{h}{l}\sin\theta\right)}{(t/l)}=\sigma_{fs} \qquad (3.49)$$

The failure criterion for mode III collapse can be derived following again the same procedure. The axial stress is given by eqn. (3.29), and the maximum bending moment is defined by eqn (3.22c). The result is:

$$\pm\frac{6\tau_{xy}\frac{h}{l}\cos\theta}{(t/l)^2}+\frac{2\sigma_y\cos\theta}{(t/l)}=\sigma_{fs} \qquad (3.50)$$

In the analysis presented here, we assumed that the cell wall material fails by tensile rupture. However, the cell walls can fail by compressive crushing under some stress states. The analysis is identical to that given above for tensile rupture in the cell walls, the only difference being in the failure condition which now becomes (see Fig. 3.19)

$$-\sigma_{cs}+\sigma_a=\frac{M_i t}{2I} \qquad (3.51)$$

with i=1, 2, and 3, for modes I, II, and III respectively, and where σ_{cs} is the crushing strength of the cell wall material. To avoid confusion, we shall use the symbols Ia, IIa, and IIIa for the three modes of failure by tensile rupture of the cell walls, and Ib, IIb, and IIIb for the three modes of failure by compressive crushing of the cell walls. The failure criterion for mode Ib is obtained as

$$\pm\left\{\frac{3\left[\sigma_x\left(\frac{h}{l}+\sin\theta\right)\sin\theta-\sigma_y\cos^2\theta-\tau_{xy}\frac{h}{l}\cos\theta\right]}{(t/l)^2}\right\}$$

$$-\frac{\sigma_x\left(\frac{h}{l}+\sin\theta\right)\cos\theta+\sigma_y\sin\theta\cos\theta+\tau_{xy}\left(1+\frac{h}{l}\sin\theta\right)}{(t/l)}=\sigma_{cs} \qquad (3.52)$$

For mode IIb, the failure criterion obtained is

$$\pm\left\{\frac{3\left[\sigma_x\left(\frac{h}{l}+\sin\theta\right)\sin\theta-\sigma_y\cos^2\theta+\tau_{xy}\frac{h}{l}\cos\theta\right]}{(t/l)^2}\right\}$$

$$-\frac{\sigma_x\left(\frac{h}{l}+\sin\theta\right)\cos\theta+\sigma_y\sin\theta\cos\theta-\tau_{xy}\left(1+\frac{h}{l}\sin\theta\right)}{(t/l)}=\sigma_{cs} \qquad (3.53)$$

Finally, the criterion for failure according to mode IIIb is

$$\pm\frac{6\tau_{xy}\frac{h}{l}\cos\theta}{(t/l)^2}-\frac{2\sigma_y\cos\theta}{(t/l)}=\sigma_{cs} \qquad (3.54)$$

The overall collapse surface in macroscopic stress space consists of three intersecting surfaces associated with tensile rupture of the cell walls (eqns (3.47), (3.49), and (3.50)) in addition to three intersecting surfaces associated with compressive crushing of the cell walls (eqns (3.52), (3.53), and (3.54)). Vertices on the collapse surface represent hybrid collapse modes. It is interesting to note that the failure surfaces corresponding to modes IIa and IIb are the mirror images of those corresponding to modes Ia and Ib, respectively, with respect to the plane τ_{xy}=0.

As in the case of elastic-plastic honeycombs, in the absense of the in-plane shear stresses, τ_{xy}, modes I and II occur simultaneously; all the inclined members fail at their ends. The combination of the remote stresses σ_x and σ_y which cancels the bending

moments acting on the members is given by eqn. (3.31), while the combination of σ_x and σ_y which cancels the axial stresses (thus leaving only bending moments) on the members is given by eqn. (3.32).

Figure 3.20 shows the intersection of the collapse surfaces with the planes $\tau_{xy}=0$ (Fig. 3.20a), $\sigma_y=0$ (Fig. 3.20b), and $\sigma_x=0$ (Fig. 3.20c), for a brittle honeycomb with regular hexagonal cells, $t/l=0.1$, and $\sigma_{cs}/\sigma_{fs}=4$ (which was the case in one of the brittle foams tested). In Fig. 3.20a, the extreme points in the tension-tension and compression-compression quadrants correspond to pure tensile stresses and pure compressive stresses in the cell walls, respectively; the strength of the honeycomb in this case is many times higher than the uniaxial strength. In Figs 3.20b and 3.20c, the envelopes corresponding to modes Ib, IIb, and IIIb (compressive crushing of cell walls) are not shown, since they fall far outside the envelopes for modes Ia, IIa, and IIIa (tensile rupture of cell walls).

Under a biaxial state of stress, if the honeycomb contains cracks or flaws (which is very often the case), in the tensile quadrant the failure envelope is truncated by fast fracture. In this case, brittle fracture occurs when either σ_x exceeds $(\sigma^*_{fr})_x$, or σ_y exceeds $(\sigma^*_{fr})_y$: the failure envelope is a rectangle bounded by lines of constant principal stresses, corresponding to the uniaxial tensile strengths of the material (McClintock and Argon, 1966; Gibson and Ashby, 1988). This concept gives the two lines labelled "fast brittle fracture" which close the failure envelope in the tensile quadrant of Fig. 3.21. Finally, in the quadrant of biaxial compression the failure envelope is most likely truncated by elastic buckling (which we analyzed above) rather than compressive crushing failure of the cell walls themselves. This, too, is illustrated in Fig. 3.21.

3.5 Summary and Conclusions

Two-dimensional cellular materials deform and fail by a number of different mechanisms. In this chapter we first reviewed the uniaxial behavior of elastomeric, elastic-plastic, and elastic-brittle honeycombs loaded in-plane. The behavior is initially linear elastic. Then, if the honeycomb is made of an elastomer its cell walls buckle in compression, giving an almost flat plateau in the stress-strain curve; in tension they rotate

and the stress-strain curve rises steeply. If it is made of a plastic material the cell walls yield by the formation of plastic hinges due to bending; this, too, gives a plateau in the stress-strain curve, associated with permanent (plastic) deformations. If the cell walls are made of a brittle material it crushes (in compression) or fractures in a brittle manner (in tension). The uniaxial tensile strength of brittle honeycombs containing macroscopic cracks was obtained in this study using a linear-elastic fracture mechanics formulation based on an equivalent continuum. The response of honeycombs to general in-plane loads is rather unusual. This is because the cell wall bending which completely dominates the in-plane properties of hexagonal cells for uniaxial loading can be suppressed completely by an appropriate choice of biaxial loads. Then the cell walls fail by axial yielding, fracture or crushing, and the strength is much higher. The analysis for biaxial buckling in elastomeric honeycombs resulted in an almost "box"-like failure envelope in the compressive quadrant. Several modes of failure were also identified for plastic or brittle honeycombs, depending on the combination of stresses σ_x, σ_y, and τ_{xy}. Failure criteria which are functions of the remote stresses (and, of course, of the cell wall material properties and the geometric characteristics of the honeycomb structure) were developed for each particular failure mechanism. The central concept here was to express the forces and moments acting on the cell walls in terms of the externally applied stresses, and to study their relationship to the strength of the cell wall material.

In the absense of shear stresses, the failure envelopes are extremely elongated, reflecting the much higher strength of the materials when the cell walls are subjected to axial stresses only, and bending is suppressed. In the case of plastic honeycombs, the failure envelope is the intersection of two ellipses, while in the case of brittle honeycombs a rhombic shape is observed with two pairs of straight lines, one corresponding to tensile rupture and another one corresponding to compressive crushing of the material. The elastic buckling failure envelope acts as a cutoff in the compressive quadrant. Finally, a maximum principal tensile stress criterion is employed for the tensile fracture of brittle honeycombs, resulting in a box-like cutoff in the tension-tension quadrant.

The upshot of all this is that the failure envelope for two-dimensional cellular materials can take a variety of shapes, from box-like to ellipsoidal, it can have corners,

and its shape in the tensile quadrant can be quite different from that in the compressive one. With a little experience, one can associate certain shapes with certain mechanisms. These curious shapes must be remembered when designing with honeycombs.

The results obtained in this chapter provide a basis for design with two-dimensional cellular materials. Equally important, they establish an understanding of mechanisms which is extremely important in the analysis of three-dimensional cellular solids (foams), to which we now proceed.

Appendix 3A: Interaction Between Elastic Buckling and Plastic Collapse Modes in Elastic-Plastic Honeycombs

A basic assumption made in the application of simple plastic theory to the analysis of elastic-plastic honeycombs (i.e., honeycombs characterized by elastic-plastic cell wall material) is that, at the stage when the plastic collapse mechanism is formed, the deformations of the honeycomb structure are insufficient to alter radically the equations of equilibrium. At certain levels of compressive axial forces in the cell walls, however, this ceases to be true and the plastic theory then gives unrealistic estimates of the failure stresses. The actual force level at which this occurs depends on the slenderness of the individual members of the honeycomb structure (Horne and Morris, 1981). This factor also governs the magnitude of the elastic critical load of the structure. Moreover, as the elastic buckling load of a honeycomb is approached, small imperfections compatible with the buckling mode become increasingly large. If these imperfections are also compatible with a plastic collapse mode, the failure load is reduced. Therefore, if the elastic buckling and plastic collapse modes are geometrically similar, the combined load factor λ_F may be estimated by (Merchant, 1954; Horne, 1963):

$$\frac{1}{\lambda_F} \approx \frac{1}{\lambda_C} + \frac{1}{\lambda_P} \tag{3A.1}$$

where λ_C and λ_P are the elastic buckling (or critical) and plastic collapse load factors, respectively. The above formula gives conservative estimates of the failure load when the elastic buckling and plastic collapse modes considered are not geometrically similar.

In elastic-plastic honeycomb structures, the plastic collapse modes I, II, and III are geometrically similar to the elastic buckling modes I^e, II^e, and III^e shown in Fig. 3A.1. These combine to form the elastoplastic collapse modes I^{ep}, II^{ep}, and III^{ep} illustrated in the same figure. Note that the buckling modes I^e, II^e, and III^e would never be observed in elastomeric honeycombs; they correspond to stress levels higher than those required to produce the buckling modes 1 or 2 (Fig. 3.4). Therefore, they are only

significant when considering the elastoplastic interaction.

Mode I^e is the result of the elastic buckling of the cell walls of family 1 (Figs 3.7b, 3A.1) due to a compressive axial force P_1 given as

$$P_1=-P_{1x}\cos\theta-P_{1y}\sin\theta \tag{3A.2}$$

Elastic buckling occurs when P_1 reaches the critical value

$$P_1=\frac{\pi^2 E_s b t^3}{12l^2} \tag{3A.3}$$

Combining eqns (3A.2) and (3A.3) and substituting for P_{1x} and P_{1y} from eqns (3.21) we obtain

$$-\frac{12\left(\frac{h}{l}+\sin\theta\right)\cos\theta}{\pi^2 E_s(t/l)^3}\sigma_x-\frac{12\sin\theta\cos\theta}{\pi^2 E_s(t/l)^3}\sigma_y-\frac{12\left(1+\frac{h}{l}\sin\theta\right)}{\pi^2 E_s(t/l)^3}\tau_{xy}=1 \tag{3A.4}$$

Finally, combining eqns (3A.4) and (3.26) on the basis of eqn. (3A.1) we find the following approximate expression for the failure surface associated with the elastoplastic mode I^{ep} of collapse:

$$\pm 2\left[\frac{\sigma_x\left(\frac{h}{l}+\sin\theta\right)\sin\theta-\sigma_y\cos^2\theta-\tau_{xy}\frac{h}{l}\cos\theta}{\sigma_{ys}(t/l)^2}\right]$$

$$-12\left[\frac{\sigma_x\left(\frac{h}{l}+\sin\theta\right)\cos\theta+\sigma_y\sin\theta\cos\theta+\tau_{xy}\left(1+\frac{h}{l}\sin\theta\right)}{\pi^2 E_s(t/l)^3}\right]$$

$$+\left[\frac{\sigma_x\left(\frac{h}{l}+\sin\theta\right)\cos\theta+\sigma_y\sin\theta\cos\theta+\tau_{xy}\left(1+\frac{h}{l}\sin\theta\right)}{\sigma_{ys}(t/l)}\right]^2=1 \tag{3A.5}$$

Equation (3A.5) holds only when the axial force in the buckled cell walls is compressive, i.e., when $-\sigma_x b(h+l\sin\theta)\cos\theta-\sigma_y bl\cos\theta\sin\theta-\tau_{xy}b(h+l\sin\theta)\geq 0$.

Following the same procedure for modes II^{ep} and III^{ep} we obtain:

Mode II^{ep}:

$$\pm 2\left[\frac{\sigma_x\left(\frac{h}{l}+\sin\theta\right)\sin\theta-\sigma_y\cos^2\theta+\tau_{xy}\frac{h}{l}\cos\theta}{\sigma_{ys}(t/l)^2}\right]$$

$$-12\left[\frac{\sigma_x\left(\frac{h}{l}+\sin\theta\right)\cos\theta+\sigma_y\sin\theta\cos\theta-\tau_{xy}\left(1+\frac{h}{l}\sin\theta\right)}{\pi^2E_s(t/l)^3}\right]$$

$$+\left[\frac{\sigma_x\left(\frac{h}{l}+\sin\theta\right)\cos\theta+\sigma_y\sin\theta\cos\theta-\tau_{xy}\left(1+\frac{h}{l}\sin\theta\right)}{\sigma_{ys}(t/l)}\right]^2=1 \qquad (3A.6)$$

under the condition $-\sigma_x b(h+l\sin\theta)\cos\theta-\sigma_y bl\cos\theta\sin\theta+\tau_{xy}b(h+l\sin\theta)\geq 0$.

Mode III^{ep}:

$$\pm\frac{4\tau_{xy}\frac{h}{l}\cos\theta}{\sigma_{ys}(t/l)^2}-\frac{24\sigma_y\cos\theta}{\pi^2E_s(t/l)(t/h)^2}+\left[\frac{2\sigma_y\cos\theta}{\sigma_{ys}(t/l)}\right]^2=1 \qquad (3A.7)$$

under the condition $-2\sigma_y bl\cos\theta\geq 0$.

Next, we consider the interaction between the elastic buckling modes 1 or 2 (Fig. 3.4) and geometrically similar plastic collapse modes. The buckling mode 1 is geometrically similar to the plastic collapse modes $1a^P$ and $1b^P$ shown in Fig. 3A.1, which have been analyzed by Klintworth and Stronge (1988), using the upper-bound theorem of plastic analysis. Mode $1a^P$ is described by the following expression:

$$\left| -\frac{2\left(\frac{h}{l}+\sin\theta\right)\sin\theta}{\sigma_{ys}(t/l)^2}\sigma_x + \frac{2\cos^2\theta}{\sigma_{ys}(t/l)^2}\sigma_y \right| = 1 \qquad (3A.8)$$

The equation for mode $1b^P$ is

$$\left| \frac{2\left(\frac{h}{l}+\sin\theta\right)\sin\theta}{\sigma_{ys}(t/l)^2}\sigma_x - \frac{2\cos^2\theta}{\sigma_{ys}(t/l)^2}\sigma_y \right| = 1 \qquad (3A.9)$$

The derivation of eqns (3A.8) and (3A.9) by Klintworth and Stronge (1988) neglects the effect of the axial force in the plastic moment of the cell walls. The elastic buckling mode 1 has been analyzed by Zhang (1987) for isotropic honeycombs. Following the procedure described in Section 3.2b, we analyzed mode 1 for anisotropic honeycombs; the failure equation is given below:

$$-\sqrt{\frac{-\sigma_y}{\varphi_y\Sigma_y}}\tan\frac{\pi}{2}\sqrt{\frac{-\sigma_y}{\Phi_y\Sigma_y}} + \frac{\pi\sqrt{-\frac{\sigma_x}{\Sigma_x}-\frac{\sigma_y}{\Sigma_y}}}{\tan\frac{\pi}{2}\sqrt{-\frac{\sigma_x}{\Sigma_x}-\frac{\sigma_y}{\Sigma_y}}} = 0 \qquad (3A.10)$$

where

$$\Sigma_x = \frac{\pi^2 E_s (t/l)^3}{12\left(\frac{h}{l}+\sin\theta\right)\cos\theta}, \qquad \Sigma_y = \frac{\pi^2 E_s (t/l)^3}{12\sin\theta\cos\theta}$$

$$\Phi_y = \frac{l^2\sin\theta}{2h^2}, \qquad \varphi_y = \frac{2\sin\theta}{\pi^2}$$

Equation (3A.10) gives a linear relationship between σ_x and σ_y; for the most common honeycomb materials ($0.67<h/l<1.5$), it is approximated within 5% of accuracy by

$$-\frac{\sigma_x}{\Sigma_x}-\frac{\sigma_y}{0.446\Phi_y\Sigma_y}=1 \qquad (3A.11)$$

The combined elastoplastic envelope describing mode $1a^{ep}$ (Fig. 3A.1) as the result of the interaction between modes 1 and $1a^{p}$ is defined as follows:

$$-\sigma_x\left[\frac{2\left(\frac{h}{l}+\sin\theta\right)\sin\theta}{\sigma_{ys}(t/l)^2}+\frac{12\left(\frac{h}{l}+\sin\theta\right)\cos\theta}{\pi^2E_s(t/l)^3}\right]$$

$$-\sigma_y\left[\frac{5.452\left(\frac{h}{l}\right)^2\cos\theta}{E_s(t/l)^3}-\frac{2\cos^2\theta}{\sigma_{ys}(t/l)^2}\right]=1 \qquad (3A.12)$$

Finally, the failure envelope for mode $1b^{ep}$ (Fig. 3A.1), the result of the interaction between modes 1 and $1b^{p}$, is described by

$$-\sigma_x\left[\frac{12\left(\frac{h}{l}+\sin\theta\right)\cos\theta}{\pi^2E_s(t/l)^3}-\frac{2\left(\frac{h}{l}+\sin\theta\right)\sin\theta}{\sigma_{ys}(t/l)^2}\right]$$

$$-\sigma_y\left[\frac{5.452\left(\frac{h}{l}\right)^2\cos\theta}{E_s(t/l)^3}+\frac{2\cos^2\theta}{\sigma_{ys}(t/l)^2}\right]=1 \qquad (3A.13)$$

The buckling mode 2 is geometrically similar to the plastic collapse mode 2^{p} (Fig. 3A.1), which is, however, associated with zero external plastic work and is, therefore, not permissible. A conservative estimate of the failure stresses can be obtained by combining mode 2 with the plastic collapse mode resulting from a biaxial stress state (modes I, II simultaneously, Fig. 3A.1); this plastic collapse mode is described by either of equations (3.26) and (3.28) with $\tau_{xy}=0$. Mode 2 buckling was analyzed in Section

3.2b; it is described by eqns (3.14)-(3.16), which, for the combination of stresses for which buckling mode 2 dominates over buckling mode 1, give an approximately linear relationship between σ_x and σ_y. For isotropic honeycombs, this relationship is well approximated by the following equation

$$-3.751\frac{l^3}{E_s t^3}\sigma_x - 1.963\frac{l^3}{E_s t^3}\sigma_y = 1 \qquad (3A.14)$$

Therefore, a conservative estimate of the elastoplastic interaction associated with mode 2 buckling is given as

$$\pm 2\left[\frac{\sigma_x\left(\frac{h}{l}+\sin\theta\right)\sin\theta - \sigma_y\cos^2\theta}{\sigma_{ys}(t/l)^2}\right] - \frac{l^3}{E_s t^3}(3.751\sigma_x + 1.963\sigma_y)$$

$$+\left[\frac{\sigma_x\left(\frac{h}{l}+\sin\theta\right)\cos\theta + \sigma_y\sin\theta\cos\theta}{\sigma_{ys}(t/l)}\right]^2 = 1 \qquad (3A.15)$$

The failure envelope for elastic-plastic honeycomb structures is described by the inner of the envelopes given by the elastoplastic interaction equations. It is illustrated in Fig. 3A.2 for isotropic honeycombs under normal in-plane stresses.

References

Abd El-Sayed, F. K., Jones, R. and Burgess, I. W. (1979) A Theoretical Approach to the Deformation of Honeycomb Based Composite Materials, *Composites*, **10**, 209.

Ashby, M. F. (1983) The Mechanical Properties of Cellular Solids, *Met. Trans.*, **14A**, 1755.

Ashby, M. F. and Jones, D. (1986) *Engineering Materials 2*, Pergamon, Oxford.

Drucker, D. C. (1960) Plasticity, *Proc. 2nd Symp. Nav. Struct. Mech., Providence, R. I., 1959*, Pergamon, New York, 170.

Elias, Z. M. (1986) *Theory and Methods of Structural Analysis*, John Wiley & Sons, Inc.

Ewalds, H. L. and Wanhill, R. J. H. (1984) *Fracture Mechanics*, Arnold DUM, London.

Forman, S. E. and Hutchinson, J. W. (1970) Buckling of Reticulated Shell Structures, *Int. J. Solids and Structures*, **6**, 909.

Gibson, L. J. (1981) The Elastic and Plastic Behaviour of Cellular Materials, Ph.D. Thesis, Cambridge University Engineering Department, Cambridge, U.K.

Gibson, L. J., Ashby, M. F., Schajer, G. S. and Robertson, C. I. (1982) The Mechanics of Two-Dimensional Cellular Materials, *Proc. R. Soc. Lond.*, **A382**, 25.

Gibson, L. J. and Ashby, M. F. (1988) *Cellular Solids: Structure and Properties*, Pergamon, Oxford.

Goldberg, J.E. (1968) Lateral Buckling of Braced Multistory Frames, *J. Struct. Div., ASCE*, **94**(12), 2963.

Griffith, A. A. (1924) The Theory of Rupture, *Proc. 1st Int. Con. Appl. Mech. Delft*, 55.

Hertzberg, R. W. (1983) *Deformation and Fracture Mechanics of Engineering Materials*, 2nd edn., John Wiley & Sons, Inc.

Hexcel TSB124 (1984) *The Basics of Bonded Sandwich Construction.*

Hexcel TSB120 (1986) *Mechanical Properties of Hexcel Honeycomb Materials.*

Horne, M. R. (1963) Elastic-Plastic Failure Loads of Plane Frames, *Proc. R. Soc. Lond.*, **A274**, 343.

Horne, M. R. and Morris, L. J. (1981) *Plastic Design of Low-Rise Frames*, Granada, London.

Kachanov, L. M. (1974) *Fundamentals of the Theory of Plasticity*, MIR Publishers, Moscow.

Kelsey, G. Gellatly, R. A. and Clark, B. W. (1958) The Shear Modulus of Foil Honeycomb Structures, *Aircraft Engineering*, **30**, 294.

Klintworth, J. and Stronge, W. (1988) Elasto-Plastic Yield Limits and Deformation Laws for Transversely Crushed Honeycombs, *Int. J. Mech. Sci.*, **30**, 273.

Malvern, L. E. (1969) *Introduction to the Mechanics of a Continuous Medium*, Prentice-Hall, Inc.

Massonnet, C. E. and Save, M. A. (1965) *Plastic Analysis and Design, I, Beams and Frames*, Blaisdell Publishing Company, Mass., U.S.A.

McClintock, F. A. and Argon, A. S. (1966) *Mechanical Behavior of Materials*, Addison-Wesley, Mass., U.S.A.

Merchant, W. (1954) The Failure Load of Rigid Jointed Frameworks as Influenced by Stability, *Struct. Engr.* **32**, 185.

Patel, M. R. and Finnie, I. (1970) Structural Features and Mechanical Properties of Rigid Cellular Plastics, *J. Materials*, **5**, 909.

Renton, J. D. (1964) On the Stability Analysis of Symmetrical Frameworks, *Quart. J. Mech. and Applied Math.*, **17**, 175.

Timoshenko, S. P. and Gere, J. M. (1961) *Theory of Elastic Stability*, 2nd edn., McGraw-Hill.

Triantafillou, T. C., Zhang, J., Shercliff, T., Gibson, L. J. and Ashby, M. F. (1989) submitted to *Int. J. Mech. Sci.*

U.S. Department of Defense (1974), *Structural Sandwich Composites*, MIL HDBK-23A.

Verticel Companies, *Structural Design of Honeycomb Sandwich Panels*.

Wah, T. (1965) The Buckling of Gridworks, *J. Mech. Phys. Solids*, **13**, 1.

Warren, W. E. and Kraynic, A. M. (1987) The Linear Elastic Properties of Open-Cell Foams, *Mechanics of Materials*, **6**, 27.

Weibull, W. (1951) A Statistical Distribution Function of Wide Applicability, *J. Appl. Mech.*, **18**, 293.

Zhang, J. (1987) Mechanics of Cellular Materials, CPGS Thesis, Cambridge University

Engineering Department, Cambridge, U.K.

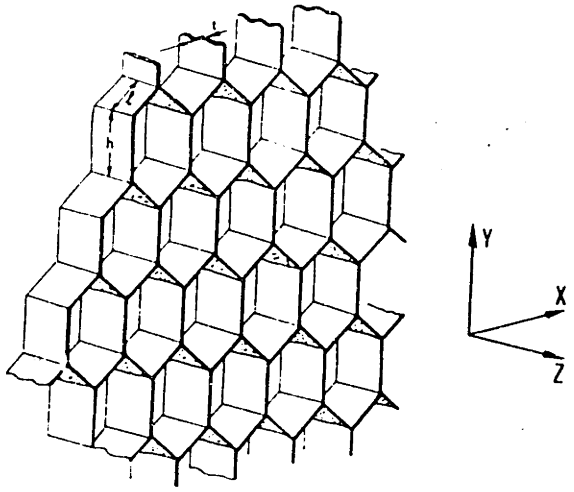

Fig. 3.1 A honeycomb with hexagonal cells (after Gibson and Ashby, 1988).

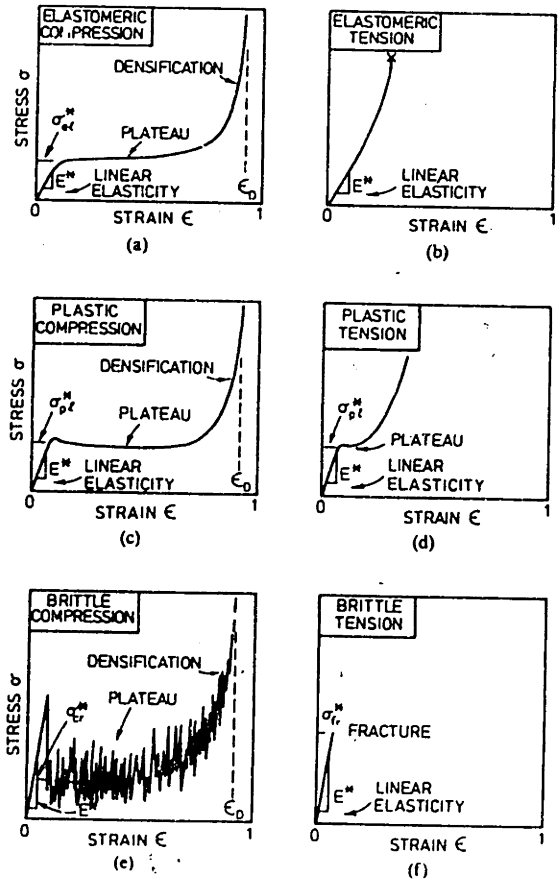

Fig. 3.2 Uniaxial compressive and tensile stress-strain curves for honeycombs: (a) and (b) elastomeric honeycomb; (c) and (d) elastic-plastic honeycomb; (e) and (f) elastic-brittle honeycomb (after Gibson and Ashby, 1988).

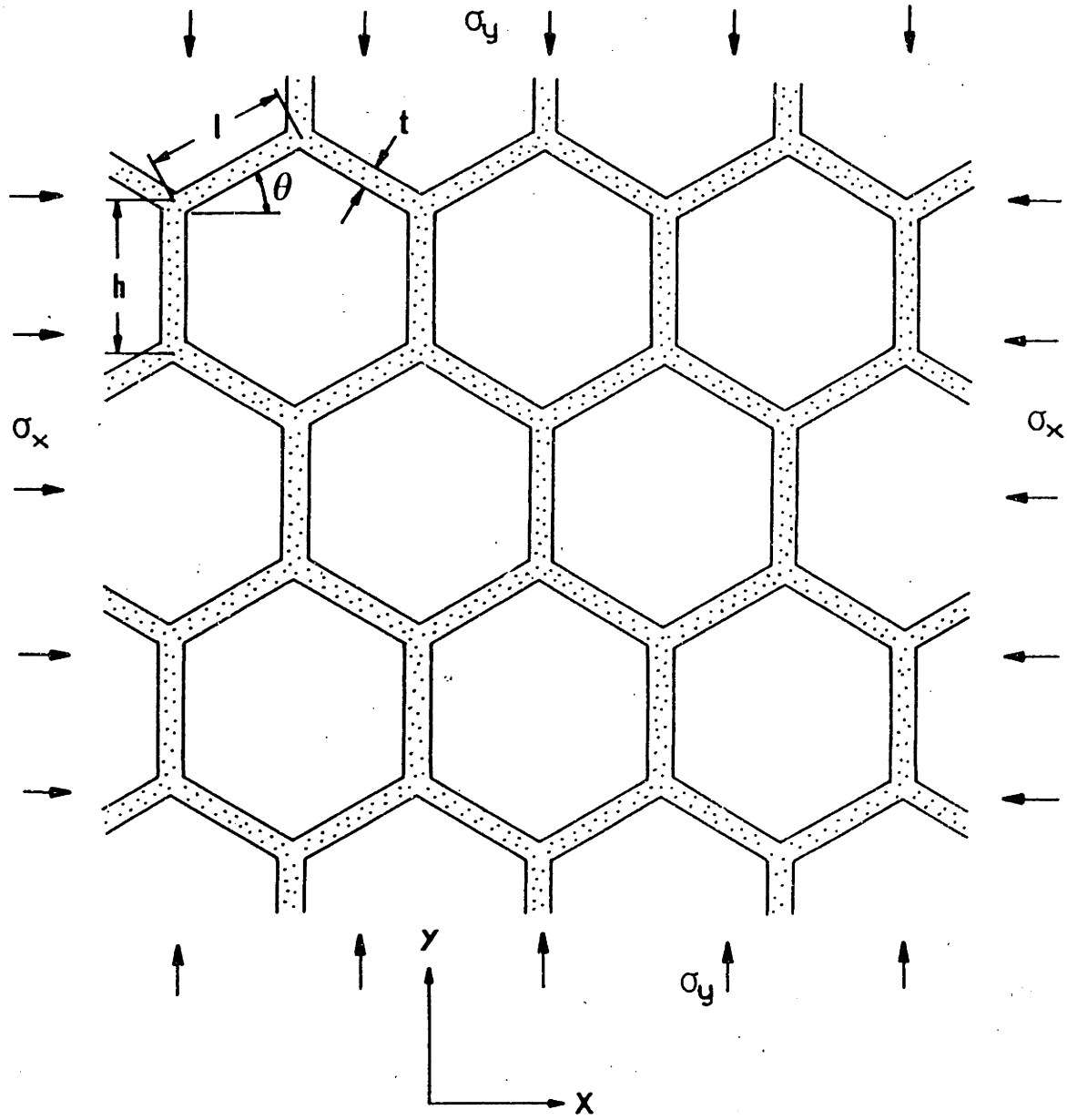

Fig. 3.3 An idealized honeycomb made up of an array of hexagonal cells and its geometric characteristics.

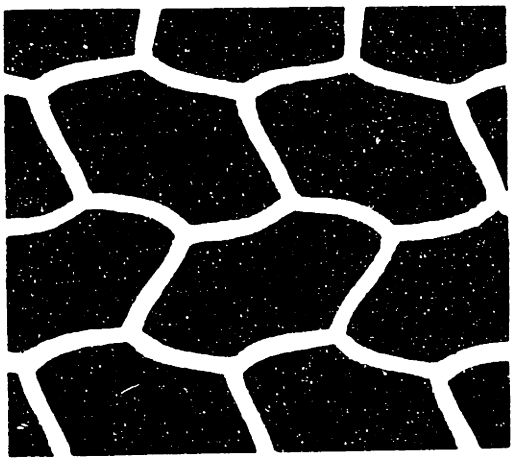

(a)

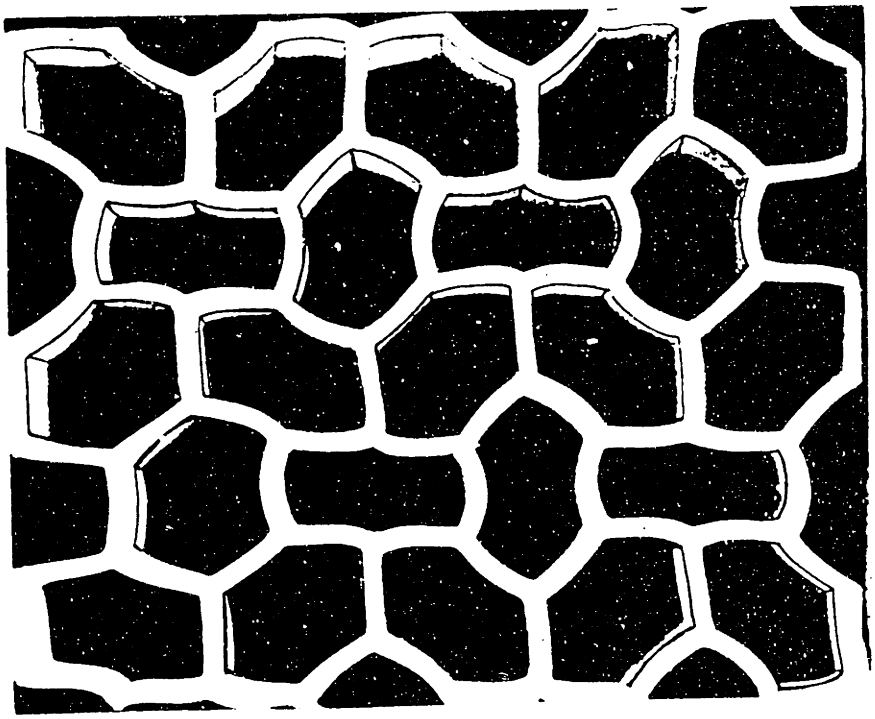

(b)

Fig. 3.4 Buckling modes for an elastomeric honeycomb: (a) mode 1; (b) mode 2 (after Gibson and Ashby, 1988).

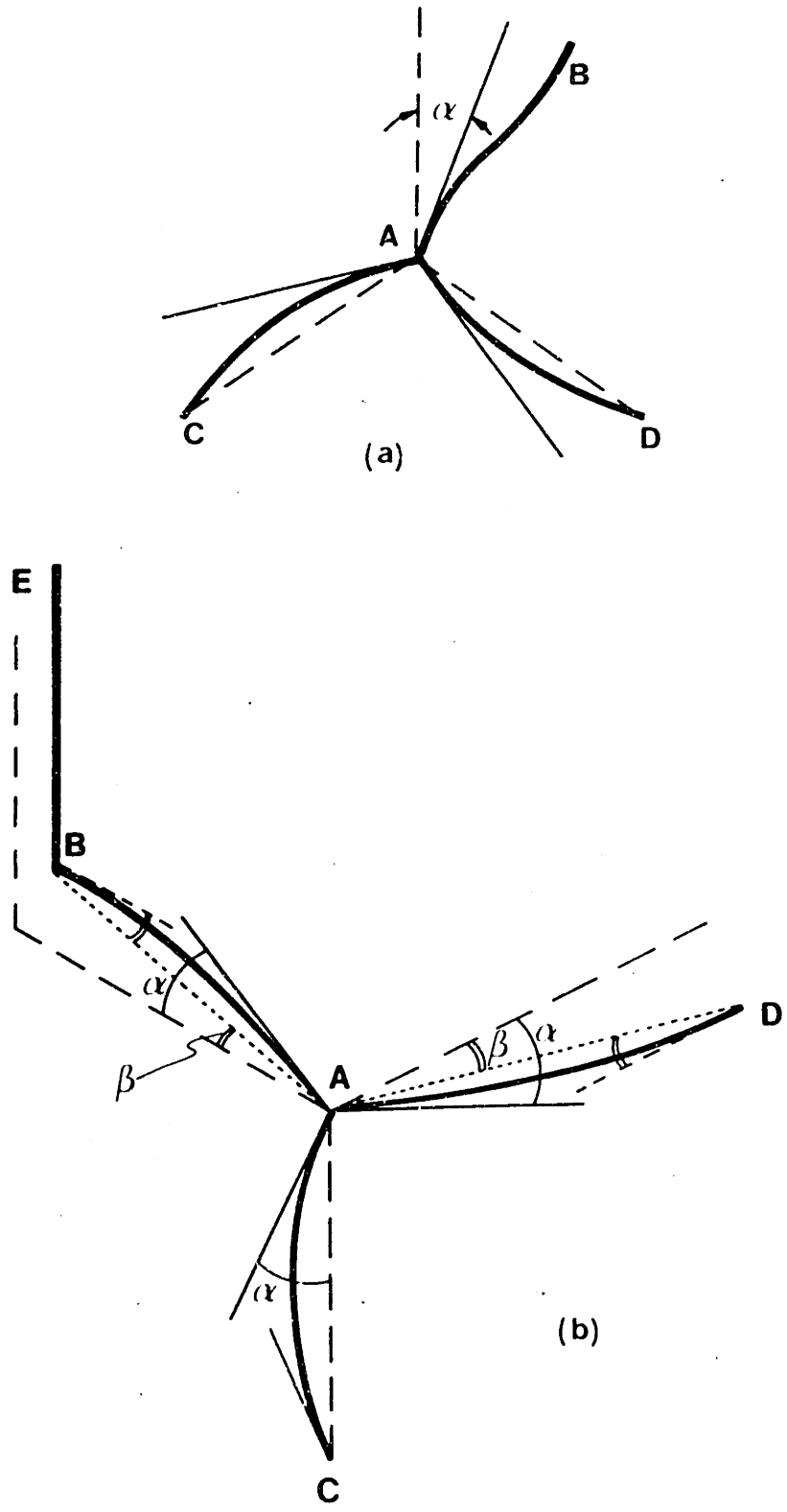

Fig. 3.5 Buckling pattern of cell walls in honeycombs: (a) mode 1; (b) mode 2.

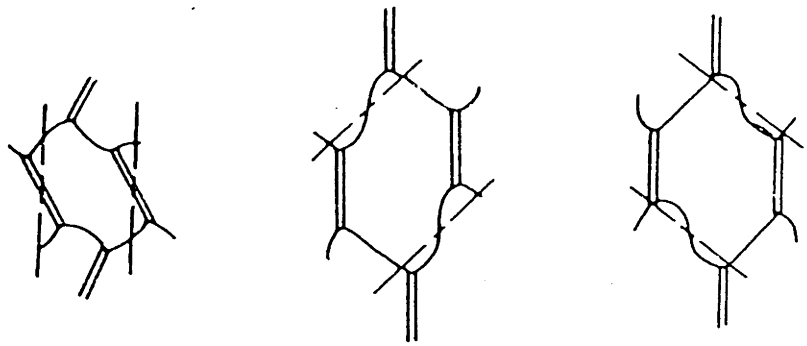

(a)

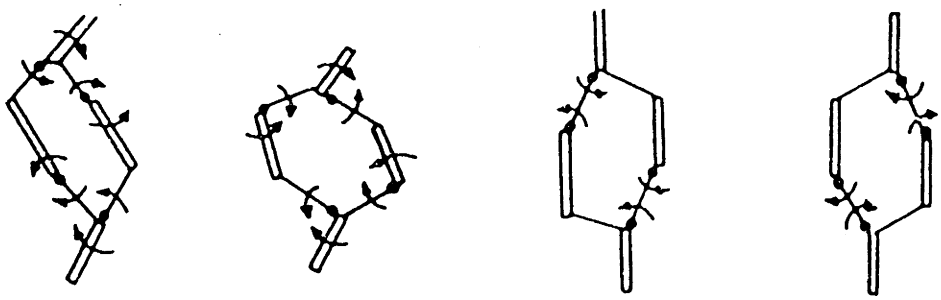

(b)

Fig. 3.6 (a) Elastic buckling collapse modes; (b) plastic collapse modes (after Klintworth and Stronge, 1988).

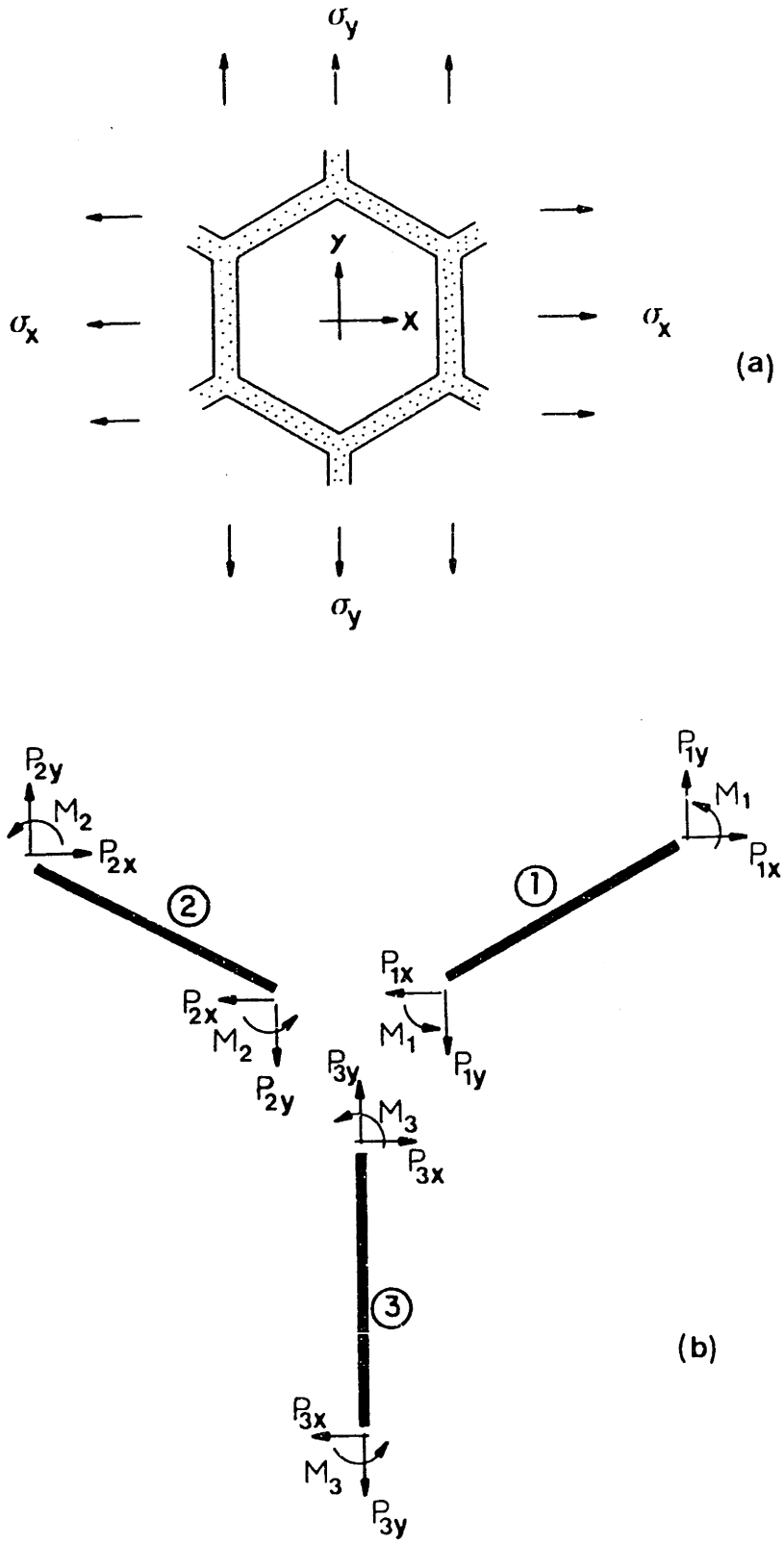

Fig. 3.7 (a) Stresses σ_x and σ_y acting on a unit cell of the honeycomb model. (b) The forces and the moments acting on the members.

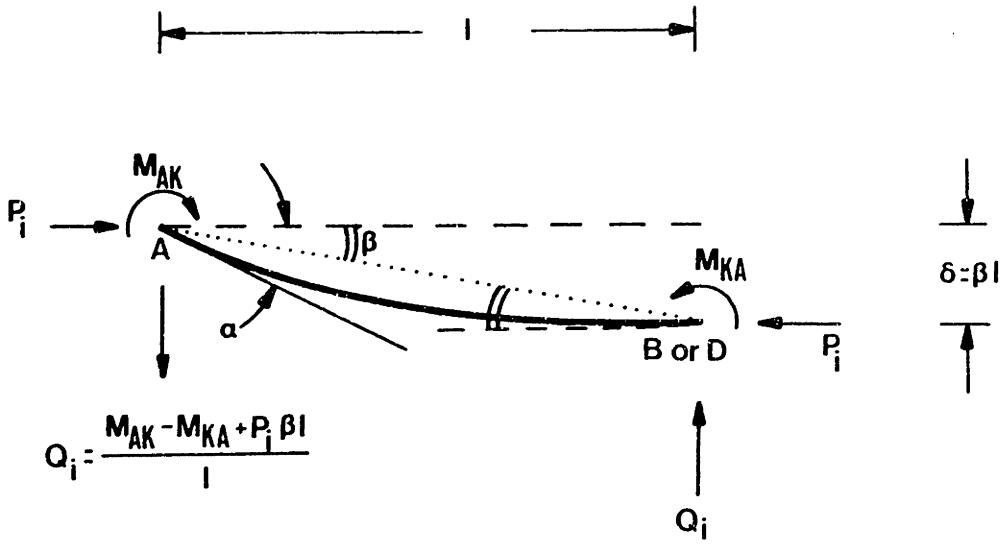

(a)

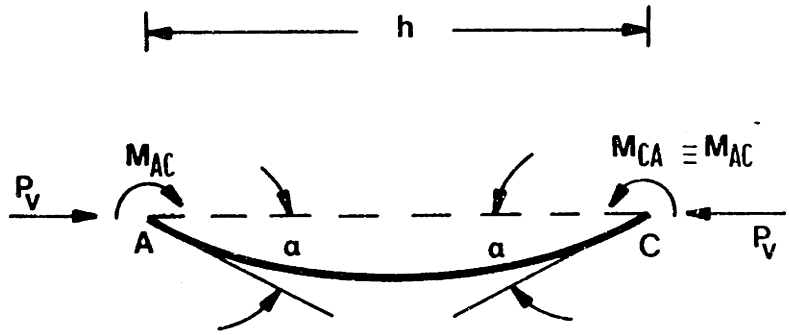

(b)

Fig. 3.8 Deformation of members and notation used in the slope-deflection equations.

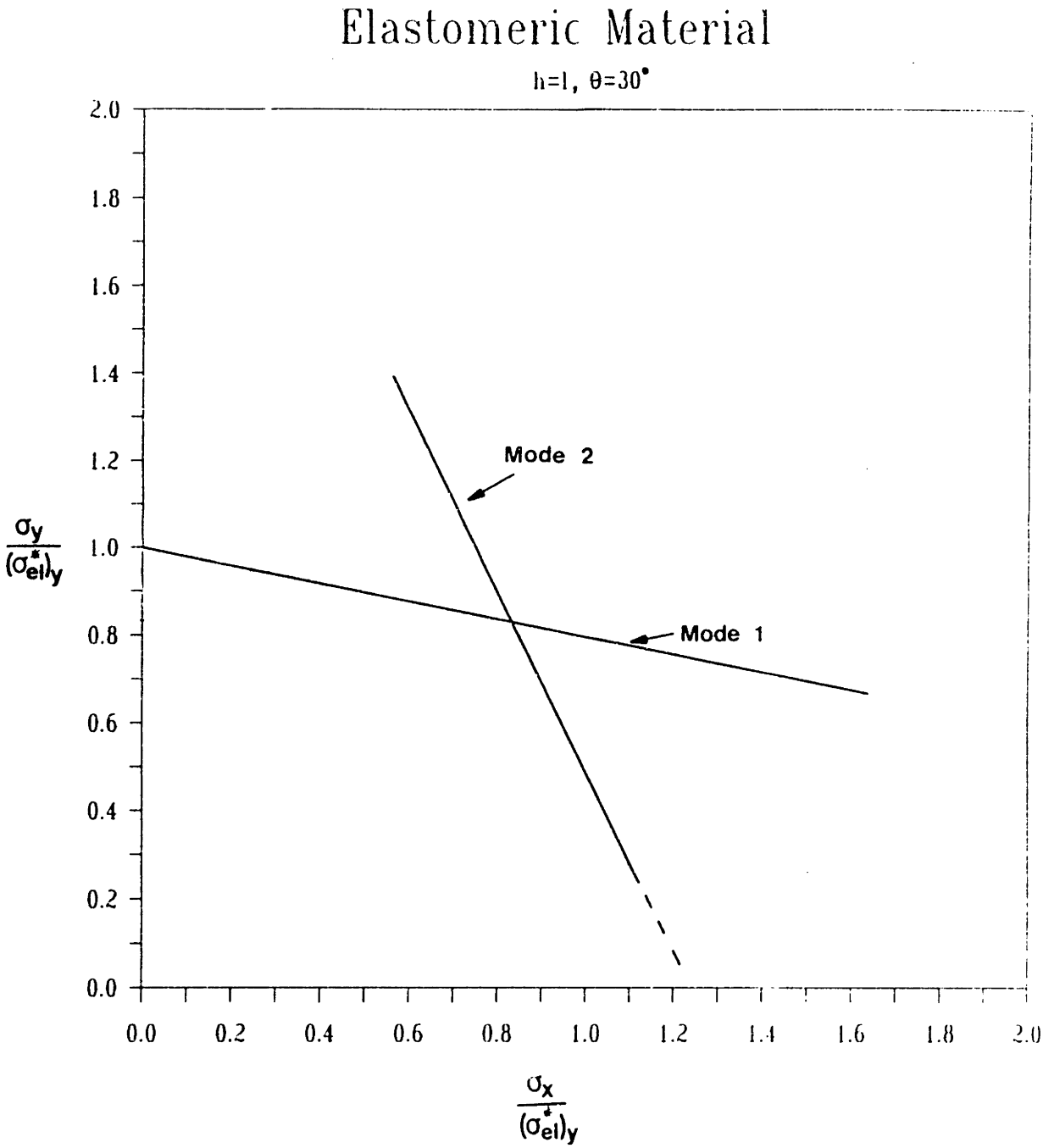

Fig. 3.9 The failure envelope for the elastic buckling of an elastomeric honeycomb with regular hexagonal cells under biaxial loading.

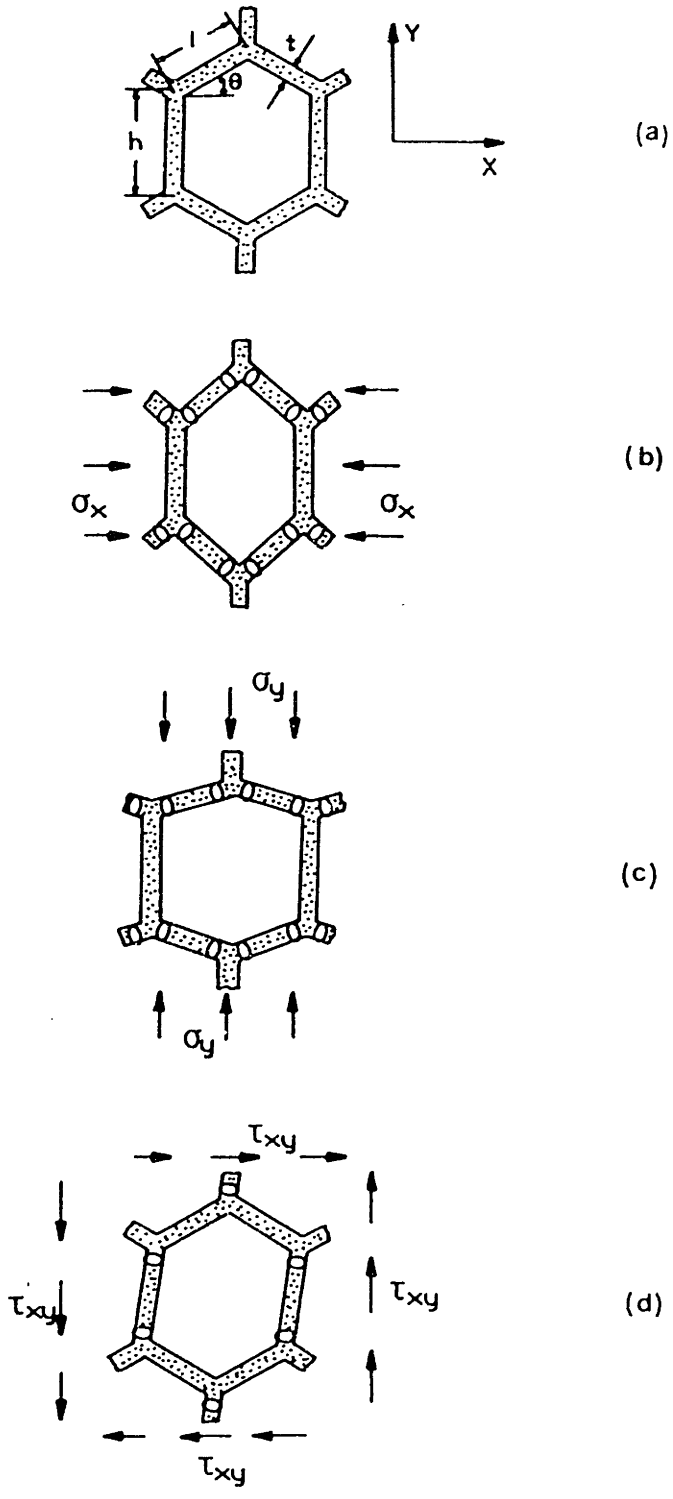

Fig. 3.10 Cell deformation and location of plastic hinges: (a) the undeformed honeycomb; (b) uniaxial loading in the X direction ; (c) uniaxial loading in the Y direction ; (d) simple shear loading in the X-Y plane.

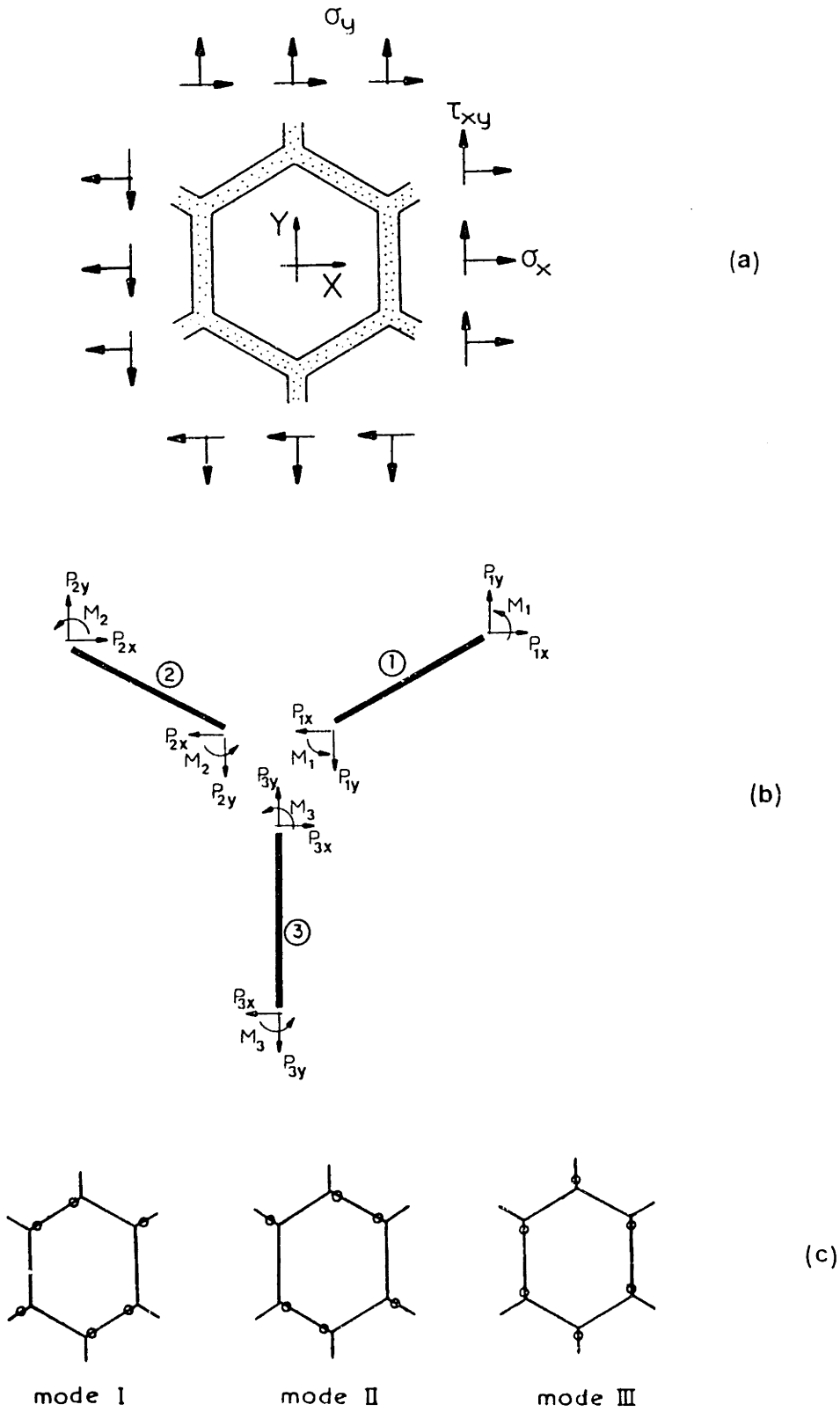

Fig. 3.11 (a) In-plane stresses acting on a unit cell of the honeycomb model. (b) The forces and the moments acting on the members. (c) The three collapse modes.

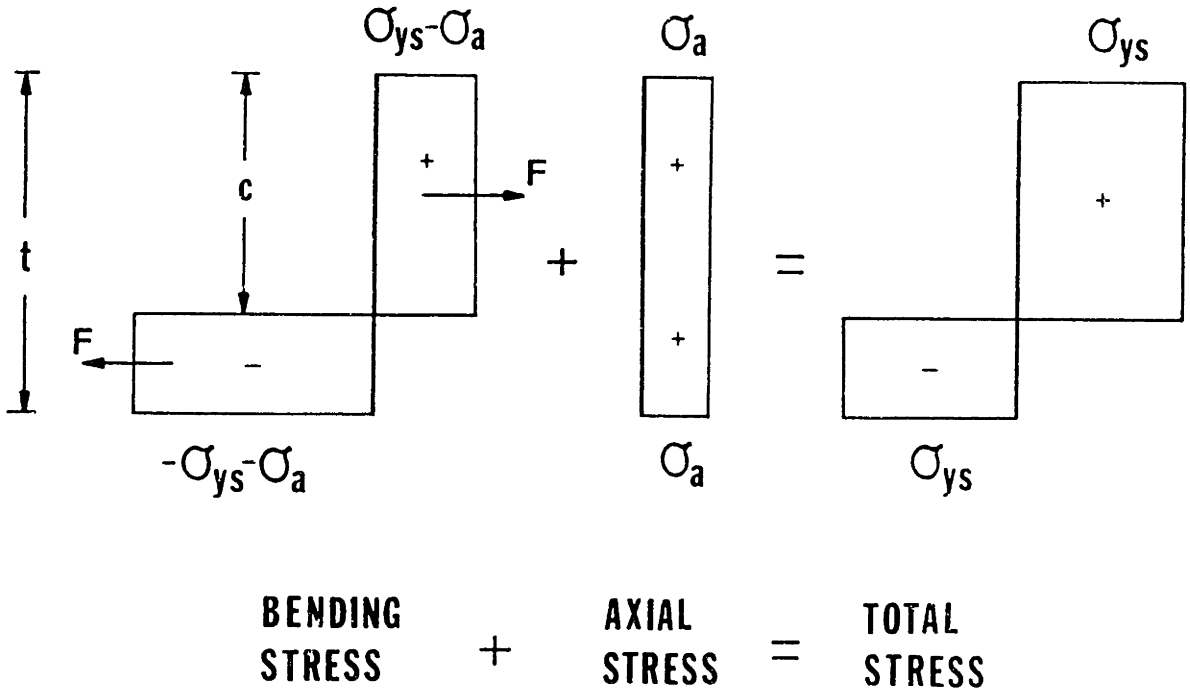

Fig. 3.12 The bending, axial, and total stress distributions across the section at the formation of a plastic hinge.

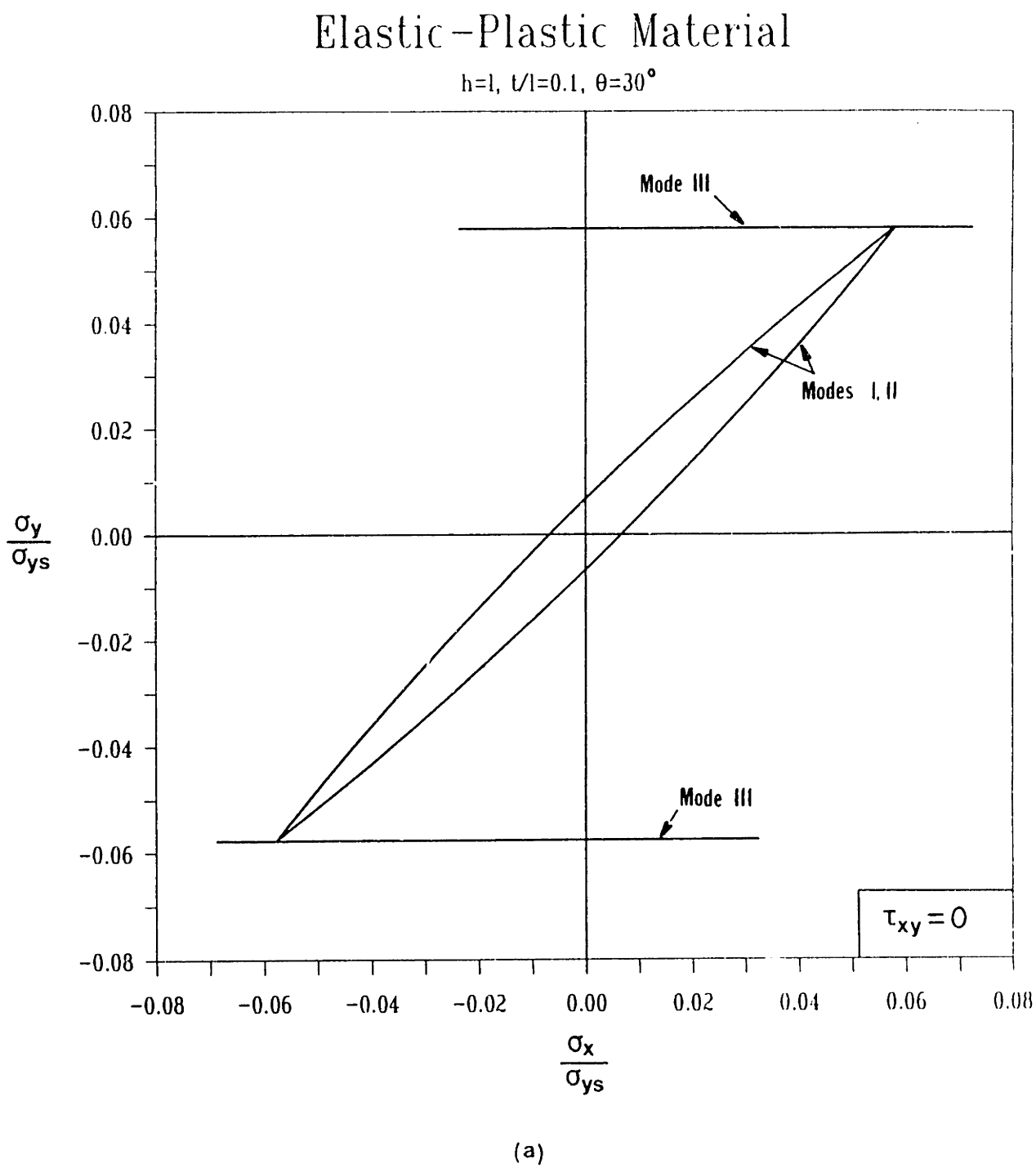

(a)

Fig. 3.13 The plastic yield surface for an idealized, two-dimensional cellular solid made up of regular cells. (a) $\tau_{xy}=0$; (b) $\sigma_y=0$; (c) $\sigma_x=0$.

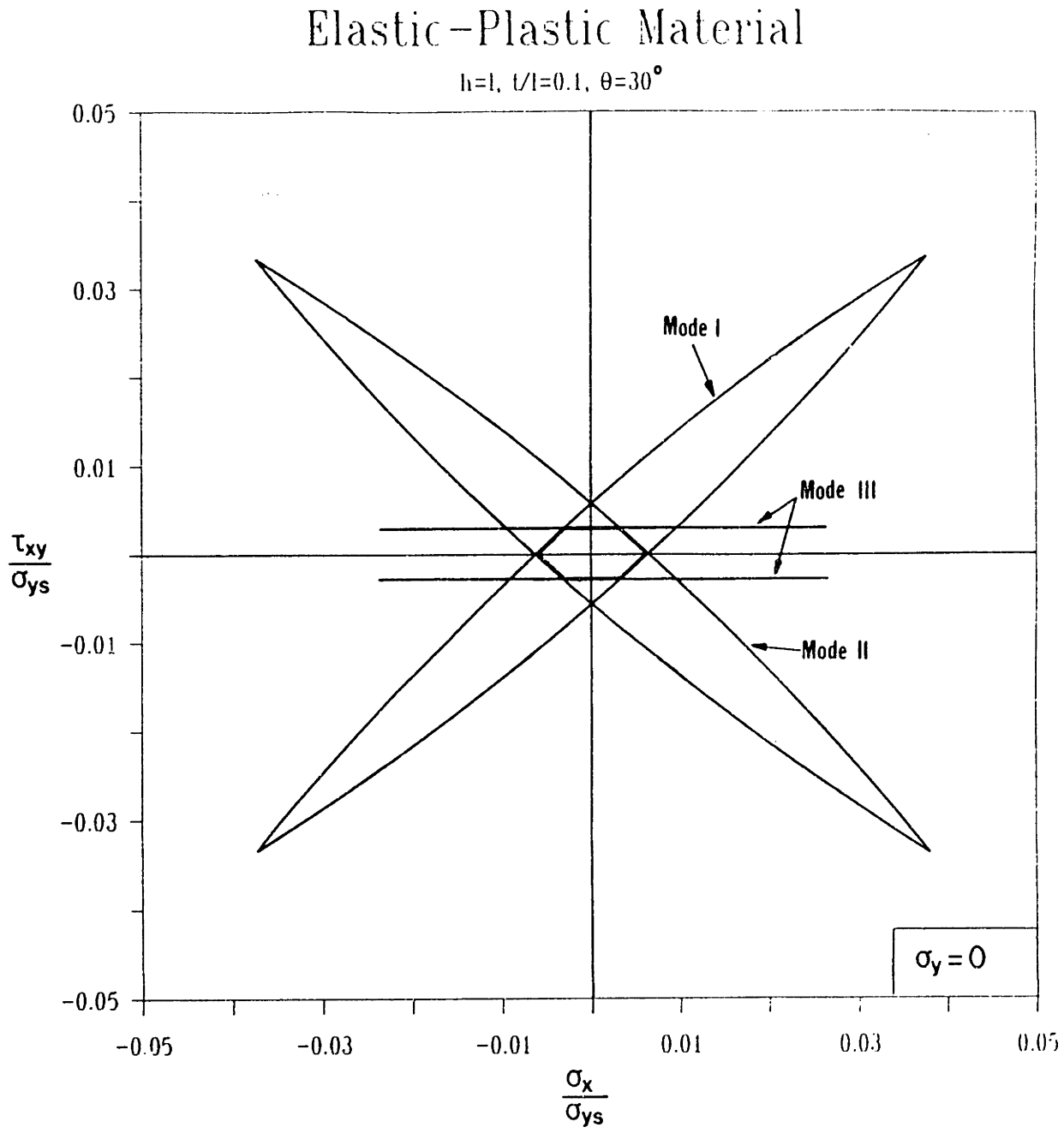

(b)

Fig. 3.13 cont'd.

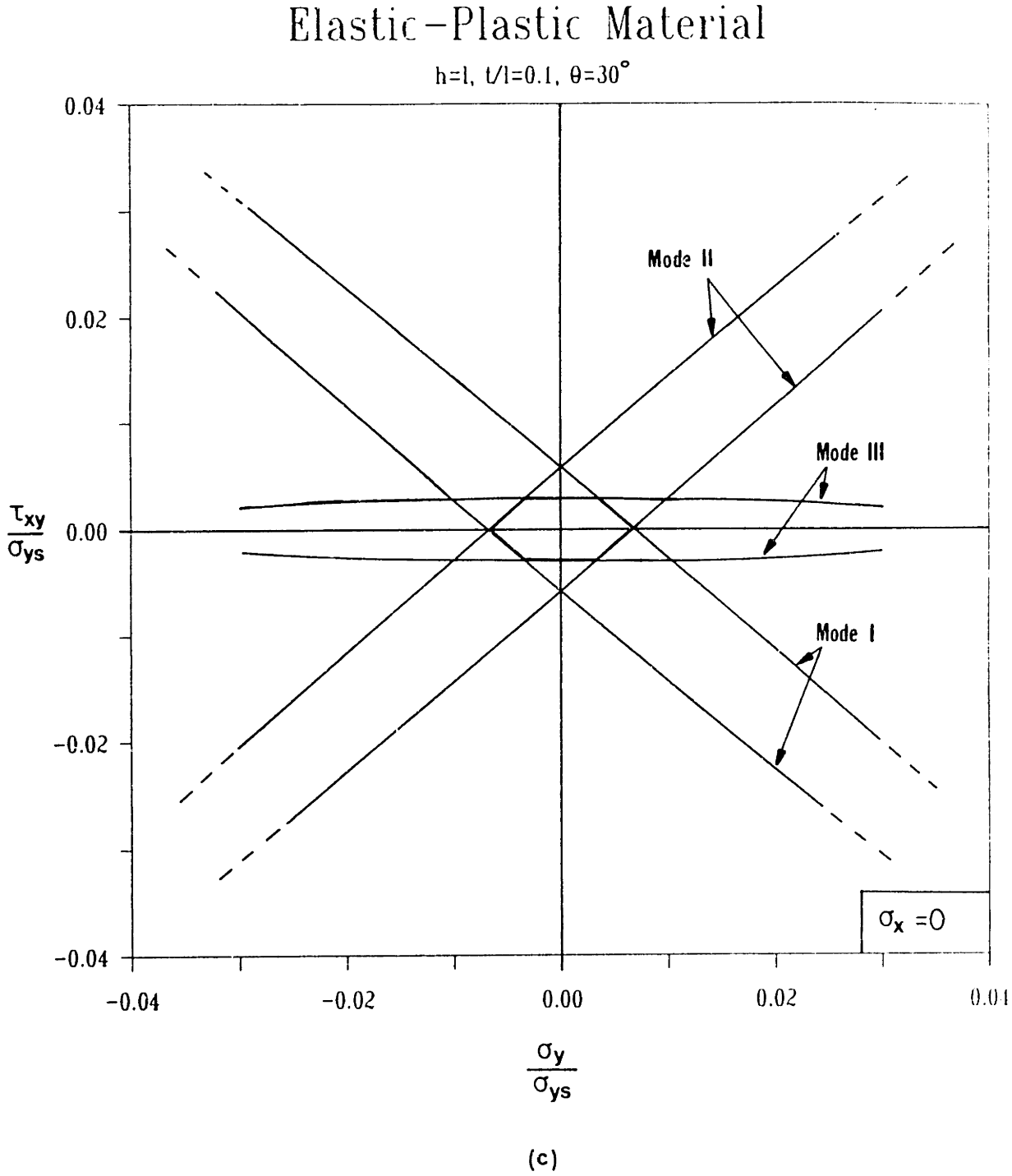

(c)

Fig. 3.13 cont'd.

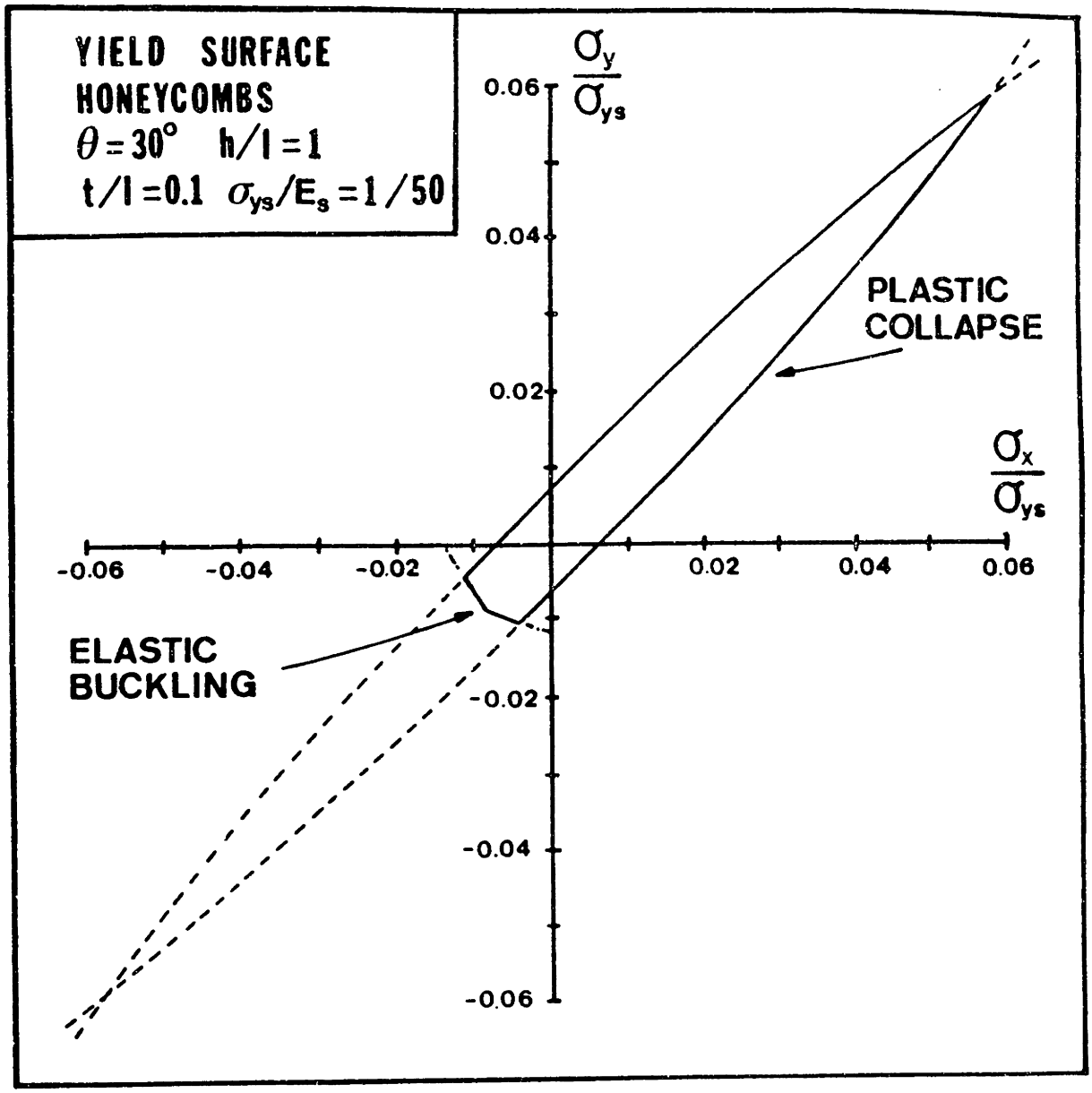

Fig. 3.14 The plastic collapse envelope for a two-dimensional cellular solid made up of regular hexagonal cells, truncated by the buckling collapse envelope in biaxial compression.

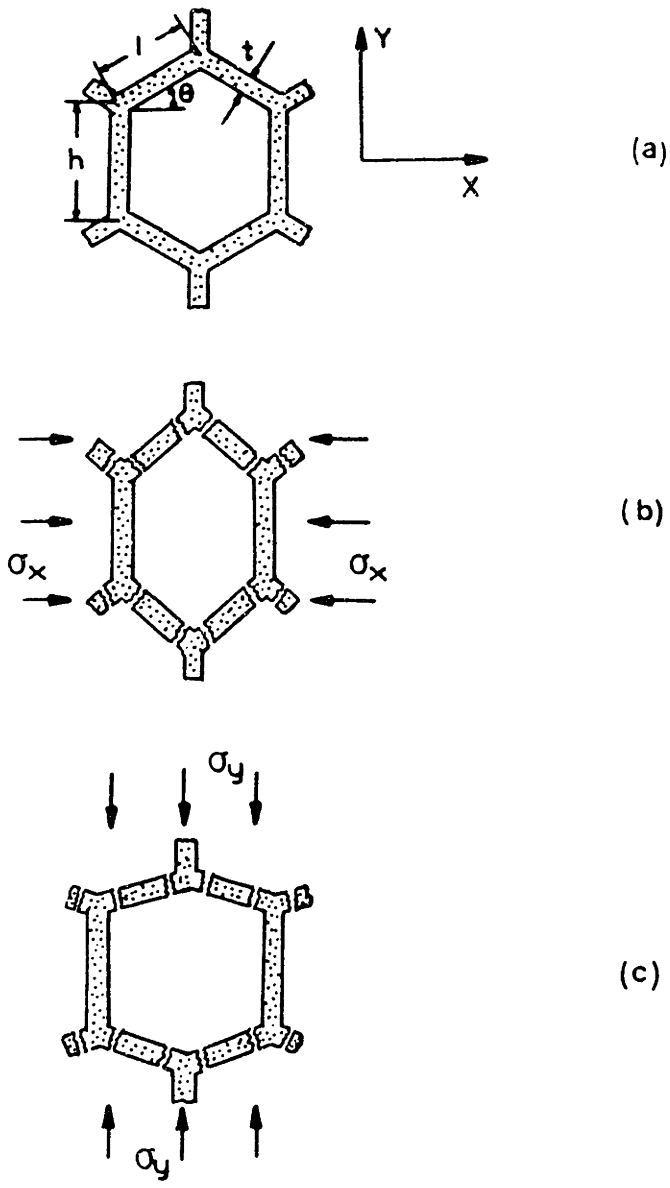

Fig. 3.15 Cell deformation and rupture: (a) the undeformed honeycomb; (b) uniaxial loading in direction X; (c) uniaxial loading in direction Y.

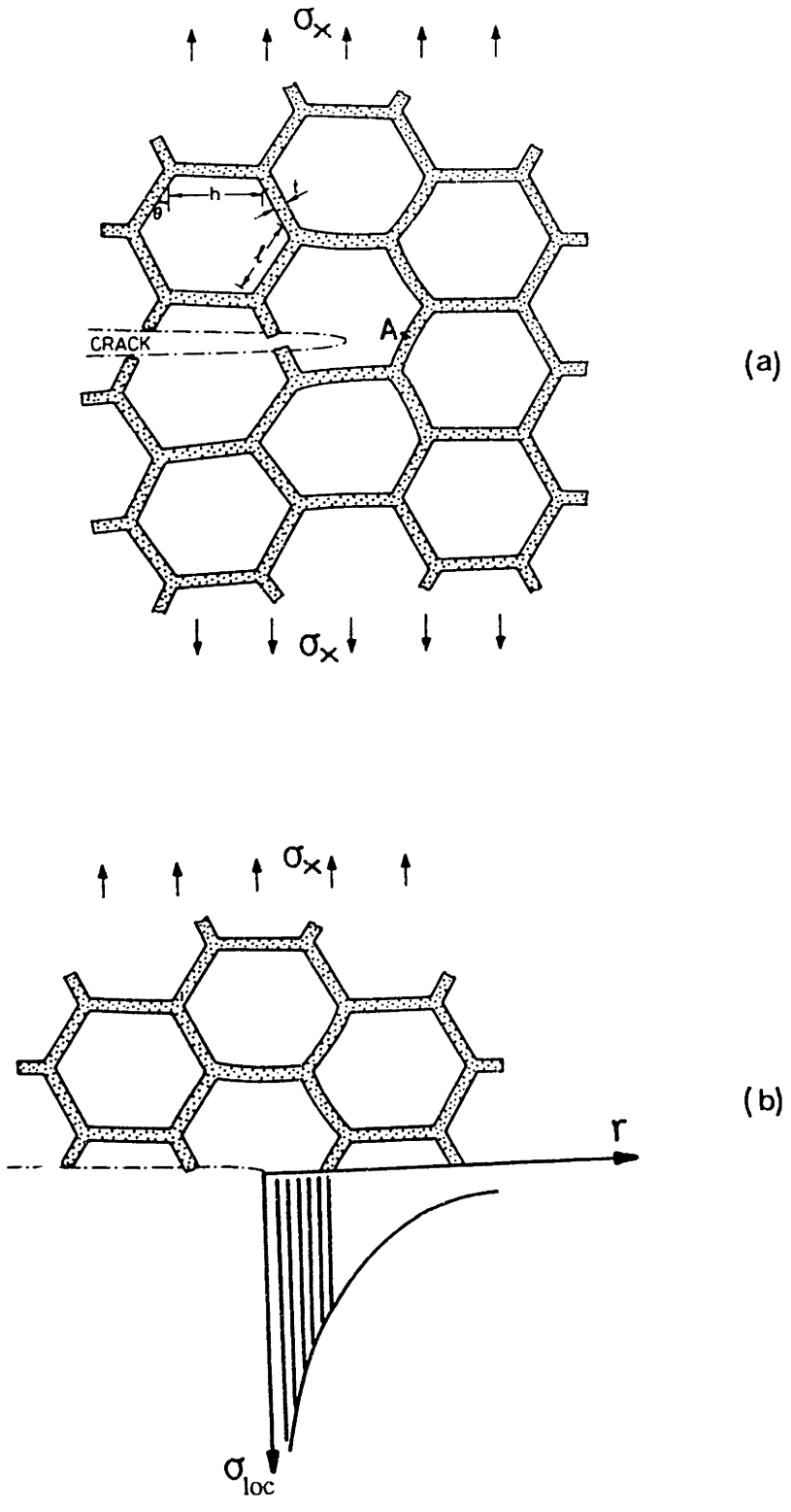

Fig. 3.16 Crack propagation leading to brittle tensile failure in a honeycomb: (a) the geometry for loading in the X direction; (b) local stress field at the crack tip.

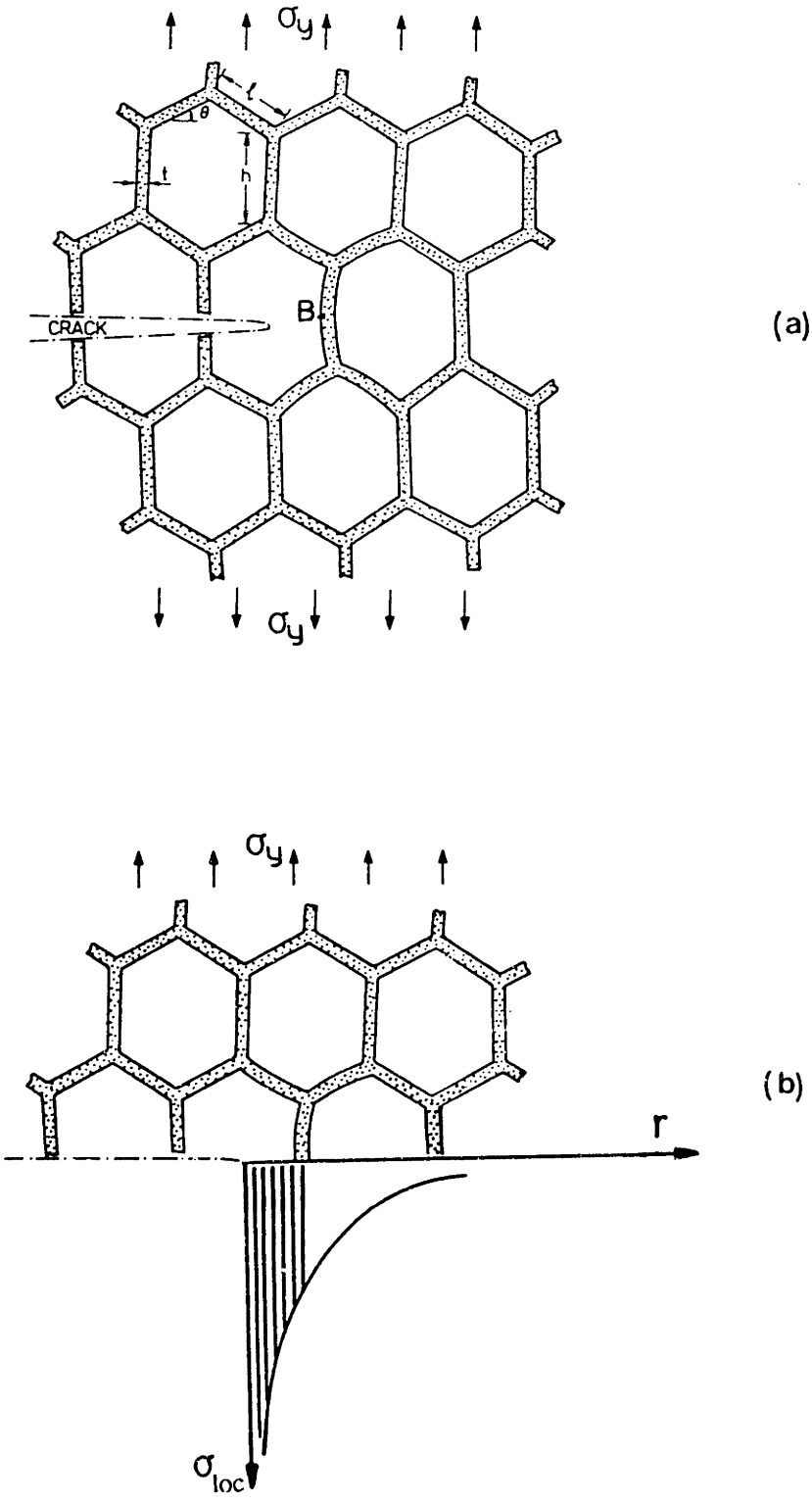

Fig. 3.17 Crack propagation leading to brittle tensile failure in a honeycomb: (a) the geometry for loading in the Y direction; (b) local stress field at the crack tip.

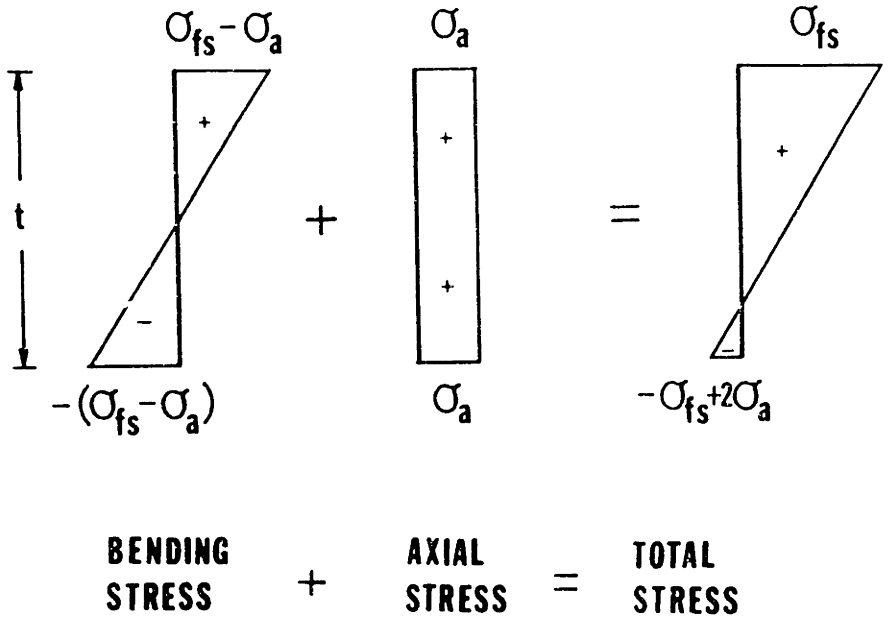

Fig. 3.18 The bending, axial, and total stress distributions across the section when the extreme tensile fiber stress reaches the modulus of rupture of the cell wall, σ_{fs}.

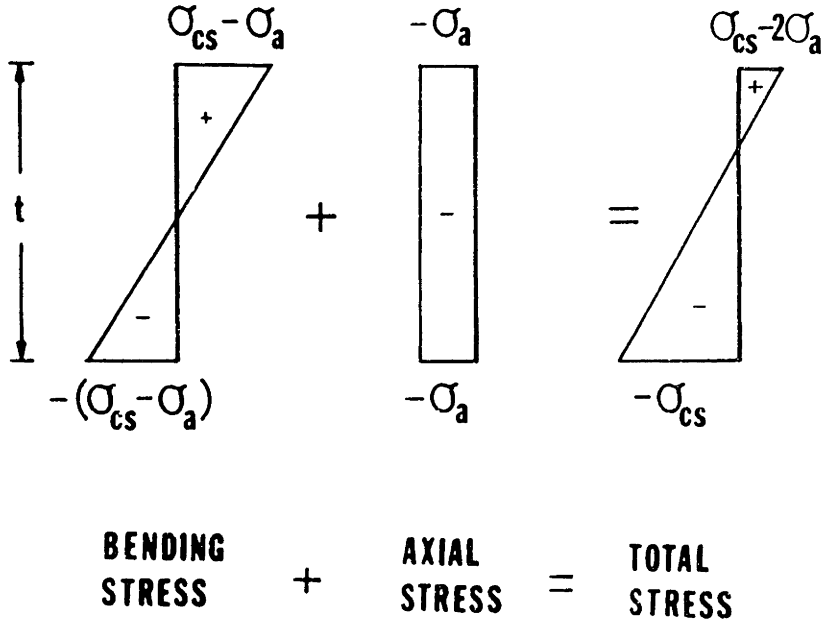

Fig. 3.19 The bending, axial, and total stress distributions across the section when the extreme compressive fiber stress reaches the compressive crushing strength of the cell wall, σ_{cs}.

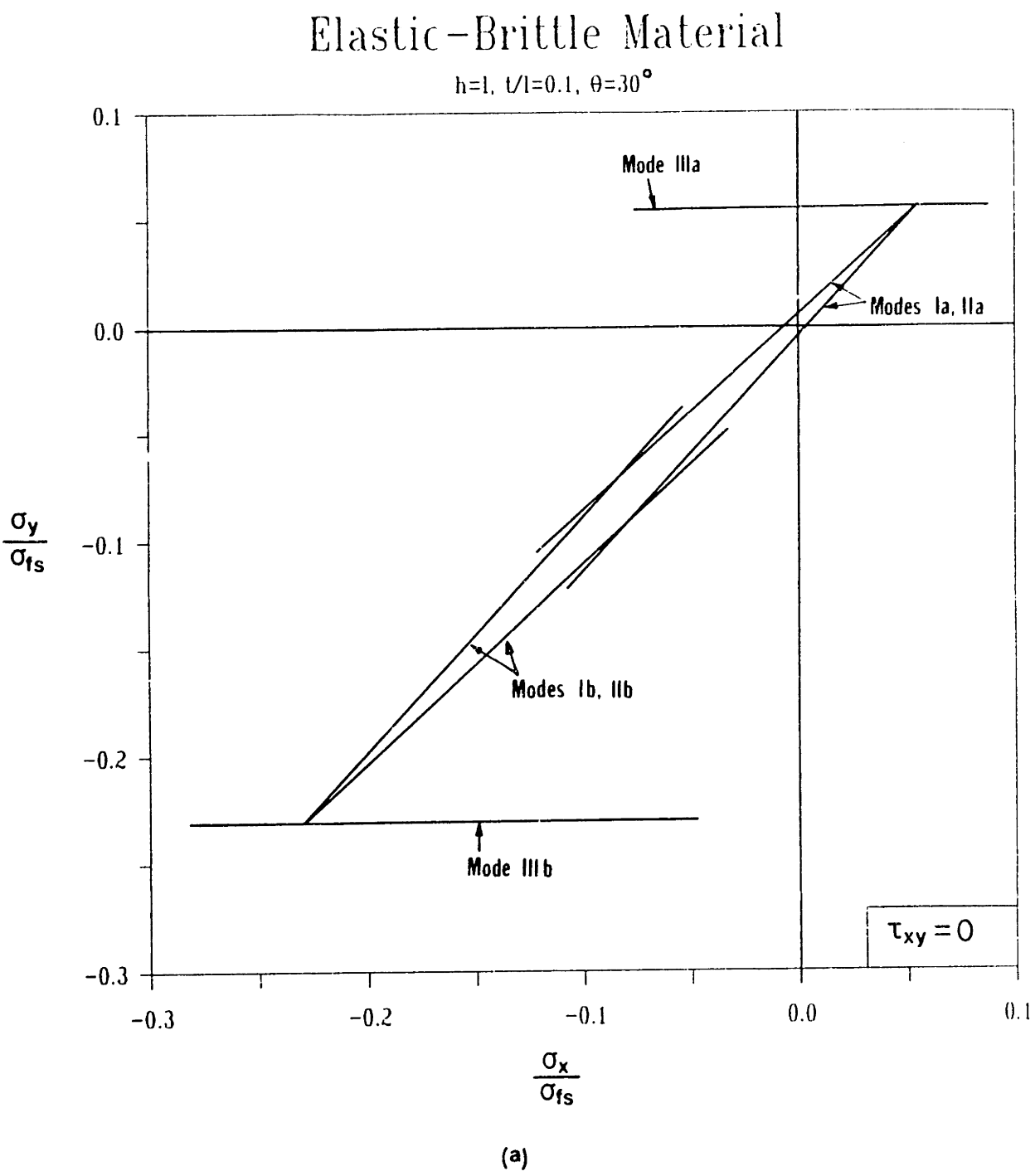

(a)

Fig. 3.20 The brittle collapse surface for an idealized, two-dimensional cellular solid with $\sigma_{cs}=4\sigma_{fs}$, made up of regular hexagonal cells. (a) $\tau_{xy}=0$; (b) $\sigma_y=0$; (c) $\sigma_x=0$.

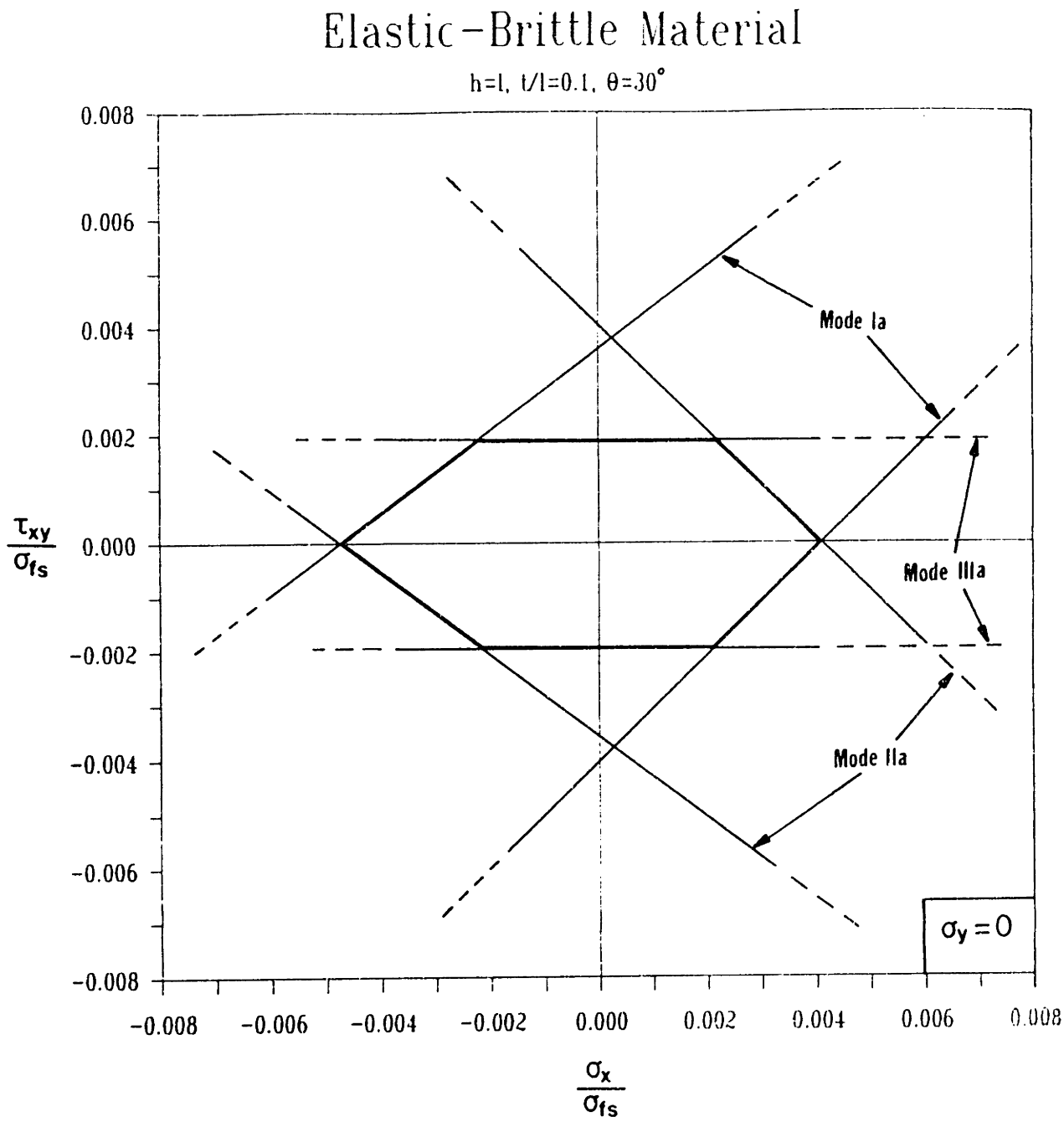

(b)

Fig. 3.20 cont'd.

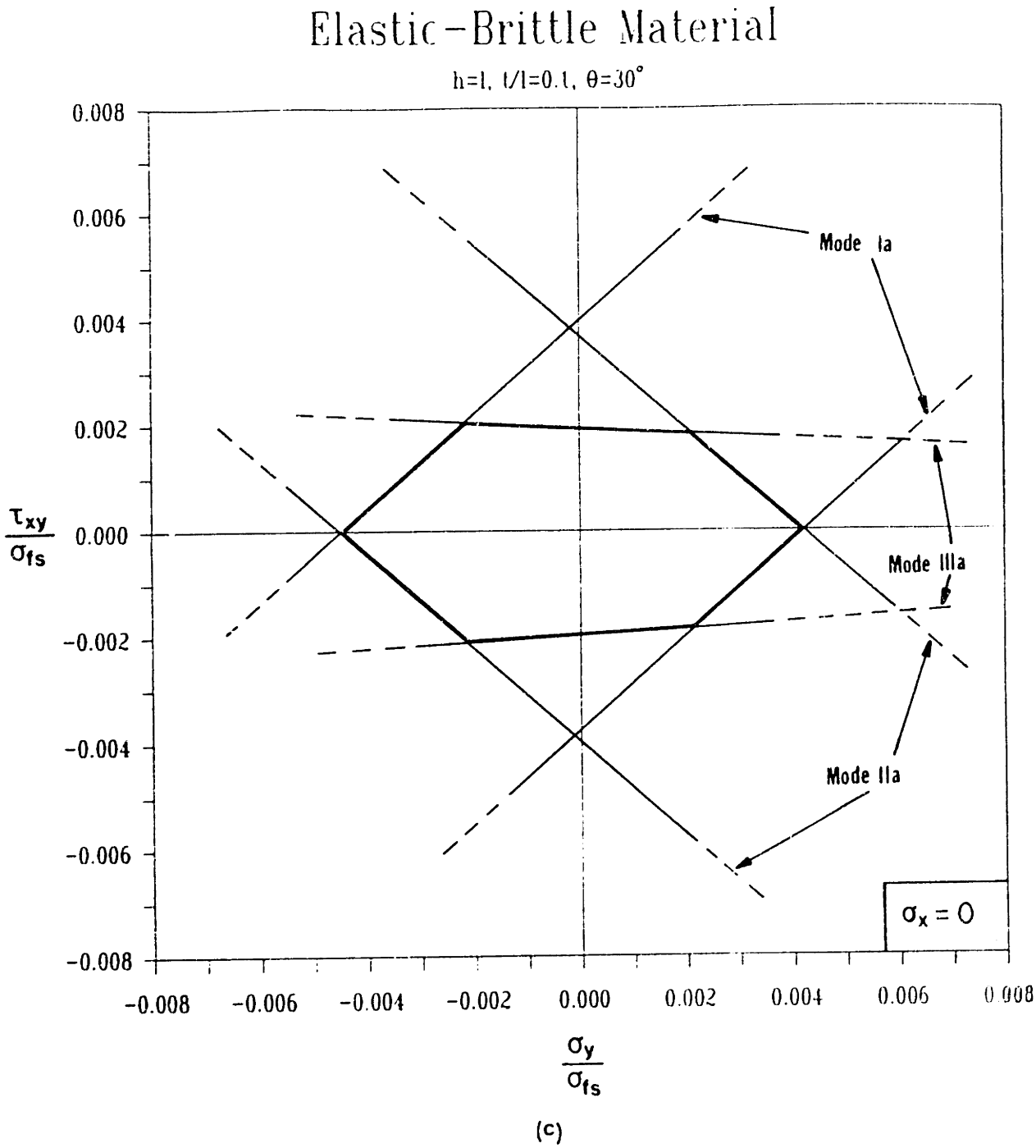

(c)

Fig. 3.20 cont'd.

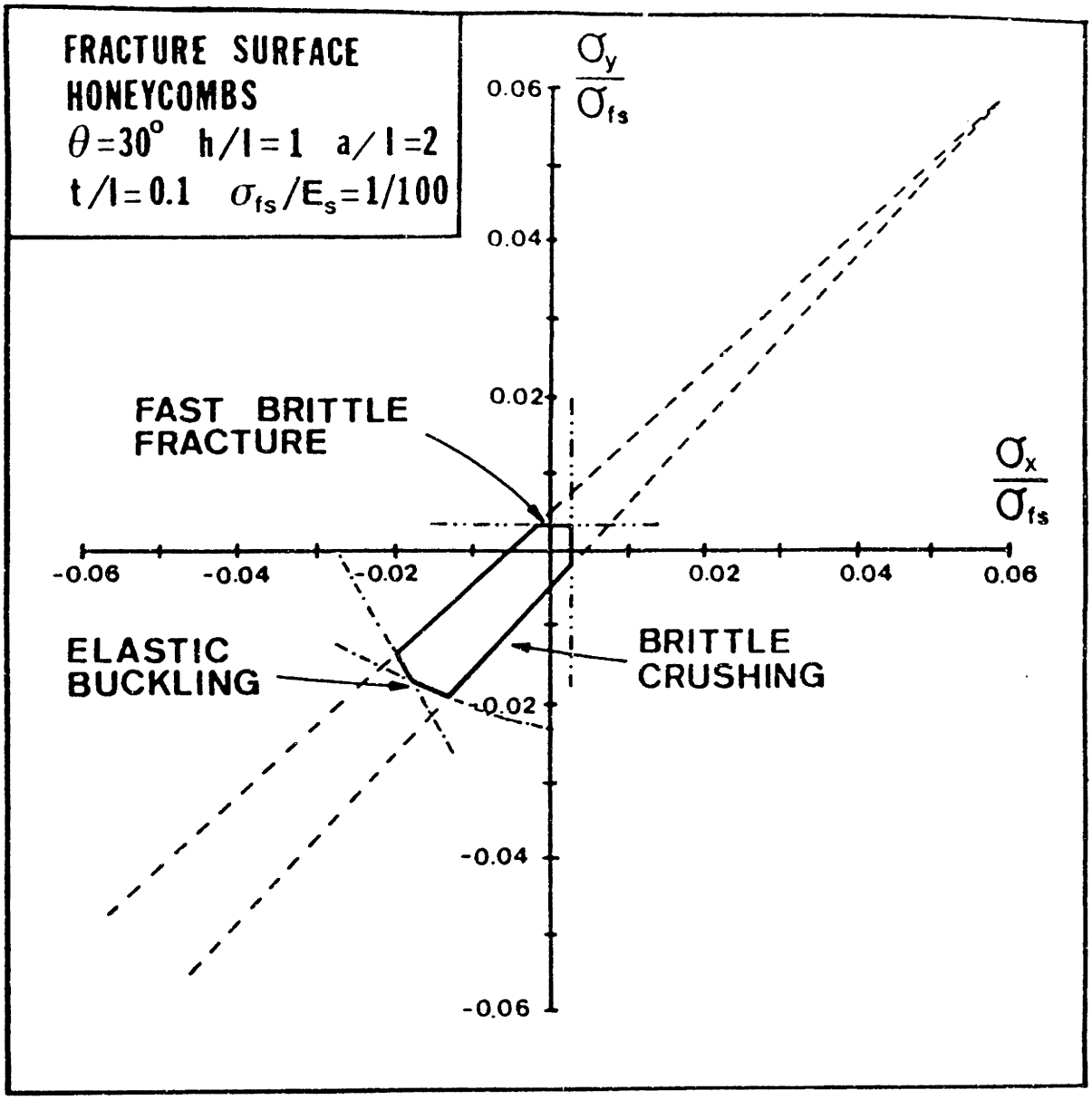

Fig. 3.21 The fracture envelope for a two-dimensional cellular solid (with $\sigma_{cs}=4\sigma_{fs}$) made up of regular hexagonal cells, truncated by fast brittle fracture in biaxial tension, and by elastic buckling in biaxial compression (the part of the envelope which corresponds to compressive crushing of the cell walls is outside the limits shown in the figure). $\tau_{xy}=0$.

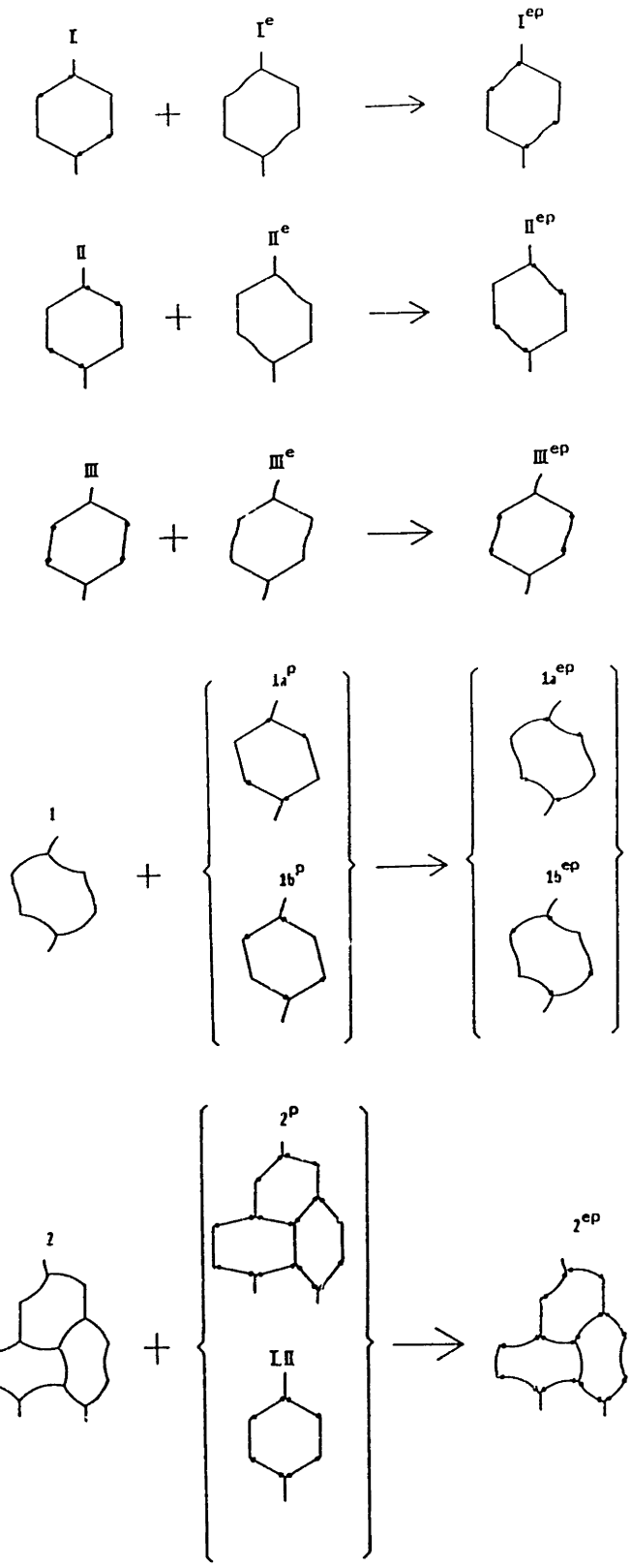

Fig. 3A.1 The elastic buckling and plastic collapse modes for honeycombs and their interaction.

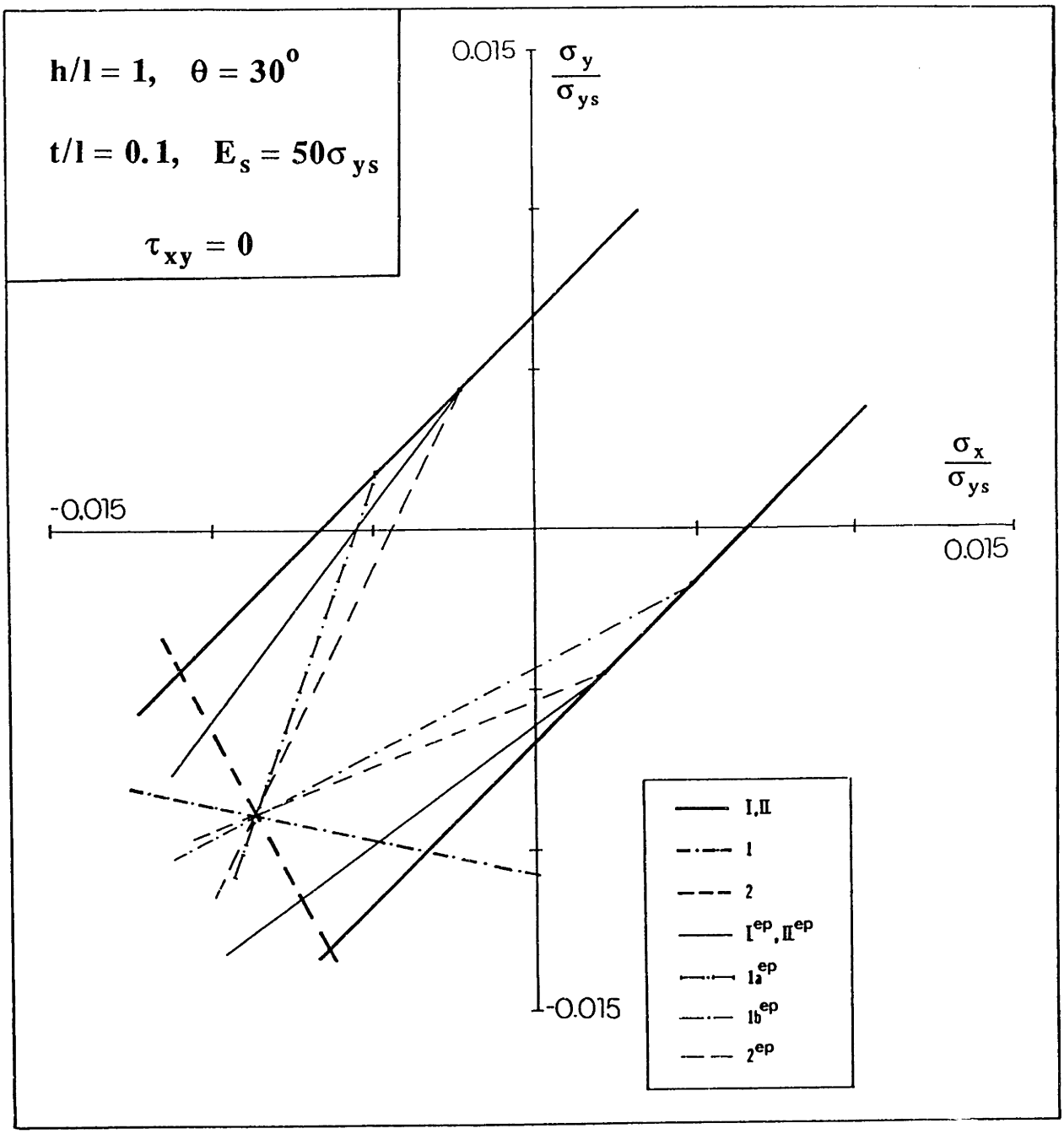

Fig. 3A.2 The elastic buckling, plastic collapse, and elastoplastic interaction failure envelopes for an isotropic honeycomb under normal in-plane stresses.

CHAPTER IV

MULTIAXIAL FAILURE CRITERIA FOR THREE-DIMENSIONAL CELLULAR MATERIALS

4.1 Introduction and Synopsis

There is a considerable literature on the mechanics of three-dimensional cellular materials (foams); reviews of it can be found in the papers by Suh and Skochdopole (1980), by Gibson and Ashby (1982), and by Suh and Webb (1985), and in the books edited by Wendle (1976), and Hilyard (1982), and written by Gibson and Ashby (1988). The literature on this topic is sometimes confused partly due to a misunderstanding of the mechanisms governing the behavior, and partly due to the geometric complexity of the materials' microstructure. Recent work has elucidated the material behavior to a great extent by combining simple mechanics with scaling ideas (Gibson and Ashby, 1982; Ashby, 1983; Maiti et al., 1984a, b).

Figure 4.1 shows uniaxial compressive stress-strain curves for elastomeric, elastic-plastic, and elastic-brittle foams. Like those for honeycombs, the initial linear elastic regime is followed by a long stress plateau truncated by a regime of densification in which the stress rises steeply. As with honeycombs, linear elasticity is controlled by *cell wall bending*, with some additional *cell face stretching* in the case of closed-cell foams. The plateau is associated with collapse of the cells: by *elastic buckling* in elastomeric foams, by the formation of *plastic hinges* in foams which yield, and by *brittle crushing* in elastic-brittle materials. The final region of rapidly increasing stress results from the compression of the solid material itself in almost completely collapsed cells, analogous to honeycombs. Tensile deformation, is different (Fig. 4.2). The initial linear elasticity is again caused by cell wall bending. But in elastomeric foams larger strains rotate the cell edges towards the tensile axis, increasing the stiffness of the

microstructure; buckling does not occur. In elastic-plastic materials the cell walls rotate towards the tensile axis, giving a yield point followed by a rising stress-strain curve, ultimately truncated by fracture. Finally, brittle foams fail by fast brittle fracture, as brittle honeycombs do, due to the propagation of pre-existing flaws.

Most foams are anisotropic because of the way in which they are made: foaming agents, for instance, cause the material to rise, producing axisymmetric cells which are elongated in the rise direction. This microstructural anisotropy results in mechanical properties which are anisotropic, too: the Young's modulus and the collapse stresses are larger in the rise direction than in the plane normal to it (Mal'tsev, 1968; Patel, 1969; Kanakkanatt, 1973; Mehta and Colombo, 1976; Hilyard, 1982; Gupta et al., 1986; Huber and Gibson, 1988). One measure of the anisotropy of cell shape in axisymmetric foams is the ratio of the largest cell dimension to the smallest; we have called this the shape-anisotropy ratio, R (Chapter I, Section 1.1). Many foams are approximately axisymmetric, but some (depending on how they are made) are orthotropic: then all three principal dimensions of the cell differ, and two values of R, or more complicated schemes (e.g., Harrigan and Mann, 1984), are needed to characterize it. The methods of analyzing the effect of shape anisotropy on properties are given by Huber and Gibson (1988): they build on the earlier work of Patel (1969), Patel and Finnie (1969, 1970) and of Gibson and Ashby (1982), who recognized the importance of bending and buckling in determining foam properties. The work of Huber and Gibson (1988) is fundamentally different from the models adapted by Kanakkanatt (1973), Mehta and Colombo (1976), Cunningham (1981) and Hilyard (1982), who assume that the material properties depend linearly on relative density (i.e., the ratio of the bulk material density over the density of the solid cell walls).

Of crucial importance is the problem of multiaxial loading: in many applications (e.g., structural sandwich panels, packaging), the material is subjected to biaxial or triaxial loading. The elastic response is straightforward and is handled in conventional ways using elasticity theory (Love, 1963; Timoshenko and Goodier, 1970). However, the strength is more complicated. The failure mechanism depends on the state of stress, as well as on the cell wall properties. Little data exist in the literature on the multiaxial

behavior of foams. The three principal studies are those of Shaw and Sata (1966), Patel and Finnie (1969), and Zaslawsky (1973), who suggest that failure is governed by the maximum principal stress.

In this chapter, we review the uniaxial and multiaxial behavior of elastomeric foams. Then, after presenting the basic results for the uniaxial behavior of elastic-plastic materials, we develop general yield criteria for both isotropic and anisotropic foams under a general state of stress. Furthermore, the uniaxial behavior of elastic-brittle materials is reviewed, and general failure (crushing or fracture) criteria are obtained for isotropic and anisotropic foams under general multiaxial stress conditions. Finally, the analyses for the uniaxial strength and the multiaxial failure criteria are extended to a class of brittle (ceramic) foams made of *hollow* cell walls. As the behavior illustrated in Figs 4.1-4.2 suggests, *failure* is defined here as the stress level corresponding to the collapse plateau for compressive stresses, and to the termination of the linear-elastic response for tensile stresses.

The analysis and procedures developed in this chapter pertain to materials made up of *open cells*, or made up of *closed cells* with a large fraction of the solid in the cell edges, which behave in a manner similar to that for open cells. Such closed-cell foams are common; during the foaming procedure, surface tension draws the solid into the cell edges, typically leaving a thin face surrounded by much thicker edges.

Throughout this work we consider stresses and bulk material uniaxial strengths positive when tensile and negative when compressive; the solid cell wall material strengths (tensile, compressive, flexural) are taken positive. In addition, symbols with a subscript "$_s$" refer to properties of the solid cell wall material, while those with a superscripted asterisk "*" refer to the bulk material properties. The subscripts "$_x$" or "$_y$" or "$_z$" are used to associate a quantity with the principal material directions X or Y or Z (for orthotropic materials), respectively.

4.2 Failure of Elastomeric 3D Cellular Solids

Elastic collapse in cellular solids is the result of the elastic buckling of the cell walls (Gent and Thomas, 1959; Matonis, 1964; Chan and Nakamura, 1969; Patel and

Finnie, 1970; Menges and Knipschild, 1975; Barma et al., 1978; Gibson and Ashby, 1982). Considering this, Gent and Thomas (1959) derived an expression for the uniaxial post-buckling stress-strain behavior of open-cell foams based on the product of the Euler buckling load of a column and an empirically determined function of the strain in a member. They did not relate the elastic collapse stress to relative density. Menges and Knipschild (1975), too, analyzed uniaxial buckling by using Euler's equation to calculate a collapse stress, but they incorrectly applied it to the interpretation of the collapse of a rigid (plastic) foam. More recently, Gibson and Ashby (1982) followed a similar type of analysis. Their result is summarized below; the ideas of their analysis were extended to the case of axisymmetric and orthotropic materials by Huber and Gibson (1988).

No attempt was made to analyze the multiaxial buckling of foams until recently, when Zhang (1987) examined the stability of a joint with four adjacent members (cell walls) forming a simple tetrahedral structure. The results he obtained are interesting in that they resemble those obtained for honeycombs in the previous chapter; they are summarized in this section.

(a) Uniaxial Isotropic Behavior

Gibson and Ashby (1982) modeled an isotropic open-cell foam as a cubic array of members of length l and square cross-section of side t (Fig. 4.3a). Adjoining cells are packed so that their members meet at their midpoints. This simple model captures the bending behavior of the cell walls when the material is loaded uniaxially (Fig. 4.3b). The relative density of the material, ρ^*/ρ_s, and the moment of inertia of a member, I, are related to the dimensions t and l by

$$\frac{\rho^*}{\rho_s} \propto \left(\frac{t}{l}\right)^2, \qquad I \propto t^4 \tag{4.1}$$

According to the model of Gibson and Ashby (1982), the cell walls of an elastomeric open-cell foam, loaded in compression, first bend, and then buckle (Fig.

4.4). The critical load at which a cell edge of length, l, Young's modulus, E_s, and moment of inertia, I, buckles is given by Euler's formula

$$F_{crit} = \frac{n^2 \pi^2 E_s I}{l^2} \tag{4.2}$$

The factor n describes the degree of constraint at the ends of the column. The elastic collapse of the material initiates when this load is reached in a layer of cells through the cross-section. This happens at a stress level σ^*_{el} given by

$$\sigma^*_{el} \propto - \frac{F_{crit}}{l^2} \propto - \frac{E_s I}{l^4} \tag{4.3}$$

and combining (4.1) and (4.2) Gibson and Ashby (1982) obtained the following expression for the elastic collapse stress:

$$\frac{\sigma^*_{el}}{E_s} = - C_1 \left(\frac{\rho^*}{\rho_s} \right)^2 \tag{4.4}$$

where C_1 contains all the constants of proportionality. Gibson and Ashby (1982) considered also the extra geometrical complications arising from larger relative densities and found the slightly modified result:

$$\frac{\sigma^*_{el}}{E_s} = - C'_1 \left(\frac{\rho^*}{\rho_s} \right)^2 \left[1 + \left(\frac{\rho^*}{\rho_s} \right)^{1/2} \right]^2 \tag{4.5}$$

The correction is insignificant for values of relative density less than 0.3, typical of cellular materials. Experimental data are fitted satisfactorily by the simple eqn. (4.4) with C_1=0.05.

(b) Multiaxial Isotropic Behavior

In multiaxial compressive stress states, foams may fail by elastic buckling. An exact analysis of the problem is complicated due to the geometry of the material microstructure. Zhang (1987) considered the node and four associated struts of length l shown in Fig. 4.5a; he assumed that the four struts meet in a pentagonal dodecahedral arrangement at equal angles of 108°. Under a given stress state (σ_x, σ_y, σ_z) one strut carries a greater axial compression than the other three, and there is a tendency for it to buckle first (strut AB, Fig. 4.5b). This tendency is opposed by the other three struts which determine the rotational stiffness of the node, and, through this, the constant n in the Euler equation for the strut which buckles. The problem is complicated by the fact that the buckling mode itself is expected to change with stress state as described for the case of honeycombs in the previous chapter. Zhang (1987), assuming that it does not, considered the single buckling mode shown in Fig. 4.5b, and calculated values of n. His results are summarized in Table 4.1.

Table 4.1 End restraint, n, for elastic buckling of foams.

Load Condition	n^2	σ^*/σ^*_{el} [1]
Uniaxial compression, $\sigma_x=\sigma$, $\sigma_y=\sigma_z=0$	0.41	1.00
Biaxial compression, $\sigma_y=\sigma_z=\sigma$, $\sigma_x=0$	0.36	0.88
Hydrostatic compression, $\sigma_x=\sigma_y=\sigma_z=\sigma$	0.34	0.83
$\sigma_x=\sigma$, $\sigma_y=\sigma_z=-\sigma/8$	0.42	1.02
$\sigma_x=-\sigma/2$, $\sigma_y=\sigma_z=\sigma$	0.37	0.90

1. σ^* is the value of σ at failure; σ^*_{el} is the uniaxial buckling strength.

The corresponding failure surface for elastic buckling is illustrated in Fig. 4.6. A comparison of theory with experiment is possible using data from a recent study of flexible polyester foams (Shercliff, 1988) in which both the uniaxial buckling stresses,

σ^*_{el}, and the hydrostatic pressures, p^*_{el}, required to cause buckling were measured. For five different materials ranging in relative density from 0.01 to 0.05, the ratio of the two was more or less constant, with an average value 0.83 and a standard deviation 0.08, which agrees well with the value predicted by Zhang (1987):

$$\frac{p^*_{el}}{\sigma^*_{el}} = 0.83 \tag{4.6}$$

This agreement supports the view that the elastic collapse surface in the compressive octant is box-like, lying just inside the surface of constant maximum principal stress (Fig. 4.6).

Sections through the failure surface for elastic buckling for axisymmetric and biaxial loading are shown in Fig. 4.7. Elastic collapse cannot occur in tension and, therefore, it cannot, by itself, give a complete failure criterion; instead, it truncates the failure surfaces corresponding to the other collapse modes (yield surface or fracture surface) in the compressive octant.

(c) Anisotropic Behavior

Some understanding of the ratios of the uniaxial elastic buckling stresses, $(\sigma^*_{el})_z/(\sigma^*_{el})_x$ and $(\sigma^*_{el})_z/(\sigma^*_{el})_x$ was given by Huber and Gibson (1988), by extending the methods of Section 4.2a. The subscripts "x", "y", and "z" here denote that stresses are parallel to the three principal material directions for an orthotropic material. Fig. 4.8 shows an idealized open cell of an orthotropic material: the rise direction is parallel to X. Let the elastic buckling stress in the rise direction be $(\sigma^*_{el})_x$, and those in the two directions normal to this be $(\sigma^*_{el})_y$ and $(\sigma^*_{el})_z$. Huber and Gibson (1988) have shown that

$$\frac{(\sigma^*_{el})_i}{(\sigma^*_{el})_j} = \left(\frac{n_i}{n_j}\right)^2 R_{ji} \tag{4.7}$$

where i, j=x, y, z. For instance, n_x describes the rotational stiffness of the buckled column for the X direction of loading and R_{xy} is the shape anisotropy ratio, given by $R_{xy} = \bar{l}_x/\bar{l}_y$; $\bar{l}_x$ is the mean cell length parallel to the principal material direction X.

The geometric complexities involved in anisotropic materials make the analytical derivation of the elastic buckling surface an extremely difficult task. Instead, we assume that the elastic buckling surface of an orthotropic foam is roughly approximated by normalizing each stress axis by the uniaxial elastic buckling stress in that direction. This concept is illustrated in Fig. 4.9.

4.3 Failure of Elastic-Plastic 3D Cellular Solids

We now examine the failure of elastic-plastic foams. The uniaxial behavior has been successfully modeled using dimensional arguments, by extending the analysis for honeycombs (Gibson and Ashby, 1982). In this section we apply the method to the analysis of the triaxial failure of foams; for completeness we first review the results of Gibson and Ashby (1982) for the uniaxial strength.

(a) Uniaxial Isotropic Behavior

Foams made from materials which have a plastic yield point (rigid polymers, metals) usually fail plastically when loaded beyond the linear-elastic regime. Plastic collapse occurs when the bending moment exerted on the cell walls by the force F (Fig. 4.10) exceeds their fully plastic moment (Thornton and Magee, 1975a, b; Gibson and Ashby, 1982), resulting in the formation of plastic hinges. For a beam with a square section of side t, the plastic moment is

$$M_p = \frac{1}{4}\sigma_{ys}t^3 \tag{4.8}$$

where σ_{ys} is the yield strength of the cell wall material. The maximum bending moment

exerted on the cell walls is proportional to Fl and the force is proportional to $-\sigma^*_{pl}l^2$ for compression. Combining these results with the first of eqns (4.1) Gibson and Ashby (1982) obtained

$$\frac{\sigma^*_{pl}}{\sigma_{ys}} = -C_2\left(\frac{\rho^*}{\rho_s}\right)^{3/2} \tag{4.9}$$

where, as in the elastic buckling analysis, C_2 contains all the constants of proportionality. A more refined version of the above equation which accounts for the fact that the relative density ratio is not always very small is given below:

$$\frac{\sigma^*_{pl}}{\sigma_{ys}} = -C'_2\left(\frac{\rho^*}{\rho_s}\right)^{3/2}\left[1+\left(\frac{\rho^*}{\rho_s}\right)^{1/2}\right] \tag{4.10}$$

This correction is insignificant when $(\rho^*/\rho_s)<0.3$ as suggested by Gibson and Ashby (1982); experimental data are adequately described by eqn. (4.9) with $C_2=0.3$ (Maiti et al., 1984a). Notice that the same equation describes the tensile strength with the minus sign replaced by a plus.

(b) Multiaxial Isotropic Behavior

We now consider triaxial loading for an isotropic foam under a remote principal stress field σ_1, σ_2, σ_3 (Fig. 4.11). If the principal stresses are all equal, the cell walls are subjected to purely axial tension or compression; there is no bending. Then plastic collapse occurs when the axial stress in the cell walls exceeds σ_{ys}, or:

$$\sigma_a = \sigma_{ys} = \frac{3\sigma_m}{(\rho^*/\rho_s)} \tag{4.11}$$

where σ_m is the *mean* stress given by $\sigma_m=(\sigma_1+\sigma_2+\sigma_3)/3$. The constant 3 in eqn. (4.11)

arises because the stress in any one direction loads only one third of the cell walls of the unit cubic cell. The uniform loading of a random distribution of cell walls in a sphere produces the same result.

Under any other combination of stresses, i.e. when σ_1, σ_2, and σ_3 are not equal, *bending moments* as well as *axial forces* are exerted on the cell walls. The average bending moment is taken proportional to the square root of the *second invariant*, J_2, of the *deviatoric stress tensor* (so that the result has units of stress) times the cube of the cell size (stress times the square of the cell size produces force applied to the cell walls; this force times the cell size produces moment):

$$M \propto \sqrt{J_2}\, l^3 = \sqrt{\frac{1}{6}\left[(\sigma_1-\sigma_2)^2+(\sigma_2-\sigma_3)^2+(\sigma_3-\sigma_1)^2\right]}\, l^3 \qquad (4.12)$$

The axial load on the cell wall modifies the moment required to bend it plastically, for the reasons discussed in Section 3.3b in the analysis of honeycombs. The fully plastic moment for the honeycomb wall was given by eqn. (3.25); replacing b by t for the cell edge of the foam we obtain:

$$M_p \propto \sigma_{ys} t^3 \left[1-\left(\frac{\sigma_a}{\sigma_{ys}}\right)^2\right] \qquad (4.13)$$

Equating this to eqn. (4.12), substituting eqn. (4.11) for σ_a, using the fact that $(\rho^*/\rho_s) \propto (t/l)^2$, assembling the constants of proportionality into a single constant α, and remembering that the applied moment may be either positive or negative, gives:

$$\frac{\sqrt{3}\sqrt{J_2}}{\sigma_{ys}} = \pm\, \alpha\left(\frac{\rho^*}{\rho_s}\right)^{3/2}\left\{1-\left[\frac{I_1}{\sigma_{ys}(\rho^*/\rho_s)}\right]^2\right\} \qquad (4.14)$$

where I_1 is the *first invariant* of the *stress tensor* and is equal to three times the mean stress, σ_m (a description of the stress invariants and their geometric interpretation is given

in Appendix 4A at the end of this chapter). The constant α is obtained from the known result for uniaxial compression (eqn. (4.9)). Setting $I_1=\sigma^*_{pl}$ and $\sqrt{3}\sqrt{J_2}=|\sigma^*_{pl}|$ in eqn. (4.14) and substituting σ^*_{pl} from eqn. (4.9) gives:

$$\alpha=\frac{0.3}{1-0.09(\rho^*/\rho_s)} \tag{4.15}$$

For all interesting values of the relative density ρ^*/ρ_s (less than about 0.3) we find $\alpha\approx 0.3$. The yield criterion for isotropic three-dimensional cellular materials under multiaxial stresses then becomes:

$$\frac{\sqrt{3}\sqrt{J_2}}{\sigma_{ys}}=\pm\,0.3\left(\frac{\rho^*}{\rho_s}\right)^{3/2}\left\{1-\left[\frac{I_1}{\sigma_{ys}(\rho^*/\rho_s)}\right]^2\right\} \tag{4.16}$$

or in terms of the uniaxial collapse stress, σ^*_{pl}:

$$f_1(I_1,J_2)=\pm\frac{\sqrt{3}\sqrt{J_2}}{\sigma^*_{pl}}+0.09\left(\frac{\rho^*}{\rho_s}\right)\left(\frac{I_1}{\sigma^*_{pl}}\right)^2-1=0 \tag{4.17}$$

The failure criterion for isotropic elastic-plastic foams is completely defined by two parameters: the uniaxial strength of the material, σ^*_{pl}, and its relative density, ρ^*/ρ_s. The function $f_1(I_1, J_2)$, plotted in the three coordinate axes of principal stress, known as the Haigh-Westergard stress space, represents the yield surface of the material. The yield surface is illustrated in Fig. 4.12a; it is extended along the direction of pure hydrostatic stress reflecting the tremendous increase of the strength of the material when it is loaded *uniformly*. The yield surface is *smooth* (except for the two points on the hydrostatic axis which correspond to uniform extension or shortening of the cell walls) and *convex*. The projection of the yield surface on a *deviatoric plane* (any plane normal to the

hydrostatic axis), known as the *yield locus*, is a circle (Fig. 4.12b), confirming the fact that the failure criterion is independent of the third invariant of the deviatoric stress tensor, J_3. The character of a meridian (the intersection curve between the failure surface and a plane containing the hydrostatic axis) is illustrated in Fig. 4.12c.

Two sections of the yield surface are shown in Figs 4.13 and 4.14. The first is for axisymmetric loading ($\sigma_2=\sigma_3$); the failure envelope is the intersection of two ellipses. The surface becomes increasingly elongated as the relative density ratio decreases. It is also truncated by elastic buckling in the compressive octant. This is analogous to Fig. 3.13 for two-dimensional honeycomb-like cellular materials. The second is for biaxial loading ($\sigma_3=0$). Equation (4.17) , for this case, gives a quartic equation relating σ_1 and σ_2; it is roughly elliptical but in the tension-tension, or the compression-compression quadrants, it is more box-like and could be approximated by assuming that yield occurs at a constant value of the maximum principal stress.

The *post-yield* behavior of the material can be formulated within the framework of the classical plasticity theory (Drucker, 1950; Hill, 1950; Mendelson, 1968) and is briefly described in Appendix 4B.

An extension of the yield criterion for anisotropic materials is described next.

(c) Anisotropic Behavior

When foams are anisotropic, the uniaxial plastic collapse stress, σ^*_{pl}, depends on direction. The idealized open cell of an orthotropic material is shown in Fig. 4.15a. Let the plastic collapse stress in the rise direction be $(\sigma^*_{pl})_x$, and those in the two directions normal to this be $(\sigma^*_{pl})_y$ and $(\sigma^*_{pl})_z$. We start the analysis from the result for the isotropic case (eqn. (4.16)) which we write in the form

$$\pm \frac{\sqrt{3}\sqrt{J_2}}{\sigma^*_{pl}} = 1 - \left(\frac{I_1}{3(\sigma^*_h)_{pl}}\right)^2 \qquad (4.18)$$

where $\sigma^*_{pl}=-0.3\sigma_{ys}(\rho^*/\rho_s)^{3/2}$ and $(\sigma^*_h)_{pl}=\sigma_{ys}(\rho^*/\rho_s)/3$.

We replace the strength-normalized second deviatoric invariant, $\sqrt{3}\sqrt{J_2}/\sigma^*_{pl}$, by the quantity:

$$\left\{\frac{1}{2}\left[\left(\frac{\sigma_x}{(\sigma^*_{pl})_x}-\frac{\sigma_y}{(\sigma^*_{pl})_y}\right)^2+\left(\frac{\sigma_y}{(\sigma^*_{pl})_y}-\frac{\sigma_z}{(\sigma^*_{pl})_z}\right)^2+\left(\frac{\sigma_z}{(\sigma^*_{pl})_z}-\frac{\sigma_x}{(\sigma^*_{pl})_x}\right)^2\right]\right\}^{1/2} \quad (4.19)$$

When this quantity is equal to 1, the material deforms plastically by a cell wall bending mechanism. When it is zero, this mechanism is suppressed; and when this is the case, the stresses σ_x, σ_y, and σ_z are related by the equations

$$\frac{\sigma_x}{(\sigma^*_{pl})_x}=\frac{\sigma_y}{(\sigma^*_{pl})_y}=\frac{\sigma_z}{(\sigma^*_{pl})_z} \quad (4.20)$$

Under the conditions of eqns (4.20), plastic failure is only possible by the axial deformation of the cell walls. This suggests that the quantity $I_1/(\sigma^*_h)_{pl}$ be replaced by the quantity

$$\left[\frac{\sigma_x}{(\sigma^*_{pl})_x}+\frac{\sigma_y}{(\sigma^*_{pl})_y}+\frac{\sigma_z}{(\sigma^*_{pl})_z}\right]\frac{\sigma^*_{pl}}{(\sigma^*_h)_{pl}}$$

The procedure described here gives a transformation of the axes from σ_1 (or σ_x) to $\sigma_x[\sigma^*_{pl}/(\sigma^*_{pl})_x]$ etc. (Ashby, 1988). This transformation is analogous to that proposed by Hill (1950) for anisotropic metals. The key idea here is to distort the failure surface for an isotropic material so that it intercepts the axes of σ_x, σ_y, and σ_z at the points of the uniaxial strengths, $(\sigma^*_{pl})_x$, $(\sigma^*_{pl})_y$, and $(\sigma^*_{pl})_z$, respectively. Assembling the above results gives the multiaxial failure (yield) criterion for orthotropic materials as follows:

$$\pm\left\{\frac{1}{2}\left[\left(\frac{\sigma_x}{(\sigma^*_{pl})_x}-\frac{\sigma_y}{(\sigma^*_{pl})_y}\right)^2+\left(\frac{\sigma_y}{(\sigma^*_{pl})_y}-\frac{\sigma_z}{(\sigma^*_{pl})_z}\right)^2+\left(\frac{\sigma_z}{(\sigma^*_{pl})_z}-\frac{\sigma_x}{(\sigma^*_{pl})_x}\right)^2\right]\right\}^{1/2}$$

$$+0.09\left(\frac{\rho^*}{\rho_s}\right)\left[\frac{\sigma_x}{(\sigma^*_{pl})_x}+\frac{\sigma_y}{(\sigma^*_{pl})_y}+\frac{\sigma_z}{(\sigma^*_{pl})_z}\right]^2-1=0 \qquad (4.21)$$

This equation reduces identically to our starting expression when all three uniaxial strengths are the same (eqn. (4.17) for isotropic materials); it also corresponds to a distortion of the failure surface in the ratios of the uniaxial yield strengths.

The preceding analysis assumes that only normal stresses σ_x, σ_y, and σ_z act parallel to the material directions X, Y, and Z, respectively. We now extend it to the case when shear stresses τ_{xy}, τ_{yz}, and τ_{zx} are also present (Fig. 4.15b). The extension is quite straightforward and comes from the definition of the second invariant of the deviatoric stress tensor. Instead of the quantity (4.19) we replace the strength-normalized second invariant, $\sqrt{3}\sqrt{J_2}/\sigma^*_{pl}$, by

$$\left\{\frac{1}{2}\left[\left(\frac{\sigma_x}{(\sigma^*_{pl})_x}-\frac{\sigma_y}{(\sigma^*_{pl})_y}\right)^2+\left(\frac{\sigma_y}{(\sigma^*_{pl})_y}-\frac{\sigma_z}{(\sigma^*_{pl})_z}\right)^2+\left(\frac{\sigma_z}{(\sigma^*_{pl})_z}-\frac{\sigma_x}{(\sigma^*_{pl})_x}\right)^2\right]\right.$$

$$\left.+3\left[\frac{\tau_{xy}}{\sqrt{3}(\tau^*_{pl})_{xy}}\right]^2+3\left[\frac{\tau_{yz}}{\sqrt{3}(\tau^*_{pl})_{yz}}\right]^2+3\left[\frac{\tau_{zx}}{\sqrt{3}(\tau^*_{pl})_{zx}}\right]^2\right\}^{1/2} \qquad (4.22)$$

where $(\tau^*_{pl})_{xy}$, $(\tau^*_{pl})_{yz}$, and $(\tau^*_{pl})_{zx}$ are the *shear strengths* of the material defined in Fig. 4.16. Note that $\sigma^*_{pl}=\sqrt{3}\tau^*_{pl}$ for isotropic materials. The resulting failure criterion for a general state of stress is

$$\pm\left\{\frac{1}{2}\left[\left(\frac{\sigma_x}{(\sigma^*_{pl})_x}-\frac{\sigma_y}{(\sigma^*_{pl})_y}\right)^2+\left(\frac{\sigma_y}{(\sigma^*_{pl})_y}-\frac{\sigma_z}{(\sigma^*_{pl})_z}\right)^2+\left(\frac{\sigma_z}{(\sigma^*_{pl})_z}-\frac{\sigma_x}{(\sigma^*_{pl})_x}\right)^2\right]\right.$$

$$\left.+\left[\frac{\tau_{xy}}{(\tau^*_{pl})_{xy}}\right]^2+\left[\frac{\tau_{yz}}{(\tau^*_{pl})_{yz}}\right]^2+\left[\frac{\tau_{zx}}{(\tau^*_{pl})_{zx}}\right]^2\right\}^{1/2}$$

$$+0.09\left(\frac{\rho^*}{\rho_s}\right)\left[\frac{\sigma_x}{(\sigma^*_{pl})_x}+\frac{\sigma_y}{(\sigma^*_{pl})_y}+\frac{\sigma_z}{(\sigma^*_{pl})_z}\right]^2-1=0 \qquad (4.23)$$

In the absense of shear stresses ($\tau_{xy}=\tau_{yz}=\tau_{zx}=0$) the failure surface for orthotropic foams is completely defined by four parameters: the three uniaxial strengths of the material and its relative density ratio. Under a general state of stress three additional parameters are required: the three simple shear strengths, which can be obtained by using the apparatus shown in Fig. 4.17 (ASTM C273).

Three sections of the yield surface for an orthotropic material with $(\sigma^*_{pl})_x=-630$ KPa, $(\sigma^*_{pl})_y=-350$ KPa, $(\sigma^*_{pl})_z=-295$ KPa, and $\rho^*/\rho_s=0.053$ are shown in Figs 4.18 and 4.19. The first is for axisymmetric loading ($\sigma_y=\sigma_z$) and is truncated by elastic buckling in the compressive octant, in analogy to the isotropic case. The second and third are for biaxial loading with $\sigma_z=0$ and $\sigma_x=0$, respectively; they are roughly elliptical but in the tension-tension, or the compression-compression quadrants, they are approximately box-like indicating that yield occurs at an almost constant value of the maximum normal stress.

4.4 Failure of Elastic-Brittle 3D Cellular Solids

The failure of elastic-brittle foams (ceramics, glasses, brittle polymers) is examined in this section. We first review the uniaxial behavior of isotropic brittle foams. The response of the material is then analyzed for multiaxial states of stress. The multiaxial failure criteria obtained are subsequently generalized to account for material

anisotropy. Finally, the same procedure is repeated for a special class of open-cell materials with *hollow* cell walls.

4.4.1 Uniaxial Isotropic Behavior

(a) Compressive Loading

Brittle foams collapse by brittle crushing (Rusch, 1970; Morgan et al., 1981; Ashby, 1983; Maiti et al., 1984a; Kurauchi et al., 1984). The uniaxial crushing strength is found by the method described by Maiti et al. (1984a). When the material is loaded uniaxially the cell wall responds primarily by bending. Let the modulus of rupture of the cell wall material be σ_{fs}. A cell wall will fail (Fig. 4.20) when the moment acting on it exceeds

$$M_f = \frac{1}{6}\sigma_{fs}t^3 \tag{4.24}$$

As before, a force F acting with a component normal to the wall of length l, exerts a moment which is proportional to Fl, and the stress on the foam is proportional to $-F/l^2$. Combining the results gives the brittle collapse stress σ^*_{cr} as

$$\frac{\sigma^*_{cr}}{\sigma_{fs}} = -C_3\left(\frac{\rho^*}{\rho_s}\right)^{3/2} \tag{4.25}$$

where C_3 contains all the constants of proportionality and the minus sign denotes compression. Maiti et al. (1984a) use handbook data for σ_{fs} and find $C_3 \approx 0.65$. Reliable data for σ_{fs} are difficult to obtain: it depends on the size of microcracks within the cell walls which, in turn, depend on cell size, due to the size effect in brittle materials first described by Weibull (1951). Noting that the analysis for brittle crushing is identical to that for plastic collapse with M_p replaced by M_f, we expect C_3 to be about $(M_f/M_p)C_2$ or (2/3)0.3=0.2. We adopt the last value in our analysis.

(b) Tensile Loading

The fracture strength of an isotropic brittle foam in tension, like that of a honeycomb, is governed by the propagation of a crack. The material is linear-elastic up to fracture, so tensile failure can be treated by the methods of linear elastic fracture mechanics; we seek an expression for the fracture toughness of the foam, K^*_{IC}, in terms of the fracture strength of the cell walls, σ_{fs}, and the relative density, ρ^*/ρ_s (Fowlkes, 1974; McIntyre and Anderton, 1979; Morgan et al., 1981; Zwissler and Adams, 1983; Ashby, 1983; Maiti et al., 1984a; Green, 1985). The analysis parallels that for brittle honeycombs. The fracture toughness has been shown to be (Maiti et al., 1984b):

$$K^*_{IC} = C_4 \sigma_{fs} \sqrt{\pi l} \, (\rho^*/\rho_s)^{3/2} \tag{4.26}$$

Maiti et al. (1984b) find C_4=0.65; for the reasons stated in the previous section, we adjust this to C_4=0.2. The fracture stress in simple tension is:

$$\sigma^*_{fr} = \frac{K^*_{IC}}{\sqrt{\pi a}} \tag{4.27}$$

where 2a is the length of the largest crack in the sample.

4.4.2 Multiaxial Isotropic Behavior

We now analyze the case of triaxial loading of brittle isotropic foams, with a remote stress field σ_1, σ_2, σ_3 (Fig. 4.11). Here, the axial stresses acting in the cell walls become important, too. The analysis parallels that for honeycombs: brittle crushing occurs when the extreme fiber stress in a member equals the modulus of rupture of the cell wall:

$$\sigma_{fs} - \sigma_a = \frac{Mt}{2I} \tag{4.28}$$

where the moment M can be either positive or negative. The axial stress, σ_a, is proportional to the mean applied stress, σ_m, divided by ρ^*/ρ_s and the bending moment is taken proportional to the square root of the second deviatoric invariant, J_2, times the cube of the cell size (eqn. (4.12)). Combining (4.28) with these observations we obtain

$$\frac{\sqrt{3}\sqrt{J_2}}{\sigma_{fs}} = \pm \beta\left(\frac{\rho^*}{\rho_s}\right)^{3/2}\left\{1-\left[\frac{I_1}{\gamma\sigma_{fs}(\rho^*/\rho_s)}\right]\right\} \tag{4.29}$$

where I_1 is the first invariant of the stress tensor. The constant γ is obtained from the result for *uniform tension* ($\sigma_1=\sigma_2=\sigma_3=\sigma$, tensile). In this case we have

$$\sigma_a = \sigma_{ts} = \frac{I_1}{(\rho^*/\rho_s)} \tag{4.30}$$

where σ_{ts} is the *tensile strength* of the solid cell wall material. The tensile strength for a brittle solid is close to, but usually a little smaller than, the modulus of rupture (McClintock and Argon, 1966; Neville, 1981; Ashby and Jones, 1986). The result for uniform tension gives $\gamma=\sigma_{ts}/\sigma_{fs}$. The constant β is obtained from the known result for uniaxial compression (eqn. (4.25)). Setting $I_1=\sigma^*_{cr}$ and $\sqrt{3}\sqrt{J_2} = |\sigma^*_{cr}|$ in eqn. (4.29) and substituting σ^*_{cr} from eqn. (4.25) gives:

$$\beta = \frac{0.2}{1+0.2(\rho^*/\rho_s)^{1/2}} \tag{4.31}$$

For small ρ^*/ρ_s ratios we find the failure criterion for isotropic brittle foams under multiaxial stresses as follows:

$$\frac{\sqrt{3}\sqrt{J_2}}{\sigma_{fs}} = \pm 0.2\left(\frac{\rho^*}{\rho_s}\right)^{3/2}\left\{1-\left[\frac{I_1}{\sigma_{ts}(\rho^*/\rho_s)}\right]\right\} \tag{4.32}$$

or in terms of the uniaxial collapse stress, σ^*_{cr} :

$$f_2(I_1, J_2) = \pm \frac{\sqrt{3}\sqrt{J_2}}{\sigma^*_{cr}} + 0.2\left(\frac{\rho^*}{\rho_s}\right)^{1/2}\left(\frac{\sigma_{fs}}{\sigma_{ts}}\right)\frac{I_1}{|\sigma^*_{cr}|} - 1 = 0 \qquad (4.33)$$

This criterion is completely defined by three parameters: the uniaxial compressive strength of the foam, σ^*_{cr}, its relative density ratio, ρ^*/ρ_s, and the ratio of the modulus of rupture of the cell wall material to its tensile strength, σ_{fs}/σ_{ts}.

In the analysis presented here, we assumed that the cell wall material fails by tensile rupture. However, the cell walls can fail by compressive crushing under some stress states. The analysis for this case is identical to that given above for tensile rupture in the cell walls, with two differences: first, the failure condition now becomes

$$-\sigma_{cs} + \sigma_a = \frac{Mt}{2I} \qquad (4.34)$$

where σ_{cs} is the compressive crushing strength of the cell wall material (from Fig. 3.19); second, when the material is subjected to *uniform compression* ($\sigma_1=\sigma_2=\sigma_3=\sigma$, compressive), we have:

$$\sigma_a = -\sigma_{cs} = \frac{I_1}{(\rho^*/\rho_s)} \qquad (4.35)$$

Following the previous procedure we find the failure criterion for isotropic brittle foams failing by compressive crushing within the cell walls as follows:

$$\frac{\sqrt{3}\sqrt{J_2}}{\sigma_{cs}} = \pm\, 0.2\left(\frac{\rho^*}{\rho_s}\right)^{3/2}\left\{1 + \left[\frac{I_1}{\sigma_{cs}(\rho^*/\rho_s)}\right]\right\} \qquad (4.36)$$

or in terms of the uniaxial collapse stress, σ^*_{cr} :

$$f_3(I_1, J_2) = \pm \frac{\sqrt{3}\sqrt{J_2}}{\sigma^*_{cr}} - 0.2\left(\frac{\rho^*}{\rho_s}\right)^{1/2} \frac{I_1}{|\sigma^*_{cr}|} - \frac{\sigma_{cs}}{\sigma_{fs}} = 0 \qquad (4.37)$$

Note that according to our sign convention σ_{cs}/σ_{fs} is a positive ratio much larger than one, while σ^*_{cr} is negative because it is compressive. The failure criterion described by equation (4.37) is completely defined by three parameters: the uniaxial compressive strength of the material, σ^*_{cr}, its relative density ratio, ρ^*/ρ_s, and the ratio of the compressive strength to the modulus of rupture of the cell wall material, σ_{cs}/σ_{fs}.

The overall collapse surface in macroscopic stress space (Haigh-Westergard stress space) consists of two intersecting surfaces of conical shape associated with tensile rupture and compressive crushing of the cell walls; they are described by eqns (4.33) and (4.37), respectively. The collapse surface is illustrated in Fig. 4.21a; it is extended along the direction of pure hydrostatic tension and compression reflecting the tremendous increase of the strength of the material under uniform loading. The collapse surface is smooth except for the two points on the hydrostatic axis corresponding to uniform extension or shortening of the cell walls, and to the points corresponding to a *balanced failure* of the cell walls by tensile rupture and brittle crushing simultaneously. The failure surface is also convex. The projection of the collapse surface on a deviatoric plane is a circle (Fig. 4.21b) and the character of a meridian is illustrated in Fig. 4.21c.

It is interesting to note that the failure surface described by equation (4.33) is of the same type as that proposed by Drucker and Prager (1952) for soils (sometimes refered to as the *extended* von Mises criterion (e.g., Chen, 1982)).

Under a multiaxial state of stress, if the foam contains cracks or flaws (which is very often the case), in the tensile octant the failure surface is truncated by fast fracture. In this case, brittle fracture occurs when the maximum principal stress reaches σ^*_{fr}: the failure surface is a box bounded by planes of constant principal stress, corresponding to the uniaxial tensile strength of the material (McClintock and Argon, 1966; Gibson and Ashby, 1988). Two sections of the collapse surface are shown in Figs 4.22 and 4.23. The first is for axisymmetric loading ($\sigma_2=\sigma_3$). The surface becomes increasingly

elongated as the relative density ratio decreases. It is also truncated by elastic buckling in the compressive octant (in analogy to Fig. 3.21 for honeycomb-like materials). The second is for biaxial loading (σ_3=0). Equation (4.33), for this case, is a quadratic expression relating σ_1 and σ_2, giving an elliptical failure surface which, in the tension-tension or in the compression-compression quadrants, is almost box-like. The elastic buckling surface lies outside of the tensile bending failure surface. In both figures, the failure envelope is truncated in the tensile regime by the two lines labeled "fast brittle fracture".

4.4.3 Anisotropic Behavior

When brittle foams are anisotropic, the uniaxial crushing stress, σ^*_{cr}, as well as the uniaxial tensile strength, σ^*_{fr}, depends on direction. The unit cell of an orthotropic material can be idealized as in Fig. 4.15a. The analysis is analogous to that described for anisotropic elastic-plastic materials. Let the crushing strength in the rise direction be $(\sigma^*_{cr})_x$, and those in the two directions normal to this be $(\sigma^*_{cr})_y$ and $(\sigma^*_{cr})_z$. We first consider failure by *tensile rupture* of the cell walls, and write the result for the isotropic case in the form

$$\pm \frac{\sqrt{3}\sqrt{J_2}}{\sigma^*_{cr}} = 1 - \frac{1}{3(\sigma^*_h)_t} \tag{4.38}$$

where $\sigma^*_{cr} = -0.2\sigma_{fs}(\rho^*/\rho_s)^{3/2}$ and $(\sigma^*_h)_t = \sigma_{ts}(\rho^*/\rho_s)/3$.

The strength-normalized second invariant, $\sqrt{3}\sqrt{J_2}/\sigma^*_{cr}$, is now replaced by the quantity

$$\left\{\frac{1}{2}\left[\left(\frac{\sigma_x}{(\sigma^*_{cr})_x} - \frac{\sigma_y}{(\sigma^*_{cr})_y}\right)^2 + \left(\frac{\sigma_y}{(\sigma^*_{cr})_y} - \frac{\sigma_z}{(\sigma^*_{cr})_z}\right)^2 + \left(\frac{\sigma_z}{(\sigma^*_{cr})_z} - \frac{\sigma_x}{(\sigma^*_{cr})_x}\right)^2\right]\right\}^{1/2} \tag{4.39}$$

When this quantity is zero, the bending mechanism which deforms the material is

suppressed and the stresses are related by the equations

$$\frac{\sigma_x}{(\sigma^*_{cr})_x} = \frac{\sigma_y}{(\sigma^*_{cr})_y} = \frac{\sigma_z}{(\sigma^*_{cr})_z} \tag{4.40}$$

Under these conditions, failure is only possible by the axial deformation of the cell walls. The quantity $I_1/(\sigma^*_h)_t$ is now replaced by

$$\left[\frac{\sigma_x}{(\sigma^*_{cr})_x} + \frac{\sigma_y}{(\sigma^*_{cr})_y} + \frac{\sigma_z}{(\sigma^*_{cr})_z}\right]\frac{\sigma^*_{cr}}{(\sigma^*_h)_t}$$

Assembling the results, we obtain the multiaxial failure criterion for orthotropic brittle foams which fail by tensile rupture of the cell walls as follows:

$$\pm\left\{\frac{1}{2}\left[\left(\frac{\sigma_x}{(\sigma^*_{cr})_x} - \frac{\sigma_y}{(\sigma^*_{cr})_y}\right)^2 + \left(\frac{\sigma_y}{(\sigma^*_{cr})_y} - \frac{\sigma_z}{(\sigma^*_{cr})_z}\right)^2 + \left(\frac{\sigma_z}{(\sigma^*_{cr})_z} - \frac{\sigma_x}{(\sigma^*_{cr})_x}\right)^2\right]\right\}^{1/2}$$

$$+ 0.2\left(\frac{\rho^*}{\rho_s}\right)^{1/2}\frac{\sigma_{fs}}{\sigma_{ts}}\left[\frac{\sigma_x}{|(\sigma^*_{cr})_x|} + \frac{\sigma_y}{|(\sigma^*_{cr})_y|} + \frac{\sigma_z}{|(\sigma^*_{cr})_z|}\right] - 1 = 0 \tag{4.41}$$

This equation reduces to our starting expression (eqn. (4.33)) when all three uniaxial compressive strengths are the same; it also corresponds to a distortion of the failure surface in the ratios of the uniaxial compressive strengths.

Based on arguments discussed in the case of elastic-plastic materials, the analysis is now extended to account for the presense of shear stresses (Fig. 4.15b). The result is as follows:

$$\pm\left\{\frac{1}{2}\left[\left(\frac{\sigma_x}{(\sigma^*_{cr})_x}-\frac{\sigma_y}{(\sigma^*_{cr})_y}\right)^2+\left(\frac{\sigma_y}{(\sigma^*_{cr})_y}-\frac{\sigma_z}{(\sigma^*_{cr})_z}\right)^2+\left(\frac{\sigma_z}{(\sigma^*_{cr})_z}-\frac{\sigma_x}{(\sigma^*_{cr})_x}\right)^2\right]\right.$$

$$\left.+\left[\frac{\tau_{xy}}{(\tau^*_{cr})_{xy}}\right]^2+\left[\frac{\tau_{yz}}{(\tau^*_{cr})_{yz}}\right]^2+\left[\frac{\tau_{zx}}{(\tau^*_{cr})_{zx}}\right]^2\right\}^{1/2}$$

$$+0.2\left(\frac{\rho^*}{\rho_s}\right)^{1/2}\frac{\sigma_{fs}}{\sigma_{ts}}\left[\frac{\sigma_x}{|(\sigma^*_{cr})_x|}+\frac{\sigma_y}{|(\sigma^*_{cr})_y|}+\frac{\sigma_z}{|(\sigma^*_{cr})_z|}\right]-1=0 \qquad (4.42)$$

where $(\tau^*_{cr})_{xy}$, $(\tau^*_{cr})_{yz}$, and $(\tau^*_{cr})_{zx}$ are the crushing shear strengths of the material defined in Fig. 4.24. In the absense of shear stresses the failure surface needs five parameters to be defined: the three uniaxial compressive strengths of the material, its relative density ratio, and the ratio of the modulus of rupture of the cell wall material to its tensile strength. Under a general state of stress three additional parameters are needed: the three simple shear strengths, which can be obtained as those for an elastic-plastic foam.

Let us now consider failure by *compressive crushing* of the cell walls. The result for the isotropic case (eqn. (4.37)) is written as:

$$\pm\frac{\sqrt{3}\sqrt{J_2}}{\left(\frac{\sigma_{cs}}{\sigma_{fs}}\right)\sigma^*_{cr}}=1-\frac{I_1}{3(\sigma^*_h)_c} \qquad (4.43)$$

where $(\sigma^*_h)_c=-\sigma_{cs}(\rho^*/\rho_s)/3$.

The strength-normalized second invariant, $\sqrt{3}\sqrt{J_2}/\sigma^*_{cr}$, is, as before, replaced by the quantity (4.39). The quantity $I_1/(\sigma^*_h)_c$ is replaced by

$$\left[\frac{\sigma_x}{(\sigma^*_{cr})_x}+\frac{\sigma_y}{(\sigma^*_{cr})_y}+\frac{\sigma_z}{(\sigma^*_{cr})_z}\right]\frac{\sigma^*_{cr}}{(\sigma^*_h)_c}$$

Combining the results, the multiaxial failure criterion for orthotropic brittle foams which fail by compressive crushing of the cell walls is obtained as

$$\pm\left\{\frac{1}{2}\left[\left(\frac{\sigma_x}{(\sigma^*_{cr})_x}-\frac{\sigma_y}{(\sigma^*_{cr})_y}\right)^2+\left(\frac{\sigma_y}{(\sigma^*_{cr})_y}-\frac{\sigma_z}{(\sigma^*_{cr})_z}\right)^2+\left(\frac{\sigma_z}{(\sigma^*_{cr})_z}-\frac{\sigma_x}{(\sigma^*_{cr})_x}\right)^2\right]\right\}^{1/2}$$

$$-0.2\left(\frac{\rho^*}{\rho_s}\right)^{1/2}\left[\frac{\sigma_x}{|(\sigma^*_{cr})_x|}+\frac{\sigma_y}{|(\sigma^*_{cr})_y|}+\frac{\sigma_z}{|(\sigma^*_{cr})_z|}\right]-\frac{\sigma_{cs}}{\sigma_{fs}}=0 \qquad (4.44)$$

The last expression reduces to eqn. (4.37) for isotropic materials, i.e. when all three uniaxial compressive strengths are equal.

The extension of the criterion described by eqn. (4.44) to account for shear stresses (Fig. 4.15b) is straightforward:

$$\pm\left\{\frac{1}{2}\left[\left(\frac{\sigma_x}{(\sigma^*_{cr})_x}-\frac{\sigma_y}{(\sigma^*_{cr})_y}\right)^2+\left(\frac{\sigma_y}{(\sigma^*_{cr})_y}-\frac{\sigma_z}{(\sigma^*_{cr})_z}\right)^2+\left(\frac{\sigma_z}{(\sigma^*_{cr})_z}-\frac{\sigma_x}{(\sigma^*_{cr})_x}\right)^2\right]\right.$$

$$\left.+\left[\frac{\tau_{xy}}{(\tau^*_{cr})_{xy}}\right]^2+\left[\frac{\tau_{yz}}{(\tau^*_{cr})_{yz}}\right]^2+\left[\frac{\tau_{zx}}{(\tau^*_{cr})_{zx}}\right]^2\right\}^{1/2}$$

$$-0.2\left(\frac{\rho^*}{\rho_s}\right)^{1/2}\left[\frac{\sigma_x}{|(\sigma^*_{cr})_x|}+\frac{\sigma_y}{|(\sigma^*_{cr})_y|}+\frac{\sigma_z}{|(\sigma^*_{cr})_z|}\right]-\frac{\sigma_{cs}}{\sigma_{fs}}=0 \qquad (4.45)$$

The failure surface described by eqn. (4.45) is defined by the same parameters which are required for the definition of the criterion given by eqn. (4.42).

The overall collapse surface in macroscopic stress space for orthotropic foams consists of two intersecting surfaces of distorted-conical shape (anisotropy-induced distortion), associated with tensile rupture and compressive crushing of the cell walls; they are described by eqns (4.41) and (4.44), respectively (or by eqns (4.42) and (4.45) when shear stresses are also considered). In the tensile octant the failure surface is

truncated by fast fracture: it is a box bounded by planes of constant normal stresses, corresponding to the uniaxial tensile strengths of the material, $(\sigma^*_{fr})_x$, $(\sigma^*_{fr})_y$, and $(\sigma^*_{fr})_z$.

Three sections of the brittle collapse surface for an axisymmetric material with $(\sigma^*_{cr})_x$=-212 KPa, $(\sigma^*_{cr})_y = (\sigma^*_{cr})_z$=-160 KPa, ρ^*/ρ_s=0.029, σ_{fs}=207 MPa, σ_{ts}=152 MPa, and σ_{cs}=690 MPa are shown in Figs 4.25 and 4.26. The first is for axisymmetric loading ($\sigma_y=\sigma_z$). It is truncated by elastic buckling in the compressive octant. The second and the third are for biaxial loading with σ_z=0 and σ_x=0, respectively; they are elliptical, and more box-like in the tension-tension or the compression-compression quadrants. In all figures, the failure envelope is closed by the two lines labelled "fast-brittle fracture" indicating the box-like tensile cutoff.

4.4.4 Materials Containing Porous Cell Walls

The theoretical analysis presented above for brittle 3D cellular materials assumes that the cell walls are fully dense and solid. Although some brittle foams made by a carbonization process are like this, not all are. For instance, those made by infiltrating a ceramic slurry into an open-cell polymeric foam and subsequently firing the ceramic are left with hollow cell walls in which the solid itself is porous. These features have been characterized in cellular ceramics by Hagiwara and Green (1987), Brezny et al. (1988), and Brezny and Green, (1988). They are illustrated in Fig. 4.27a which shows the microstructure of a typical cellular ceramic as observed in the scanning electron microscope. A cross-section of a typical cell strut containing a nearly-triangular cusped hole is shown in Fig. 4.27b. The porosity of the cell strut itself is illustrated in Fig. 4.27c which is a magnification of a portion of the cross-section shown in Fig. 4.27b.

In this section, we attempt to model the mechanical behavior of brittle cellular solids with the microstructure shown in Fig. 4.27. As a first step we model the uniaxial behavior of isotropic materials. We then develop the multiaxial failure criterion making use of the uniaxial strength. Finally, the failure criterion is extended to the case of orthotropic materials.

(a) Uniaxial Isotropic Behavior

Compressive Loading

The prismatic model of Gibson and Ashby (1982) (Fig. 4.28a) is the starting point of the analysis; the cell walls are idealized as linear members with a circular cross-section containing triangular holes (Fig. 4.28b). This configuration was used by Brezny et al. (1988) in the evaluation of the tensile strength of single cell struts. The material is characterized by three parameters: the *macroporosity*, p (%), defined as the ratio of the volume of the cell walls as if they were solid, to the volume of the bulk material (i.e., the macroporosity would be equal to the relative density if the cell walls contained no hole); the ratio b/d (see Fig. 4.28b); and the *microporosity*, p_s (%), of the cell wall material itself.

When the material is loaded uniaxially, its response is controlled by cell wall bending. A strut will fail when the moment acting on it exceeds

$$M_f = \frac{2\sigma_{fs} I}{d} \tag{4.46}$$

where

$$I = \frac{\pi d^4}{64} - \frac{\sqrt{3}\, b^4}{96} \tag{4.47}$$

σ_{fs} is the modulus of rupture of the porous cell wall material. One can relate σ_{fs} to σ^o_{fs}, the modulus of rupture at zero porosity, according to the empirical formula

$$\sigma_{fs} = \sigma^o_{fs} e^{-\lambda p_s} \tag{4.48}$$

where λ is a constant. Equation (4.48) has been used by Rice et al. (1985) to describe the modulus of rupture of reaction sintered Si_3N_4 (RSSN). Using a series expansion for the term $e^{-\lambda p_s}$, we can also write

$$\sigma_{fs} \approx \sigma^{o}_{fs}\left(\frac{\rho_s}{\rho^{o}_s}\right)^{\lambda}$$

where ρ_s is the density of the cell wall material surrounding the triangular hole, and ρ^{o}_s is the density of the same material at zero porosity. Following previous arguments, the moment acting on a cell wall is proportional to the remote stress, σ, times l^3 (l is the length of the cell walls). At failure, σ equals σ^{*}_{cr}, the crushing strength of the cellular ceramic, so we can write:

$$\sigma^{*}_{cr} \propto \frac{M_f}{l^3} \tag{4.49}$$

From eqns (4.46), (4.47), and (4.49) we obtain

$$\frac{\sigma^{*}_{cr}}{\sigma_{fs}} \propto 2.72\left(\frac{d}{l}\right)^3 - \left(\frac{b}{l}\right)^3\left(\frac{b}{d}\right) \tag{4.50}$$

The macroporosity, p, of the material is related to the dimensions d and l by

$$p \propto \left(\frac{d}{l}\right)^2 \tag{4.51}$$

Combining eqns (4.50) and (4.51) gives the brittle collapse stress σ^{*}_{cr} as

$$\frac{\sigma^{*}_{cr}}{\sigma_{fs}} = -C_5 p^{3/2}\left[2.72 - \left(\frac{b}{d}\right)^4\right] \tag{4.52}$$

where C_5 contains all the constants of proportionality and the minus sign denotes compression. Note that an average b/d ratio can be estimated by using for instance

scanning electron microscopy techniques. From Fig. 4.28b, the ratio of the area of the triangle shown to that of the circle is $0.55(b/d)^2$. Therefore, the macroporosity, p, is related to the relative density, ρ^*/ρ_s, as:

$$\frac{\rho^*}{\rho_s} = p\left[1 - 0.55\left(\frac{b}{d}\right)^2\right] \tag{4.53}$$

From eqns (4.52) and (4.53), the expression for the uniaxial compressive strength of cellular ceramics now becomes

$$\frac{\sigma^*_{cr}}{\sigma_{fs}} = -C_5\left(\frac{\rho^*}{\rho_s}\right)^{3/2}\left\{\frac{2.72 - \left(\frac{b}{d}\right)^4}{\left[1 - 0.55\left(\frac{b}{d}\right)^2\right]^{3/2}}\right\} \tag{4.54}$$

In the special case of solid cell walls (b=0) eqn. (4.54) should identically reduce to expression (4.25). This implies that the constant of proportionality, C_5, is approximately equal to 0.073.

Tensile Loading

Following the method of Maiti et al. (1984b), the fracture toughness for mode I fracture is found to be

$$K^*_{IC} = C_6\sigma_{fs}\sqrt{\pi l}\left(\frac{\rho^*}{\rho_s}\right)^{3/2}\left\{\frac{2.72 - \left(\frac{b}{d}\right)^4}{\left[1 - 0.55\left(\frac{b}{d}\right)^2\right]^{3/2}}\right\} \tag{4.55}$$

with $C_6 \approx 0.073$. From this, the tensile strength is

$$\sigma^*_{fr} = \frac{K^*_{IC}}{\sqrt{\pi a}} \tag{4.56}$$

where 2a is the largest crack length in the sample.

(b) Multiaxial Isotropic Behavior

To obtain the multiaxial failure criterion for cellular ceramics we simply follow the methodology described in Section 4.4.2 for brittle foams with solid struts. Consider first the case of tensile bending failure of the cell walls (i.e., when the extreme fiber stress in a member equals the modulus of rupture, σ_{fs}). The analogous to eqn. (4.32) now becomes

$$\frac{\sqrt{3}\sqrt{J_2}}{\sigma_{fs}} = \pm\, 0.073\left(\frac{\rho^*}{\rho_s}\right)^{3/2}\left\{\frac{2.72 - \left(\frac{b}{d}\right)^4}{\left[1 - 0.55\left(\frac{b}{d}\right)^2\right]^{3/2}}\right\}\left\{1 - \left[\frac{I_1}{\sigma_{ts}(\rho^*/\rho_s)}\right]\right\} \tag{4.57}$$

or in terms of the uniaxial collapse stress, σ^*_{cr} :

$$f_4(I_1, J_2) = \pm\frac{\sqrt{3}\sqrt{J_2}}{\sigma^*_{cr}}$$

$$+\, 0.073\left(\frac{\rho^*}{\rho_s}\right)^{1/2}\left(\frac{\sigma_{fs}}{\sigma_{ts}}\right)\left\{\frac{2.72 - \left(\frac{b}{d}\right)^4}{\left[1 - 0.55\left(\frac{b}{d}\right)^2\right]^{3/2}}\right\}\frac{I_1}{|\sigma^*_{cr}|} - 1 = 0 \tag{4.58}$$

The failure condition obtained is defined by four parameters: the uniaxial compressive strength of the material, σ^*_{cr}, its relative density ratio, ρ^*/ρ_s, the ratio of the modulus of rupture of the cell wall material to its tensile strength, σ_{fs}/σ_{ts}, and the ratio b/d defined in Fig. 4.28b.

When failure is caused by compressive crushing of the cell walls, the analogous to eqn. (4.37) is

$$f_5(I_1, J_2) = \pm \frac{\sqrt{3}\sqrt{J_2}}{\sigma^*_{cr}}$$

$$- 0.073\left(\frac{\rho^*}{\rho_s}\right)^{1/2}\left\{\frac{2.72 - \left(\frac{b}{d}\right)^4}{\left[1 - 0.55\left(\frac{b}{d}\right)^2\right]^{3/2}}\right\}\frac{I_1}{|\sigma^*_{cr}|} - \frac{\sigma_{cs}}{\sigma_{fs}} = 0 \qquad (4.59)$$

where σ_{cs} is the compressive crushing strength of the cell wall material. Four parameters are needed to define the failure criterion described by eqn. (4.59): σ^*_{cr}, ρ^*/ρ_s, b/d, and σ_{cs}/σ_{fs}.

The overall failure surface in macroscopic stress space is of the same form as that shown in Fig. 4.21a. In the tensile octant it is truncated by a box-like cutoff made of planes of constant principal stresses equal to the uniaxial tensile strength of the material. The surface is also truncated in the compressive octant by elastic buckling, as described in previous sections.

(c) Anisotropic Behavior

Both the uniaxial compressive strength, σ^*_{cr}, and the uniaxial tensile strength, σ^*_{fr}, of anisotropic cellular ceramics depend on direction. The procedure described in Section 4.4.3 yields the following failure criterion for orthotropic materials which fail by tensile rupture of the cell walls:

$$\pm\left\{\frac{1}{2}\left[\left(\frac{\sigma_x}{(\sigma^*_{cr})_x}-\frac{\sigma_y}{(\sigma^*_{cr})_y}\right)^2+\left(\frac{\sigma_y}{(\sigma^*_{cr})_y}-\frac{\sigma_z}{(\sigma^*_{cr})_z}\right)^2+\left(\frac{\sigma_z}{(\sigma^*_{cr})_z}-\frac{\sigma_x}{(\sigma^*_{cr})_x}\right)^2\right]\right.$$

$$\left.+\left[\frac{\tau_{xy}}{(\tau^*_{cr})_{xy}}\right]^2+\left[\frac{\tau_{yz}}{(\tau^*_{cr})_{yz}}\right]^2+\left[\frac{\tau_{zx}}{(\tau^*_{cr})_{zx}}\right]^2\right\}^{1/2}$$

$$+0.073\left(\frac{\rho^*}{\rho_s}\right)^{\frac{1}{2}}\left(\frac{\sigma_{fs}}{\sigma_{ts}}\right)\left\{\frac{2.72-\left(\frac{b}{d}\right)^4}{\left[1-0.55\left(\frac{b}{d}\right)^2\right]^{\frac{3}{2}}}\right\}\left[\frac{\sigma_x}{\left|(\sigma^*_{cr})_x\right|}+\frac{\sigma_y}{\left|(\sigma^*_{cr})_y\right|}+\frac{\sigma_z}{\left|(\sigma^*_{cr})_z\right|}\right]$$

$$-1=0 \qquad (4.60)$$

Moreover, when the material fails by compressive crushing of the cell walls we obtain:

$$\pm\left\{\frac{1}{2}\left[\left(\frac{\sigma_x}{(\sigma^*_{cr})_x}-\frac{\sigma_y}{(\sigma^*_{cr})_y}\right)^2+\left(\frac{\sigma_y}{(\sigma^*_{cr})_y}-\frac{\sigma_z}{(\sigma^*_{cr})_z}\right)^2+\left(\frac{\sigma_z}{(\sigma^*_{cr})_z}-\frac{\sigma_x}{(\sigma^*_{cr})_x}\right)^2\right]\right.$$

$$\left.+\left[\frac{\tau_{xy}}{(\tau^*_{cr})_{xy}}\right]^2+\left[\frac{\tau_{yz}}{(\tau^*_{cr})_{yz}}\right]^2+\left[\frac{\tau_{zx}}{(\tau^*_{cr})_{zx}}\right]^2\right\}^{1/2}$$

$$-0.073\left(\frac{\rho^*}{\rho_s}\right)^{\frac{1}{2}}\left\{\frac{2.72-\left(\frac{b}{d}\right)^4}{\left[1-0.55\left(\frac{b}{d}\right)^2\right]^{\frac{3}{2}}}\right\}\left[\frac{\sigma_x}{\left|(\sigma^*_{cr})_x\right|}+\frac{\sigma_y}{\left|(\sigma^*_{cr})_y\right|}+\frac{\sigma_z}{\left|(\sigma^*_{cr})_z\right|}\right]$$

$$-\frac{\sigma_{cs}}{\sigma_{fs}}=0 \qquad (4.61)$$

All the parameters involved in the above equations have been defined before. The overall collapse surface (eqns (4.60) and (4.61)) is truncated by brittle fracture and elastic

buckling as for the surfaces for brittle foams described previously. One section of the collapse surface for an orthotropic cellular ceramic (Lithium Alumina Silicate foam) with $(\sigma^*_{cr})_x$=-875 KPa, $(\sigma^*_{cr})_y$=-640 KPa, $(\sigma^*_{cr})_z$=-500 KPa, b/d=2/3, p=0.13, σ_{fs}/σ_{ts}=1.1, and σ_{cs}/σ_{fs}=7.5 (typical values for this material, see for instance, Brennan and Prewo, 1982; Marshall and Evans, 1985; Mah et al., 1985) is shown in Fig. 4.29 for axisymmetric loading.

4.5 Summary and Conclusions

The deformation and failure mechanisms of 3D cellular solids are analogous to those observed in honeycomb-like materials. The uniaxial behavior is initially linear elastic. Then, an elastomeric foam fails by elastic buckling in compression, giving a flat plateau in the stress-strain curve; in tension the stress-strain curve rises due to rotation of the cell walls. An elastic-plastic foam yields by the formation of plastic hinges due to bending, resulting in a plateau in the stress-strain curve in both compression and tension. The tensile plateau is shorter than that for compression due to the rotation of the cell walls towards the tensile axis. If the cell wall material is brittle, the foam crushes in compression and fractures in a brittle manner in tension. Under multiaxial stresses the response is different; this is so because the cell struts are subjected to significant axial loads in addition to bending moments. Defining failure of the material at the termination of the linear elastic behavior (i.e., at stress levels corresponding to the collapse plateau) we can associate a failure surface to each mode of collapse. For elastic buckling, the failure surface is almost box-like and exists only in the compressive octant of the principal stress space. Failure criteria which are functions of the first stress invariant and the second deviatoric stress invariant (and, of course, of the cell wall material properties) were developed for the plastic and brittle collapse of elastic-plastic and elastic-brittle isotropic foams, respectively. To account for material anisotropy, the failure criteria were extended by distorting the failure surfaces so that they intersect the stress axes at the points corresponding to the uniaxial strengths of the material in different directions.

For plastic materials, the failure surface obtained is elongated along the

hydrostatic axis, reflecting the high strength of the material when the bending mechanism is suppressed (Fig. 4.12). For brittle materials, the failure surface consists of two cones (Fig. 4.21) associated with tensile and compressive bending failure of the cell struts (the first takes place when the tensile stress at the extreme fiber of the cell wall exceeds its modulus of rupture, while the second takes place when the compressive stress at the extreme fiber of the cell wall exceeds its compressive strength). The vertex of each cone corresponds to purely axial deformations of the cell struts: one is associated with uniform extension and the other with uniform shortening of the material. The plastic collapse surface is usually truncated by the elastic buckling surface in the compressive octant. The same is true for the brittle collapse surface; it, in addition, is also truncated by a box-like cutoff in the tensile octant corresponding to a maximum principal tensile stress criterion.

Building on the ideas used in the modeling of open-cell materials made up of solid cell walls, we developed models for the uniaxial and multiaxial response of isotropic and anisotropic brittle foams with hollow, porous cell walls (cellular ceramics). The results resemble those obtained for foams with solid struts to a great extent.

Due to the complex structure of foams, the identification of exact plastic collapse or elastic buckling modes is an extremely difficult task. Consequently, elastoplastic interactions cannot be quantified. It is expected that the transition between the failure surfaces for elastic buckling and plastic yielding will be smooth.

The analytical results obtained in this chapter provide a basis for design with three-dimensional cellular materials. Their experimental validation is the subject of the next two chapters.

Appendix 4A: Invariants of Stress Tensor

The invariants of the *stress tensor*, σ_{ij}, are defined as follows (e.g., Malvern, 1969; Chen, 1982):

$$I_1 = \sigma_{ii} = \sigma_x + \sigma_y + \sigma_z = \sigma_1 + \sigma_2 + \sigma_3$$

$$I_2 = \frac{1}{2}\left(I_1^2 - \sigma_{ij}\sigma_{ji}\right) = \begin{vmatrix} \sigma_y & \tau_{yz} \\ \tau_{zy} & \sigma_z \end{vmatrix} + \begin{vmatrix} \sigma_x & \tau_{xy} \\ \tau_{zx} & \sigma_z \end{vmatrix} + \begin{vmatrix} \sigma_x & \tau_{xy} \\ \tau_{yx} & \sigma_y \end{vmatrix} = \sigma_1\sigma_2 + \sigma_2\sigma_3 + \sigma_3\sigma_1$$

$$I_3 = \frac{1}{6}\left(2\sigma_{ij}\sigma_{jk}\sigma_{ki} - 3I_1\sigma_{ij}\sigma_{ji} + I_1^3\right) = \begin{vmatrix} \sigma_x & \tau_{xy} & \tau_{xz} \\ \tau_{yx} & \sigma_y & \tau_{yz} \\ \tau_{zx} & \tau_{zy} & \sigma_z \end{vmatrix} = \sigma_1\sigma_2\sigma_3 \qquad (4A.1)$$

The subscripts x, y, and z refer to any Cartesian axes set; the subscripts 1, 2, and 3 refer to principal stresses.

The invariants of the *deviatoric stress tensor*, $s_{ij}=\sigma_{ij}-\sigma_m\delta_{ij}$ ($\sigma_m=I_1/3$), are defined as:

$$J_1 = s_{ii} = s_x + s_y + s_z = s_1 + s_2 + s_3 = 0$$

$$J_2 = \frac{1}{2}s_{ij}s_{ji} = -\begin{vmatrix} s_y & \tau_{yz} \\ \tau_{zy} & s_z \end{vmatrix} - \begin{vmatrix} s_x & \tau_{xy} \\ \tau_{zx} & s_z \end{vmatrix} - \begin{vmatrix} s_x & \tau_{xy} \\ \tau_{yx} & s_y \end{vmatrix} = \frac{1}{2}\left(s_1^2 + s_2^2 + s_3^2\right)$$

$$= \frac{1}{6}\left[(\sigma_x - \sigma_y)^2 + (\sigma_y - \sigma_z)^2 + (\sigma_z - \sigma_x)^2\right] + \tau_{xy}^2 + \tau_{yz}^2 + \tau_{zx}^2 \qquad (4A.2)$$

$$= \frac{1}{6}\left[(\sigma_1 - \sigma_2)^2 + (\sigma_2 - \sigma_3)^2 + (\sigma_3 - \sigma_1)^2\right]$$

$$J_3 = \frac{1}{3}s_{ij}s_{jk}s_{ki} = \begin{vmatrix} s_x & \tau_{xy} & \tau_{xz} \\ \tau_{yx} & s_y & \tau_{yz} \\ \tau_{zx} & \tau_{zy} & s_z \end{vmatrix} = \frac{1}{3}\left(s_1^3 + s_2^3 + s_3^3\right)$$

The simplest geometric representation of the stress at a point P(σ_1, σ_2, σ_3) is

described by treating the principal stresses σ_1, σ_2, σ_3 as coordinates of a point in three-dimensional stress space (Fig. 4A.1a). The *hydrostatic axis* in the stress space is defined as the diagonal d which has equal distances from the three axes. The planes perpendicular to d are called *deviatoric planes*. The length of ON is

$$|ON| = \xi = \frac{I_1}{\sqrt{3}} \tag{4A.3}$$

ON=[σ_m σ_m σ_m] defines the hydrostatic part of the stress state; NP=[s_1 s_2 s_3] defines the deviatoric part of the stress state and

$$|NP| = \rho = \sqrt{2J_2} \tag{4A.4}$$

To obtain a geometric interpretation of J_3, the deviatoric plane as shown in Fig. 4A.1b is considered. It can be shown that (e.g., Chen and Saleeb, 1982):

$$\cos 3\theta = \frac{3\sqrt{3}}{2} \frac{J_3}{J_2^{3/2}} \tag{4A.5}$$

Therefore, the failure surface $f(\sigma_1, \sigma_2, \sigma_3)=0$ or $f(I_1, J_2, J_3)=0$ can also be represented by $f(\xi, \rho, \theta)=0$.

Appendix 4B: Constitutive Modeling and Post-Yield Behavior of Elastic-Plastic 3D Cellular Solids in the Framework of the Classical Plasticity Theory

The stress-strain curves for elastic-plastic foams indicate that the materials are best described as elastic-perfectly plastic: the total strain is considered the sum of the reversible *elastic strain* ε_{ij}^{e} and the irreversible *plastic strain* ε_{ij}^{p}. The strain increments are similarly decomposed into reversible and irreversible components:

$$d\varepsilon_{ij} = d\varepsilon_{ij}^{e} + d\varepsilon_{ij}^{p} \tag{4B.1}$$

The elastic strain increments are assumed to be given by a generalized Hooke's law in the form:

$$d\varepsilon_{ij}^{e} = S_{ijkl}\, d\sigma_{kl} \tag{4B.2}$$

where S_{ijkl} is the *material compliance.* For isotropic elastic materials $d\varepsilon_{ij}^{e}$ takes the form

$$d\varepsilon_{ij}^{e} = \frac{1}{9K} dI_1 \delta_{ij} + \frac{1}{2G} ds_{ij} \tag{4B.3}$$

where K and G are the elastic bulk and shear moduli, respectively.

The material is elastic until it reaches the yield limit, i.e., until a certain function of the stress components reaches a certain value. This is known as the *yield function*:

$$f(\sigma_{ij})=0 \tag{4B.4}$$

Then, plastic deformation takes place without limit. When *loading* occurs, the

consistency condition (Prager, 1956) must be fulfilled to ensure that the stress point remains in contact with the yield surface:

$$f = 0; \qquad df = \frac{\vartheta f}{\vartheta \sigma_{ij}} d\sigma_{ij} = 0 \tag{4B.5}$$

The *unloading* criterion is expressed as

$$f = 0; \qquad df = \frac{\vartheta f}{\vartheta \sigma_{ij}} d\sigma_{ij} < 0 \tag{4B.6}$$

The yield function is interpreted geometrically as a fixed surface in the stress space (it is a *hypersurface* in a nine-dimensional stress space when the material is anisotropic).

In general, the concept of *plastic potential function* $g(\sigma_{ij})$, enables us to write the equations of plastic flow in the form

$$d\varepsilon_{ij}^{p} = d\lambda \frac{\vartheta g}{\vartheta \sigma_{ij}} \tag{4B.7}$$

where $d\lambda$ is a positive scalar factor of proportionality; this is the *normality rule*. By Drucker's stability postulate (Drucker, 1951), the flow rule must be *associated* (i.e., the yield function and plastic potential function must coincide, f=g) so that

$$d\varepsilon_{ij}^{p} = d\lambda \frac{\vartheta f}{\vartheta \sigma_{ij}} \tag{4B.8}$$

The relation (4B.8) implies that the plastic flow vector $d\varepsilon_{ij}^{p}$ is directed along the normal to the yield surface. In view of eqns (4B.1), (4B.3), and (4B.8), the complete stress-strain relations for an ideally elastic-perfectly plastic material are

$$d\varepsilon_{ij} = \frac{dI_1}{9K}\delta_{ij} + \frac{ds_{ij}}{2G} + d\lambda\frac{\vartheta f}{\vartheta\sigma_{ij}} \tag{4B.9}$$

$$\text{where } d\lambda \begin{cases} =0 & \text{wherever } f<0 & \text{(elastic loading)} \\ =0 & \text{wherever } f=0 \text{ but } df<0 & \text{(unloading after plastic flow has occured)} \\ >0 & \text{wherever } f=0 \text{ and } df=0 & \text{(plastic deformation)} \end{cases}$$

The form of the factor $d\lambda$ is determined from the consistency condition $df=0$; it is as follows:

$$d\lambda = \frac{\frac{\vartheta f}{\vartheta\sigma_{ij}}d\varepsilon_{ij} + \frac{3K-2G}{6G}d\varepsilon_{kk}\frac{\vartheta f}{\vartheta\sigma_{ij}}\delta_{ij}}{\frac{\vartheta f}{\vartheta\sigma_{ij}}\frac{\vartheta f}{\vartheta\sigma_{ij}} + \frac{3K-2G}{6G}\left(\frac{\vartheta f}{\vartheta\sigma_{ij}}\delta_{ij}\right)^2} \tag{4B.10}$$

The stress-strain law is also written in the form

$$d\sigma_{ij} = 2Gde_{ij} + Kd\varepsilon_{kk}\delta_{ij} - d\lambda\left[\left(K-\frac{2}{3}G\right)\frac{\vartheta f}{\vartheta\sigma_{mn}}\delta_{mn}\delta_{ij} + 2G\frac{\vartheta f}{\vartheta\sigma_{ij}}\right] \tag{4B.11}$$

where $e_{ij}=\varepsilon_{ij}-(1/3)\varepsilon_v\delta_{ij}$ is the *deviatoric strain tensor* ($\varepsilon_v=\varepsilon_x+\varepsilon_y+\varepsilon_z$ is the *dilatation*).

For elastic-plastic 3D cellular materials, the yield function is expressed in terms of the invariants I_1 and J_2 in the form

$$f\left(I_1^2, \sqrt{J_2}\right) = 0 \tag{4B.12}$$

Therefore, we can write:

$$\frac{\vartheta f}{\vartheta \sigma_{ij}} = \frac{\vartheta f}{\vartheta I_1}\frac{\vartheta I_1}{\vartheta \sigma_{ij}} + \frac{\vartheta f}{\vartheta \sqrt{J_2}}\frac{\vartheta \sqrt{J_2}}{\vartheta \sigma_{ij}} \tag{4B.13}$$

which reduces to

$$\frac{\vartheta f}{\vartheta \sigma_{ij}} = \frac{\vartheta f}{\vartheta I_1}\delta_{ij} + \frac{\vartheta f}{\vartheta \sqrt{J_2}}\frac{1}{2\sqrt{J_2}}s_{ij} \tag{4B.14}$$

With this expression, eqn. (4B.11) (constitutive equation) becomes

$$d\sigma_{ij} = 2G^* de_{ij} + K^* d\varepsilon_{kk}\delta_{ij} - d\lambda\left[3K^*\frac{\vartheta f}{\vartheta I_1}\delta_{ij} + \frac{G^*}{\sqrt{J_2}}\frac{\vartheta f}{\vartheta \sqrt{J_2}}s_{ij}\right] \tag{4B.15}$$

where, since G and K denote properties of the foam, they are replaced by G^* and K^*, respectively. $d\lambda$ has the form

$$d\lambda = \frac{3K^* d\varepsilon_{kk}(\vartheta f/\vartheta I_1) + \left(G^*/\sqrt{J_2}\right)\left(\vartheta f/\vartheta \sqrt{J_2}\right)s_{mn}de_{mn}}{9K^*\left(\vartheta f/\vartheta I_1\right)^2 + G^*\left(\vartheta f/\vartheta \sqrt{J_2}\right)^2} \tag{4B.16}$$

and the foilowing relationships hold:

$$\frac{\vartheta f}{\vartheta I_1} = 0.18\left(\frac{\rho^*}{\rho_s}\right)\frac{I_1}{(\sigma^*_{pl})^2} \tag{4B.17}$$

$$\frac{\vartheta f}{\vartheta \sqrt{J_2}} = \pm\frac{\sqrt{3}}{\sigma^*_{pl}} \tag{4B.18}$$

Note that eqn. (4B.18) is used with the plus sign for the portion of the yield surface

obtained by eqn. (4.17) with a plus sign. A similar argument holds for the minus sign of eqn. (4B.18). Finally, eqn. (4B.15) can be written in the preferable form

$$d\sigma_{ij} = C_{ijmn} d\varepsilon_{mn} \tag{4B.19}$$

for the direct use in a finite element displacement formulation, (Yamada et al., 1968; Zienkiewicz et al., 1969; Zienkiewicz, 1977), where

$$C_{ijmn} = 2G^*\delta_{im}\delta_{jn} + \left(K^* - \frac{2}{3}G^*\right)\delta_{ij}\delta_{mn}$$

$$- \frac{\left(\pm\frac{\sqrt{3}}{\sigma^*_{pl}}\right)\left(\frac{G^*}{\sqrt{J_2}}\right)s_{ij} + 0.54K^*\left(\frac{\rho^*}{\rho_s}\right)\left[\frac{I_1}{(\sigma^*_{pl})^2}\right]\delta_{ij}}{\left[\frac{3G^*}{(\sigma^*_{pl})^2}\right] + 0.2916K^*\left(\frac{\rho^*}{\rho_s}\right)^2\left[\frac{I_1^2}{(\sigma^*_{pl})^4}\right]}\left[\frac{\pm\sqrt{3}G^* s_{mn}}{\sqrt{J_2}\sigma^*_{pl}} + \frac{0.54K^*\left(\frac{\rho^*}{\rho_s}\right)I_1\delta_{mn}}{(\sigma^*_{pl})^2}\right]$$

(4B.20)

The matrix C_{ijmn} is the *elastoplastic constitutive matrix* of isotropic 3D cellular solids.

References

Ashby, M. F. (1983) The Mechanical Properties of Cellular Solids, *Met. Trans.*, **14A**, 1755.

Ashby, M. F. (1988) Personal Communication.

Ashby, M. F. and Jones, D. (1986) *Engineering Materials 2*, Pergamon, Oxford.

ASTM C273-61 Shear Test in Flatwise Plane of Sandwich Constructions or Sandwich Cores, **15.03**, 6.

Barma, P., Rhodes, M. B. and Salovey, R. (1978) Mechanical Properties of Particulate-Filled Polyurethane Foams, *J. Appl. Phys.*, **49**, 4985.

Brennan, J. J. and Prewo, K. M. (1982) Silicon Carbide Fibre Reinforced Glass-Ceramic Matrix Composites Exhibiting High Strength and Toughness, *J. Mat. Sci.*, **17**, 2371.

Brezny, R. and Green, D. J. (1988) Fracture Behavior of Open Cell Ceramics, *90th Annual Meeting of the American Ceramic Society, Cincinnati, Ohio.*

Brezny, R., Green, D. J. and Dam, C. Q. (1988) Evaluation of Strut Strength in Open Cell Ceramics, *12th Annual Conference on Composites and Advanced Ceramics, Cocoa Beach, Florida.*

Chan, R. and Nakamura, M. (1969) Mechanical Properties of Plastic Foams, *J. Cell. Plastics*, **5**, 112.

Chen, W. F. (1982) *Plasticity in Reinforced Concrete,* McGraw-Hill, New York.

Chen, W. F. and Saleeb, A. F. (1982) *Constitutive Equations for Engineering Materials, Vol. 1: Elasticity and Modeling*, John Wiley & Sons, Inc., New York.

Cunningham, A. (1981) Modulus Anisotropy of Low-Density Cellular Plastics: An Aggregate Model, *Polymer*, **22**, 882.

Drucker, D. C. (1950) Some Implications of Work Hardening and Ideal Plasticity, *Quart. Appl. Math.*, **7**, 411.

Drucker, D. C. (1951) A More Fundamental Approach to Plastic Stress-Strain Relations, *Proceedings, 1st U.S. National Congr. Appl. Mech., ASME*, **1**, 487.

Drucker, D. C. and Prager, W. (1952) Soil Mechanics and Plastic Analysis or Limit Design, *Quart. Appl. Math.*, **10**(2) 157.

Fowlkes, C. W. (1974) Fracture Toughness Tests of a Rigid Polyurethane Foam, *Int. J.*

Fracture, **10**, 99.

Gent, A. N. and Thomas, A. G. (1959) The Deformation of Foamed Elastic Materials, *J. Appl. Polymer Sci.*, **1**, 107.

Gibson, L. J. and Ashby, M. F. (1982) The Mechanics of Three-Dimensional Cellular Materials, *Proc. Roy. Soc.*, **A382**, 43.

Gibson, L. J. and Ashby, M. F. (1988) *Cellular Solids: Structure and Properties*, Pergamon, Oxford.

Green, D. J. (1985) Fabrication and Mechanical Properties of Lightweight Ceramics Produced by Sintering of Hollow Spheres, *J. Amer. Ceram. Soc.*, **68**, 403.

Gupta, S., Watson, B., Beaumont, P. W. R. and Ashby, M. F. (1986) Final Year Project, Cambridge University Engineering Department, Cambridge, U.K.

Hagiwara, H. and Green, D. J. (1987) Elastic Behavior of Open-Cell Alumina, *J. Amer. Ceram. Soc.*, **70**, 811.

Harrigan, T. P. and Mann, R. W. (1984) Characterization of Microstructural Anisotropy in Orthotropic Materials Using a Second Rank Tensor, . *Mater. Sci.*, **19**, 761.

Hill, R. (1950) *The Mathematical Theory of Plasticity,* Oxford University Press, London.

Hilyard, N. C. (ed.) (1982) *Mechanics of Cellular Plastics*, MacMillan Publishing Co., Inc., New York.

Huber, A. T. and Gibson, L. J. (1988) Anisotropy of Foams, *J. Mater. Sci.*, **23**, 3031.

Kanakkanatt, S. V. (1973) Mechanical Anisotropy of Open-Cell Foams, *J. Cell. Plast.*, **9**, 50.

Kurauchi, T., Sato, N., Kamigaito, O. and Komatsu, N. (1984) Mechanism of High Energy Absorption by Foamed Materials-Foamed Rigid Polyurethane and Foamed Glass, *J. Mat. Sci.*, **19**, 871.

Love, A. E. H. (1963) *A Treatise on the Mathematical Theory of Elasticity*, Dover, New York.

Mah, T., Mendiratta, M. G., Katz, A. P., Ruh, R. and Mazdiyasni, K. S. (1985) Room-Temperature Mechanical Behavior of Fiber-Reinforced Ceramic-Matrix Composites, *J. Amer. Ceram. Soc.*, **68**, C-27.

Maiti, S. K., Gibson, L. J. and Ashby, M. F. (1984a) Deformation and Energy Absorption Diagrams for Cellular Materials, *Acta Metal.*, **32**, 1963.

Maiti, S. K., Ashby, M. F. and Gibson, L. J. (1984b) Fracture Toughness of Brittle

Cellular Solids, *Scripta Metal.*, **18**, 213.

Mal'tsev, K. I. (1968) Elastic Characteristics of Semi-Rigid Polyurethane Foam Plastic Under Small Deformations, *J. Soviet Phys.-Acoustics*, **13**, 391.

Malvern, L. E. (1969) *Introduction to the Mechanics of a Continuous Medium*, Prentice-Hall, Inc.

Marshall, D. B. and Evans, A. G. (1985) Failure Mechanisms in Ceramic-Fiber/Ceramic-Matrix Composites, *J. Amer. Ceram. Soc.*, 68, 225.

Matonis, V. A. (1964) Elastic Behavior of Low Density Figid Foams in Structural Applications, *Soc. Plast. Eng. J.*, **20**, 1024.

McClintock, F. A. and Argon, A. S. (1966) *Mechanical Behavior of Materials*, Addison-Wesley, Mass., U.S.A.

McIntyre, A. and Anderton, G. E. (1979) *Polymer*, **20**, 247.

Mehta, B. S. and Colombo, E. A. (1976) Mechanical Properties of Foamed Thermoplastics, *J. Cell. Plast.*, **12**, 59.

Mendelson, A. (1968) *Plasticity: Theory and Applications*, Macmillan Publishing Co., Inc., New York.

Menges, G. and Knipschild, F. (1975) Estimation of Mechanical Properties for Rigid Polyurethane Foams, *Polymer Eng. Sci.*, **15**, 23.

Morgan, J. S., Wood, J. L. and Bradt, R. C. (1981) Cell Size Effects on the Strength of Foamed Glass, *Mat. Sci. Eng.*, **47**, 37.

Neville, A. M. (1981) *Properties of Concrete*, 3rd edn., Pitman, London.

Patel, M. R. (1969) The Deformation and Fracture of Rigid Cellular Plastics Under Multiaxial Stress, Ph.D. Thesis, University of California at Berkeley, U.S.A.

Patel, M. R. and Finnie, I. (1969) The Deformation and Fracture of Rigid Cellular Plastics Under Multiaxial Stress, Lawrence Livermore Laboratory Report UCRL-13420.

Patel, M. R. and Finnie, I. (1970) Structural Features and Mechanical Properties of Rigid Cellular Plastics, *J. Materials*, **5**, 909.

Prager, W. (1956) A New Method of Analyzing Stresses and Strains in Work-Hardened Plastic Solids, *ASME, J. Appl. Mech.*, **23**(E), 493.

Rice, R. W., McKinney, K. R., Wu, C. C. and Freiman, S. W. (1985) Fracture Energy of Si_3N_4, *J. Mat. Sci.*, **20**, 1392.

Rusch, K. C. (1970) Load-Compression Behavior of Brittle Foams, *J. Appl. Polymer*

Sci., **14**, 1263.

Shaw, M. C. and Sata, T. (1966) The Plastic Behavior of Cellular Materials, *Int. J. Mech. Sci.*, **8**, 469.

Shercliff, T. (1988) Response of Cellular Solids to Multiaxial Loading, Cambridge University Engineering Department Report, Cambridge, U.K.

Suh, K. W. and Skochdopole, R. E. (1980) Foamed Plastics, in *Encyclopedia of Chemical Technology*, **2**, 3rd edn., John Wiley & Sons, Inc., New York.

Suh, K. W. and Webb, D. D. (1985) Cellular Materials, in *Encyclopedia of Polymer Science*, **3**, 2nd. edn., John Wiley & Sons, Inc., New York.

Thornton, P. H. and Magee, C. L. (1975a) The Deformation of Aluminum Foams, *Met. Trans.*, **6A**, 1253.

Thornton, P. H. and Magee, C. L. (1975b) Deformation Characteristics of Zinc Foam, *Met. Trans.*, **6A**, 1801.

Timoshenko S. P. and Goodier, J. N. (1970) *Theory of Elasticity*, 3rd edn., McGraw-Hill, New York.

Weibull, W. (1951) A Statistical Distribution Function of Wide Applicability, *J. Appl. Mech.*, **18**, 293.

Wendle, B. C. (ed.) (1976) *Engineering Guide to Structural Foams*, Technomic Publishing Co., Westport, Conn.

Yamada, Y., Yishimura, N. and Sakurai, T. (1968) Plastic Stress-Strain Matrix and its Applications for the Solution of Elastic-Plastic Problems by the Finite Element Method, *Int. J. Mech. Sci.*, **10**, 343.

Zaslawsky, M. (1973) Multiaxial-Stress Studies on Rigid Polyurethane Foam, *Exp. Mech.*, **2**, 70.

Zhang, J. (1987) Mechanics of Cellular Materials, CPGS Thesis, Cambridge University Engineering Department, Cambridge, U.K.

Zienkiewicz, O. C. (1977) *The Finite Element Method*, 3rd edn., McGraw-Hill, New York.

Zienkiewicz, O. C., Valliapan, S. and King, I. P. (1969) Elasto-Plastic Solutions of Engineering Problems. Initial-Stress, Finite Element Approach, *Int. J. Num. Meth. Eng.*, **1**, 75.

Zwissler, J. G. and Adams, M. A. (1983) Fracture Mechanics of Cellular Glass, in *Fracture Mechanics of Ceramics*, **6**, 211, (ed. Bradt, R. C.), Plenum Press, New York.

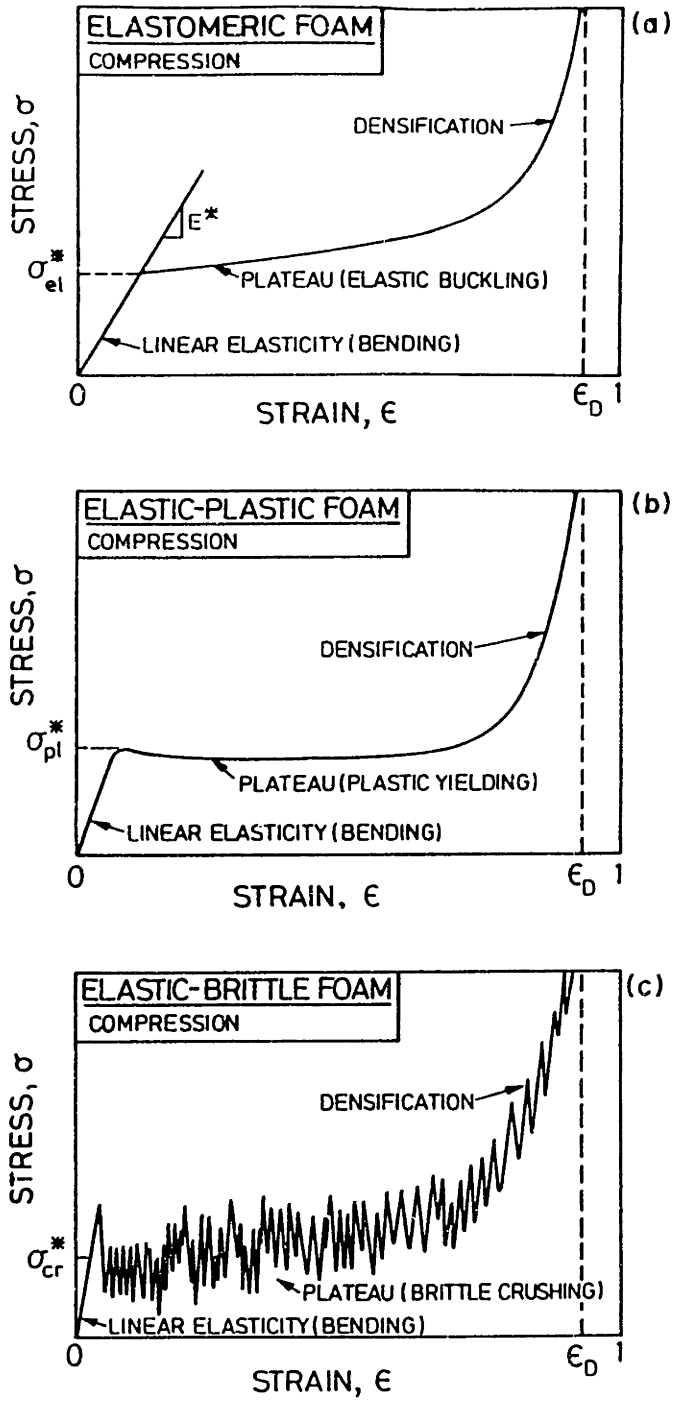

Fig. 4.1 Schematic compressive stress-strain curves for 3D cellular materials, showing the three regimes of linear elasticity, collapse, and densification: (a) elastomeric foam; (b) elastic-plastic foam; (c) elastic-brittle foam (after Gibson and Ashby, 1988).

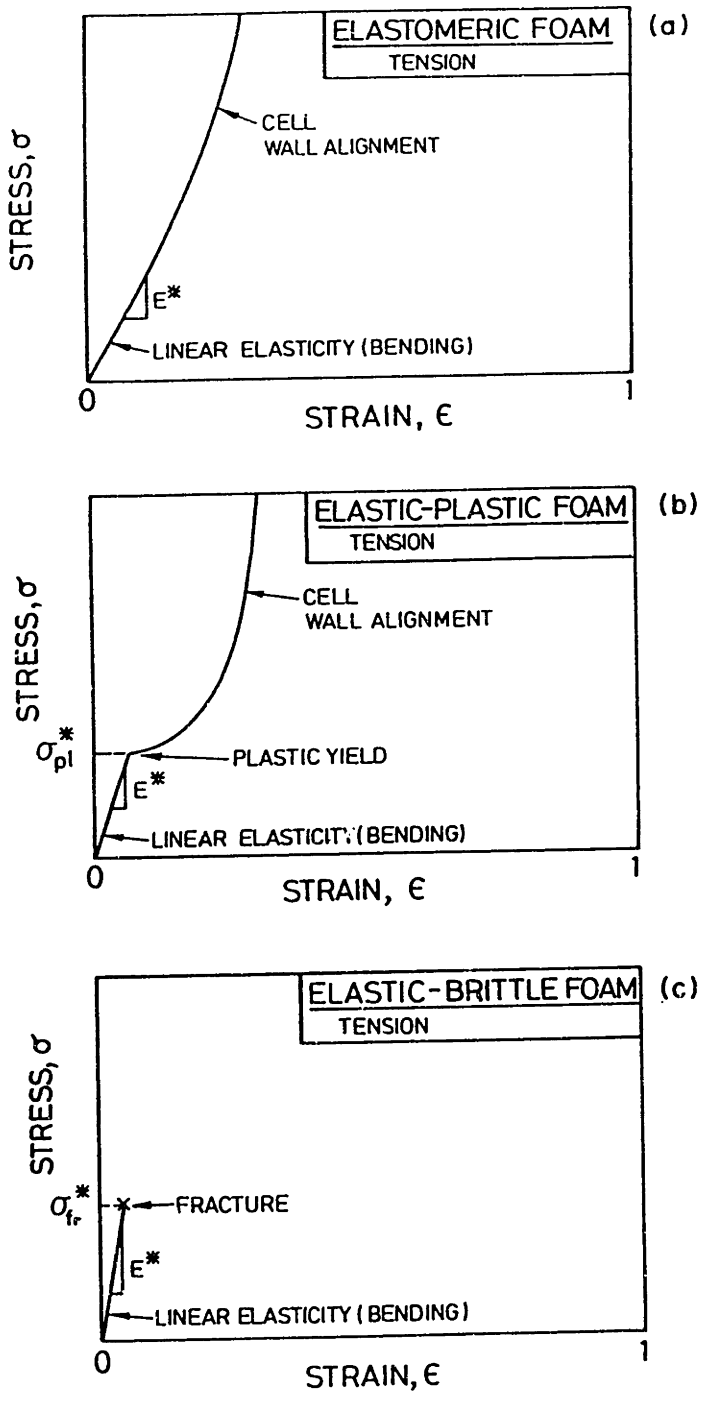

Fig. 4.2 Schematic tensile stress-strain curves for 3D cellular materials, showing the regimes of behavior: (a) elastomeric foam; (b) elastic-plastic foam; (c) elastic-brittle foam (after Gibson and Ashby, 1988).

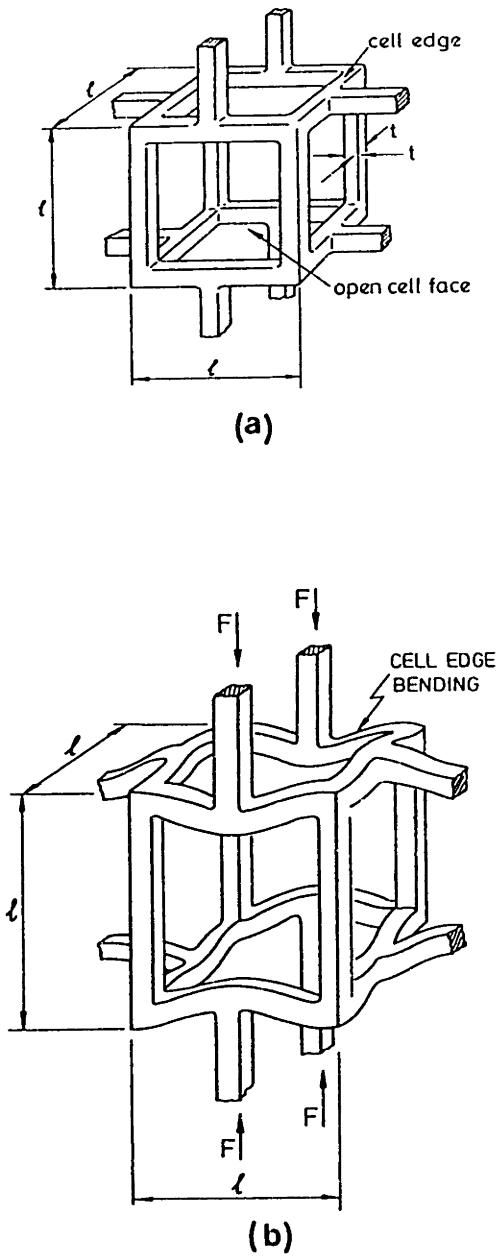

Fig. 4.3 (a) A cubic model for an isotropic open-cell foam showing the edge length, l, and the edge thickness, t. (b) Cell edge bending during linear elastic deformation (after Gibson and Ashby, 1988).

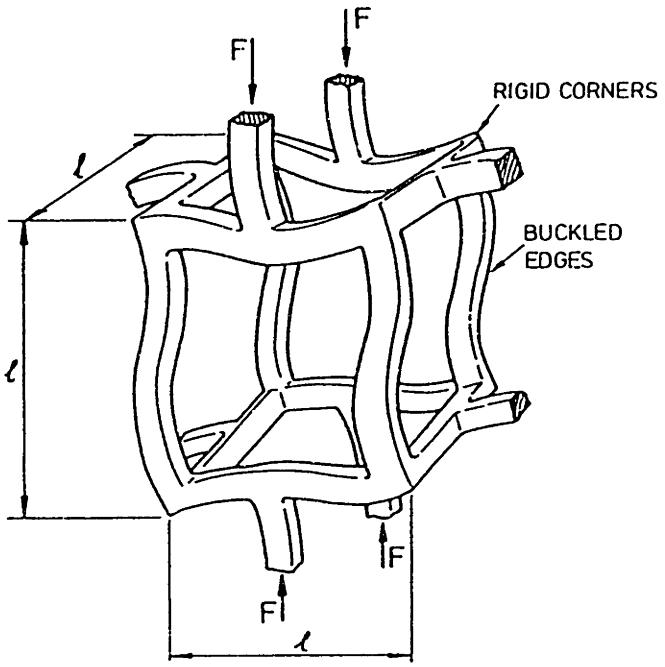

Fig. 4.4 Elastic buckling in the cell walls of an isotropic open-cell foam (after Gibson and Ashby, 1988).

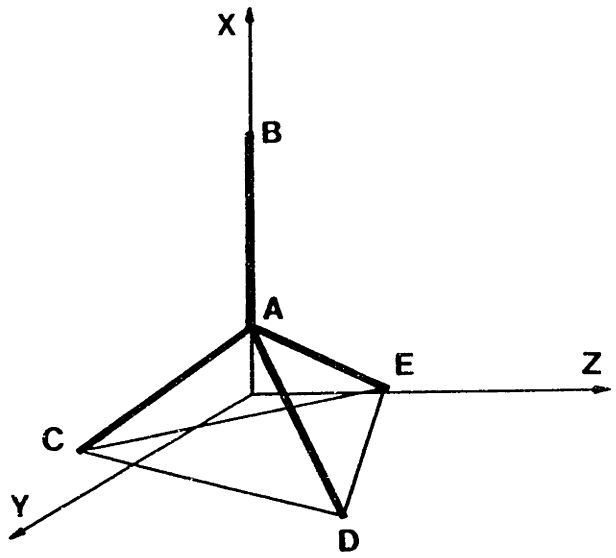

(a)

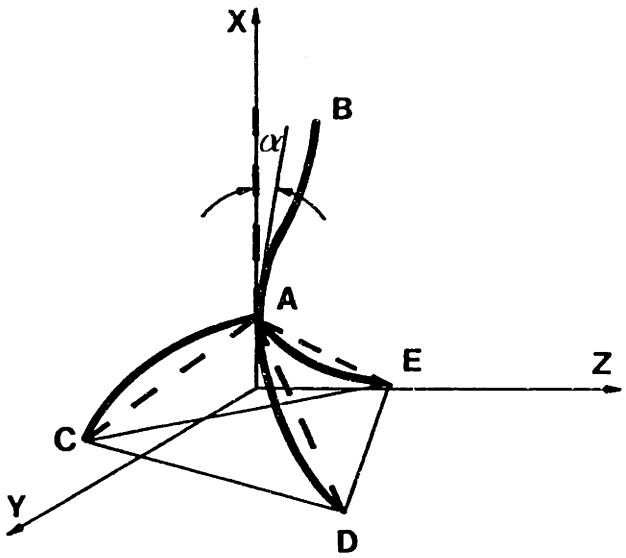

(b)

Fig. 4.5 (a) The four members at a node of a pentagonal dodecahedral cell. (b) The assumed deflected shape of the members under compressive loading.

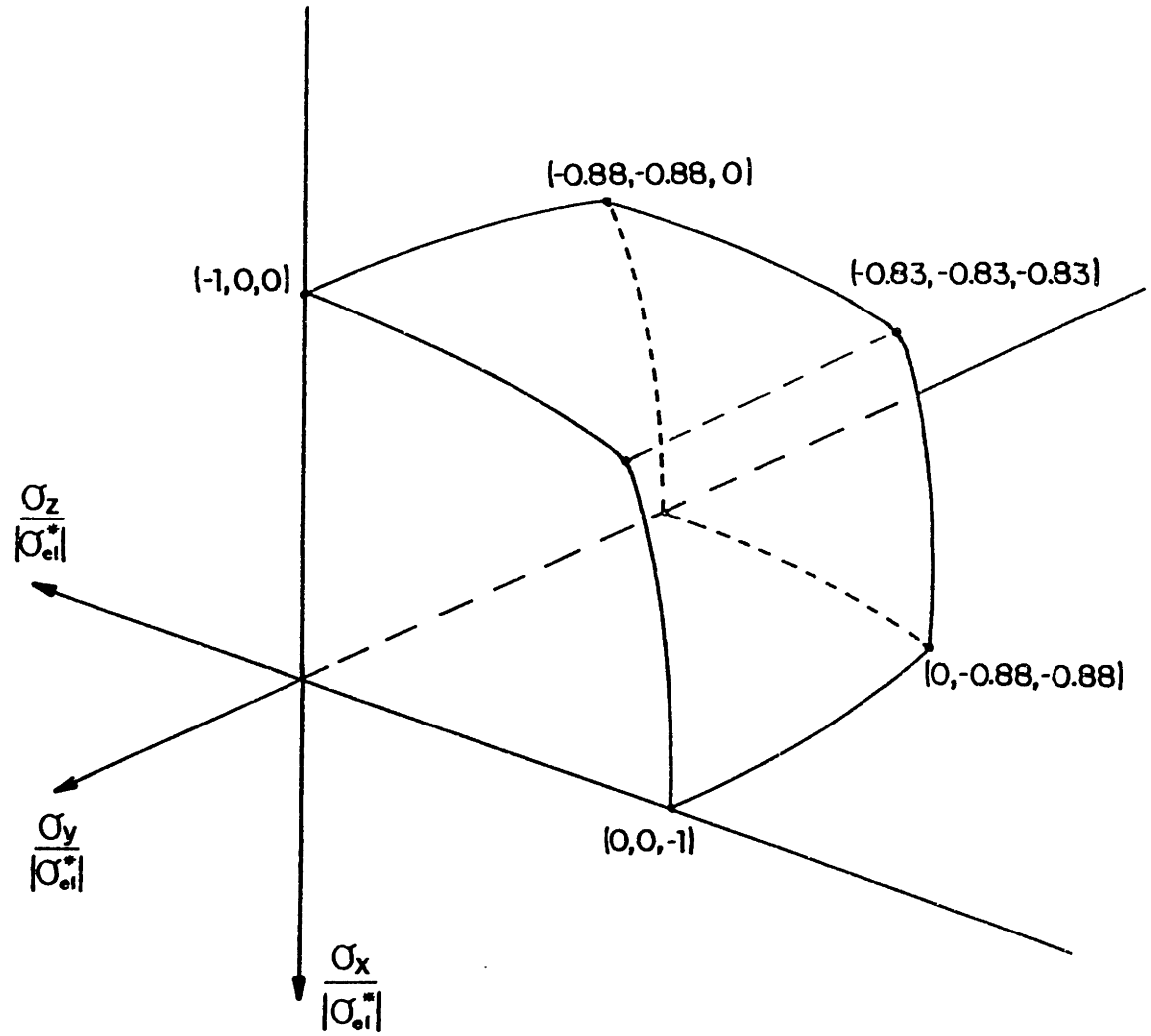

Fig. 4.6 The elastic buckling failure surface for an isotropic material.

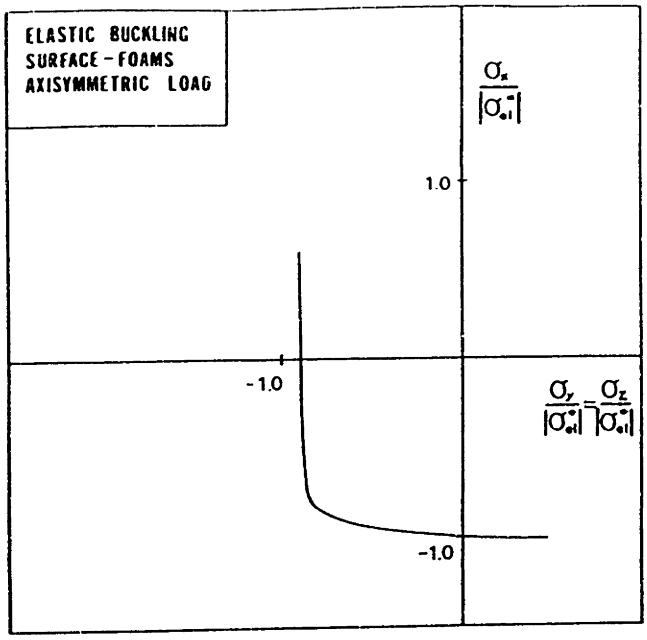

(a)

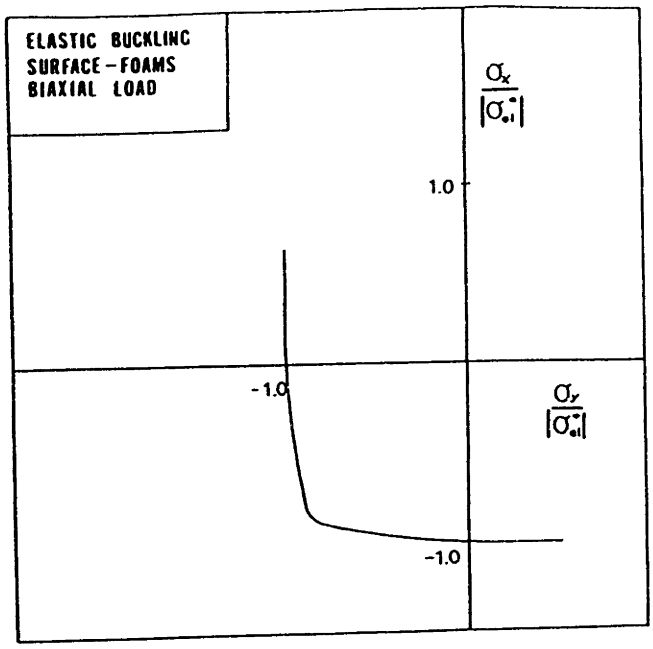

(b)

Fig. 4.7 Sections through the elastic buckling surface for an isotropic material under (a) axisymmetric loading and (b) biaxial loading.

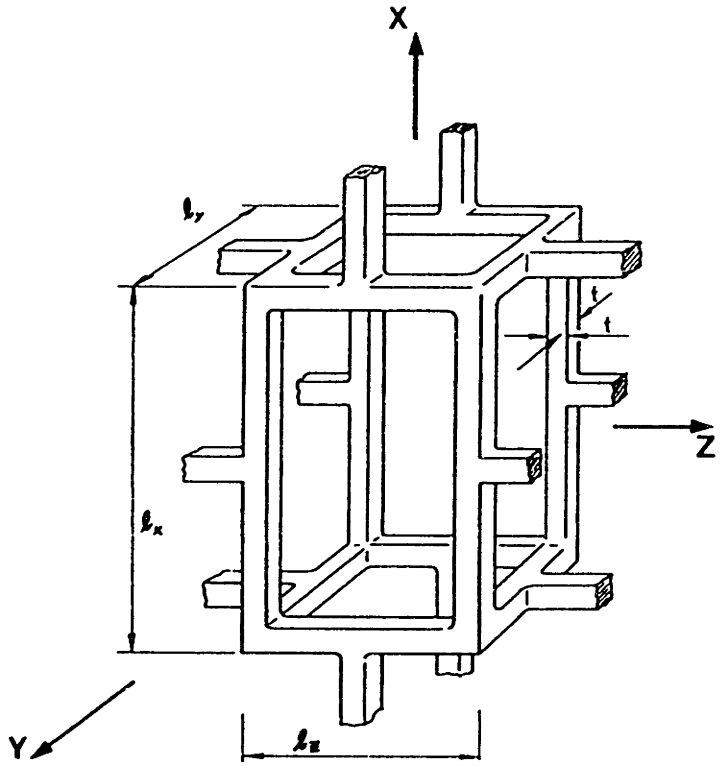

Fig. 4.8 An orthotropic unit cell (after Huber and Gibson, 1988).

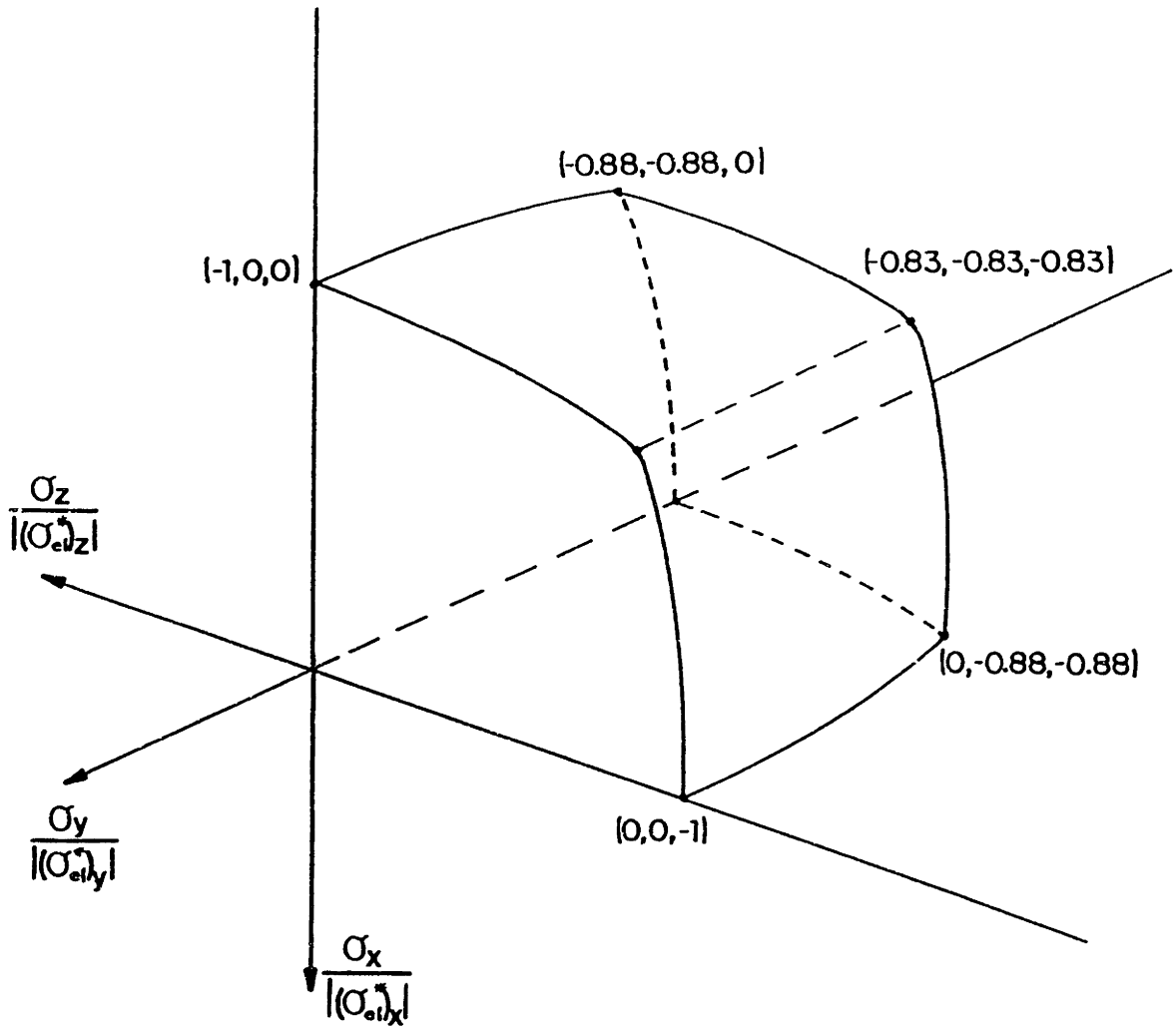

Fig. 4.9 The elastic buckling failure surface for an orthotropic material.

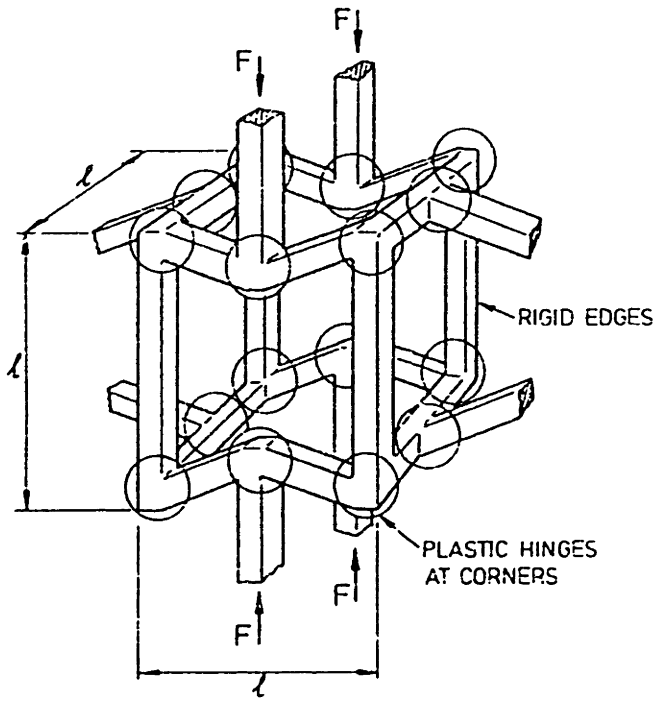

Fig. 4.10 The formation of plastic hinges in an open-cell foam (after Gibson and Ashby, 1988).

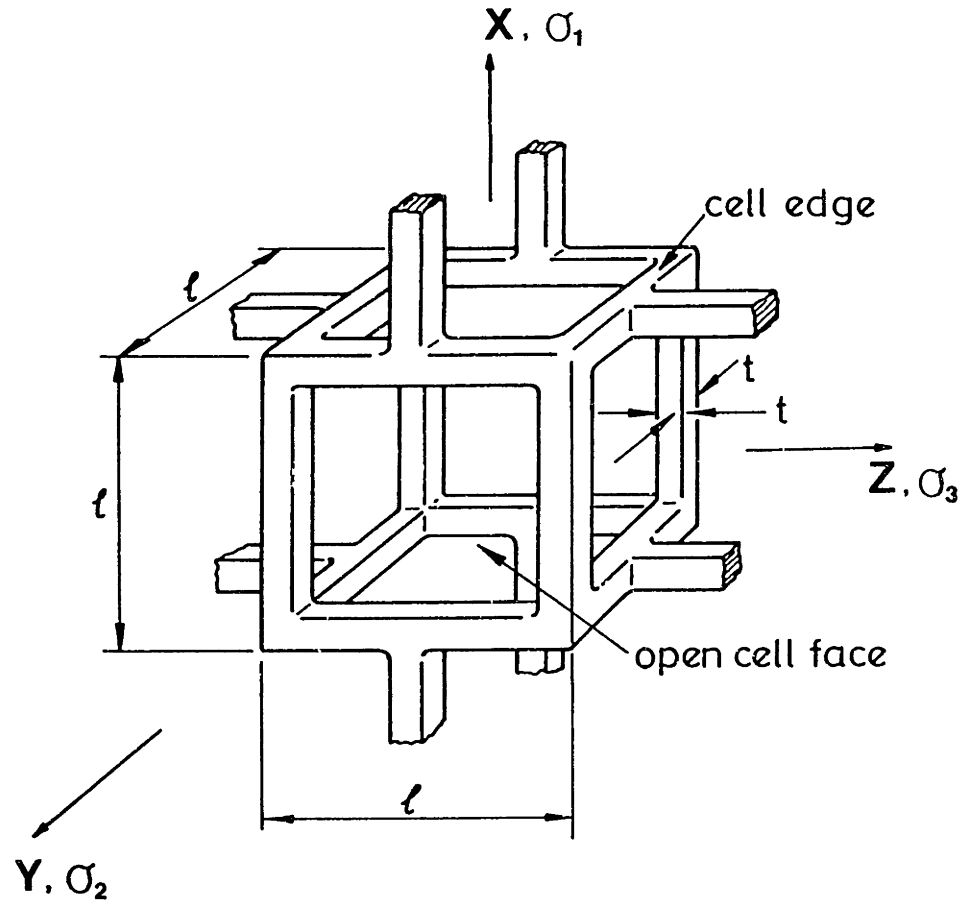

Fig. 4.11 Isotropic open cubic cell under triaxial loading (after Gibson and Ashby, 1988).

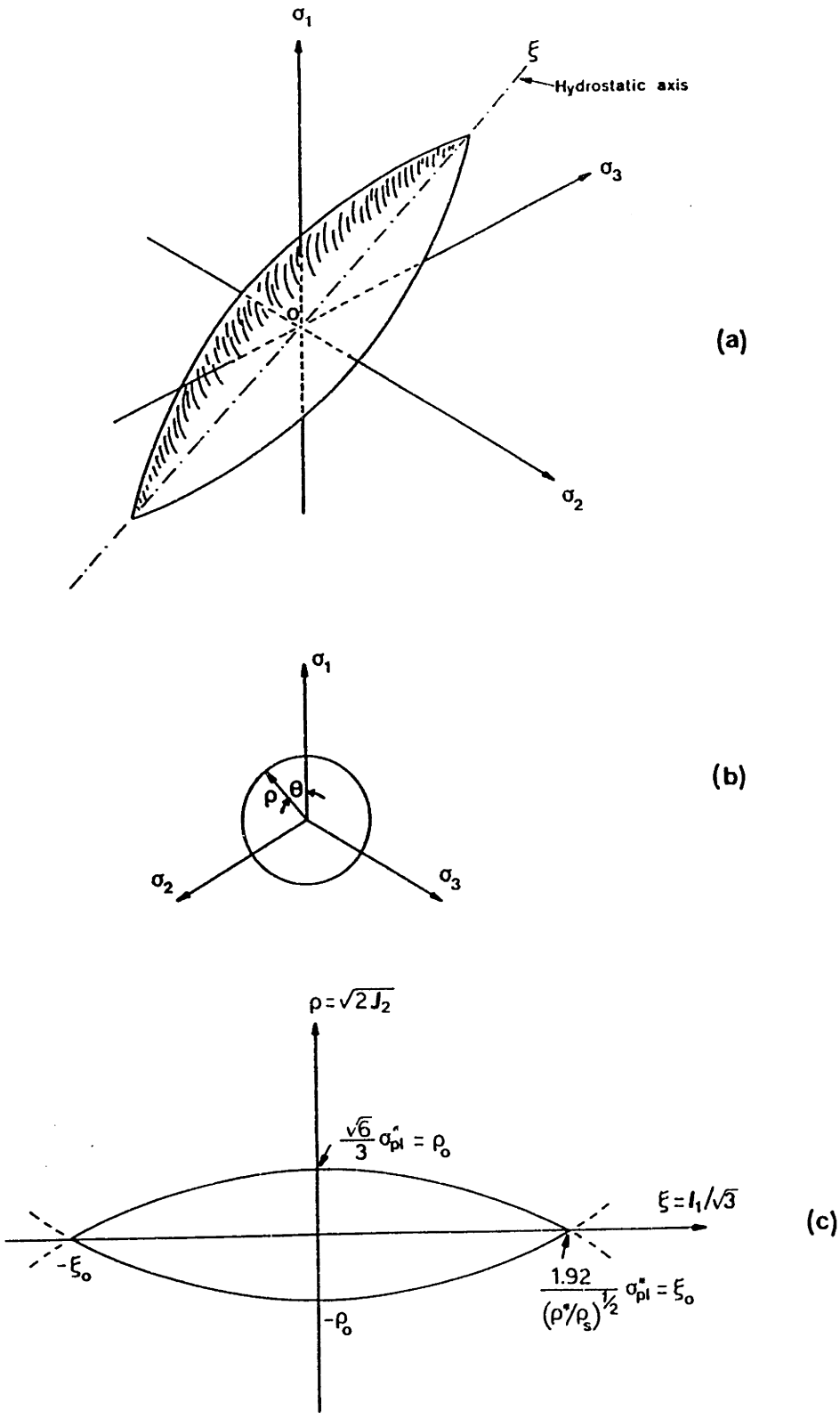

Fig. 4.12 (a) The plastic collapse surface of an isotropic 3D cellular material in principal stress space. (b) Projections on the deviatoric plane of the coordinate axes σ_1, σ_2, and σ_3. (c) General character of the meridians.

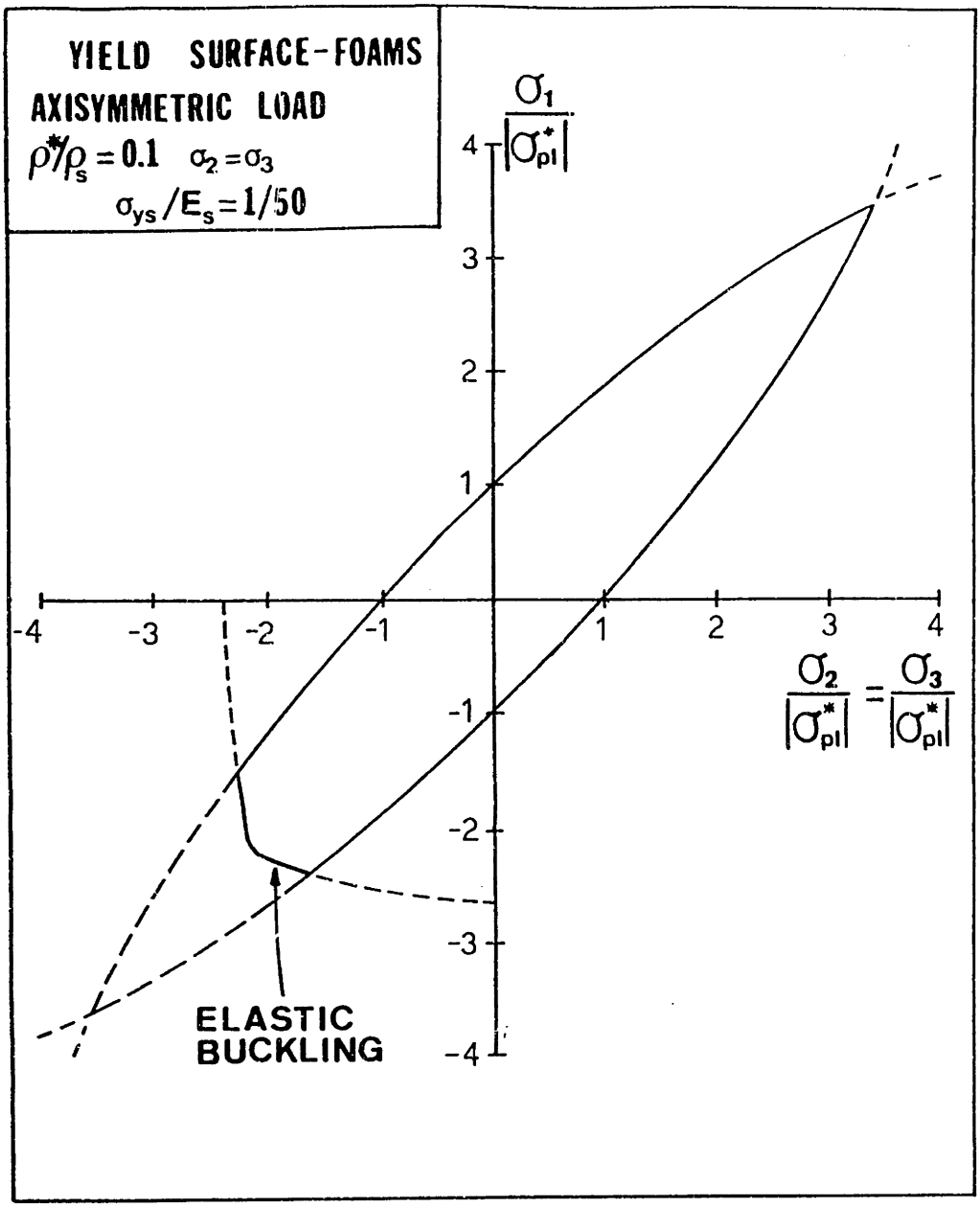

Fig. 4.13 Section through the plastic collapse surface for an isotropic foam under axisymmetric loading; the section is truncated by the elastic buckling surface in the compressive octant.

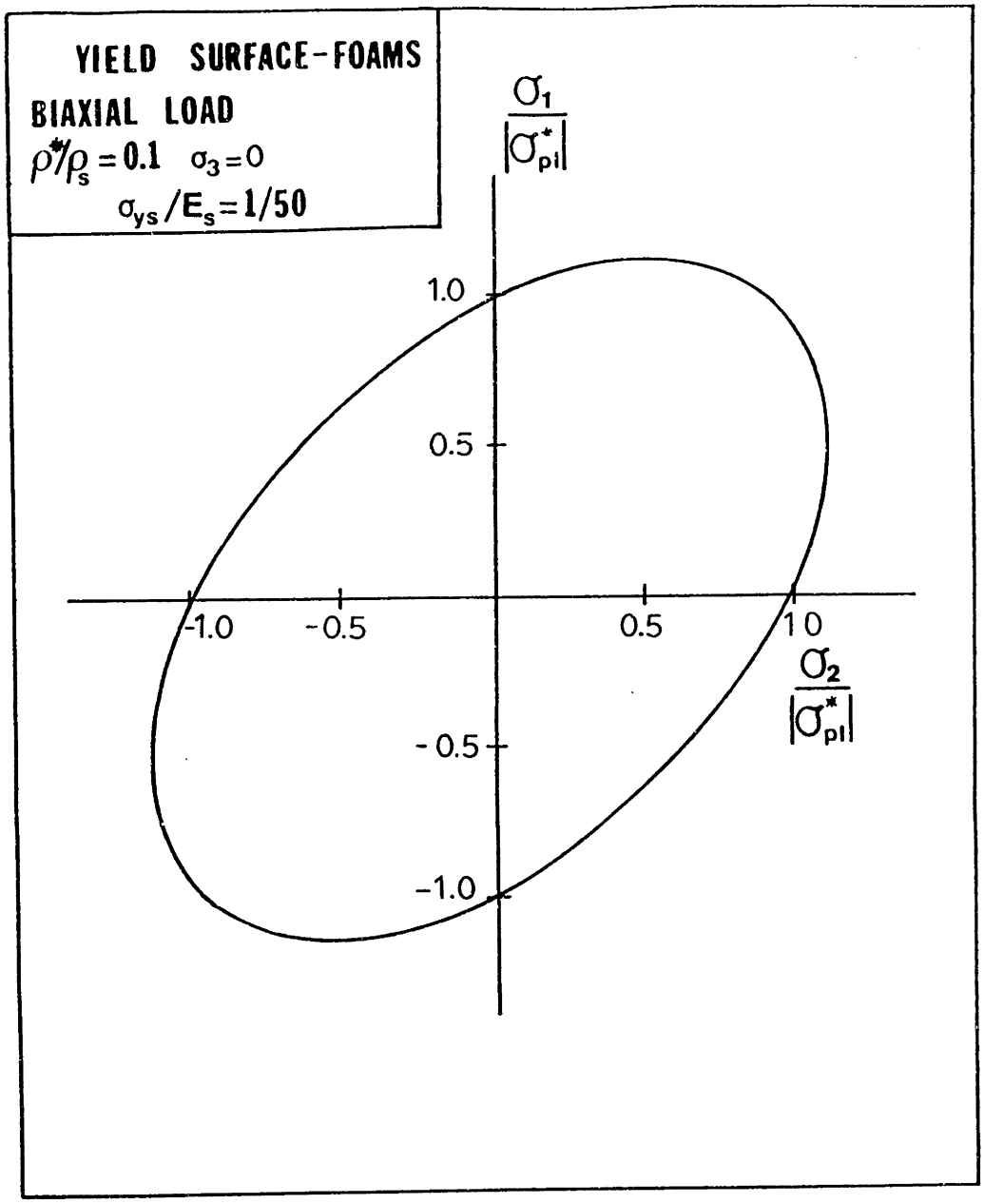

Fig. 4.14 Section through the plastic collapse surface for an isotropic foam under biaxial loading.

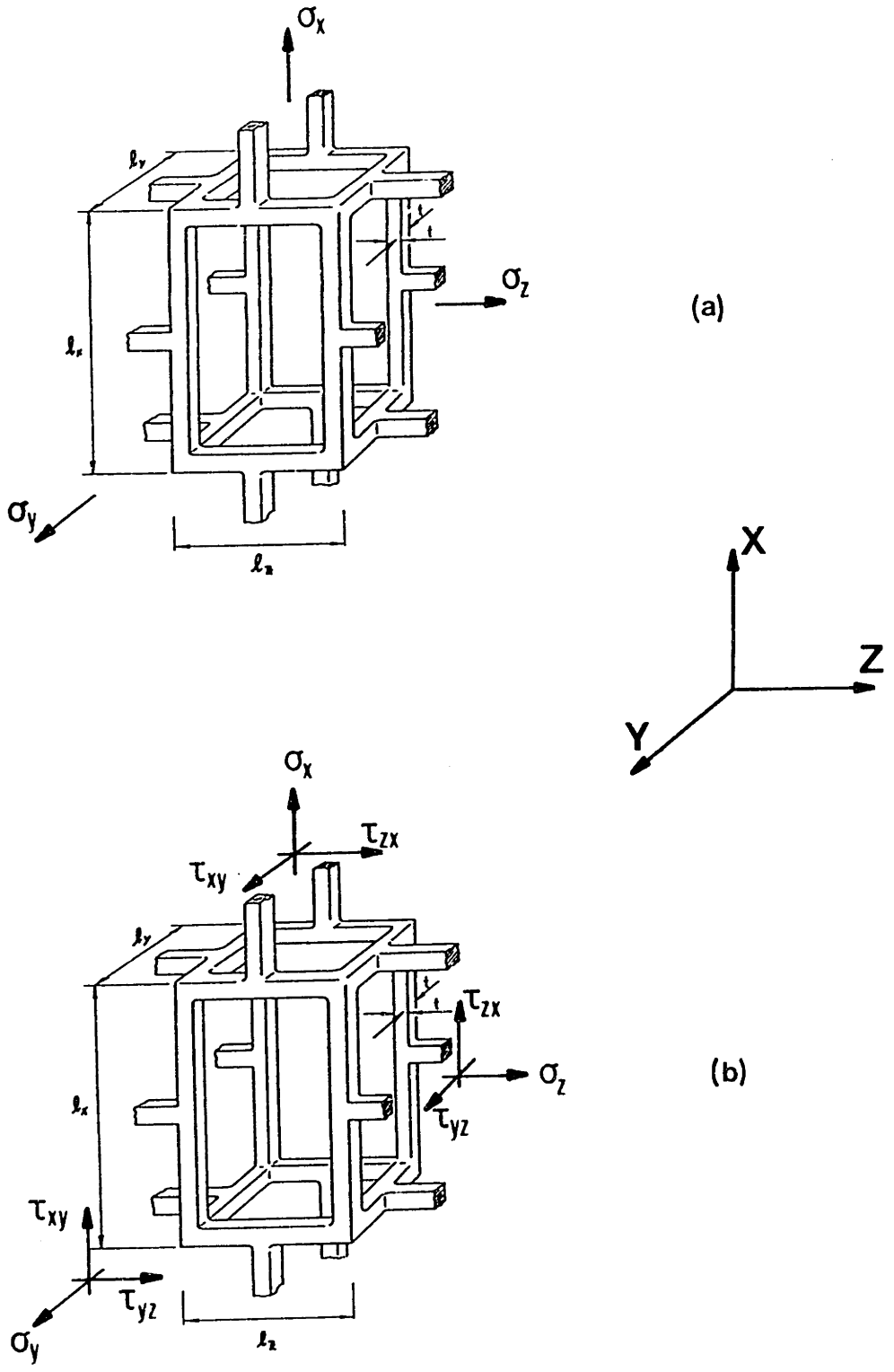

Fig. 4.15 An orthotropic unit cell: (a) the material is subjected to normal stresses acting parallel to its principal directions; (b) the material is under a general state of stress.

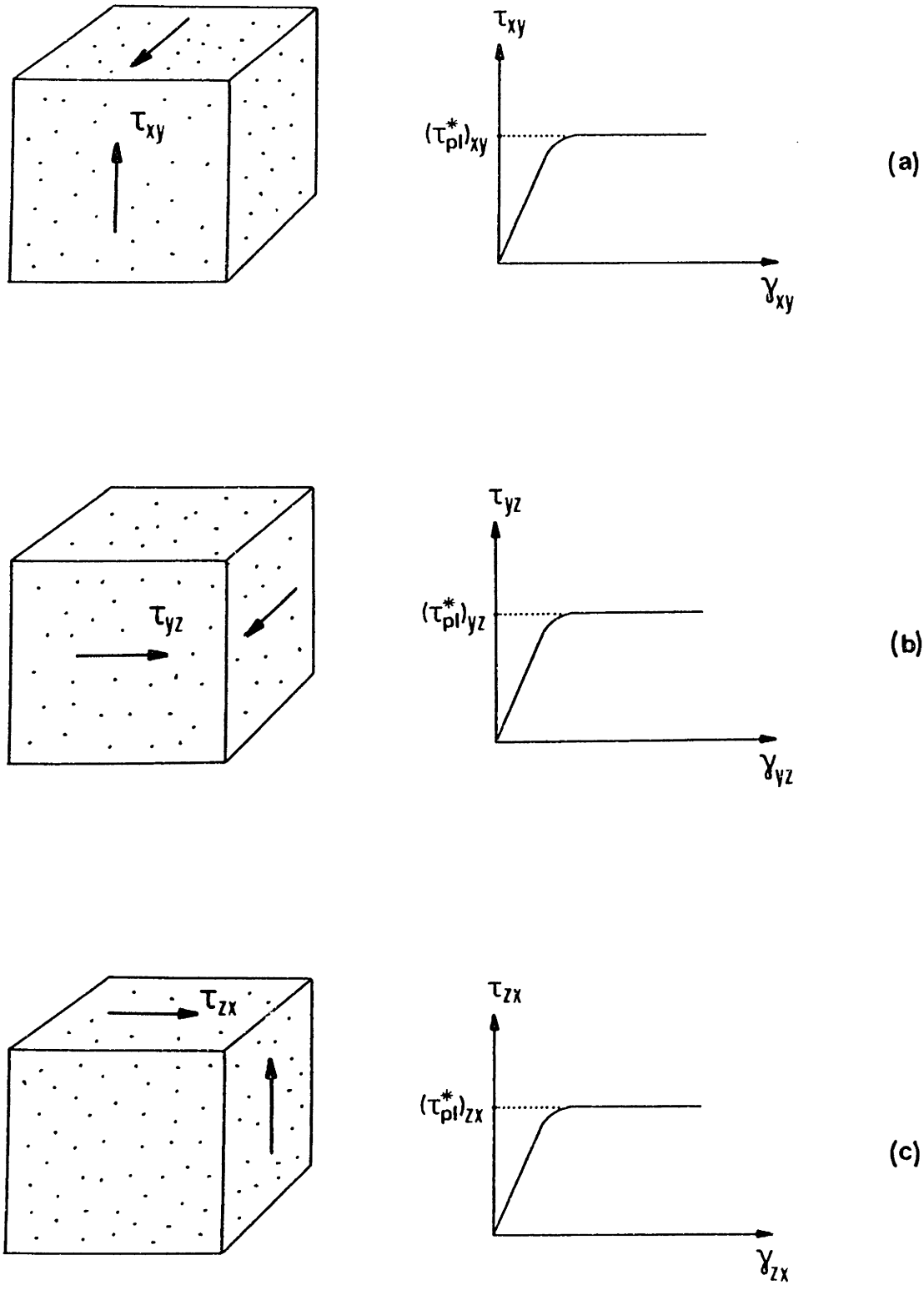

Fig. 4.16 Schematic representation of the definition of the plastic shear strengths: (a) $(\tau^*_{pl})_{xy}$; (b) $(\tau^*_{pl})_{yz}$; (c) $(\tau^*_{pl})_{zx}$.

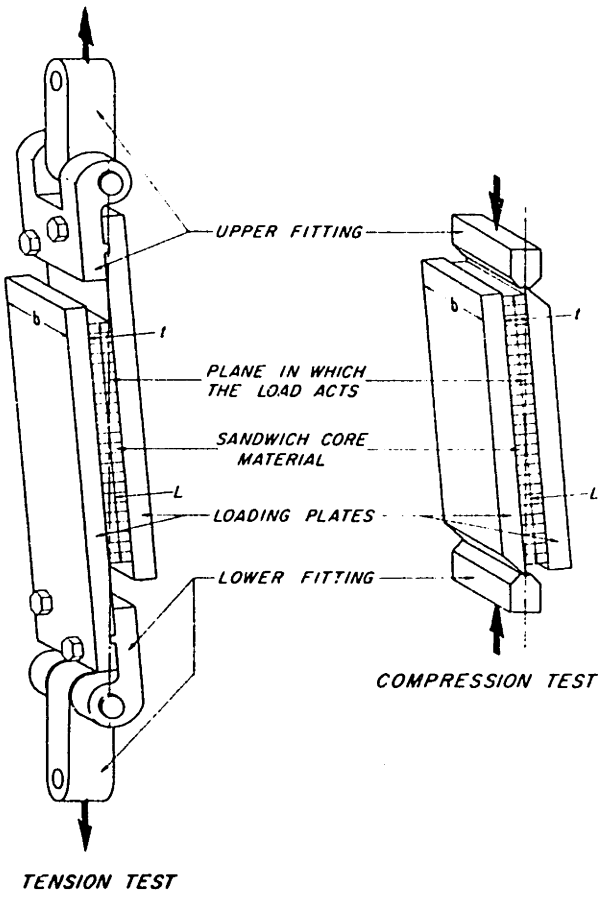

Fig. 4.17 Arrangement of apparatus and test specimen for shear tests in tension and in compression (after ASTM, C273).

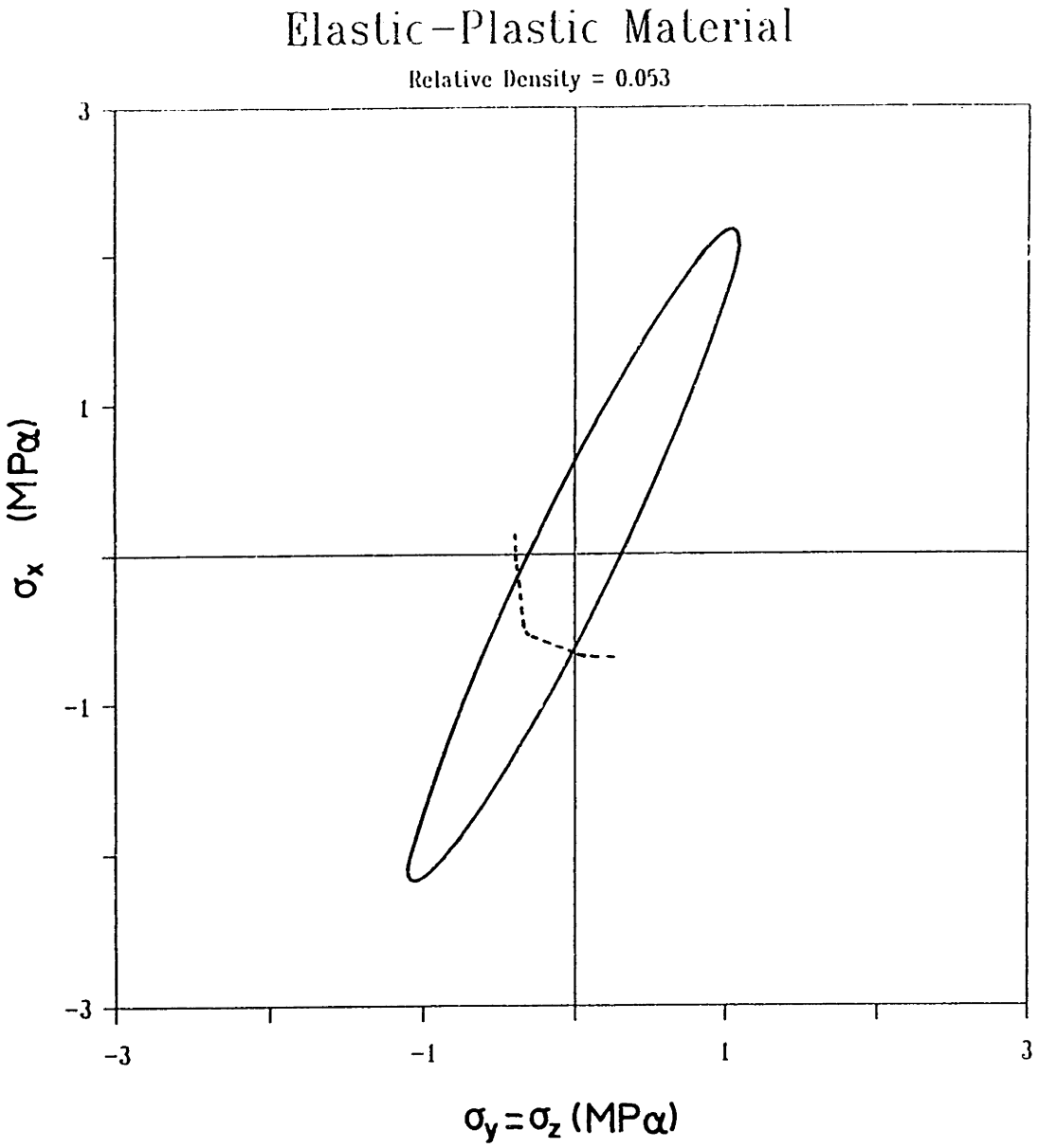

Fig. 4.18 Section through the plastic collapse surface for an orthotropic foam under axisymmetric loading; the section is truncated by the elastic buckling surface in the compression octant (dashed line). $(\sigma^*_{pl})_x$=-630 KPa, $(\sigma^*_{pl})_y$=-350 KPa, $(\sigma^*_{pl})_z$=-295 KPa.

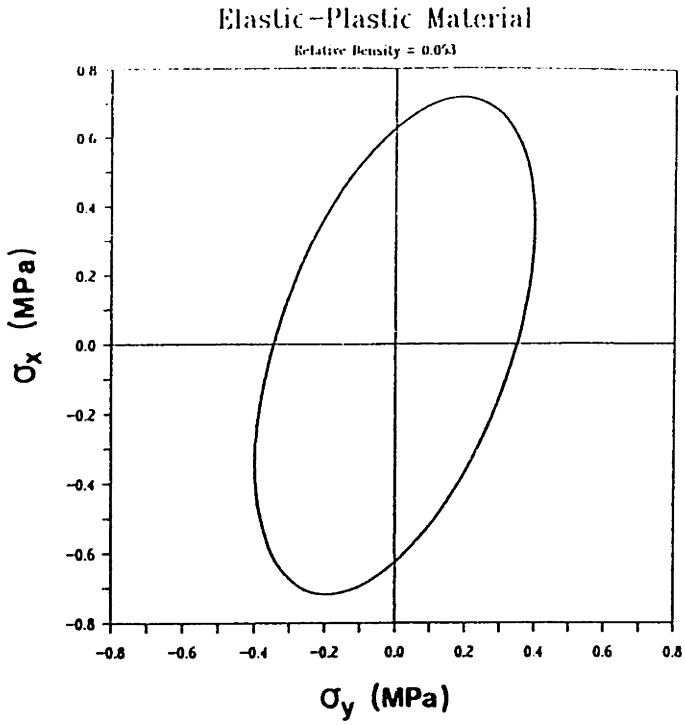

(a)

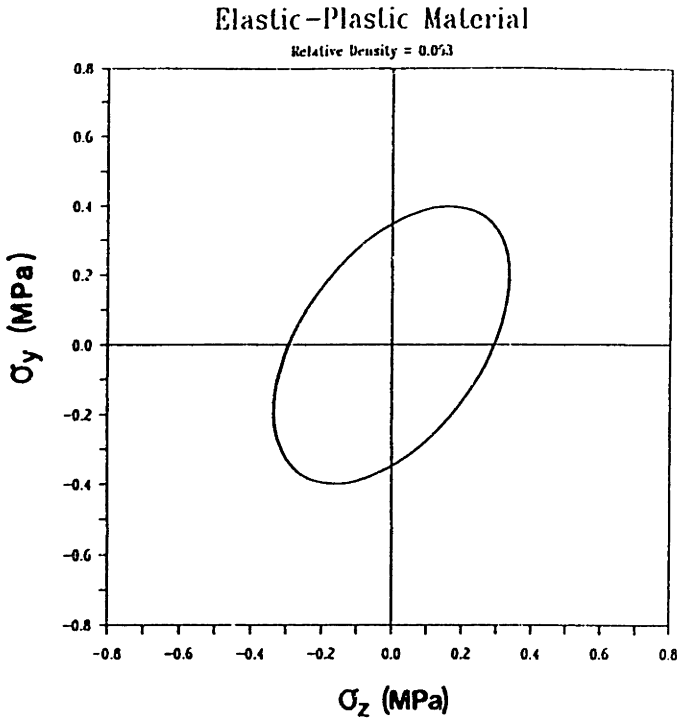

(b)

Fig. 4.19 Sections through the plastic collapse surface for an orthotropic foam under biaxial loading: (a) normal stresses act parallel to the material directions X and Y; (b) normal stresses act parallel to the material directions Y and Z. $(\sigma^*_{pl})_x$=-630 KPa, $(\sigma^*_{pl})_y$=-350 KPa, $(\sigma^*_{pl})_z$=-295 KPa.

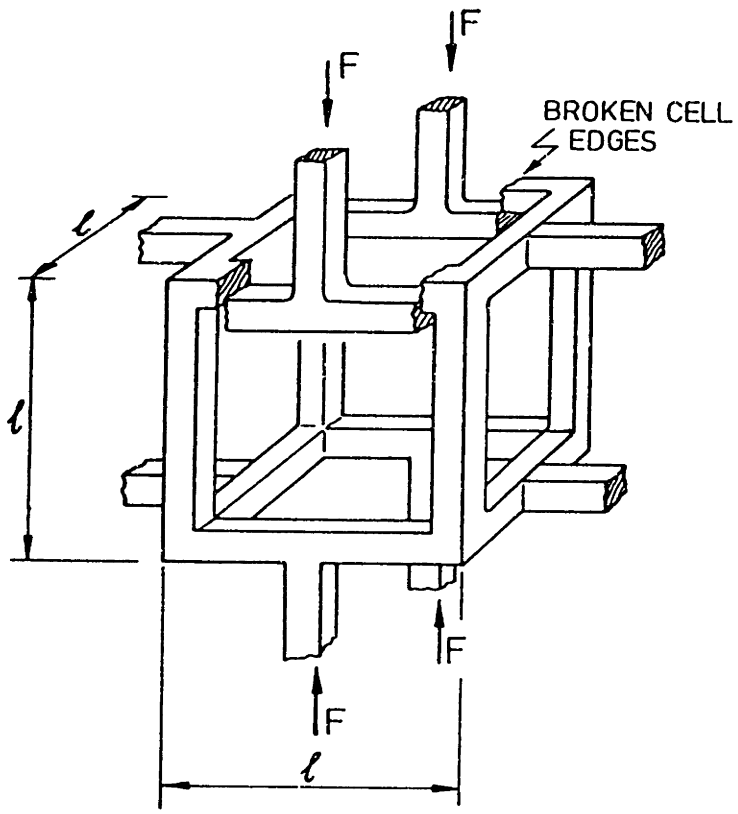

Fig. 4.20 Cell wall fracture during crushing of a brittle open-cell foam (after Gibson and Ashby, 1988).

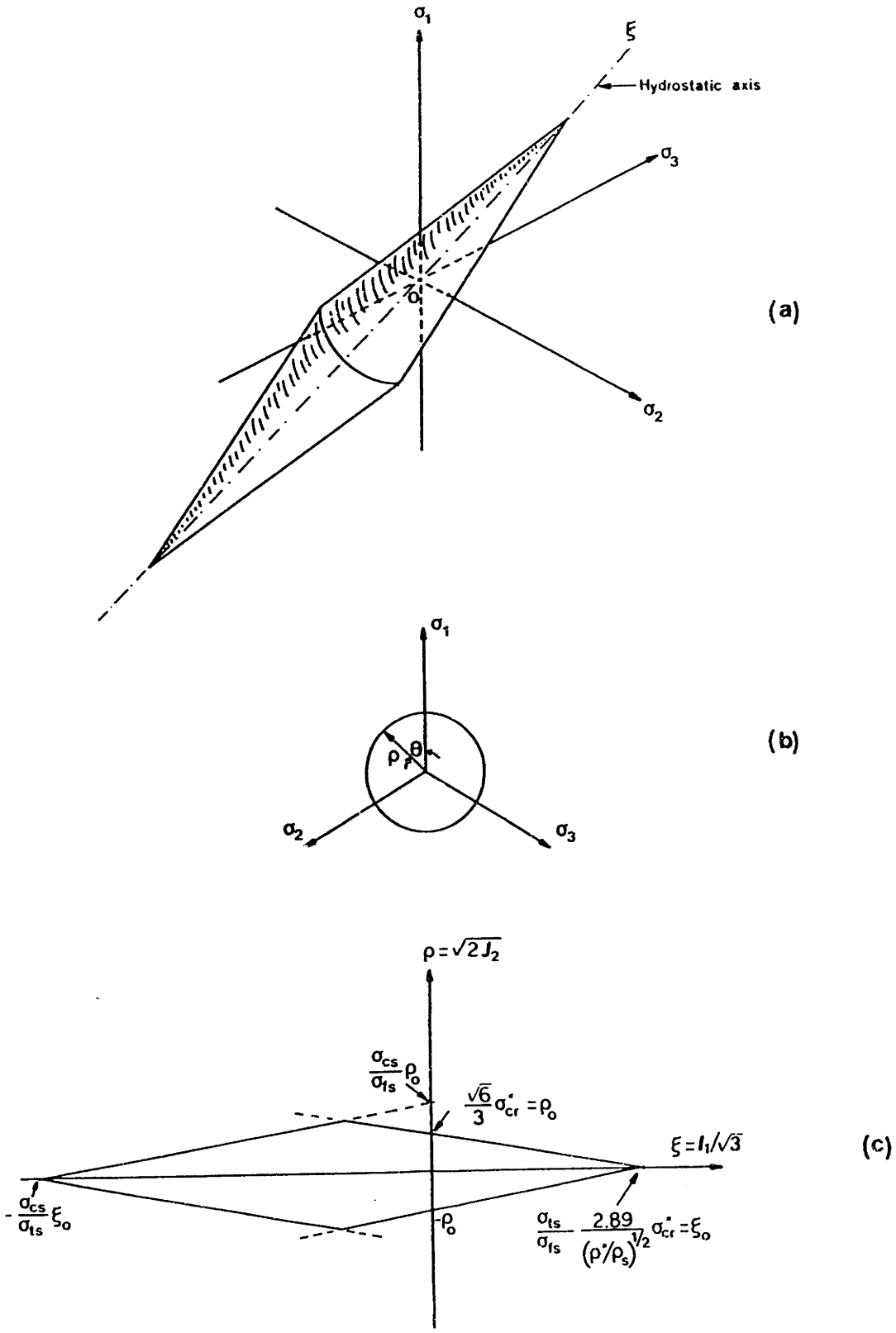

Fig. 4.21 (a) The brittle collapse surface of an isotropic 3D cellular material in principal stress space. (b) Projections on the deviatoric plane of the coordinate axes σ_1, σ_2, and σ_3. (c) General character of the meridians.

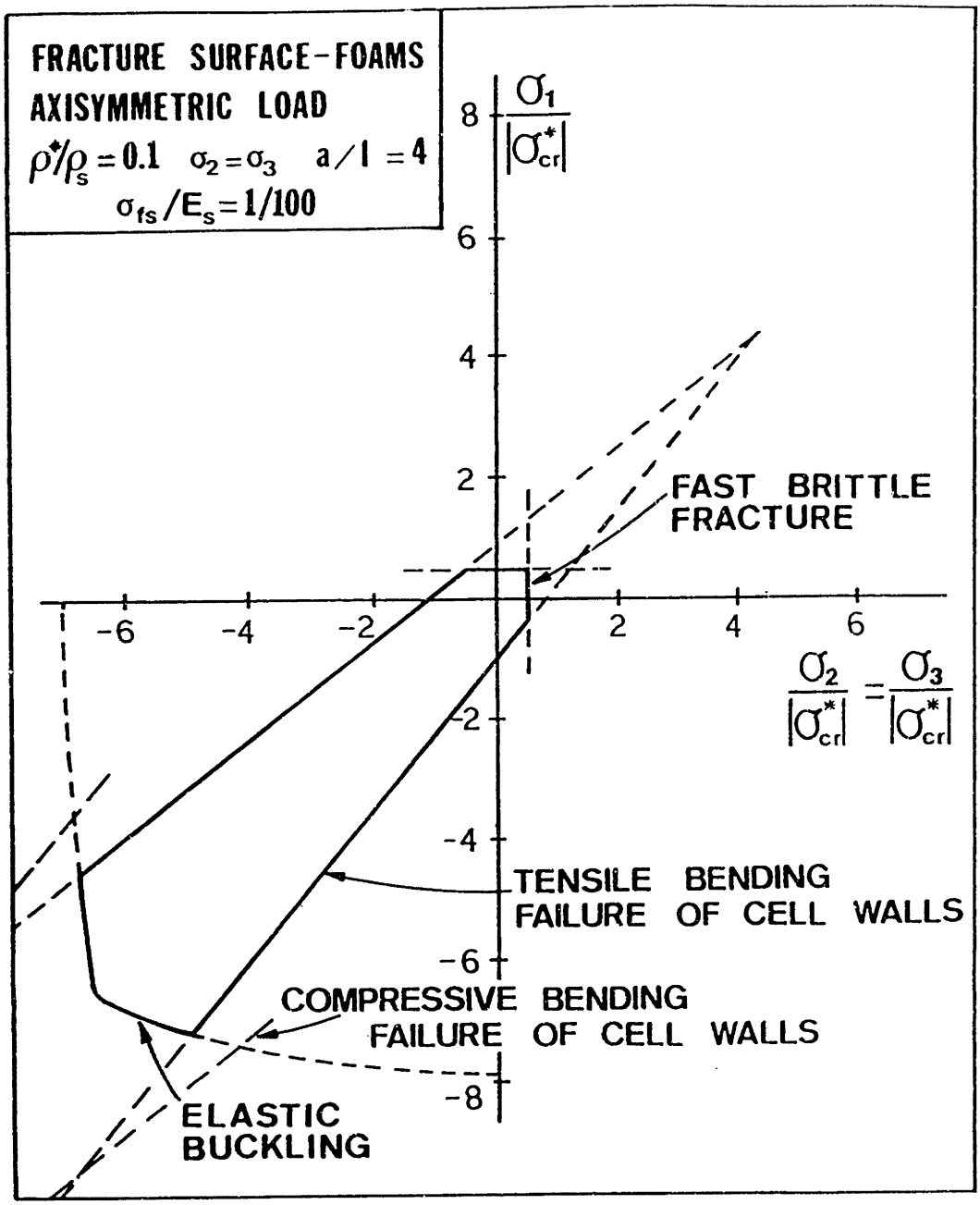

Fig. 4.22 Section through the brittle collapse surface for an isotropic foam under axisymmetric loading; the section is truncated by elastic buckling in the compression octant and by fast brittle fracture in the tension octant (σ_{fs}/σ_{ts}=1.2; σ_{cs}/σ_{fs}=4).

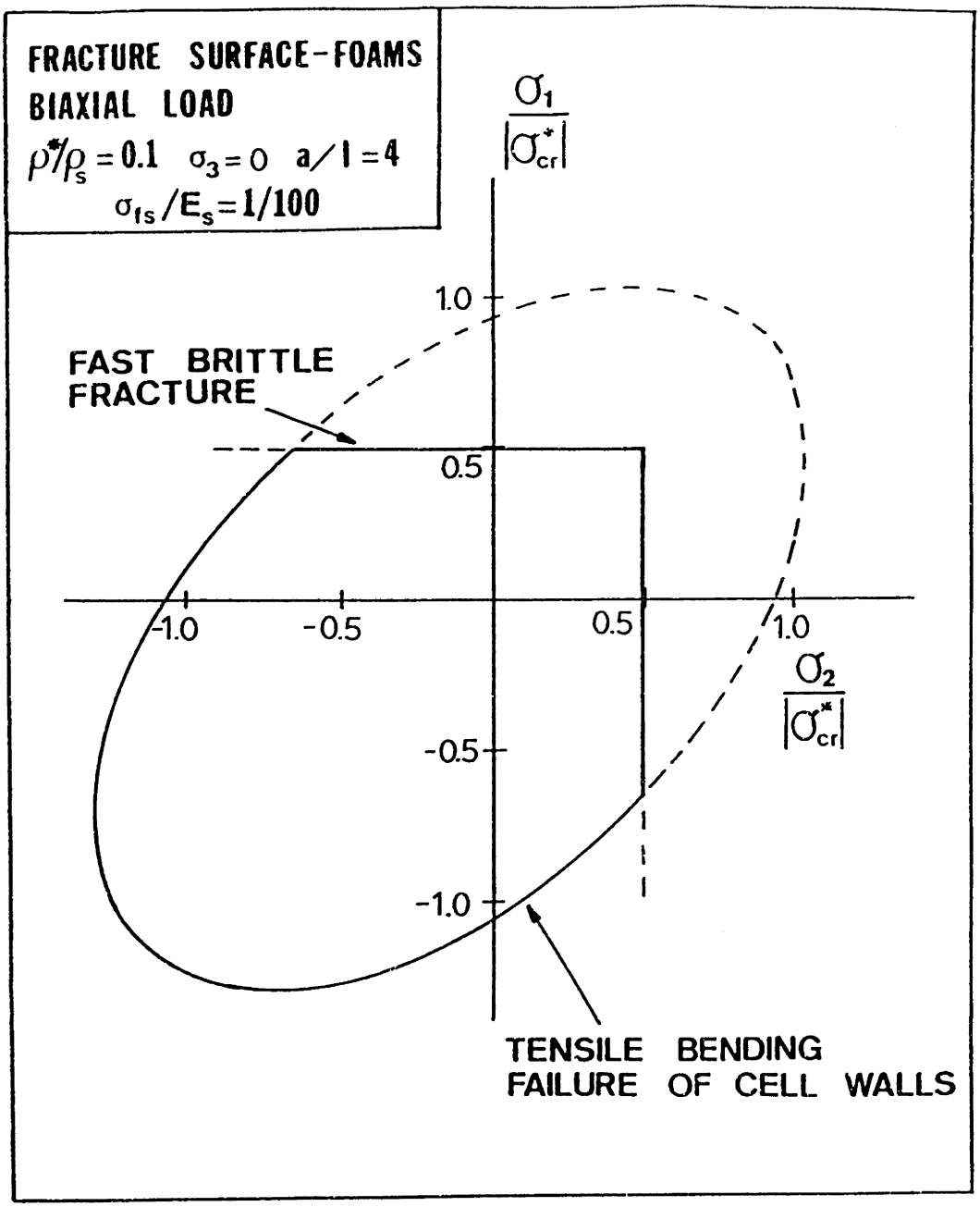

Fig. 4.23 Section through the brittle collapse surface for an isotropic foam under biaxial loading; the section is truncated by fast brittle fracture in the tension quadrant (σ_{fs}/σ_{ts}=1.2; σ_{cs}/σ_{fs}=4).

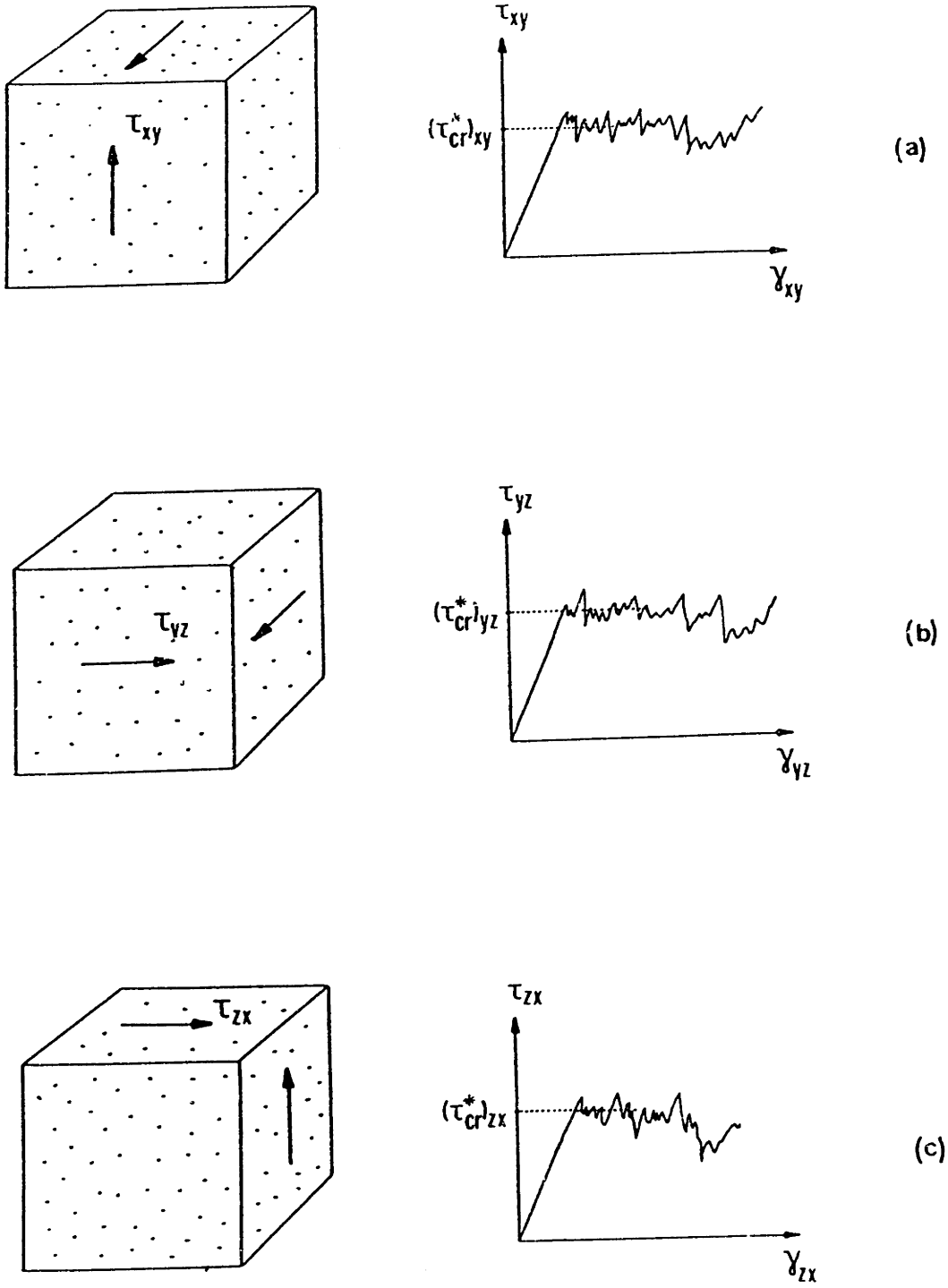

Fig. 4.24 Schematic representation of the definition of the crushing shear strengths: (a) $(\tau^*_{cr})_{xy}$; (b) $(\tau^*_{cr})_{yz}$; (c) $(\tau^*_{cr})_{zx}$.

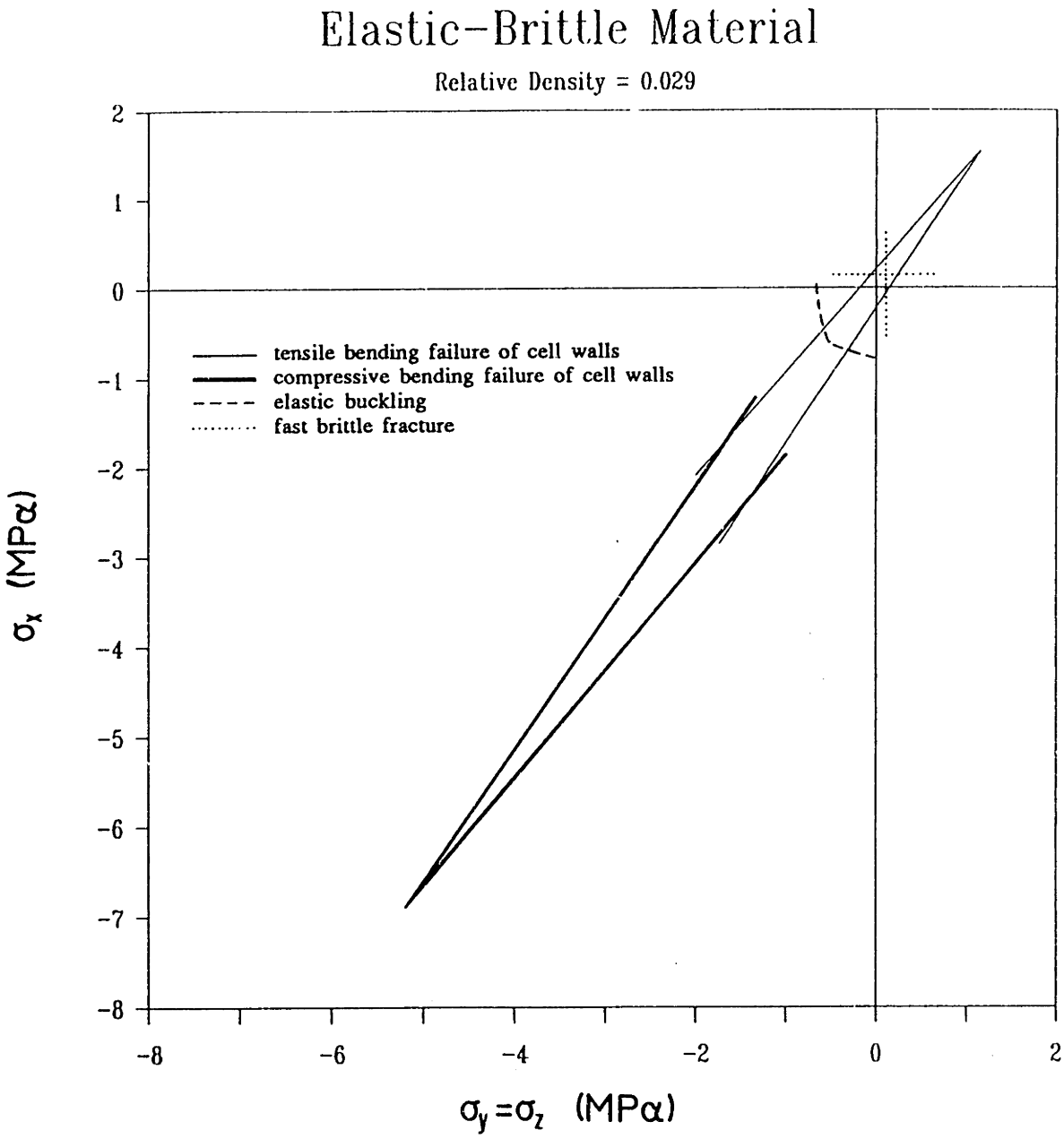

Fig. 4.25 Section through the brittle collapse surface for an axisymmetric foam under axisymmetric loading (σ_{fs}/σ_{ts}=1.36; σ_{cs}/σ_{fs}=4). $(\sigma^*_{cr})_x$=-212 KPa, $(\sigma^*_{cr})_y = (\sigma^*_{cr})_z$=-160 KPa.

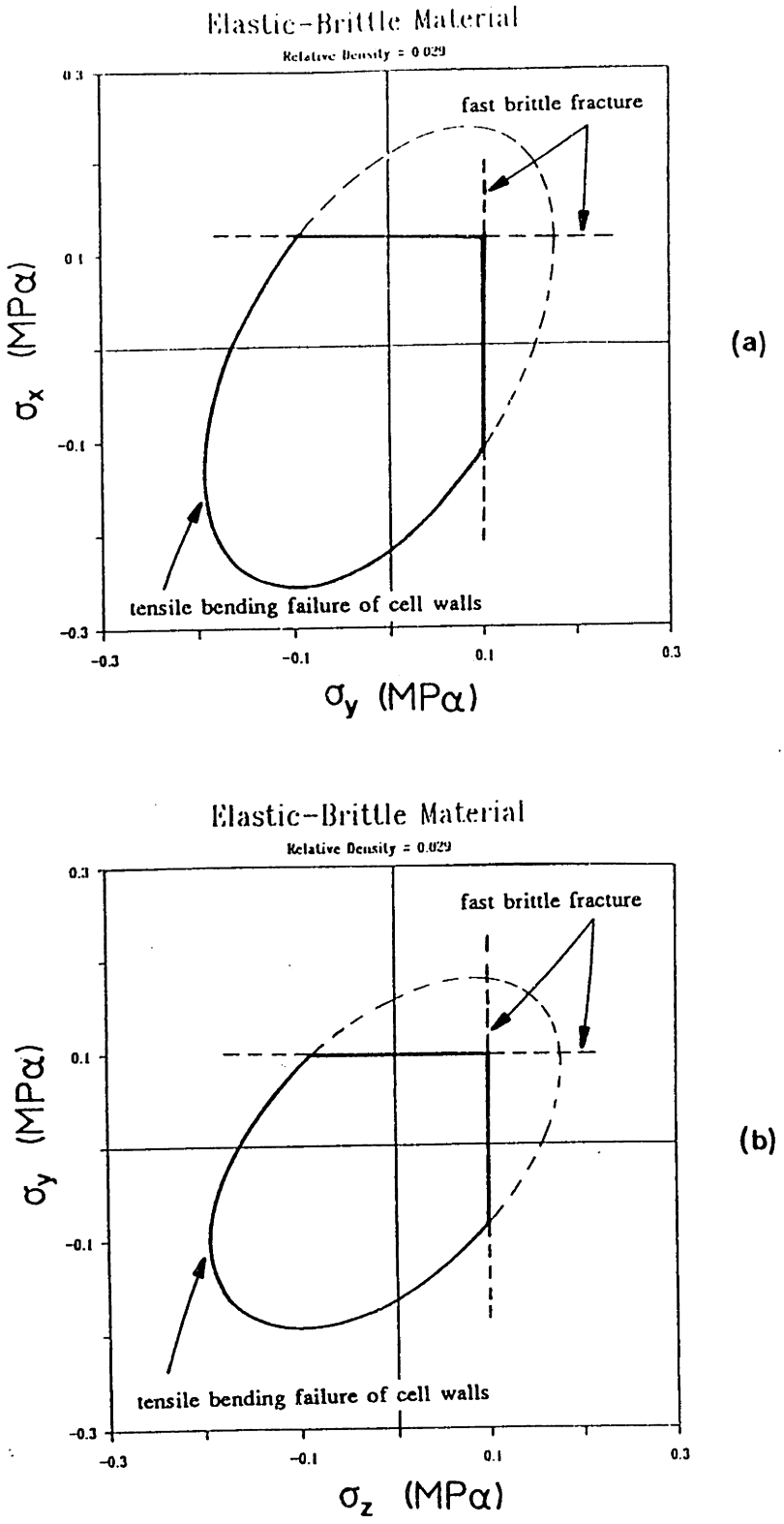

Fig. 4.26 Sections through the brittle collapse surface for an axisymmetric foam under biaxial loading (σ_{fs}/σ_{ts}=1.36; σ_{cs}/σ_{fs}=4): (a) normal stresses act parallel to the material directions X and Y; (b) normal stresses act parallel to the material directions Y and Z. $(\sigma^*_{cr})_x$=-212 KPa, $(\sigma^*_{cr})_y = (\sigma^*_{cr})_z$=-160 KPa.

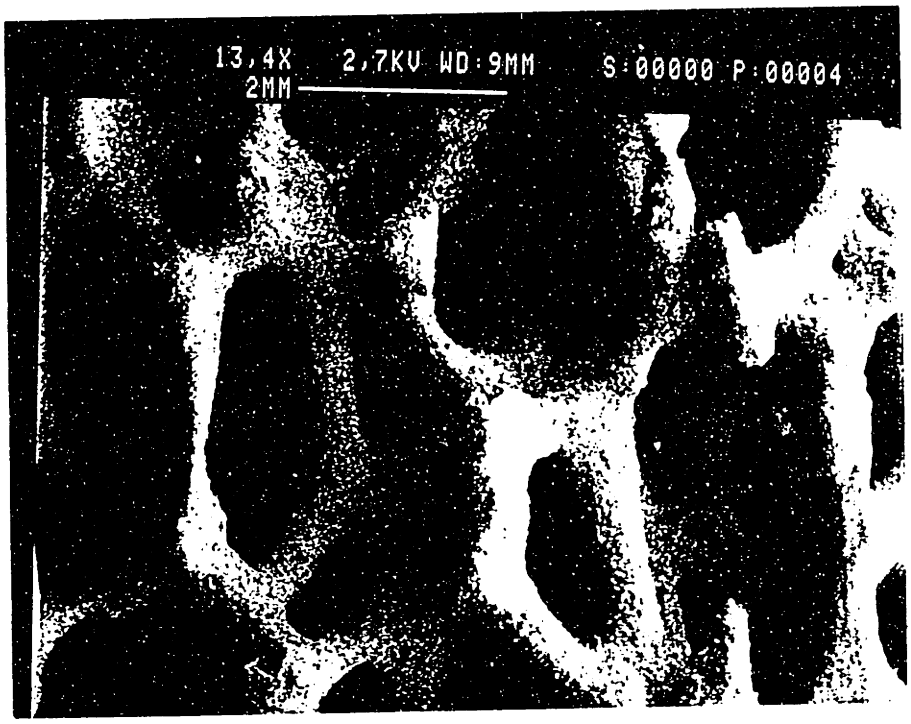

(a)

Fig. 4.27 The microstructure of an anisotropic cellular ceramic (Lithium Alumina Silicate): (a) an array of cell walls; (b) the cross-section of a cell wall; (c) the microporosity within a cell wall.

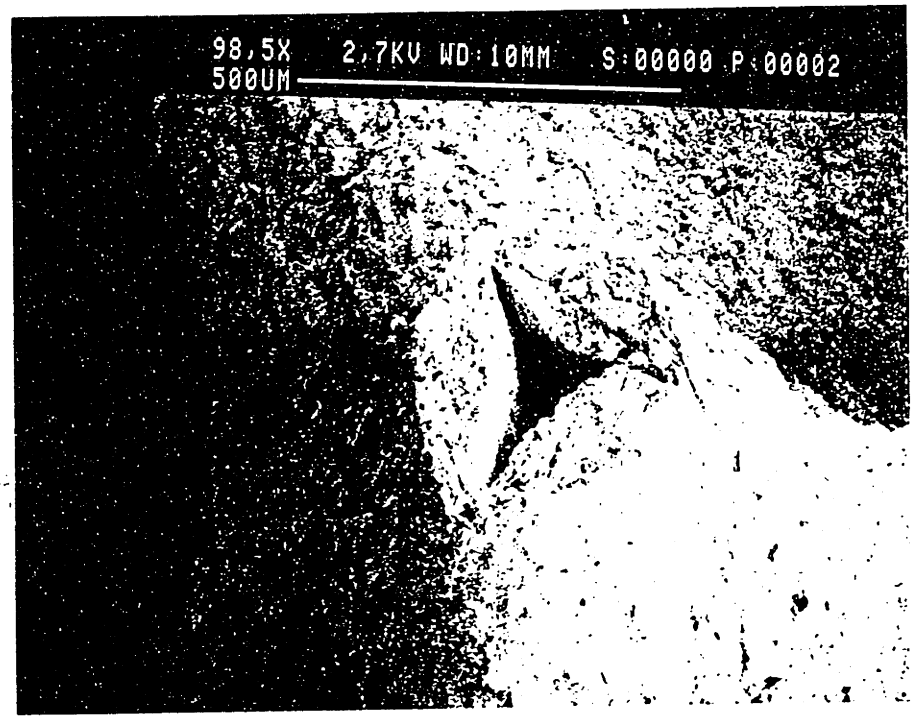

(b)

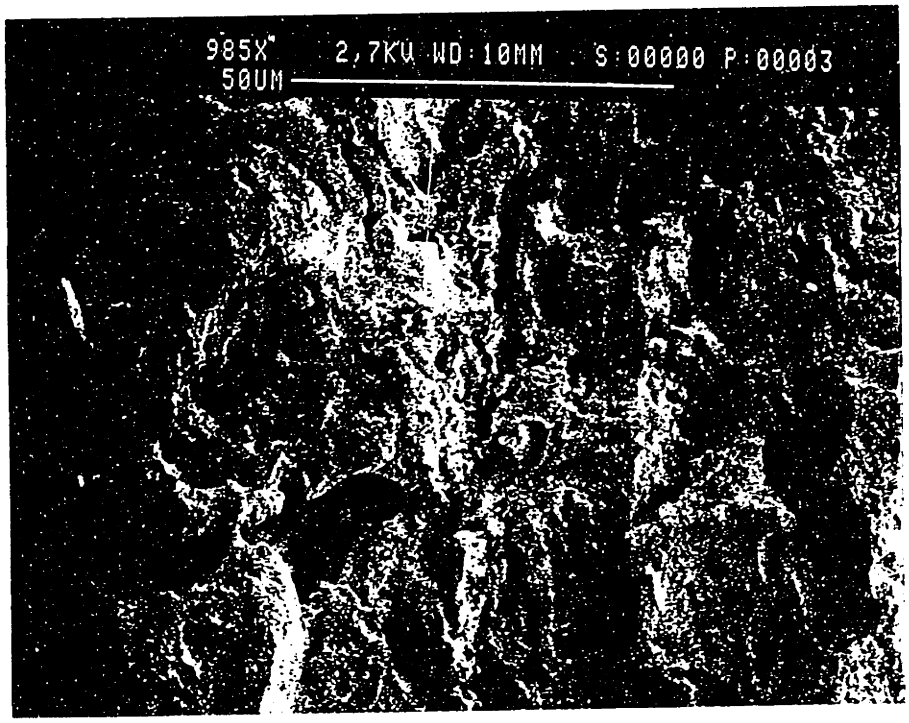

(c)

Fig. 4.27 cont'd.

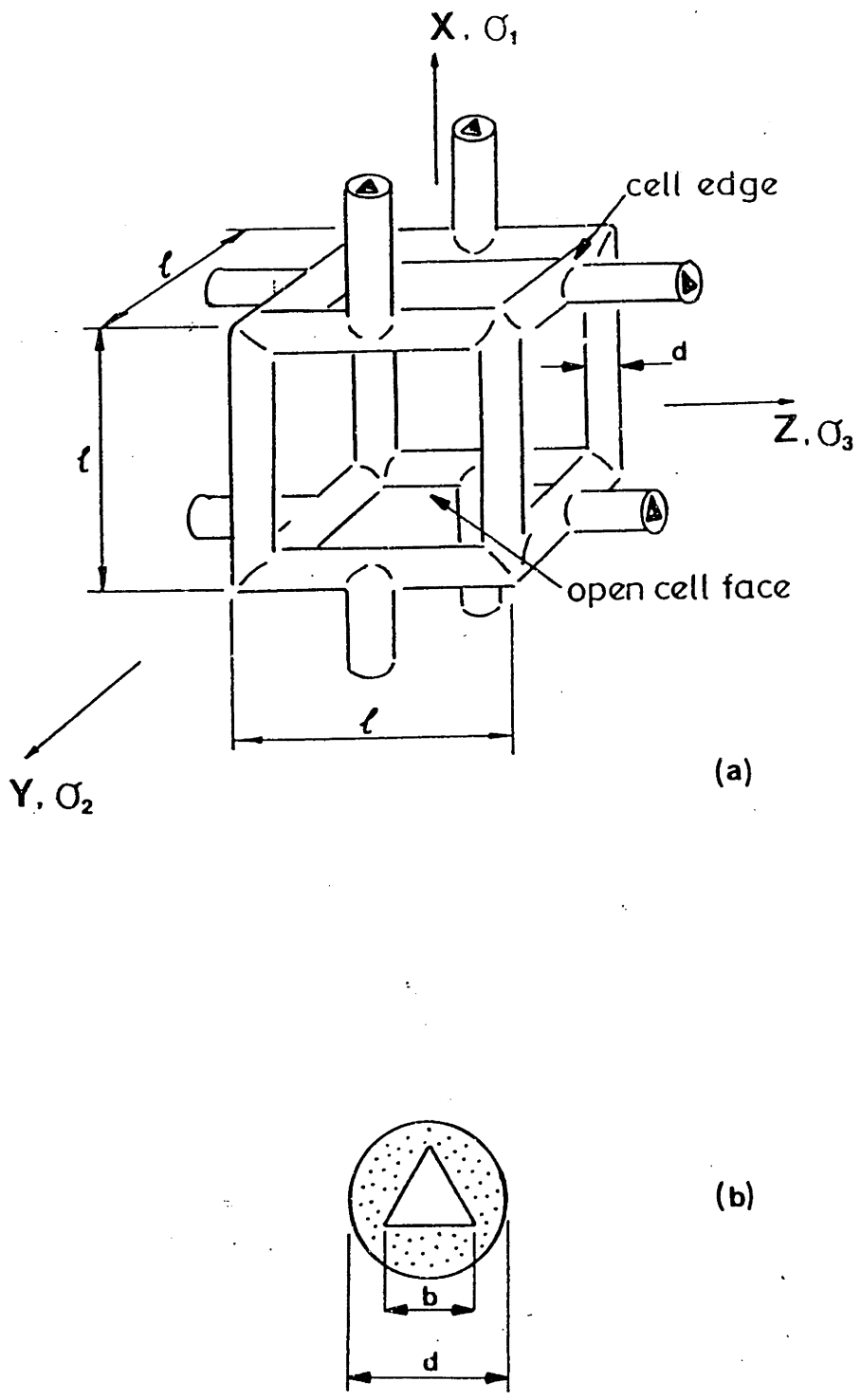

Fig. 4.28 (a) An isotropic unit cell of a cellular ceramic. (b) The idealized cross-section of a cell wall.

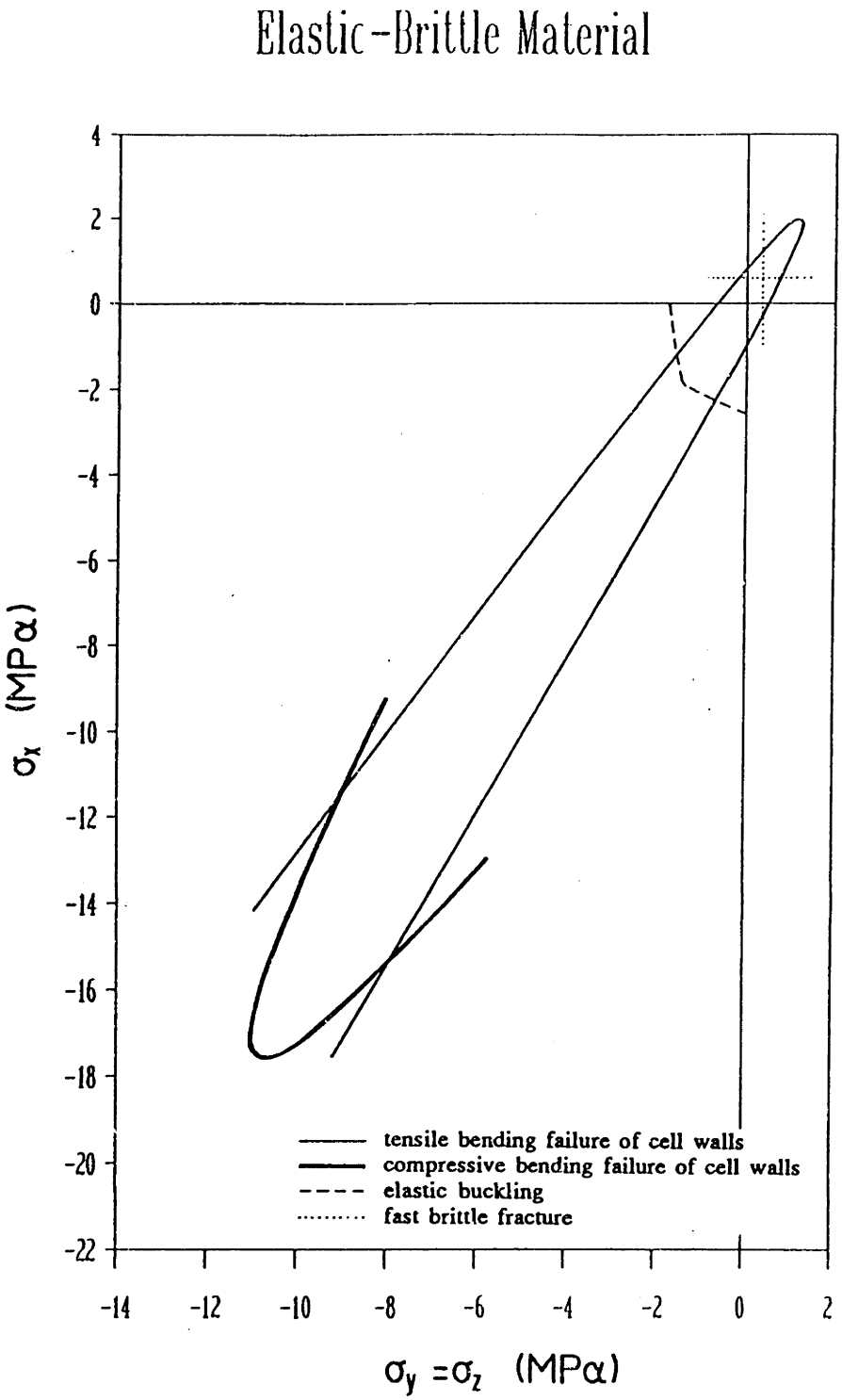

Fig. 4.29 Section through the brittle collapse surface for an orthotropic cellular ceramic with hollow and porous cell walls under axisymmetric loading; the section is truncated by elastic buckling and by fast brittle fracture.

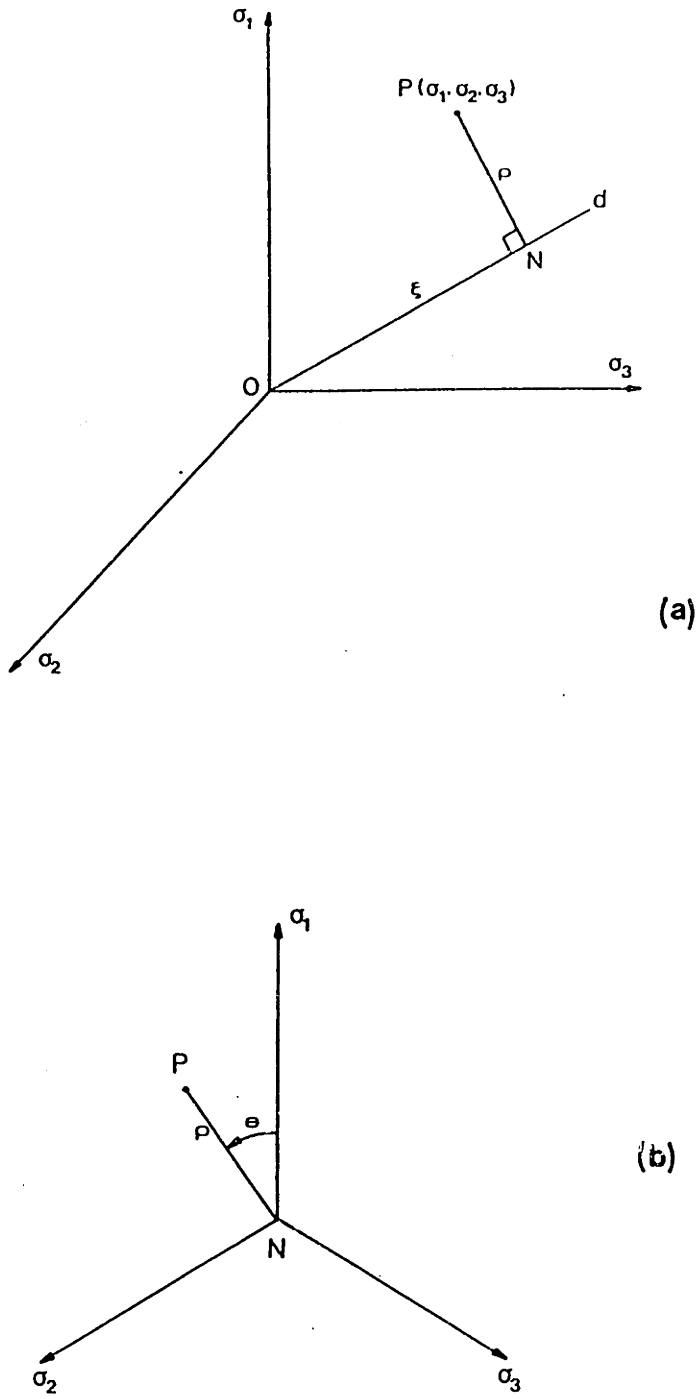

Fig. 4A.1 (a) Decomposition of stress in principal stress space. (b) Projections on the deviatoric plane of the coordinate axes σ_1, σ_2, and σ_3.

CHAPTER V

EXPERIMENTAL PROCEDURE

5.1 Introduction

In this chapter we describe the experimental methodology used in this study to obtain data for the multiaxial behavior of cellular materials. Mechanical tests were carried out on flexible honeycombs and flexible, plastic, and brittle foams. First, the properties of the different materials from which the honeycombs and foams were made are presented. Then, the methodology used for the microstructural characterization is described. Finally, the techniques used in the preparation and mechanical testing of the specimens are described, along with a discussion of possible experimental errors. Information about the number of tests performed, the mean value of the results, and their standard deviation is presented in Chapter 6.

The testing program was focussed on establishing the failure criteria for foams. The *elastic buckling surface* was characterized by tests on flexible polyurethane foams under a range of compressive stress states. The effect of the buckling mode on the failure surface was studied on model silicone rubber honeycombs loaded in uniaxial and biaxial compression. The *plastic yield surface* was characterized primarily by tests on closed-cell rigid polyurethane foams. In the course of the test program a new technique for triaxial testing in tension was developed; because it is limited to open-cell foams, an open-cell aluminum foam was used in place of the closed-cell rigid polyurethane. The *brittle failure surface* was characterized by tests on a reticulated vitreous carbon foam made by carbonizing a polyacrylonitrile foam; the resulting carbon foam had fully dense cell walls.

5.2 Materials

A silicone rubber model of a two-dimensional honeycomb was used for uniaxial and biaxial testing. The model was made using ICI Silcoset 105 silicone rubber; it had the following geometry: t=2.35 mm, l=h=12.35 mm, θ=30°, b=23.61 mm (see Fig. 3.3). The model was made by pouring a mixture of silicone rubber, hardener, and thinner into a mould consisting of machined brass formers (regular hexagons) screwed onto a base at constant spacings to produce the correct wall thickness (Gibson, 1981).

Mechanical tests were carried out on four types of foam: an open-cell flexible polyurethane, a closed-cell rigid polyurethane, an open-cell aluminum, and an-open cell reticulated vitreous carbon (RVC). Some of their properties are listed in Table 5.1; the data were obtained from reference texts and articles. The bulk density of each material was calculated from the measured weight and dimensions of specimens.

5.3 Microstructural Characterization

The cell sizes were measured experimentally using the scanning electron microscope. Details of its use can be found in the book by Goldstein et al., (1981). The materials were prepared by slicing small cubes from the same blocks used in the mechanical tests. Each cube was cut with a new razor blade, mounted, gold-coated, and then viewed and photographed with a scanning electron microscope.

Cell lengths were measured directly from micrographs such as the ones shown in Fig. 5.1. The best resolution in a scanning electron microscope occurs when the specimen is tilted at 45° about a horizontal axis. However, measurements taken from a tilted specimen are only accurate in the horizontal direction. At the low magnifications necessary for our work, resolution was not an important issue, so micrographs were taken at 0° tilt. Accurate measurements of cell dimensions could then be made at all angles in the plane of the surface. Each specimen was not perfectly flat; the angle of inclination of the surface of each specimen was measured using a digital caliper by measuring the two heights and the width of the specimen (Huber, 1987). Typically, these angles ranged between 1° and 4°. The angle was then corrected in the microscope

Table 5.1 Properties of materials tested.

Type of material	Manufacturer	Bulk Densities (kg/m^3)	Cell Wall Properties					
			ρ_s (kg/m^3)	E_s (GPa)	σ_{ys} (MPa)	σ_{fs} (MPa)	σ_{ts} (MPa)	σ_{cs} (MPa)
Flexible polyurethane	Foamfab [a]	28	1200[1]	0.045[2]	-	-	-	-
Rigid polyurethane	Strux Corp.[b]	64, 96, 192	1200[1]	1.6[3]	127[3]	-	-	-
Aluminum foam	ERG [c]	135	2700[4]	70[4]	190[5]	-	-	-
Reticulated vitreous carbon	ERG	48	1650[6]	23.4[6]	-	207[6]	152[6]	690[6]

References

1. Roff and Scott (1971).
2. Lazan (1968).
3. Patel and Finnie (1970).
4. Weast (1985).
5. Lyman (1961).
6. Wang (1981).

a. Foamfab, Mansfield, MA.
b. Strux Corporation, Lindenhurst, L. I., NY.
c. Energy Research and Generation, Inc., Oakland, CA.

stage so that the sample was viewed at 0°.

Six specimens were viewed from each material and each density: two specimens for each of the three material directions, i.e., the rise direction (X) and the two orthogonal directions in the plane normal to it (Y and Z); three pictures were taken from different locations in each specimen.

A formal approach to the characterization of cell geometry uses the concepts developed by Underwood (1970). When viewing one plane of a material, the *mean intercept length* in any direction can be determined from the number of intersections a microstructural feature makes in a given length of a line or a grid of parallel lines (defined as N_l). Then the mean intercept length, $\bar{l}$, is simply given by:

$$\bar{l} = \frac{1}{N_l} \tag{5.1}$$

The three mean intercept lengths $\bar{l}_x$, $\bar{l}_y$, and $\bar{l}_z$ parallel to the material (orthotropic) directions X, Y, and Z, were measured using three parallel lines on each micrograph.

5.4 Testing of 2D Cellular Materials

Uniaxial compression tests were performed by loading the silicone rubber honeycomb model parallel to the Y direction, between two parallel platens of an Instron testing machine at a deformation rate of 5 mm/min, and recording the applied load and crosshead deflection. The geometry of the specimen used is described in Fig. 5.2a.

Biaxial compression tests were performed by using the same apparatus as above and simultaneously preventing the two sides of the honeycomb structure from moving, by putting the specimen into a steel jig specially built for this purpose (Fig. 5.2b); this is equivalent to prescribing the strain of the specimen perpendicular to the loading direction. The distance between the two parallel legs of the jig was fixed at the beginning of each biaxial test, so that the maximum lateral strain of the specimen was known. The three interior faces of the jig were covered by oil in order to minimize any frictional effects at

the interfaces between the specimen and the jig.

The same honeycomb specimen was used for all the uniaxial and biaxial tests because the material was elastomeric and could recover all the deformations upon unloading; it always failed by elastic buckling. The elastic constitutive relations for a linear elastic regular hexagonal honeycomb loaded in-plane are given as follows (Gibson and Ashby, 1988):

$$\varepsilon_x = \frac{1}{2.3E_s(t/l)^3}(\sigma_x - \sigma_y) + \frac{\sqrt{3}}{4E_s(t/l)}(3\sigma_x + \sigma_y) \tag{5.2}$$

$$\varepsilon_y = \frac{1}{2.3E_s(t/l)^3}(\sigma_y - \sigma_x) + \frac{\sqrt{3}}{4E_s(t/l)}(\sigma_x + 3\sigma_y) \tag{5.3}$$

Solving for the stresses, we can write:

$$\frac{\sigma_x}{E_s} = \frac{2(t/l)}{4\sqrt{3} + 6.9(t/l)^2}(\varepsilon_x + \varepsilon_y) + \frac{2.3(t/l)^3}{8 + 4.6\sqrt{3}(t/l)^2}(3\varepsilon_x - \varepsilon_y) \tag{5.4}$$

$$\frac{\sigma_y}{E_s} = \frac{2(t/l)}{4\sqrt{3} + 6.9(t/l)^2}(\varepsilon_x + \varepsilon_y) + \frac{2.3(t/l)^3}{8 + 4.6\sqrt{3}(t/l)^2}(3\varepsilon_y - \varepsilon_x) \tag{5.5}$$

The last two equations, with t/l=0.19 (which is the case with the test specimen) yield:

$$\frac{\sigma_x}{E_s} = 0.0587\,\varepsilon_x + 0.0511\varepsilon_y \tag{5.6}$$

$$\frac{\sigma_y}{E_s} = 0.0511\varepsilon_x + 0.0587\,\varepsilon_y \tag{5.7}$$

Consider now uniaxial loading in the Y direction only. From eqns (5.6) and

(5.7) we obtain

$$\frac{\sigma_y}{E_s} = 0.0142\varepsilon_y \tag{5.8}$$

Defining failure at the initiation of the stress plateau and based on the uniaxial test results one can measure both the stress and strain at failure, $(\sigma^*_{el})_y$ and ε^*_y. Inserting these values in eqn. (5.8) we obtain

$$\frac{(\sigma^*_{el})_y}{E_s} = 0.0142\varepsilon^*_y \tag{5.9}$$

Solving eqn. (5.9) for E_s and substituting into eqns (5.6) and (5.7) we finally have

$$\frac{\sigma_x}{(\sigma^*_{el})_y} = \left(\frac{4.134}{\varepsilon^*_y}\right)\varepsilon_x + \left(\frac{3.599}{\varepsilon^*_y}\right)\varepsilon_y \tag{5.10}$$

$$\frac{\sigma_y}{(\sigma^*_{el})_y} = \left(\frac{3.599}{\varepsilon^*_y}\right)\varepsilon_x + \left(\frac{4.134}{\varepsilon^*_y}\right)\varepsilon_y \tag{5.11}$$

Performing the biaxial tests according to the description presented above, one of ε_x or ε_y is prescribed and the other one is recorded and can, therefore, be measured at failure (elastic buckling) of the specimen. Knowing both ε_x and ε_y at failure, the ratios $\sigma_x/(\sigma^*_{el})_y$ and $\sigma_y/(\sigma^*_{el})_y$ can be evaluated from eqns (5.10) and (5.11) and the experimental failure envelope can thus be defined. The results obtained by following this procedure are presented in the next chapter.

5.5 Testing of 3D Cellular Materials

A summary of the mechanical tests performed on each material is given in Table 5.2. The flexible polyurethane foam, used to characterize the elastic buckling surface,

Table 5.2 Summary of tests on 3D cellular materials.

Material	Density	Uniaxial[1]		Biaxial				Axisymmetric[5]			
	(kg/m^3)	C	T	CC	CT	TC	TT	CC	CT	TC	TT
PU(F)	28	x	-	x^2	-	-	-	x	-	-	-
PU(R)	64	x	x	x^3	x^3	x^3	x^3	x	x	-	-
	96	x	x	x^3	-	-	-	x	x	-	-
	192	x	x	-	-	-	-	x	x	-	-
AL	135	x	x	-	-	-	-	-	-	x	x
RVC	48	x	x	x^4	-	-	-	x	x	x	x

PU(F) : flexible polyurethane (elastomeric)
PU(R) : rigid polyurethane (elastic-plastic)
AL : aluminum (elastic-plastic)
RVC : reticulated vitreous carbon (elastic-brittle)

C: compression
T: tension

1. Uniaxial tests were performed for loading in the X, Y, and Z material directions.
2. The flexible polyurethane was tested in compression in the Y-Z plane.
3. The rigid polyurethane was tested in the X-Y and Y-Z planes.
4. The reticulated vitreous carbon was tested in the X-Y plane.
5. The first letter indicates compression or tension in the radial direction (Y-Z plane), the second, in the axial direction (X direction).

was tested in uniaxial, biaxial, and triaxial compression. Three densities of rigid polyurethane foam were used to characterize the plastic yield surface under a range of stress states: uniaxial compression and tension, biaxial compression and tension, and triaxial tests with radial compression. Biaxial tests in tension on the two highest densities were unsuccessful due to the failure of the adhesive between the specimen and the loading platen before yielding. Triaxial tests with radial tension could only be carried out on an open-cell material; for this reason the closed-cell polyurethane foam was replaced with an open-cell aluminum foam for this portion of the test program. Finally, a reticulated vitreous carbon foam with fully dense cell walls was used to characterize the brittle failure envelope; it was tested in uniaxial compression and tension, in biaxial compression, and triaxial stress with all combinations of compression and tension. In each case, the applied loads were aligned with one of the axes of symmetry of the material (orthotropic). The test methods are described below.

(a) Uniaxial Compression

Uniaxial compression tests were performed by loading cubic specimens between two parallel platens of an Instron testing machine with a 5 KN maximum loading capacity (Fig. 5.3a) at a deformation rate 5mm/min and at room temperature, recording the applied load and crosshead deflection. The cubes had an edge length as follows: the flexible polyurethane: 50.8 mm; the 64 kg/m^3, 96 kg/m^3, and 192 kg/m^3 density rigid polyurethanes: 40.1 mm, 38.9 mm, and 31.5 mm, respectively; the aluminum foam: 26.3 mm; and the reticulated vitreous carbon: 45.9 mm.

(b) Uniaxial Tension

Uniaxial tension tests were performed on dogbone rigid polyurethane specimens, on cylindrical aluminum foam specimens, and on *notched* cylindrical reticulated vitreous carbon specimens. All tests were performed using the Instron machine and under the conditions described above. The dogbone specimens (Fig. 5.3b) were 11 mm thick and 9-16 mm wide, with a gauge length of 30-40 mm; due to difficulties in shaping the

aluminum foam in the dogbone configuration, this material was tested in direct uniaxial tension using cylindrical specimens bonded with five-minute epoxy between two paralliel platens of the Instron machine and pulled apart. The aluminum foam cylinders had a diameter of 16 mm and a height of 40 mm.

Finally, notched cylindrical specimens of reticulated vitreous carbon were tested uniaxially in the X direction (rise direction) to estimate the mode I fracture toughness of the material; the specimen dimensions are shown in Fig. 5.4. The mode I stress intensity factor for this configuration is given as (Koiter and Benthem, 1973)

$$K_I = \sigma\sqrt{\pi a}\left(\frac{D}{d} + \frac{1}{2} + \frac{3}{8}\frac{d}{D} - 0.36\frac{d^2}{D^2} + 0.73\frac{d^3}{D^3}\right)\frac{1}{2}\sqrt{\frac{D}{d}} \qquad (5.12)$$

This configuration was chosen because it could be conveniently used in the triaxial (axisymmetric) tests, described later.

(c) Biaxial Loading

Biaxial tests were performed on cubic specimens using the loading jig shown in Fig. 5.5. Finger joints at the ends of the plates allowed them to mesh together during compressive loading, accomodating 15% strain before the plates interfered. One pair of plates screwed into the base and crosshead of the Instron machine while a second pair, normal to the first, was attached to a hydraulic jack through a small loading frame. Compressive loads were applied by moving the platens against the specimen; tensile loads by gluing the faces of the specimen to the platens (using five-minute epoxy) and pulling them apart. The foam rubber base shown in the figure allowed the load frame to move down with the specimen as the crosshead descended. Loads were applied in two ways: by starting with a lateral stress caused by the hydraulic jack and increasing the vertical stress produced by the Instron until failure occurred, or, by incrementally increasing the stress caused by the hydraulic jack and Instron in alternate steps until failure occurred (the stress caused by the Instron was increased indirectly, by controlling

the displacement of the crosshead). The load-deflection curve of the Instron was recorded on an X-Y plotter; a pressure gauge in the hydraulic line of the jack gave the load it applied to the specimen at failure. All tests were performed at a deformation rate 5 mm/min and at room temperature. The cubic specimens had an edge length of 45.7 mm except for the reticulated vitreous carbon ones which had an edge length of 45.9 mm.

(d) Triaxial (Axisymmetric) Loading

Standard soil mechanics triaxial cells (Wykeham Farrance Model T57, 2MPa radial pressure, 8.9 KN axial load capacity) were used for the triaxial tests (σ_x, σ_y=σ_z). Detailed descriptions of the test apparatus can be found in the book by Bishop and Henkel (1962). The axial load was applied through a screw-driven crosshead within the cell. The radial stress was applied by water pressurized by compressed air by means of a piston. Stepwise increments of radial pressure and axial load were applied until the specimen failed, while recording the axial load and deformation and the radial stress every 8 seconds. The load, axial deformation, and radial stress were measured by a load cell, a LVDT, and a pressure transducer, respectively. The signals from all three devices were sent to a computerized data acquisition system. With the calibration factors as the input quantities, a computer program was then used to transform the values (in volts) recorded by the data acquisition system to the desired quantities: Newtons (N) for the axial load, millimeters (mm) for the axial deformation, and MegaPascals (MPa) for the radial stress. All tests were performed at a deformation rate of 0.76 mm/min and at room temperature; the specimens were cylindrical with the strong material axis parallel to the cylinder axis.

Radial Compression-Axial Compression

Cylindrical specimens were encased in a flexible rubber membrane and placed in the triaxial cell, as shown in Fig. 5.6. "O" rings were used to seal the specimen at both ends. The compressive radial stress was applied by introducing pressurized water into the cell. The diameters of the flexible polyurethane, rigid polyurethane, and reticulated

vitreous carbon specimens were 33 mm, 35.6 mm, and 36 mm respectively; the corresponding heights of the cylinders were 50.8 mm, 71.1 mm, and 71.1 mm. The weight of the crosshead as well as the axial stresses induced in the specimen by the confining pressure, were taken into account in the calculation of the stresses at failure.

Radial Compression-Axial Tension

Standard soil mechanics triaxial cells are designed to apply compressive loads only. Tensile axial loads were produced by bonding the specimen to a cage specially built to convert the downward motion of the crosshead into a tensile axial load on the specimen. This concept is illustrated in Fig. 5.7. Photographs of the cage are shown in Fig. 5.8. The specimens were attached to the cage by bonding them on two platens using five-minute epoxy adhesive; the platens were then screwed on two of the horizontal disks of the cage. A flexible rubber membrane and "O" rings were used to seal the specimen from the pressurizing water. The weights of the crosshead and the cage, as well as the axial stresses induced in the specimen by the pressurizing water, were taken into account in the calculation of the stresses developed in the materials at failure. Fig. 5.9a shows the apparatus used for triaxial (axisymmetric) loading with radial compression-axial compression; the modified for axial tension apparatus is shown in Fig. 5.9b.

The rigid polyurethane specimens had a diameter of 24 mm. The height of the 64 kg/m^3, 96 kg/m^3, and 192 kg/m^3 density rigid polyurethane specimens was 42 mm, 43.3 mm, and 43.5 mm, respectively. The diameter and height of the reticulated vitreous carbon specimens were 24.2 mm and 45.6 mm correspondingly; some of the specimens of this material contained a crack along their periphery at the middle of the height, with a depth of 4 mm (see geometry in Fig. 5.4).

Radial Tension-Axial Compression

Tensile radial stresses were produced by sealing the surface of open-cell foams with silicone rubber and applying internal pressure. To do this, a flexible rubber membrane was first placed around the cylindrical specimen. Liquid silicone rubber (plus

hardener and thinner) was introduced into the specimen and forced to the outer surface by rotating it (Fig. 5.10a); when it hardened (after about ten hours) it gave a thick layer of silicone rubber embedded in the outer wall of the specimen which could withstand internal pressurization of the material. The thickness of this layer was controlled by measuring the volume of the silicone rubber used for each specimen. Several specimens were cut to check the uniformity in thickness of the silicone rubber layer. The photograph in Fig. 5.10b shows part of the cross-section of an aluminum foam with the silicone rubber layer; it also illustrates the uniformity in thickness achieved with this technique. The concept of the method described herein is better explained in Fig. 5.11. Note that it is applicable only if the material is characterized by a continuous porosity (Germaine, 1988). A schematic representation of the triaxial apparatus for radial tension-axial compression is given in Fig. 5.12. A photograph of a specimen pressurized internally and compressed axially is shown in Fig. 5.13.

The effect of the rubber layer on the stresses developed in the specimen was modeled and studied using finite element computations; it is described in detail later in this chapter. It was found that minor corrections to the radial and axial stresses should be applied. Two other factors were also taken into account in the calculation of the stresses developed in the specimens at failure: the weight of the crosshead, and the axial stresses produced from the action of the internal water pressure on the crosshead.

The diameter and height of the specimens were 35.6 mm and 71.1 mm respectively; the thickness of the composite foam+rubber wall was 5.1 mm in the aluminum specimens, and 5.7 mm in the reticulated vitreous carbon.

Radial Tension-Axial Tension

Tests with radial and axial tension were performed combining the two modifications to the standard triaxial testing procedure described above (Figs 5.14, 5.15): the cage for axial tension, and the use of specimens with rubber silicone impregnated external walls for radial tension. The stresses developed in the specimens were calculated taking into account the weight of the cage, the axial stresses induced from the action of

the internal water pressure on the cage, and the minor corrections resulting from the rubber layer (computed using the finite element method and described in the next section).

The aluminum foam specimens had a diameter of 35.6 mm and a height of 50.8 mm. The thickness of the rubber silicone impregnated wall was 5.1 mm. The diameter and height of the reticulated vitreous carbon specimens were 35.6 mm and 50.7 mm respectively, while the impregnated wall was 5.7 mm thick; these specimens also contained a crack along their periphery in the middle of their height, as illustrated in Fig. 5.16. Note that the geometry of all the notched specimens used in this work is such that they have the same stress intensity factor for mode I loading, K_I (a=4 mm, d/D=0.67 in eqn. (5.12)); this allows direct comparisons of the axial stresses at failure (for brittle materials) for various degrees of lateral loading (compressive or tensile).

Finite Element Analysis of Specimens used in the Axisymmetric Tests with Radial Tension

The stress distribution in the silicone rubber impregnated cylindrical specimens was obtained numerically using the finite element method. Our aim was to evaluate the stress field in the specimens produced by the internal water pressure (see Fig. 5.11). The structure that was analyzed is shown in Fig. 5.17 along with the global system of coordinates. The analyses were performed with ADINA (ADINA R&D, Inc., 1984) using 4-node axisymmetric elements (see for instance Bathe, 1982) and were all linear elastic. Four types of specimens were analyzed; their geometrical characteristics are given in Table 5.3.

All analyses revealed that the central part of the specimens (the one surrounded by the silicone rubber impregnated wall and far from the two flat sides) was the most highly stressed one, and thus the one to fail first.

The finite element mesh of type A is illustrated in Fig. 5.18. The analysis showed that the internal water pressure, p_i, produced a radial stress, σ_R, in the central part of the specimen, which was approximately constant and equal to $0.87p_i$ along about

Table 5.3 Geometry of specimens used in finite element analysis.

Material	Test type	External diameter, d_e (mm)	Impregnated wall thickness, r (mm)	Height h (mm)	Mesh type
Aluminum foam	Radial tension-axial compression	35.6	5.1	71.1	A
	Radial tension-axial tension	35.6	5.1	50.8	B
Reticulated vitreous carbon	Radial tension-axial compression	35.6	5.7	71.1	C
	Radial tension-axial tension	35.6	5.7	50.7	D

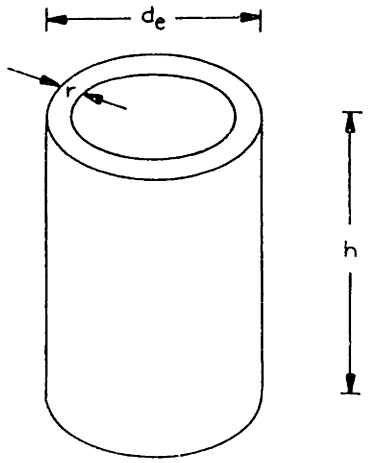

80% of its height; this is illustrated in Figs 5.19a and 5.19b. Furthermore, a tensile axial stress, σ_A, was also produced, which was constant at nearly 50% of the specimen's height, and equal to $0.19p_i$; this stress dropped to zero towards the two ends of the specimen (Figs 5.19c and 5.19d). Similar arguments hold for the analyses of the meshes of types B, C, and D, as discussed below.

Figure 5.20 illustrates the finite element idealization of type B. The internal pressure, p_i, resulted in radial stresses $0.87p_i$ along about 60% of the height of the specimen (Figs 5.21a and 5.21b), and in tensile axial stresses $0.18p_i$ at nearly 40% of the specimen's height (Figs 5.21c and 5.21d).

The mesh of type C is shown in Fig. 5.22. In this case, the internal water pressure produced a radial stress $0.85p_i$ along about 80% of the specimen's height (Figs 5.23a and 5.23b) and a tensile axial stress $0.21p_i$ at nearly 50% of the height of the specimen (Figs 5.23c and 5.23d).

Finally, the analysis of the type D mesh (Fig. 5.24) resulted the following: a radial stress $0.86p_i$ at approximately 60% of the specimen's height (Figs 5.25a and 5.25b), and a tensile axial stress $0.20p_i$ at nearly 40% of the height (Figs 5.25c and 5.25d).

The state of stress in the most highly stressed region of the specimens used in the tests involving radial tension is summarized in Fig. 5.26. The values given in this figure were used in the estimation of the stresses developed in the specimens when failure was first observed, i.e. at the initiation of the deviation from linearity in the axial load-deformation curves.

5.6 Possible Experimental Errors

One source of possible experimental errors is the effect of displacement constraints at the loading surfaces. These constraints restrict the admissible modes of deformation; hence, they may alter the failure stress and initiate failure near the loading surfaces. It is rather difficult to assess the contribution of this effect on the results. It is hoped that it was minimized in the tests on honeycombs, through the use of oil at the interface between the specimen and the platens.

One might also consider the effect of the hydrostatic pressures applied on the cell walls of the foam specimens under radial tension (see Fig. 5.11) another possible source of experimental error. However, these pressures were less than 1% of the strength of the cell wall material (yield stress in aluminum foam, tensile or rupture strength in reticulated vitreous carbon) in all cases, and it is believed that their contribution to the failure of the cell walls is negligible.

The errors associated with the accuracy of the instruments used in the mechanical tests are considered insignificant; they are all of the order of 0.5%, and their cumulative effect (approximately 1%) on the results was not of important concern.

5.7 Summary

The behavior of cellular solids under multiaxial loads was modeled in previous chapters. Here, we presented the experimental procedure for characterizing the microstructure of the materials used in this research; moreover, the experimental techniques employed for testing 2D elastomeric and 3D elastomeric, elastic-plastic, and elastic-brittle cellular materials were discussed, along with possible experimental errors. During the tests the specimens were subjected to uniaxial, biaxial, and triaxial (axisymmetric) stress states. The results are presented in the next chapter.

References

ADINA R&D, Inc. (1984) ADINA-IN Users Manual, Report ARD 84-6.

Bathe, K.-J. (1982) *Finite Element Procedures in Engineering Analysis,* Prentice-Hall, Inc., New Jersey.

Bishop, A. W. and Henkel, D. J. (1962) The Measurement of Soil Properties in the Triaxial Test, 2nd edn., Edward Arnold Ltd., London.

Germaine, J. (1988) Personal Communication.

Gibson, L. J. (1981) The Elastic and Plastic Behaviour of Cellular Materials, Ph.D. Thesis, Cambridge University Engineering Department, Cambridge, U.K.

Gibson, L. J. and Ashby, M. F. (1988) *Cellular Solids: Structure and Properties*, Pergamon, Oxford.

Goldstein, J. I., Newbury, D. E., Echlin, P., Joy, D. C., Fiori, C. and Lifshin, E. (1981) *Scanning Electron Microscopy and X-Ray Microanalysis*, Plenum Press, New York.

Huber, A. T. (1987) Anisotropy in Cellular Materials, S.M. Thesis, Civil Engineering Department, Massachusetts Institute of Technology, Cambridge.

Koiter, W. T. and Benthem, J. P. (1973) in *Mechanics of Fracture*, G. C. Sih (ed.), Noordhoft, Leyden, **1**, 131.

Lazan, B. J. (1968) *Damping of Materials and Members in Structural Mechanics*, Pergamon, Oxford.

Lyman, T. (ed.) (1961) *Properties and Selection of Metals, Metals Handbook, 1*, 8th edn., American Society of Metals.

Patel, M. R. and Finnie, I. (1970) Structural Features and Mechanical Properties of Rigid Cellular Plastics, *J. Materials,* **5**, 909.

Roff, W. F. and Scott, J. R. (1971) *Fibres, Films, Plastics and Rubbers-A Handbook of Common Polymers*, Butterworths, London.

Underwood, E. E. (1970) *Quantitative Stereology*, Addison-Wesley Publishing Co., Massachusetts.

Wang, J. (1981) Reticulated Vitreous Carbon-A New Versatile Electrode Material, *Electrochimica Acta*, **26**(12), 1721.

Weast, R. C. (1985) *Handbook of Chemistry and Physics*, Chemical Rubber Co., Boca Raton, Florida, U.S.A.

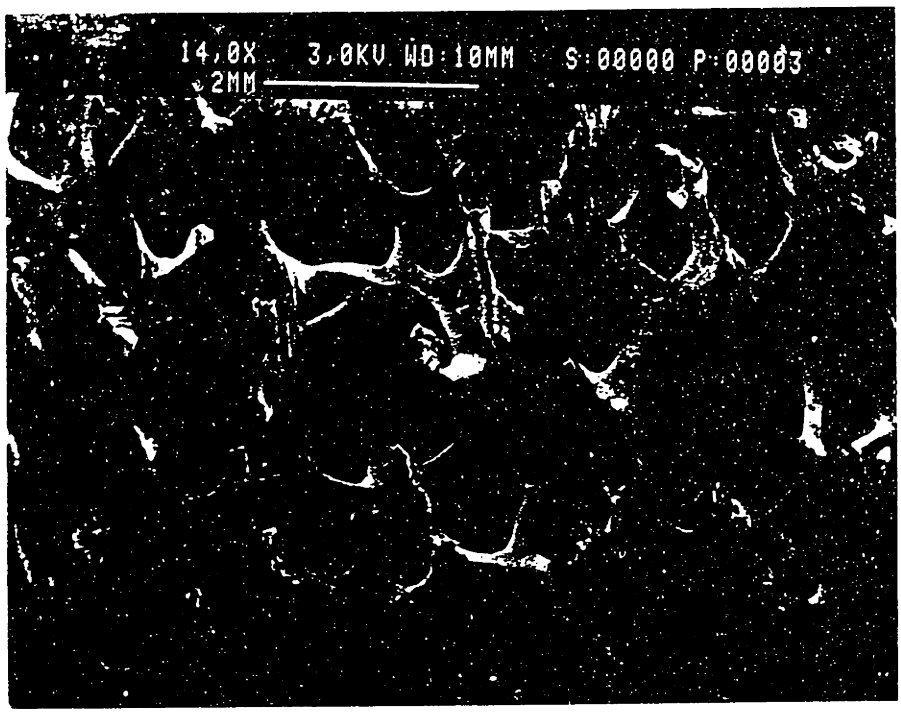

(a)

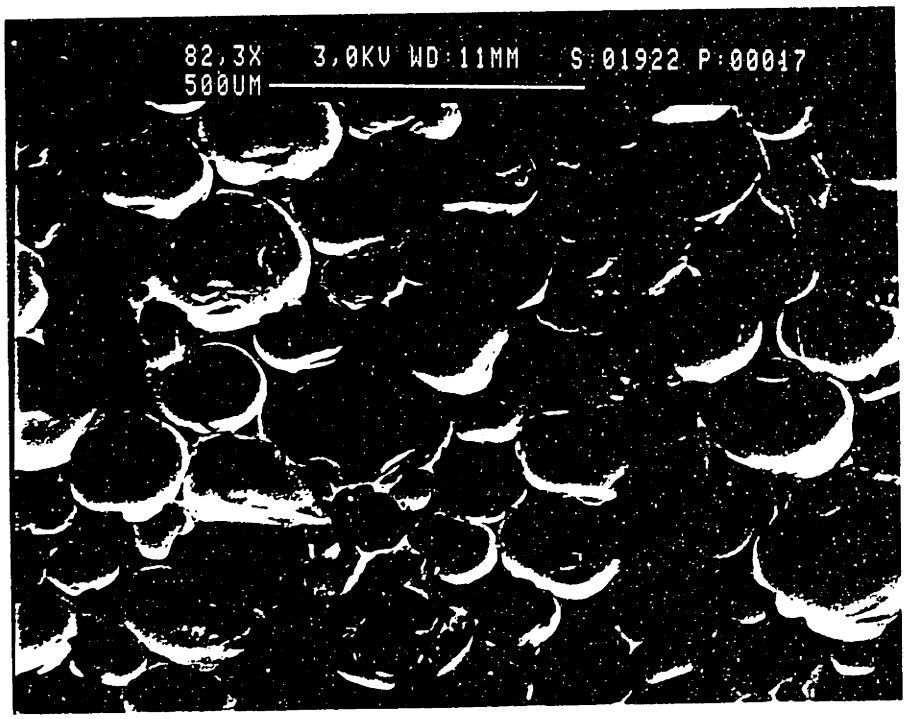

(b)

Fig. 5.1 Micrographs showing the cellular structure of (a) an open-cell aluminum foam and (b) a closed-cell rigid polyurethane foam.

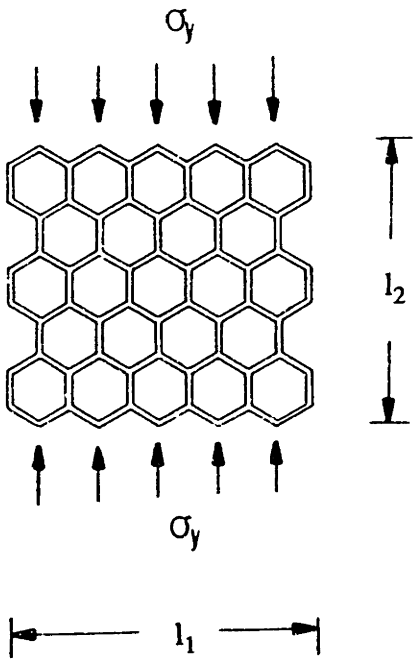

l_1=108.2 mm

l_2=99.5 mm

l=h=12.35 mm

θ=30°

t=2.35 mm

b=23.61 mm

(a)

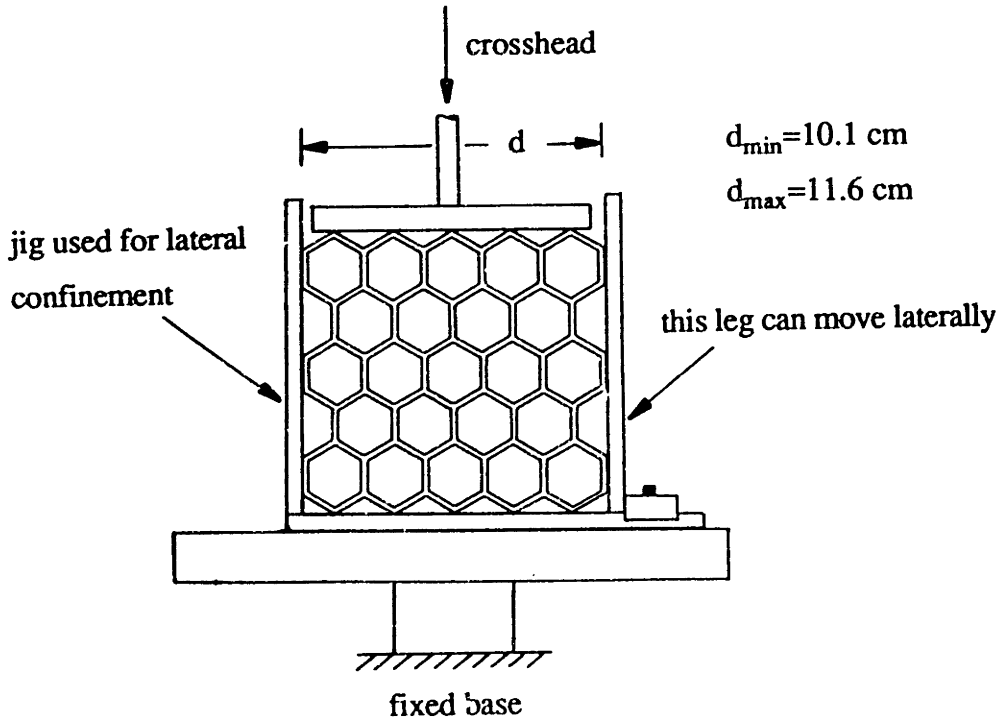

d_{min}=10.1 cm

d_{max}=11.6 cm

(b)

Fig. 5.2 (a) Uniaxial testing of honeycombs and specimen geometry. (b) The apparatus used for biaxial testing of honeycombs.

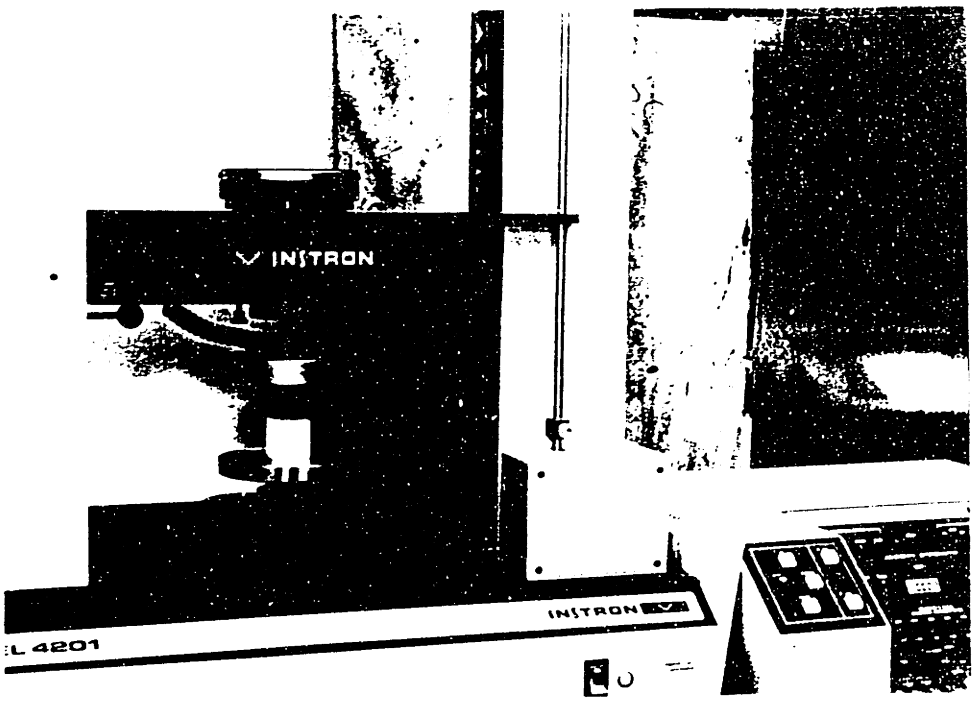

(a)

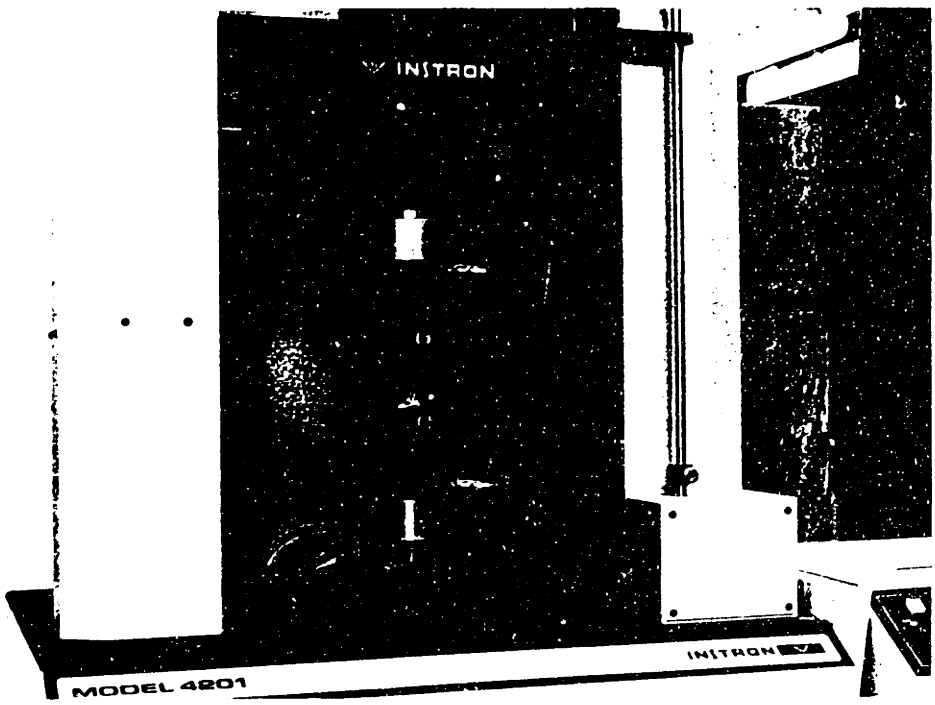

(b)

Fig. 5.3 Uniaxial testing: (a) compression of cubic specimens; (b) tension of dogbone specimens.

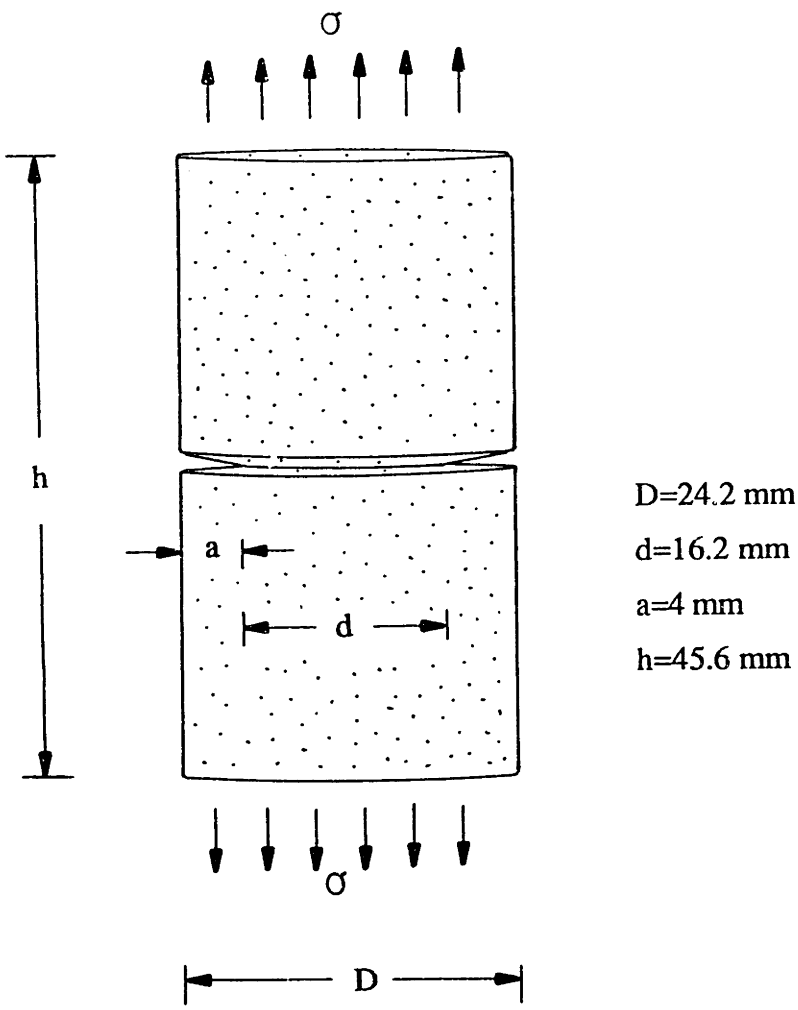

Fig. 5.4 Geometrical characteristics of the notched cylindrical specimens used in uniaxial tension.

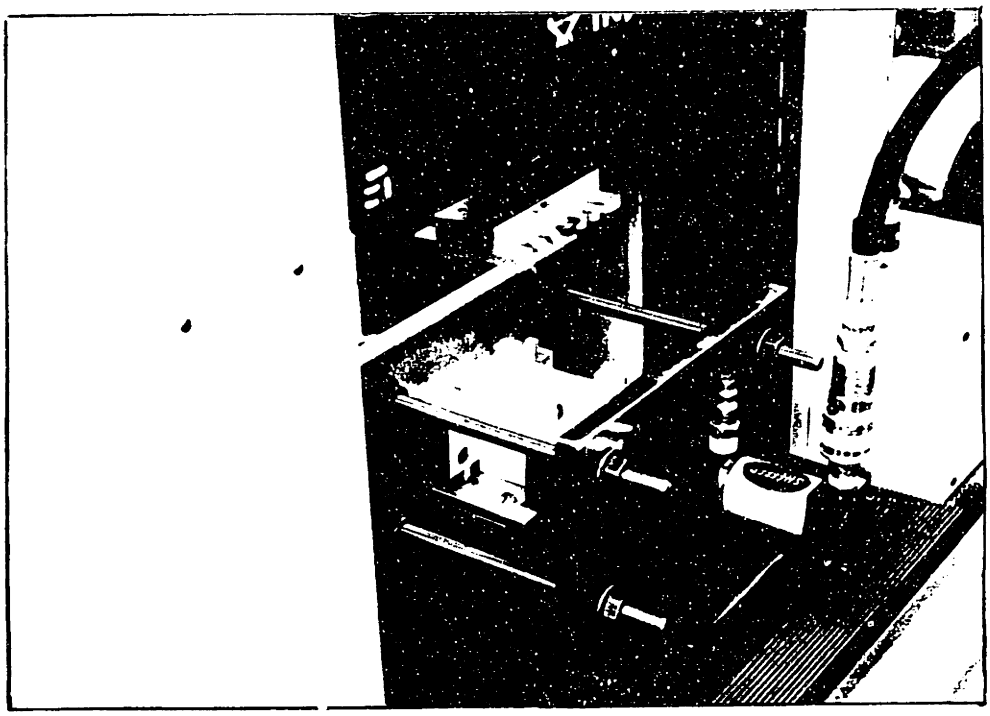

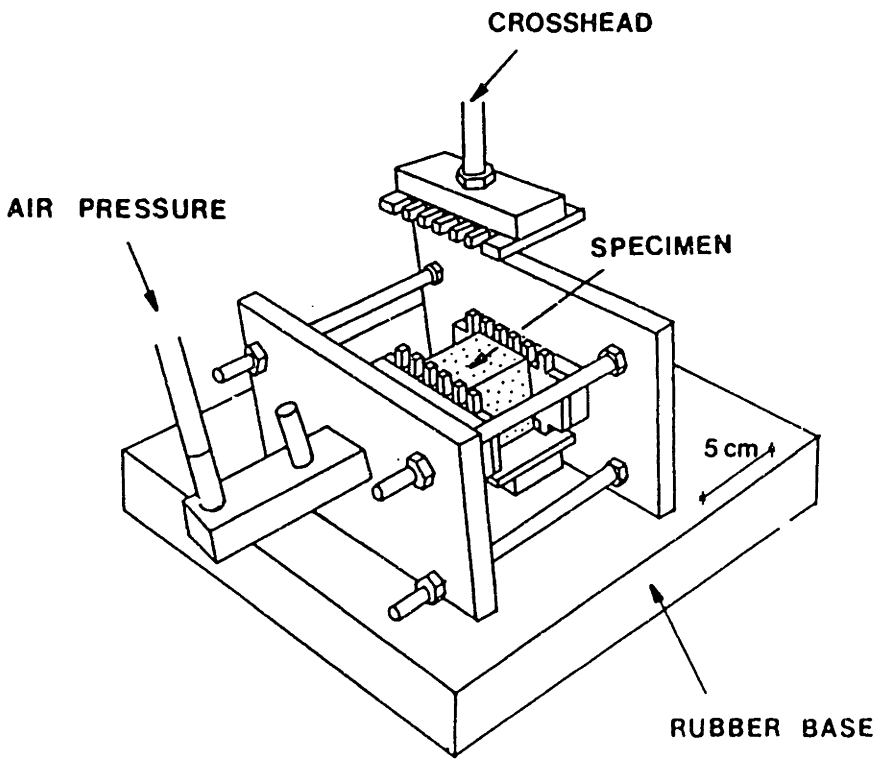

Fig. 5.5 The biaxial loading jig.

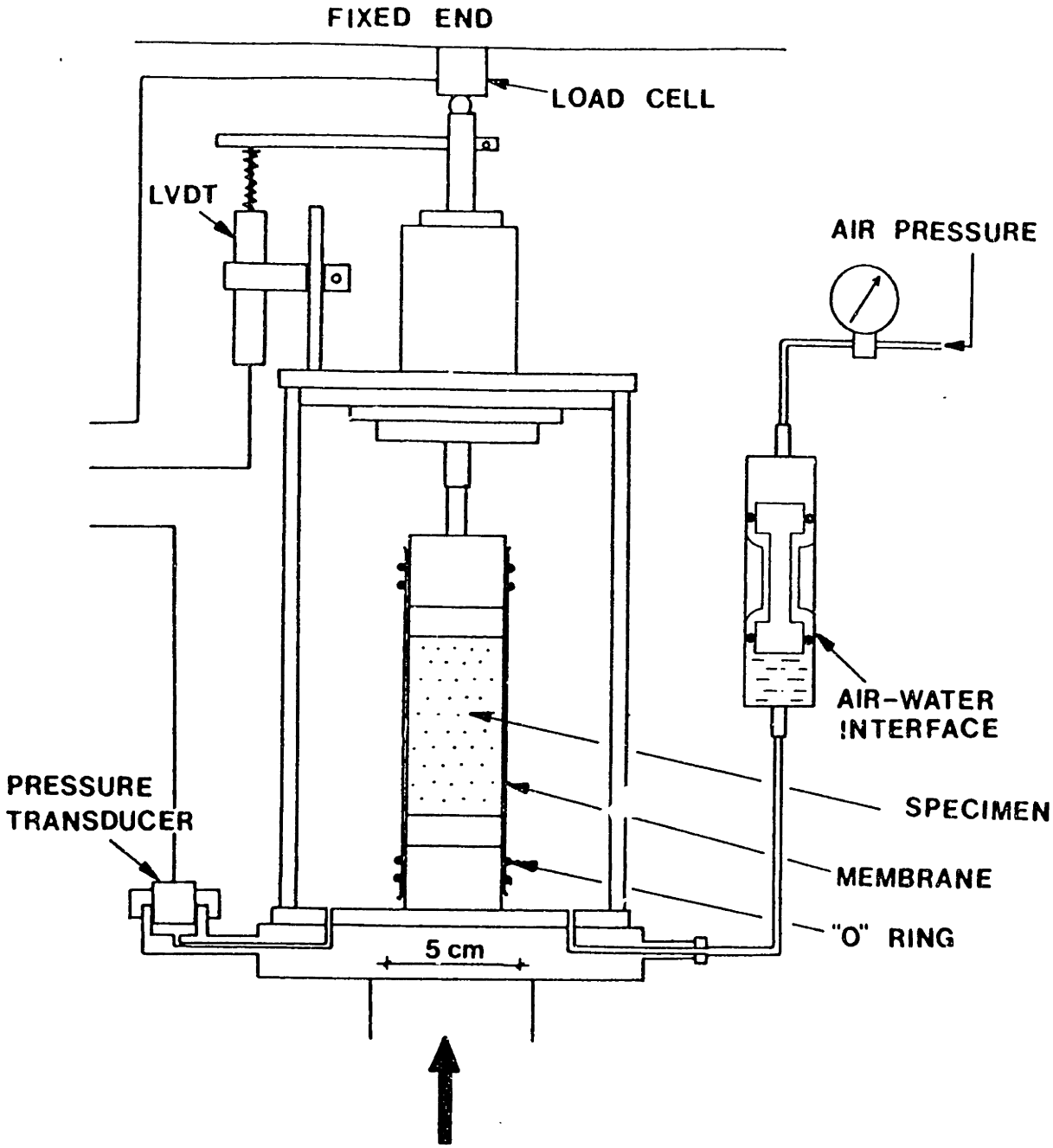

Fig. 5.6 The triaxial cell used for applying simultaneous compressive radial and axial stresses.

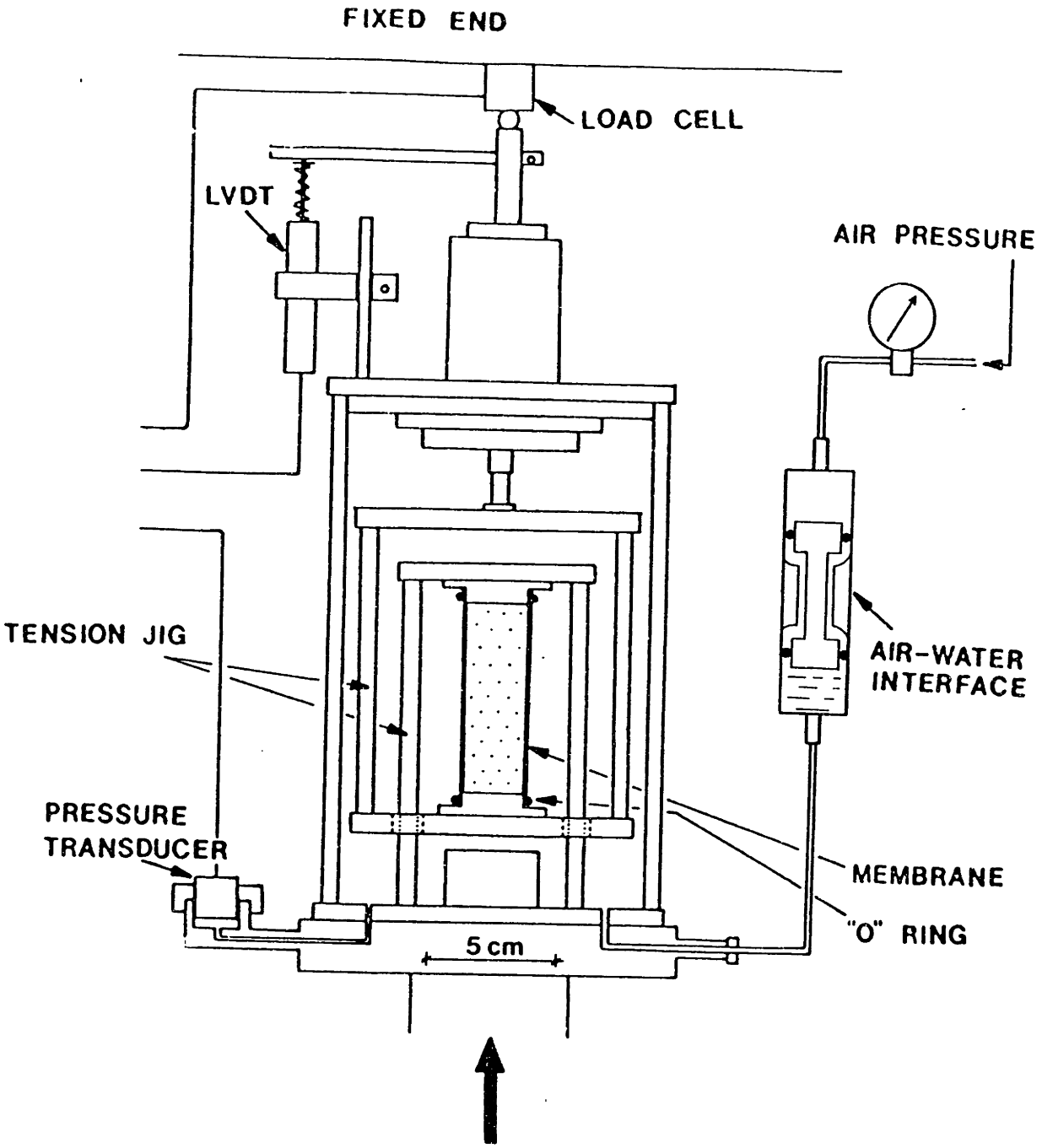

Fig. 5.7 The modified triaxial cell used for applying simultaneous compressive radial and tensile axial stresses.

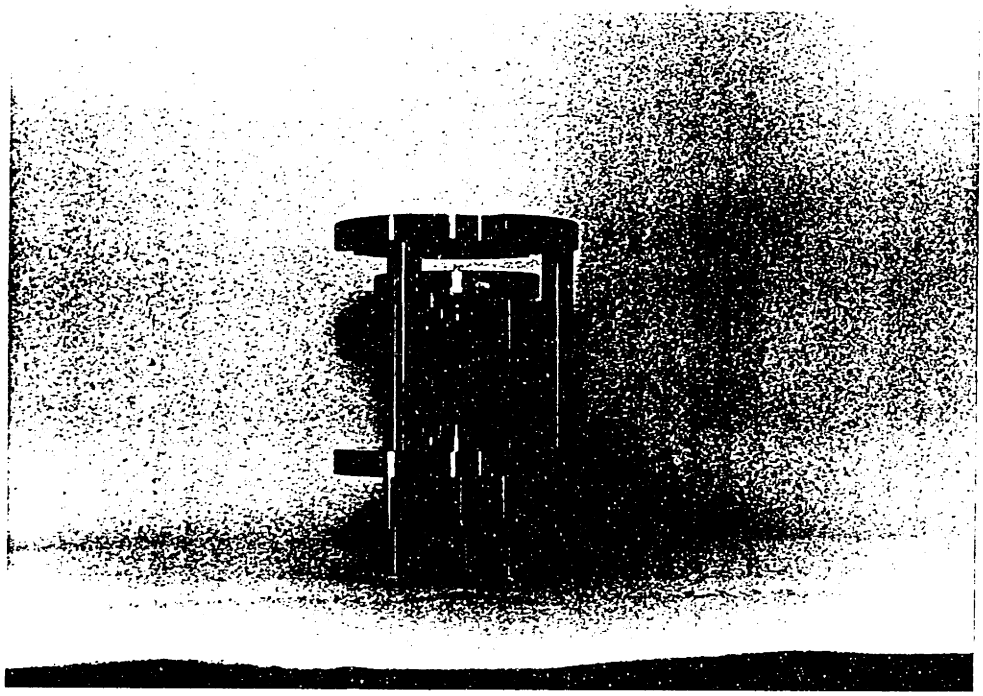

(a)

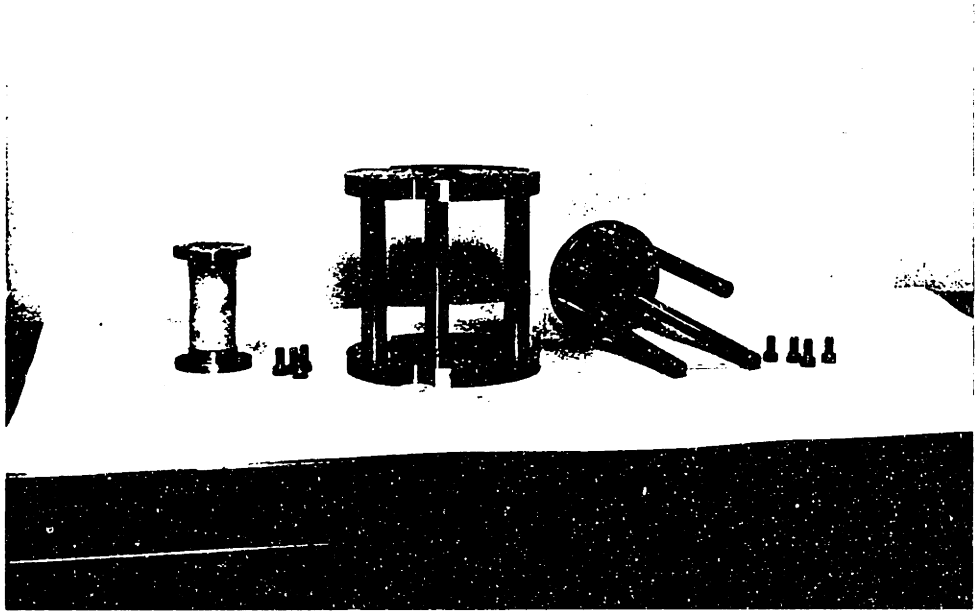

(b)

Fig. 5.8 (a) and (b) The axial tension cage for the triaxial cell.

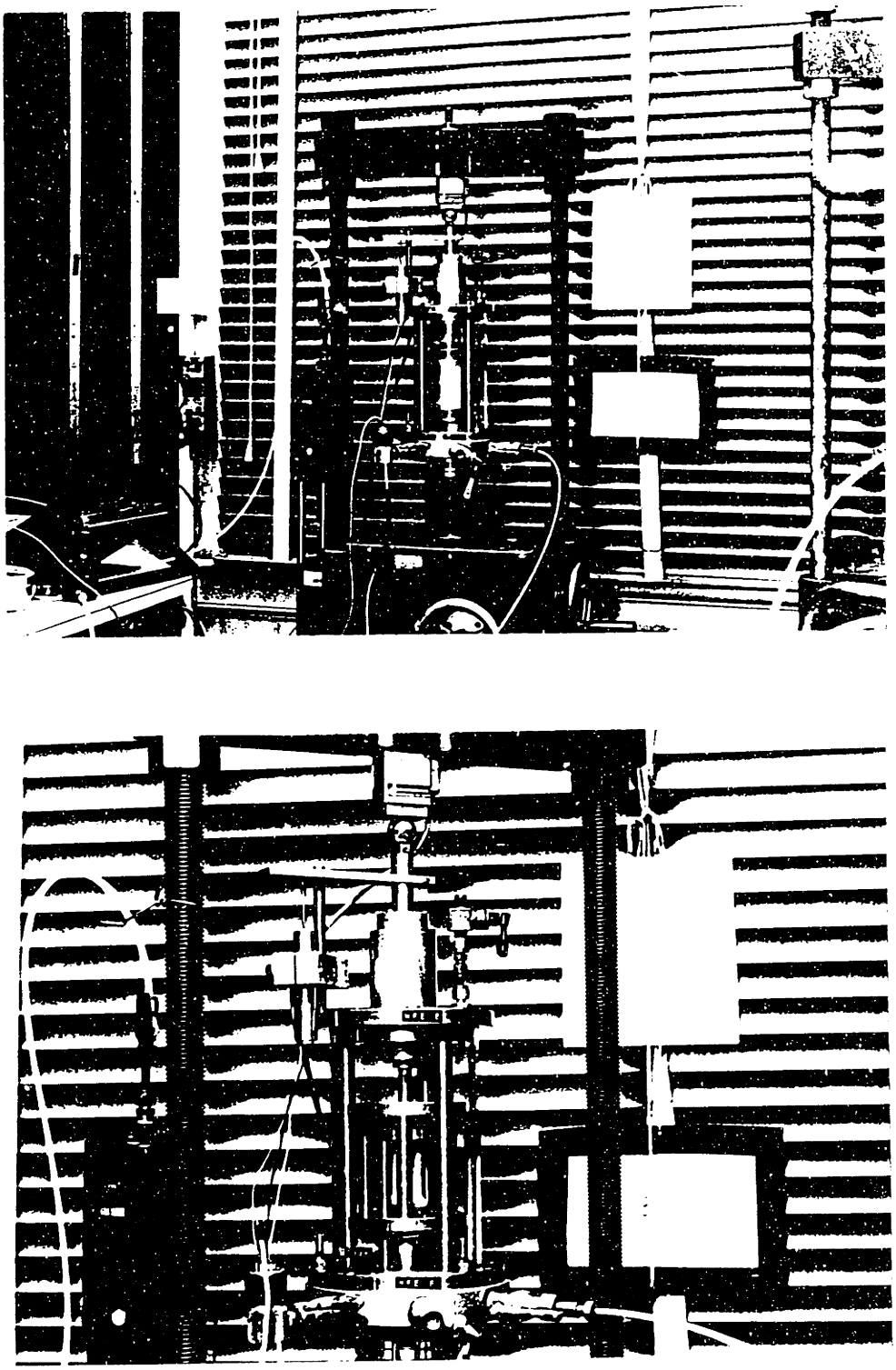

Fig. 5.9 Photographs of the apparatus used for triaxial testing with: (a) radial and axial compression; (b) radial compression and axial tension.

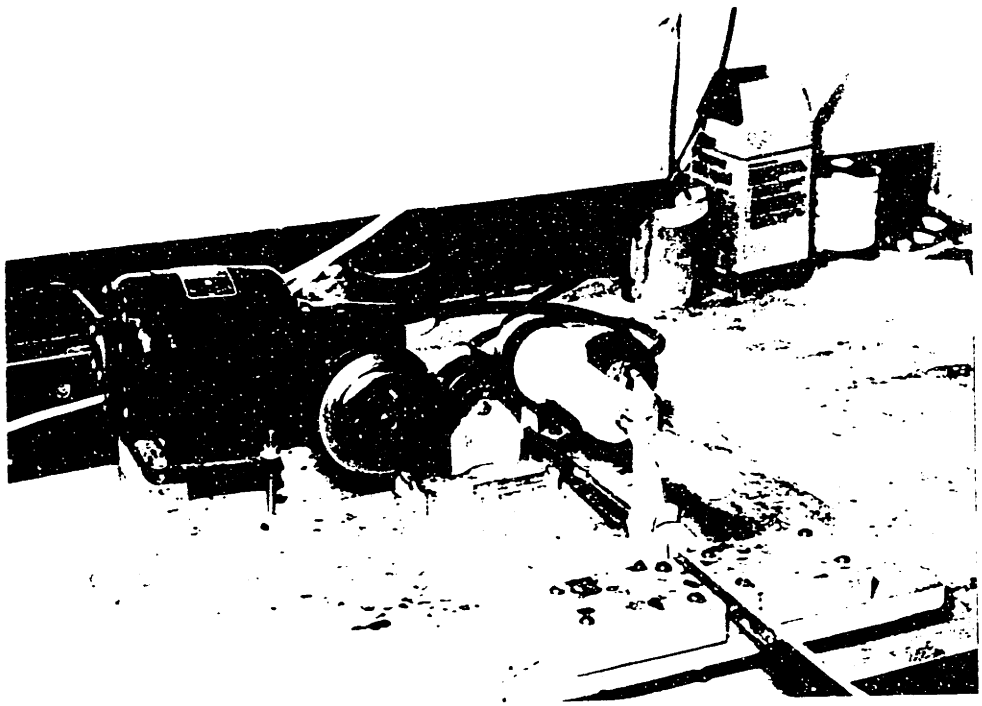

(a)

(b)

Fig. 5.10 (a) The rotating jig used to force the liquid silicone rubber to the outer surface of open-cell materials. (b) Part of the cross-section of an-open-cell material with the silicone rubber layer.

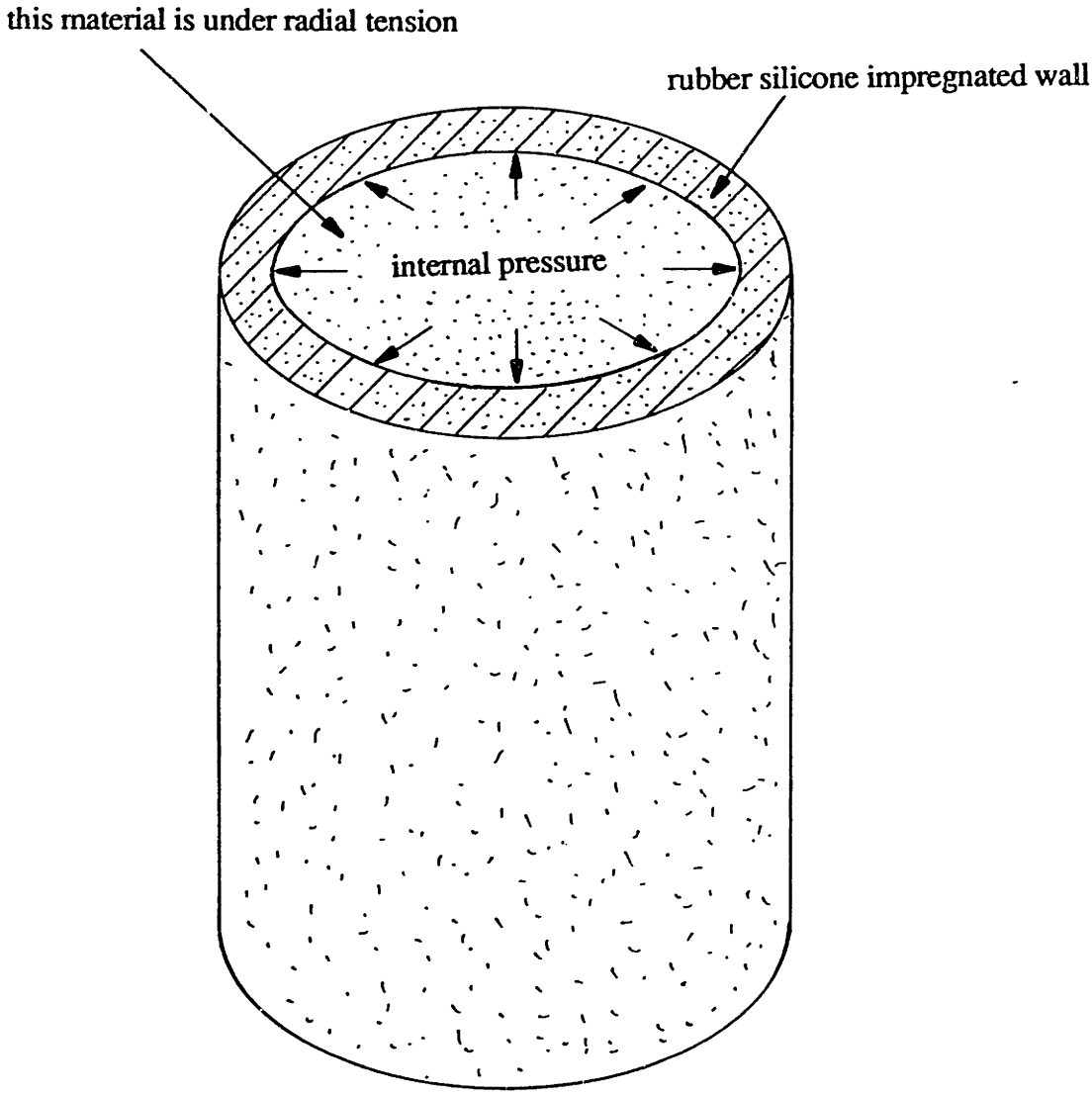

Fig. 5.11 Specimen under radial tension.

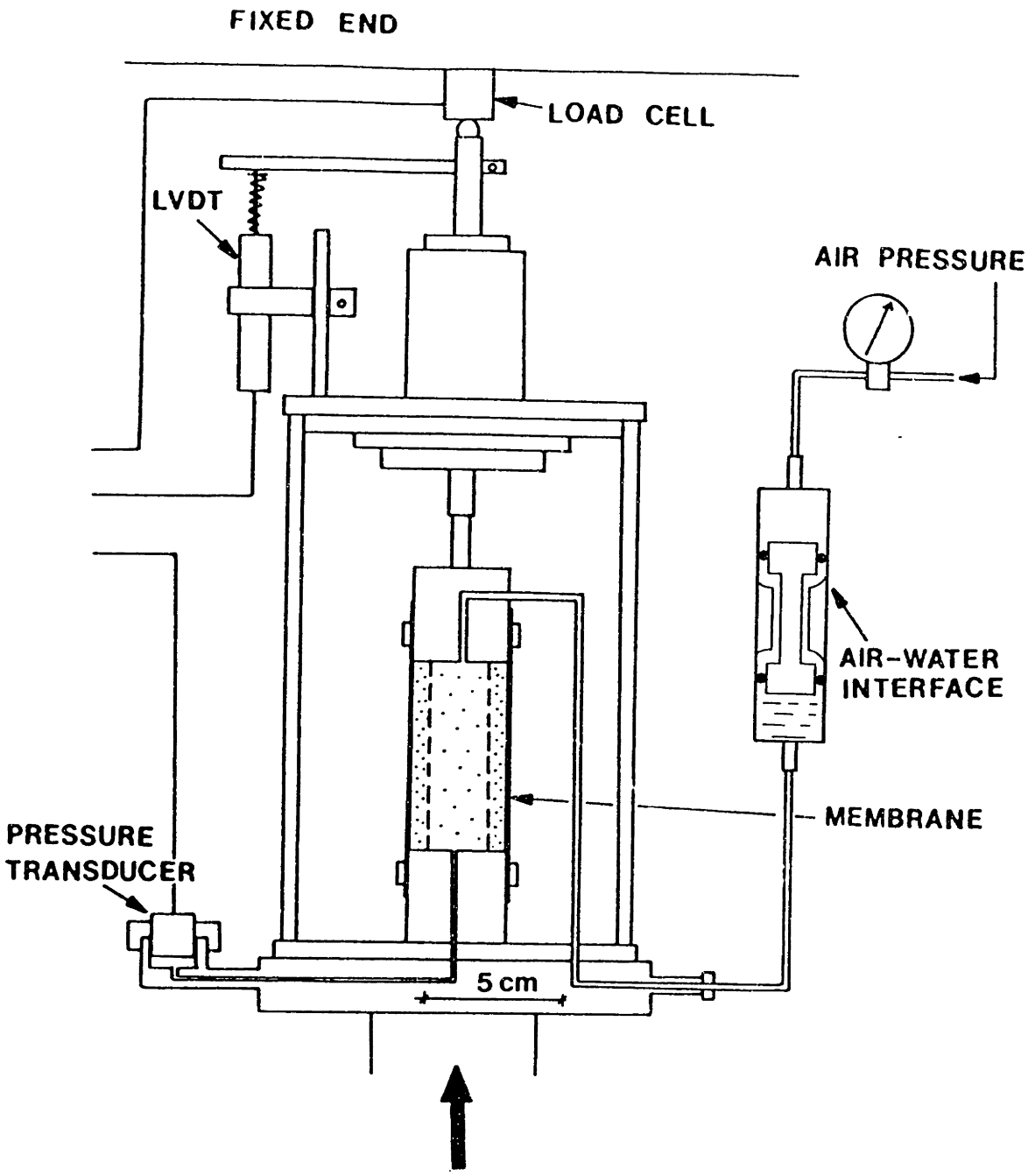

Fig. 5.12 The apparatus used for applying simultaneous tensile radial and compressive axial stresses.

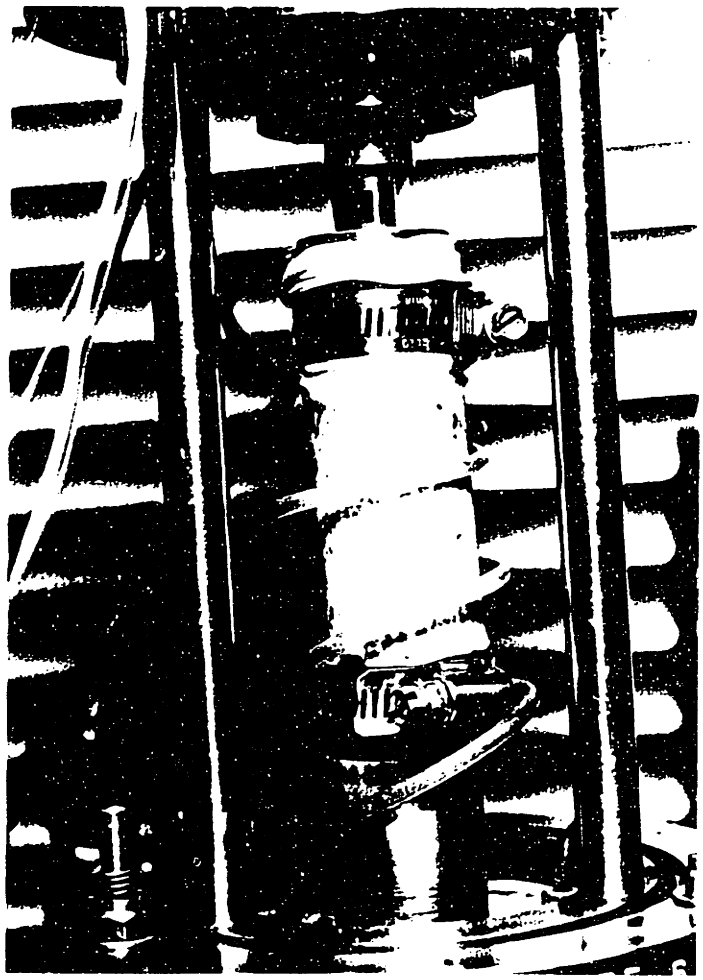

Fig. 5.13 Photograph of a specimen under radial tension and axial compression.

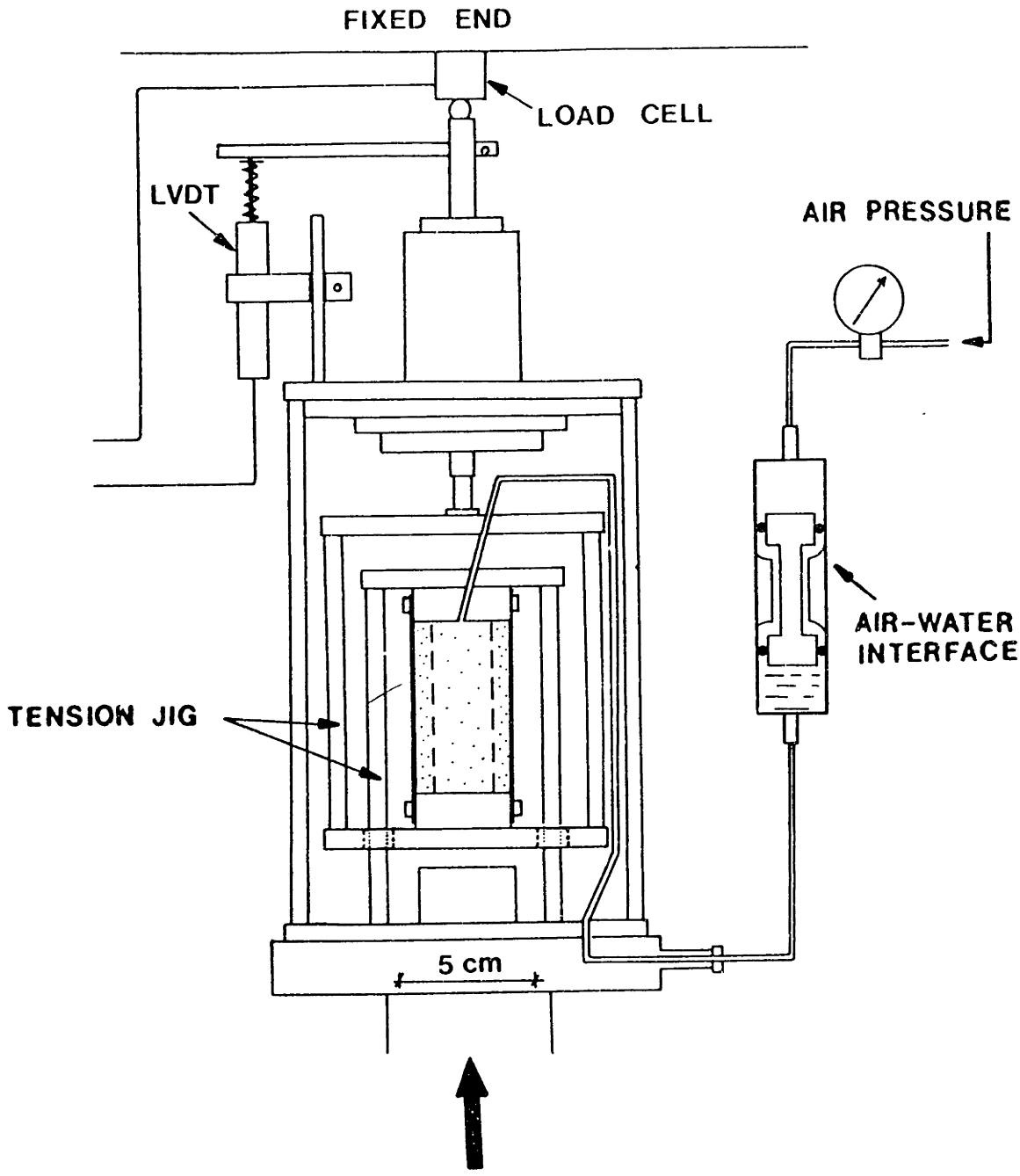

Fig. 5.14 The apparatus used for applying simultaneous tensile radial and axial stresses.

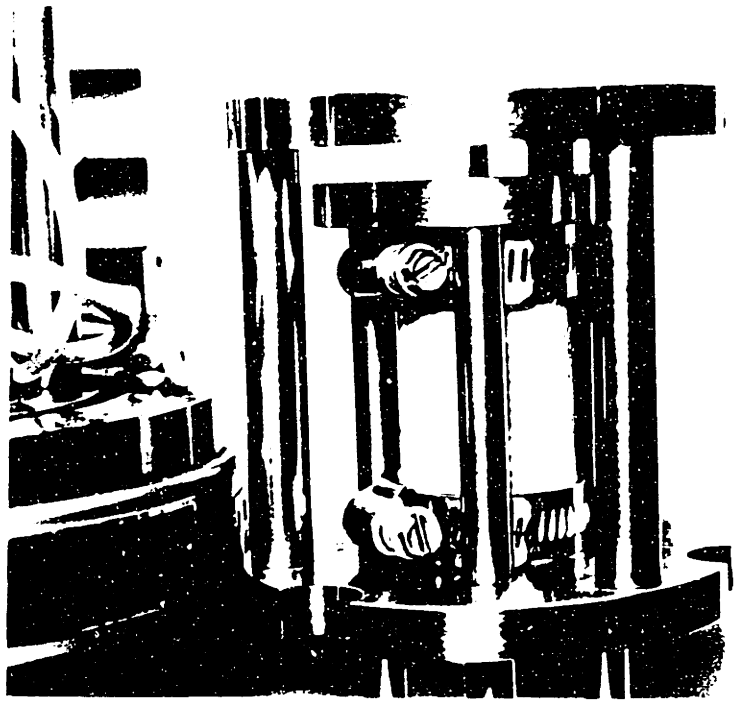

(a)

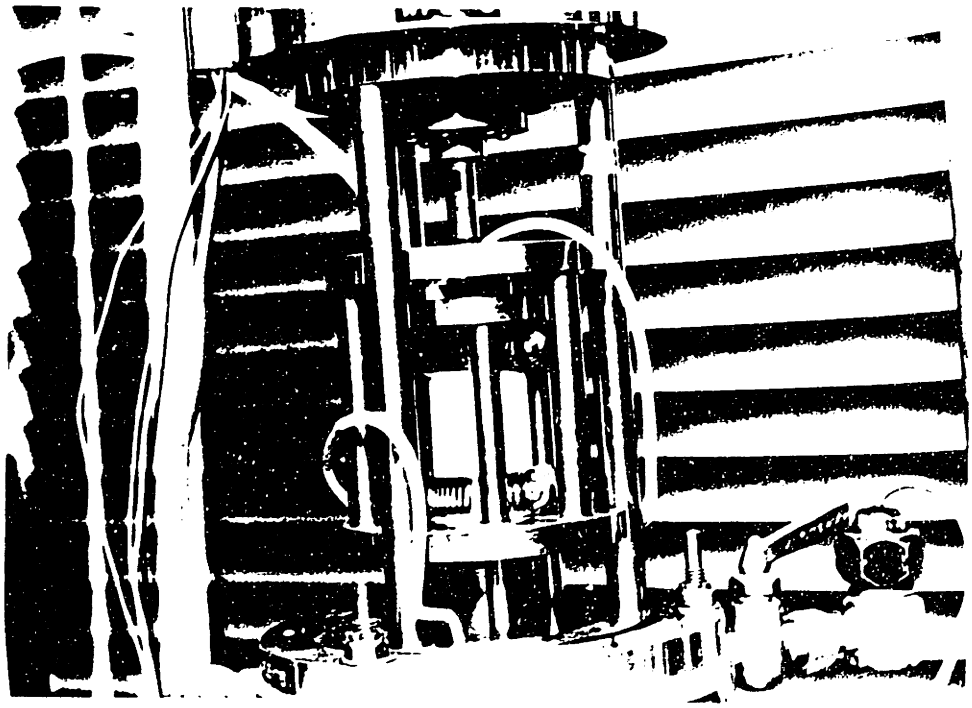

(b)

Fig. 5.15 (a) Specimen contained in the tension cage; (b) photograph of a specimen under tensile radial and axial stresses.

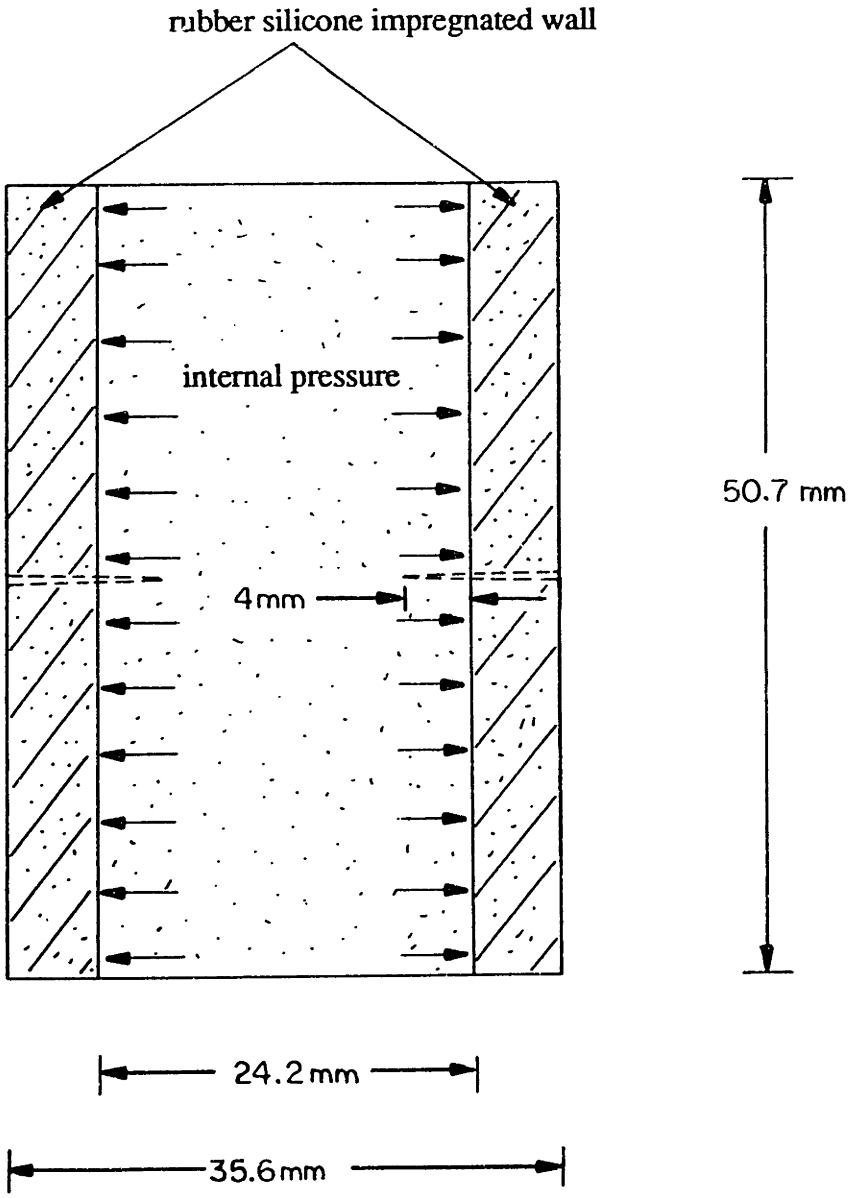

Fig. 5.16 The configuration of notched cylindrical specimens used in the triaxial apparatus for tests involving tensile radial and axial stresses.

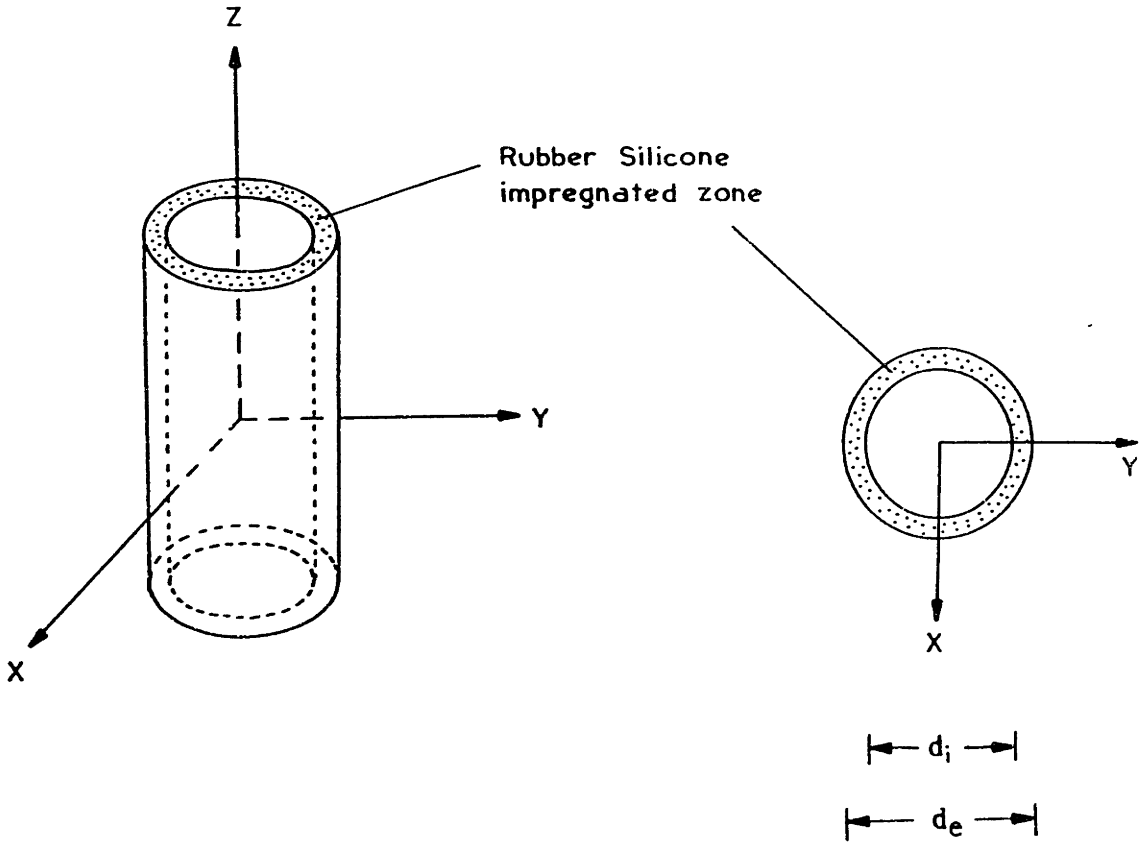

Fig. 5.17 Schematic representation of the specimens analyzed by the finite element method, along with the global system of coordinates.

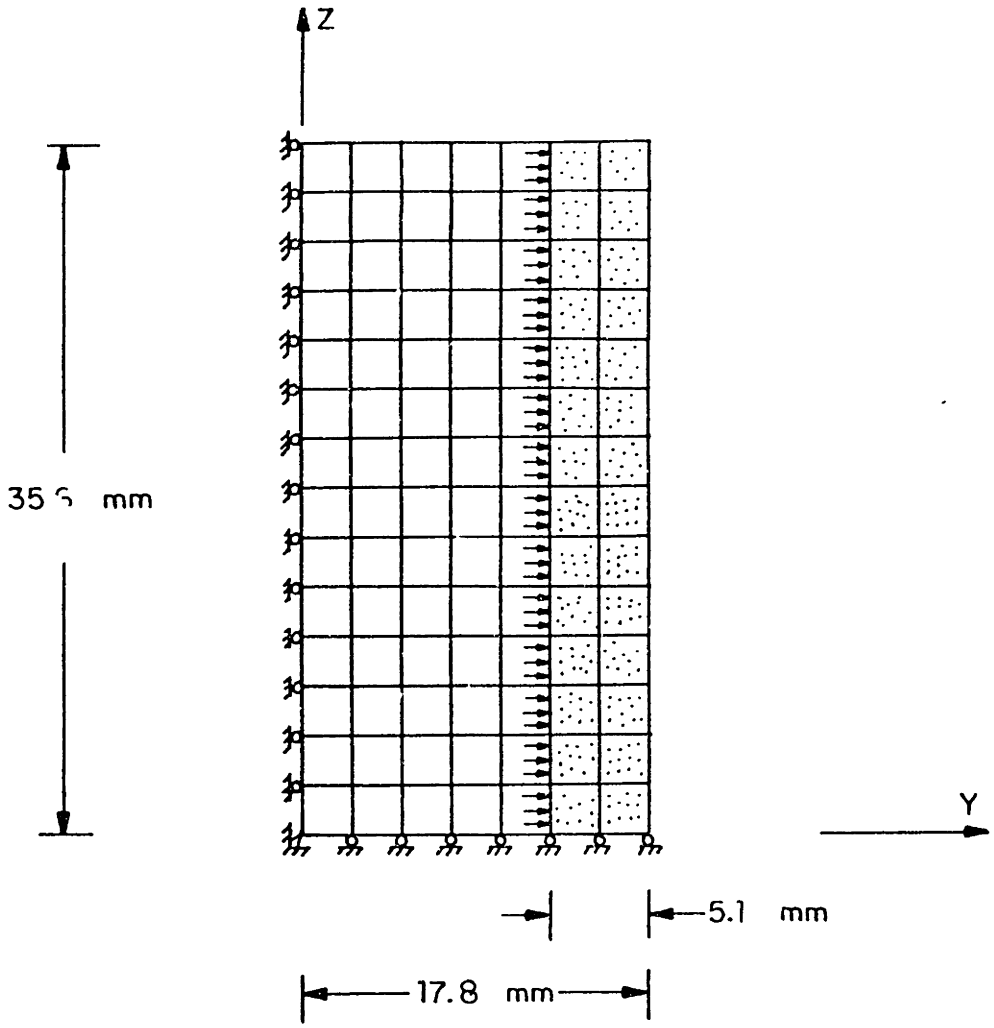

Fig. 5.18 The finite element mesh of type A.

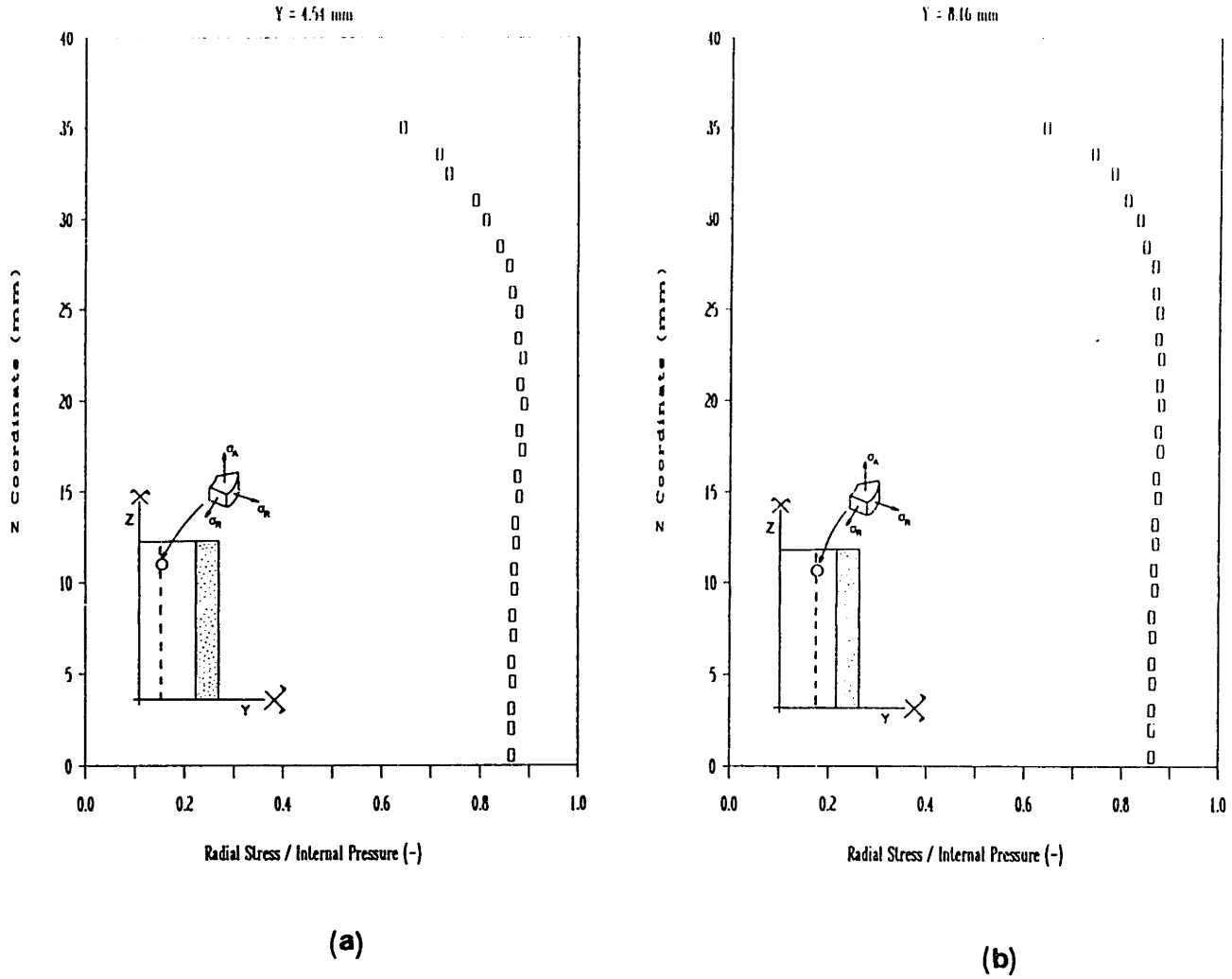

(a) (b)

Fig. 5.19 Stress distribution along the height of the specimens in two different sections, for the mesh of type A. (a) and (b) Radial stress; (c) and (d) axial stress.

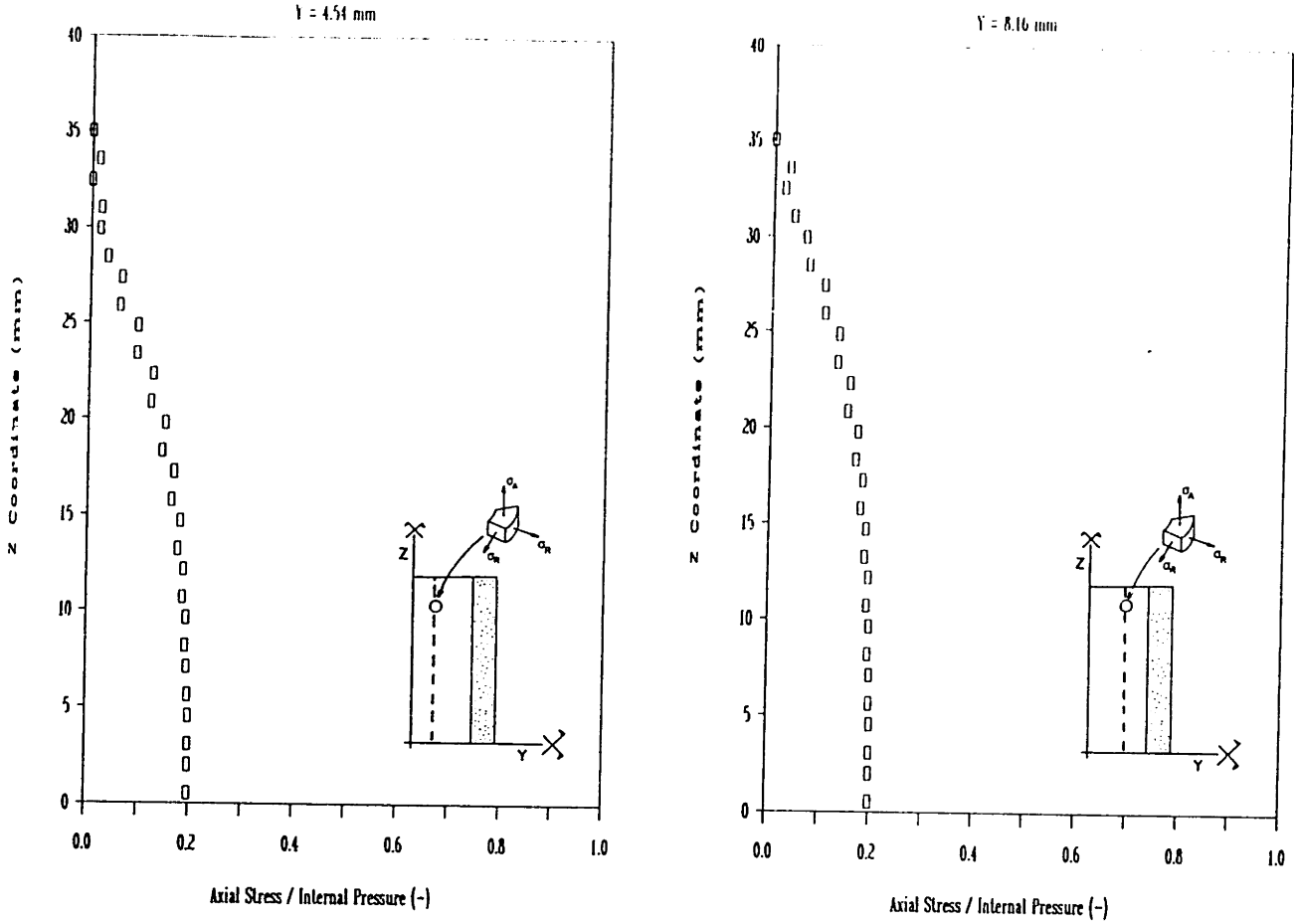

(c) (d)

Fig. 5.19 cont'd.

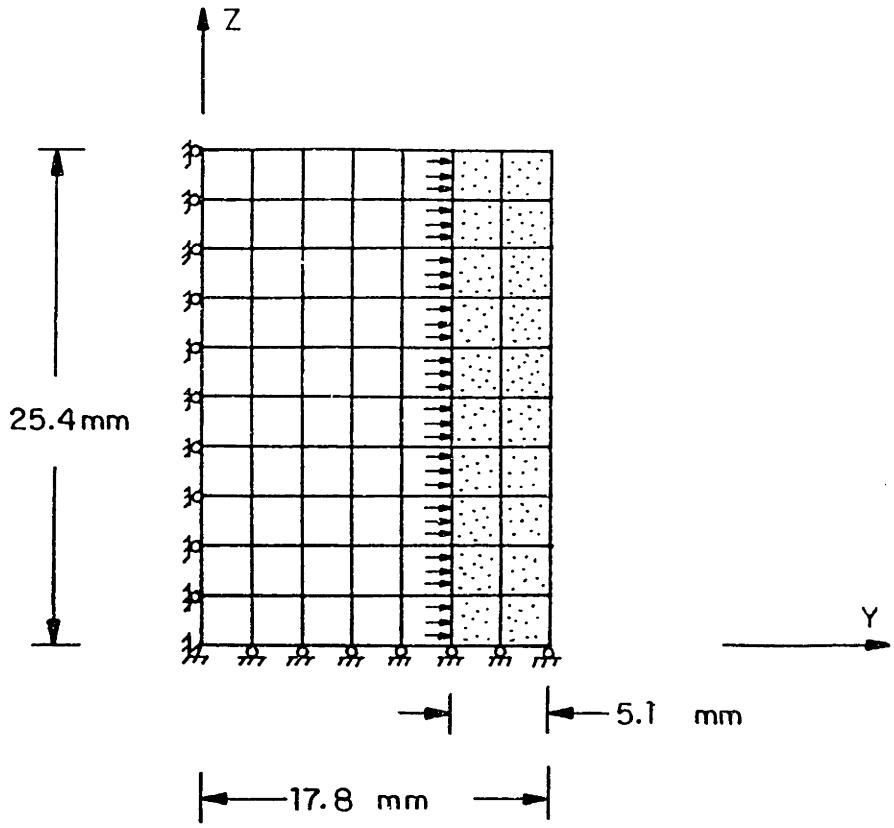

Fig. 5.20 The finite element mesh of type B.

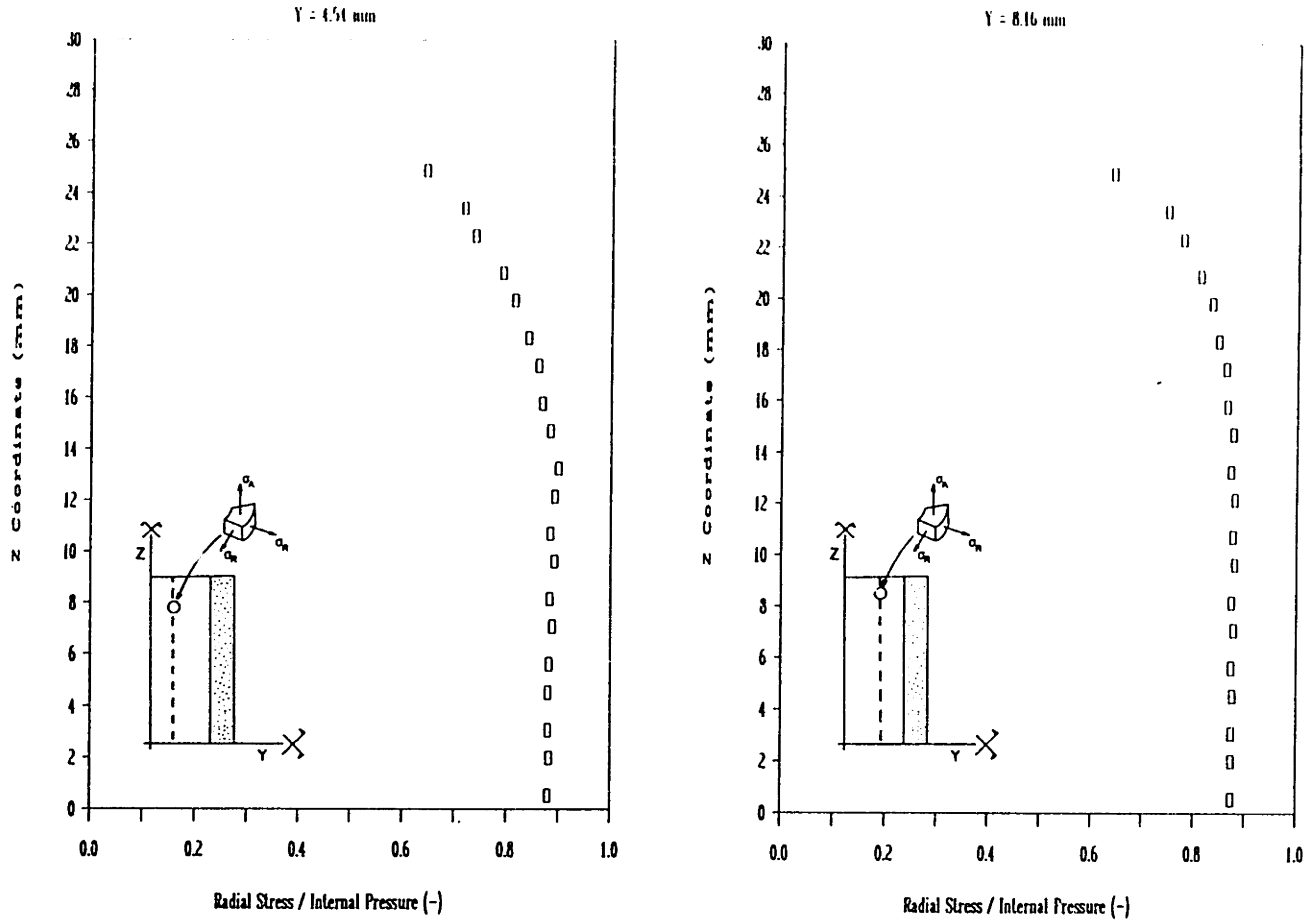

Fig. 5.21 Stress distribution along the height of the specimens in two different sections, for the mesh of type B. (a) and (b) Radial stress; (c) and (d) axial stress.

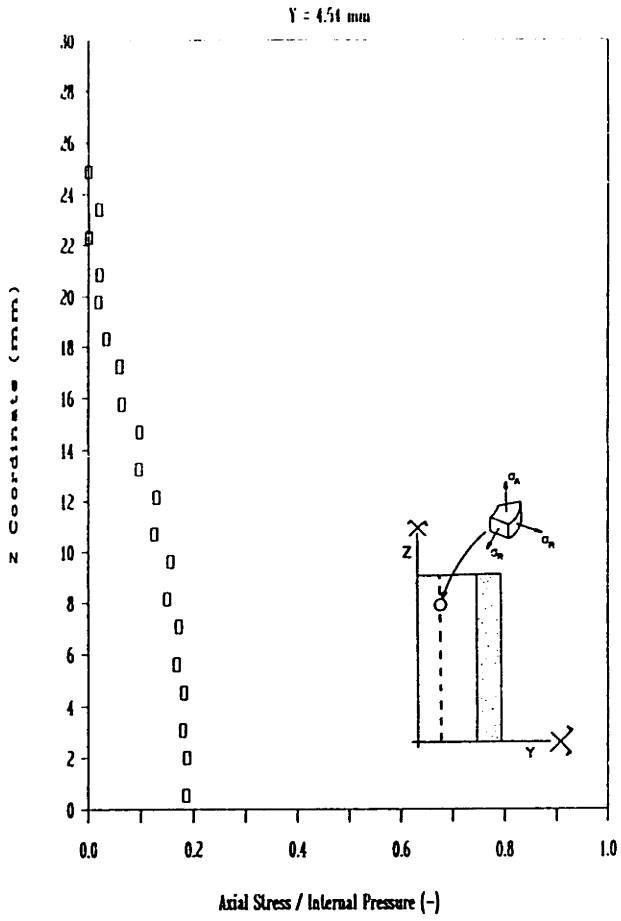

(c)

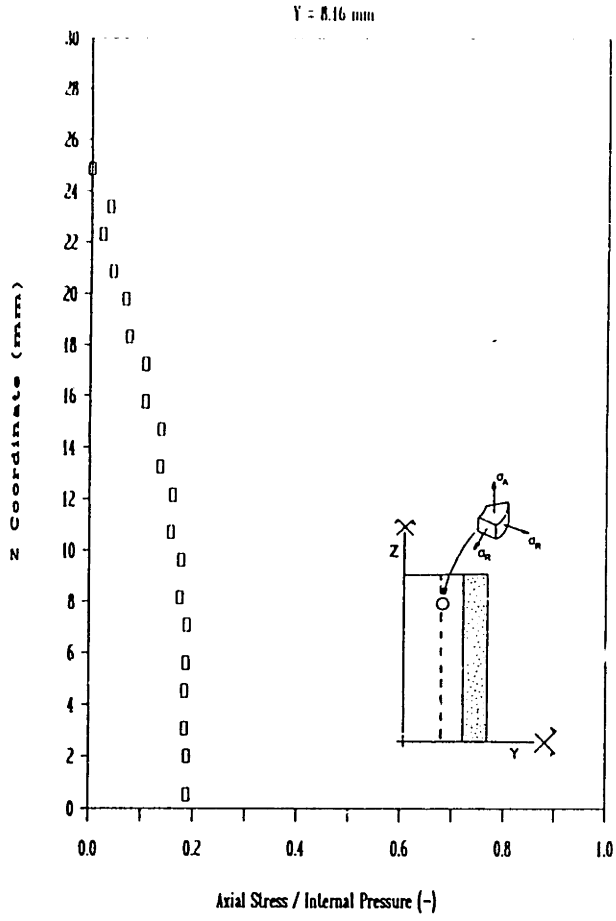

(d)

Fig. 5.21 cont'd.

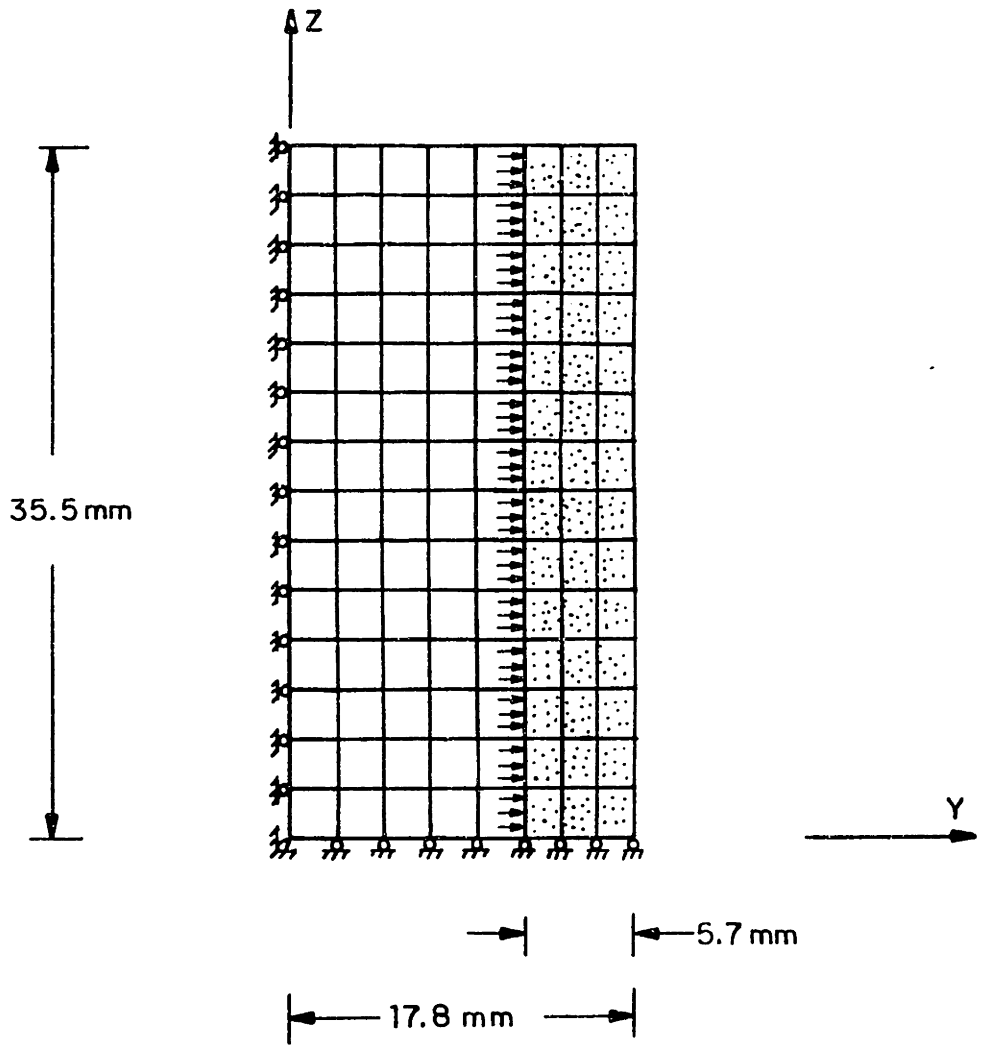

Fig. 5.22 The finite element mesh of type C.

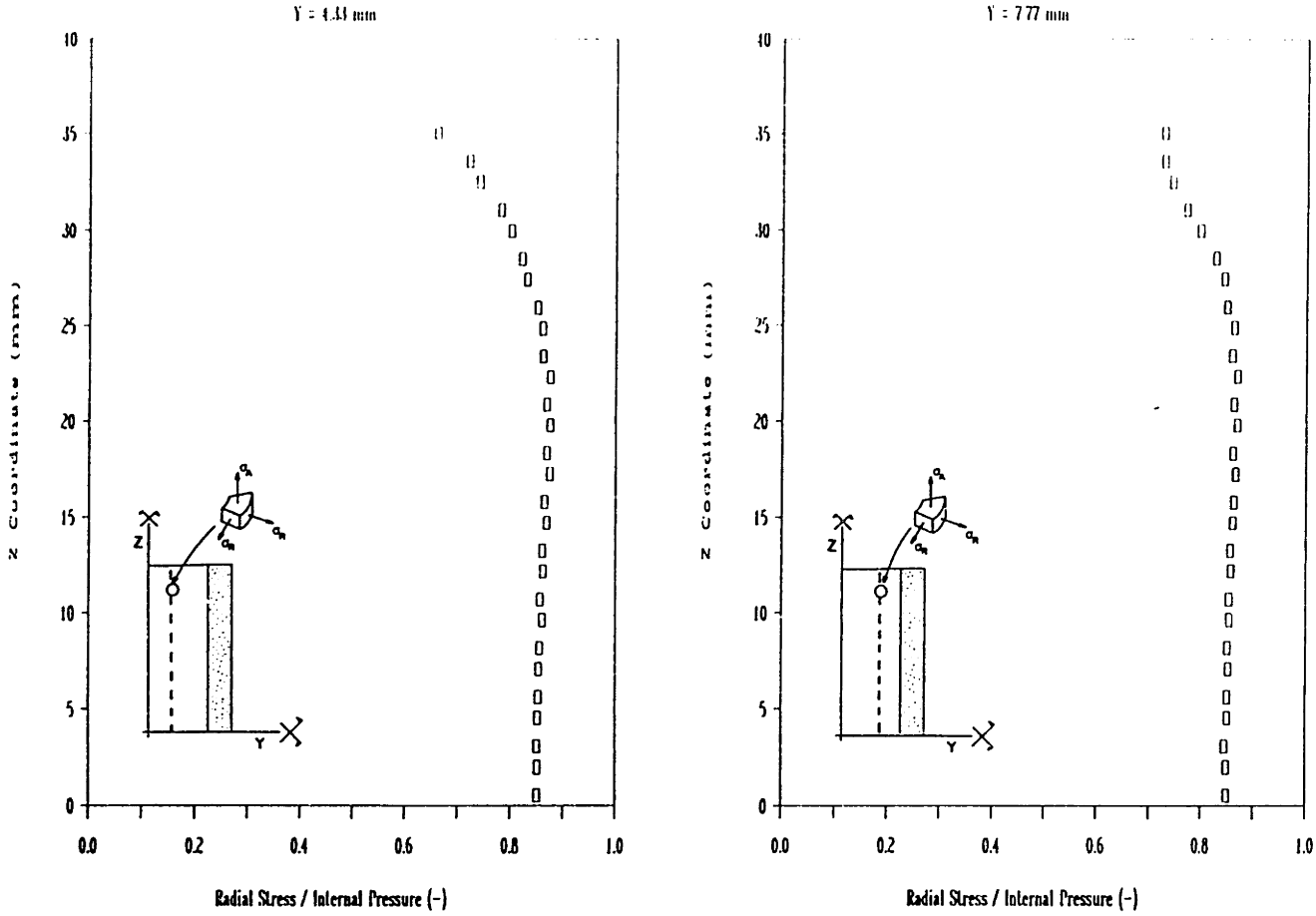

(a) (b)

Fig. 5.23 Stress distribution along the height of the specimens in two different sections, for the mesh of type C. (a) and (b) Radial stress; (c) and (d) axial stress.

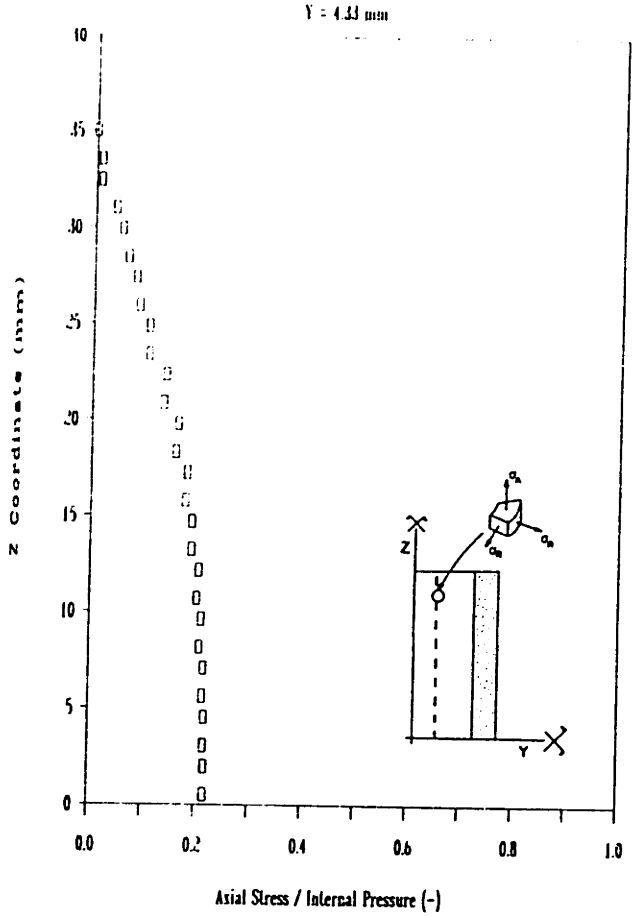

(c)

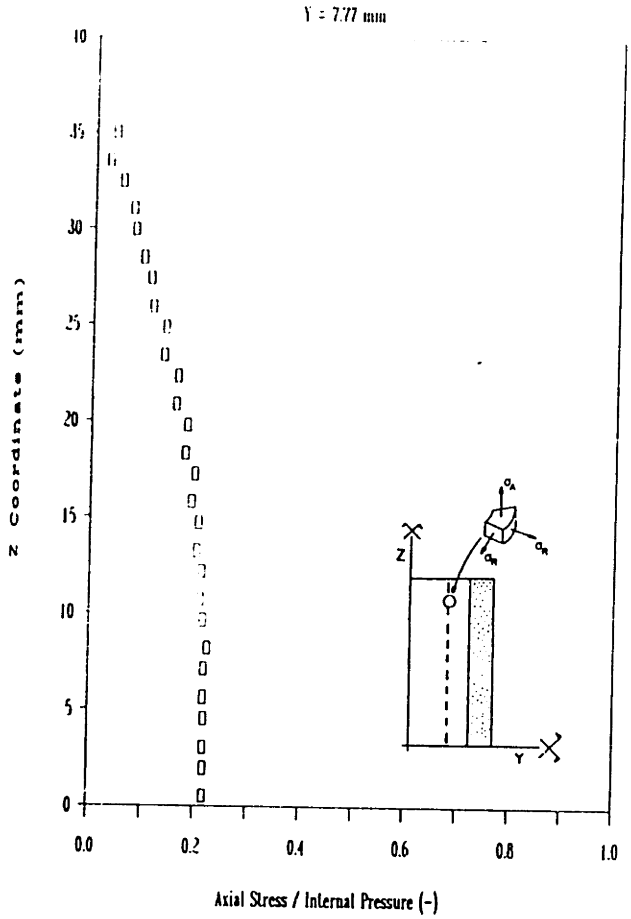

(d)

Fig. 5.23 cont'd.

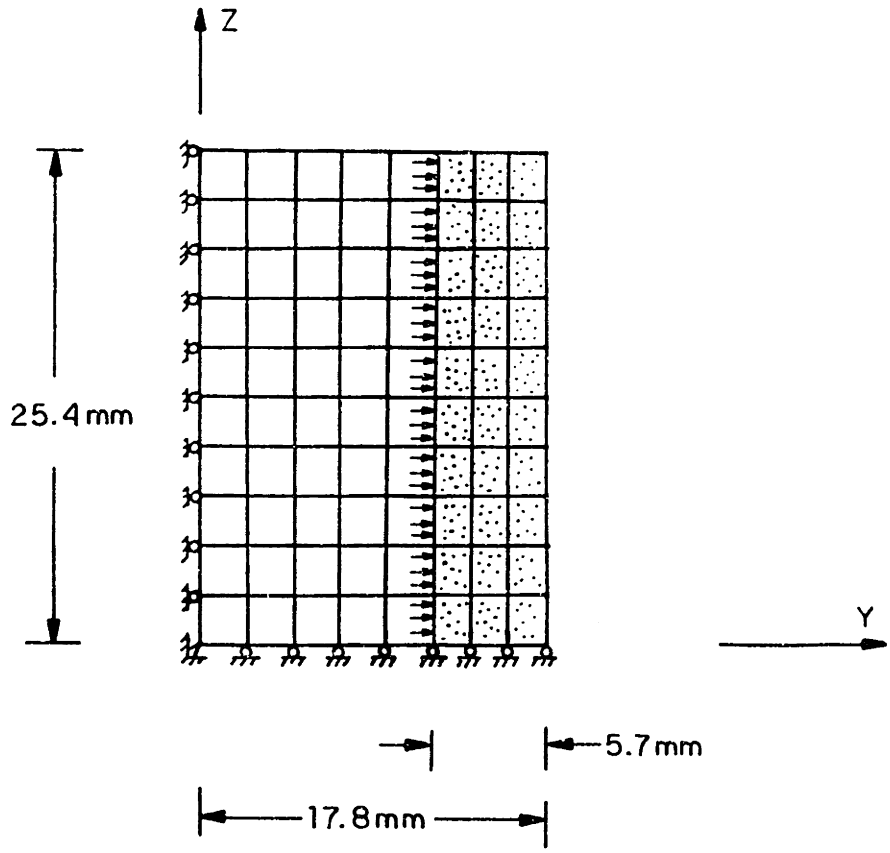

Fig. 5.24 The finite element mesh of type D..

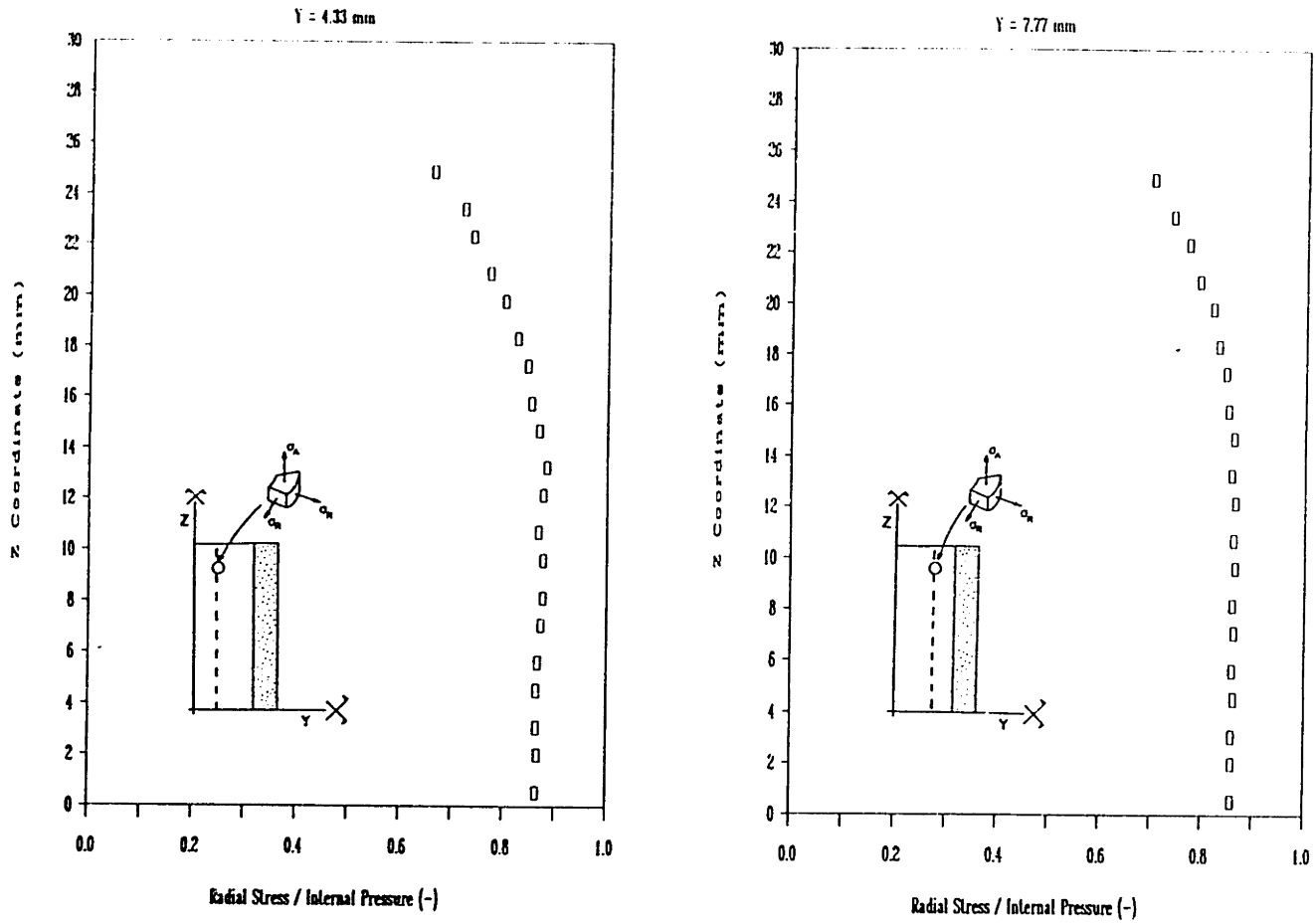

(a) (b)

Fig. 5.25 Stress distribution along the height of the specimens in two different sections, for the mesh of type D. (a) and (b) Radial stress; (c) and (d) axial stress.

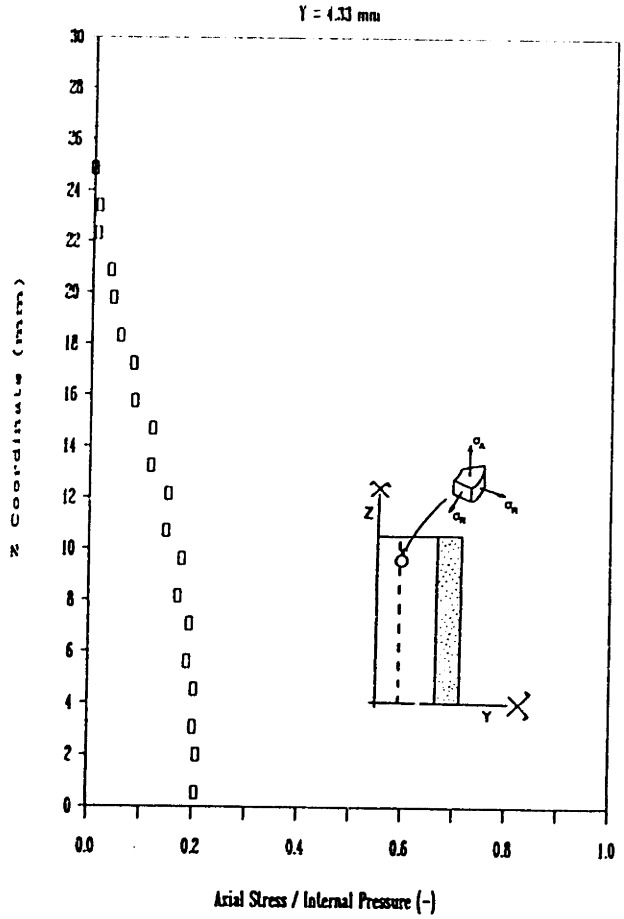

(c)

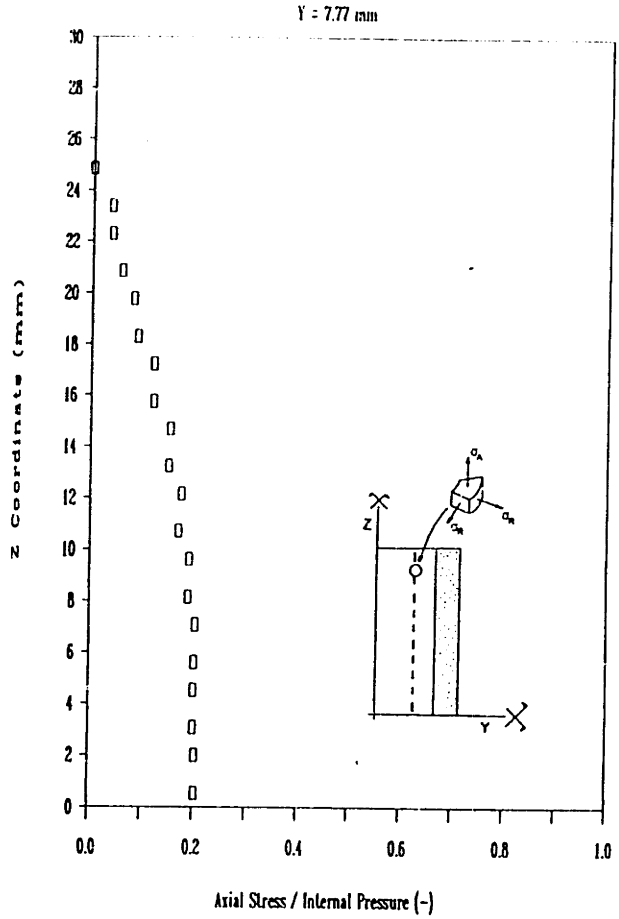

(d)

Fig. 5.25 cont'd.

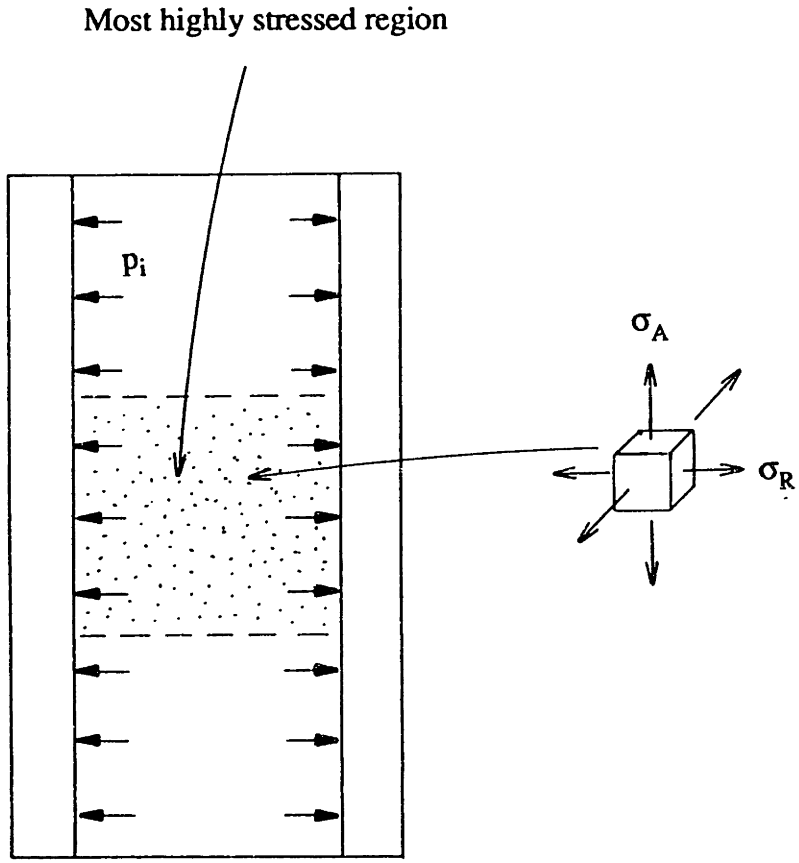

Mesh type	σ_R/p_i	σ_A/p_i
A	0.87	0.19
B	0.87	0.18
C	0.85	0.21
D	0.86	0.20

Fig. 5.26 The state of stress in the most highly stressed region of the specimens used in the tests with radial tension.

CHAPTER VI

RESULTS AND DISCUSSION

6.1 Introduction

In this chapter we present the results of a series of tests on flexible honeycombs under uniaxial and biaxial loading conditions, and on flexible, plastic, and brittle foams under uniaxial, biaxial, and axisymmetric loading conditions. A description of the experimental procedures followed for characterizing the specimens and measuring their mechanical properties was given in the previous chapter. This chapter describes the findings of the microstructural characterization of the materials tested, the results of the mechanical tests, and an evaluation of the analysis presented earlier based on the available test results. The results, assembled to give failure envelopes in stress space, give a good description of the failure of the materials under multiaxial loads.

6.2 Results of Microstructural Characterization

Representative micrographs used to characterize the microstructure of the flexible and rigid polyurethanes, the aluminum, and the reticulated carbon foams are shown in Figs 1a-k. The cell sizes of the flexible polyurethane (PU(F), Fig. 1a), were not obtained by the author; instead, those obtained by Huber (1987) and Huber and Gibson (1988) are reported here; note that the PU(F) specimens used in the mechanical tests were cut from the same blocks used in the two aforementioned studies. The closed cell structure of the rigid polyurethane foam is illustrated in Figs 1b-c, 1d-e, and 1f-g for the 64 kg/m^3, 96 kg/m^3, and 192 kg/m^3 density material, respectively. Figures 1h-i and 1j-k show the open cell structure of the aluminum foam and the reticulated vitreous carbon. The mean values and standard deviations of the cell lengths in the three mutually

orthogonal directions X, Y, and Z are listed in Table 6.1. The measurements indicate that the materials used in this study are orthotropic; they can also be modeled as axisymmetric without significant error.

6.3 Experiments on Elastomeric 2D Cellular Solids

A total of 10 compression tests (2 uniaxial, 8 biaxial) were run using the flexible honeycomb described in Section 5.4. The failure of the specimens loaded uniaxially occured by mode 1 buckling (Fig. 6.2a). A typical load-deflection curve for this case is given in Fig. 6.3a. Point F in the figure is the first point corresponding to the elastic buckling of the honeycomb; the associated strain was measured to be -0.145 ($=\varepsilon^*_y$) in both uniaxial tests. In 3 of the biaxial tests the honeycomb structure buckled according to mode 1, while in 5 tests it failed according to mode 2 buckling (Fig. 6.2b).

Figure 6.3b shows the load-deflection curve for biaxial loading with the crosshead moving parallel to the material direction Y. At point T, the two sides of the honeycomb touch the internal faces of the biaxial jig and the stiffness increases. The lateral strain, ε_x, is kept constant thereafter, and equal to 0.072. Elastic buckling occurs at point F, with an associated vertical strain ε_y= -0.093 (calculated from the load-deflection curve). Similar behavior is illustrated in Fig. 6.3c; the crosshead motion in this case is parallel to the material direction X (specimen rotated at 90°). Figure 6.3d gives the result of a biaxial test in which a lateral strain (ε_y in this case) was imposed on the specimen right at the beginning, before any stress was applied from the crosshead; the vertical strain at failure (ε_x) is calculated at point F. The pairs of strains at failure (ε_x and ε_y) are inserted in eqns (5.10) and (5.11) along with the uniaxial failure strain (ε^*_y), to obtain the ratios $\sigma_x/(\sigma^*_{el})_y$ and $\sigma_y/(\sigma^*_{el})_y$ at failure of the honeycomb. These pairs are summarized in Table 6.2. The experimentally obtained failure envelope is given in Fig. 6.4. The two lines shown there represent the analytical predictions (eqns (3.3) and (3.17) for modes 1 and 2 respectively). The agreement is quite good.

Table 6.1 Characterization of materials microstructure (SEM results).

Material	Density (kg/m^3)	$\bar{l}_x$ (mm)	$\bar{l}_y$ (mm)	$\bar{l}_z$ (mm)
Flexible polyurethane	28	0.58[1]	0.47[1]	0.44[1]
Rigid polyurethane	64	0.23 (0.01)[2]	0.16 (0.013)	0.15 (0.014)
	96	0.22 (0.009)	0.18 (0.012)	0.16 (0.011)
	192	0.15 (0.011)	0.12 (0.008)	0.11 (0.007)
Aluminum	135	1.77 (0.22)	1.13 (0.06)	0.98 (0.06)
Reticulated vitreous carbon	48	1.67 (0.27)	1.23 (0.20)	1.12 (0.14)

1. From Huber (1987).
2. Numbers in parentheses indicate the standard deviation.

X=rise direction (*strong* material direction).

Table 6.2 Results of uniaxial and biaxial compression tests on elastomeric honeycombs.

Test #	Crosshead direction	ε_x at failure	ε_y at failure	Buckling mode
1	Y	-	-0.145[1]	1
2	Y	-	-0.145[1]	1
3	Y	0.072[2]	-0.093	1
4	X	-0.067	0.044	2
5	X	-0.025	-0.003	2
6	Y	0.033	-0.056	1
7	Y	0.018	-0.045	1
8	X	-0.082	0.056	2
9	X	-0.110	0.085	2
10	X	-0.147	0.121	2

1. ε^*_y in eqns (5.10) and (5.11).
2. The underlined numbers correspond to the strains imposed laterally by the biaxial jig.

6.4 Experiments on 3D Cellular Materials

(a) Uniaxial Loading

Elastomeric Material--Compression

Typical load-deformation curves resulting from the compressive loading of cubic flexible polyurethane foam specimens parallel to each of the three material directions are shown in Fig. 6.5. The stresses at failure, $(\sigma^*_{el})_x$, $(\sigma^*_{el})_y$, and $(\sigma^*_{el})_z$ are calculated from the loads corresponding to the elastic buckling plateau in the load-deflection curve. The results from 9 tests are summarized in Table 6.3.

Table 6.3 Uniaxial elastic collapse stresses for the flexible polyurethane foam.

	$-(\sigma^*_{el})_x$ (KPa)	$-(\sigma^*_{el})_y$ (KPa)	$-(\sigma^*_{el})_z$ (KPa)
	5.52	4.90	4.86
	5.42	4.80	4.87
	5.48	4.90	4.89
Mean value:	5.47	4.89	4.87
Standard deviation:	0.05	0.06	0.015

The results are consistent with the geometry of the material's microstructure: higher strength and elastic modulus are obtained when the material is loaded parallel to the rise direction, in this case, the X direction.

Elastic-Plastic Materials--Compression

Compressive load-deflection curves from tests on rigid polyurethane (PU(R)) foam specimens are given in Figs 6.6a, b, and c, for the 64 kg/m^3, 96 kg/m^3, and 192 kg/m^3 densities, respectively. A linear elastic regime is followed by a yield plateau in all cases; the behavior can be modeled as elastic-perfectly plastic (bilinear model) with sufficient accuracy. Failure of the material is defined at the upper yield point (which is close to the yield plateau) of the load-deformation curve. The material orthotropy is reflected in these experimental results too: both the elastic modulus and the plastic collapse stress drop as we change the loading direction from X to Y and then to Z. The results from 27 tests are summarized in Table 6.4.

Table 6.4 Uniaxial plastic collapse stresses for the rigid polyurethane foams.

ρ^* (kg/m^3)	$-(\sigma^*_{pl})_x$ (KPa)		$-(\sigma^*_{pl})_y$ (KPa)		$-(\sigma^*_{pl})_z$ (KPa)	
	644	630[1]	321	350	286	295
64	616	(14)[2]	362	(26)	291	(45)
	634		367		308	
	1092	1080	761	750	752	740
96	1081	(9)	754	(13)	737	(10)
	1076		736		734	
	3396	3350	2606	2615	2442	2435
192	3330	(40)	2670	(50)	2453	(27)
	3322		2570		2401	

1. Mean value. 2. Standard deviation.

Figure 6.7 shows typical load-deformation curves from tests on aluminum foam specimens; the specimens were loaded parallel to each of the material directions X, Y, and Z. A similar behavior is observed here: the material behaves in an approximately linear elastic-perfectly plastic manner and the foam is roughly axisymmetric. Failure is defined at the yield plateau. The results from 9 tests are given below:

Table 6.5 Uniaxial plastic collapse stresses for the aluminum foam.

	$-(\sigma^*_{pl})_x$ (KPa)	$-(\sigma^*_{pl})_y$ (KPa)	$-(\sigma^*_{pl})_z$ (KPa)
	1616	964	858
	1715	927	876
	1787	928	822
Mean value:	1705	940	850
Standard deviation:	86	21	27

Elastic-Brittle Material--Compression

The last series of uniaxial compression tests was performed on cubic reticulated vitreous carbon specimens which were brittle. As Fig. 6.8 illustrates, the initial elastic behavior is followed by a serrated plateau corresponding to successive crushing of the cell walls. The crushing collapse stresses for loading parallel to each of the three material directions (X, Y, and Z) are defined at an average value of the load in the initial part of the crushing plateau (Fig. 6.8). They were found to be almost the same for loading in either direction in the plane normal to the rise direction; the material is therefore treated as

axisymmetric. A summary of the 15 test results performed is given in Table 6.6.

Table 6.6 Uniaxial compressive crushing stresses for the reticulated vitreous carbon foam.

	$-(\sigma^*_{cr})_x$ (KPa)	$-(\sigma^*_{cr})_y$ (KPa)	$-(\sigma^*_{cr})_z$ (KPa)
	214	147	159
	209	161	151
	171	176	157
	242	161	147
	223	164	173
Mean value:	212	162[1]	158[1]
Standard deviation:	25	10	10

1. The material is considered axisymmetric with a compressive strength normal to the rise direction equal to -160 KPa.

Elastic-Plastic Materials--Tension

Results from uniaxial tension tests on the rigid polyurethane foams are presented in Figs 6.9, 6.10, and 6.11 for the 64 kg/m^3, 96 kg/m^3, and 192 kg/m^3 density materials, respectively. One typical load-deformation curve is given for loading parallel to each of the three principal material directions. The behavior observed here is different from that in compression in that the stress plateau is replaced by a plastic strain

hardening branch which is terminated by fracture. This phenomenon is due to the stretching of the cell faces in closed-cell foams. In the absence of a well defined yield plateau, failure is defined here as the first deviation from the linear elastic behavior on the load-deformation curve. This definition is consistent with that given before for compressive failure, in which case the termination of the linear regime is very close to the yield plateau. The results of 27 tests on the rigid polyurethane foam specimens are summarized next:

Table 6.7 Uniaxial tensile yield stresses for the rigid polyurethane foams.

ρ^* (kg/m^3)	$(\sigma^*_{pl})^t_x$[1] (KPa)		$(\sigma^*_{pl})^t_y$ (KPa)		$(\sigma^*_{pl})^t_z$ (KPa)	
64	710 645 565	640[2] (73)[3]	455 455 460	455 (3)	400 390 370	385 (15)
96	1295 1310 845	1150 (264)	660 710 690	685 (25)	640 610 645	630 (19)
192	2620 2305 2395	2440 (162)	1685 1745 1600	1675 (73)	1400 1480 1600	1495 (101)

1. The superscript "t" is used here to denote tension.
2. Mean value.
3. Standard deviation.

Typical load-deformation curves from uniaxial tension tests on aluminum foam specimens for each of the three material directions are shown in Fig. 6.12. A short yield plateau is followed by a softening branch associated with progressive rupture (after yielding) of the aluminum cell walls. Failure here is defined at the yield plateau. The tensile yield stresses for this material are given in Table 6.8 (6 test results).

Table 6.8 Uniaxial tensile yield stresses for the aluminum foam.

	$(\sigma^*_{pl})^t_x$ (KPa)	$(\sigma^*_{pl})^t_y$ (KPa)	$(\sigma^*_{pl})^t_z$ (KPa)
	1805	983	898
	1735	958	911
Mean value:	1770	970	905
Standard deviation:	49	18	9

Elastic-Brittle Material--Tension

Notched cylindrical RVC specimens were subjected to uniaxial tensile loading parallel to the strong material direction (3 tests). A typical load-deformation curve is given in Fig. 6.13. All specimens failed by fast brittle fracture which terminated their linear elastic behavior. This result validates the application of linear elastic fracture mechanics in the study of the fracture behavior of the elastic-brittle RVC material (Broek, 1986). The results obtained are given in Table 6.9. The failure stress was calculated by dividing the ultimate load recorded by the "uncracked" area of the specimens. The mean value of the failure stress (128 KPa) gives a critical stress intensity factor K^*_{IC} =0.64 $N/mm^{3/2}$ calculated for the specific geometry from eqn. (5.12).

Table 6.9 Uniaxial tensile strength of notched RVC cylinders.

	$(\sigma^*_{fr})_x$ (KPa)
	125
	112
	147
Mean value:	128
Standard deviation:	18

The average values of the uniaxial strengths obtained above were used in the calibration of the failure criteria for 3D cellular materials developed in Chapter 4.

(b) Biaxial Loading

Elastomeric Material

Cubic flexible polyurethane specimens were used in 8 biaxial compression tests. The specimens failed by elastic buckling of the cell walls in all cases. The loads were applied in the Y-Z plane of the material. A stress σ_z applied by the hydraulic jack was kept constant during the test, while a second stress σ_y was imposed by the crosshead, resulting in a biaxial stress field. A typical load-deformation curve is given in Fig. 6.14. The stress σ_y at failure was calculated by dividing the failure load indicated in the figure by the area of the specimen, while the stress σ_z at failure was read directly from the pressure gauge of the hydraulic jack accounting for the area of the jack and the area of the specimen. The results obtained are summarized in Fig. 6.15 along with a typical stress path followed during one of the tests. The theoretical failure envelope proposed by Zhang (1987) is also given in the same figure. The data lie on a roughly circular curve

somewhat inside the envelope predicted by the model.

Elastic-Plastic Materials

The 64 kg/m^3 and 96 kg/m^3 density rigid polyurethane foam specimens were loaded biaxially in the X-Y and Y-Z planes. Figs 6.16a and 6.16b show typical crosshead load-deformation curves obtained from tests on the 64 kg/m^3 density foam loaded in the X-Y plane; a total number of 22 such tests were performed. In the first figure, the load applied by the crosshead corresponds to σ_x, while, in the second, it corresponds to σ_y. Figures 6.16c and 6.16d illustrate load-deformation curves obtained from tests on the 64 kg/m^3 density material loaded in the Y-Z plane; 21 tests were performed in this case. In Fig. 6.16c, the crosshead load corresponds to a stress σ_y, while in Fig. 6.16d it corresponds to a stress σ_z. The results for the 64 kg/m^3 density foam are summarized in Figs 6.17a and 6.17b for loading in the X-Y and Y-Z planes, respectively, producing the experimental failure envelopes; typical stress paths are illustrated in these figures too. Failure, as Fig. 6.16 indicates, is defined consistently with the uniaxial case: at the yield plateau when the recorded load is compressive, and at the first deviation from linearity when it is tensile. The solid lines in Figs 6.17a and 6.17b represent the predicted failure envelope according to the model developed in Section 4.3c. The agreement between analytical and experimental results is discussed in Section 6.5.

A total of 9 biaxial compression tests were run using the 96 kg/m^3 density specimens with loading in the X-Y plane. Typical load-deformation curves are presented in Figs 6.18a and 6.18b. Moreover, 10 specimens of the same material were loaded in the Y-Z plane (Figs 6.18c and 6.18d illustrate typical results). The experimental failure envelopes for this material are given in Figs 6.19a and 6.19b for loading in the X-Y and Y-Z planes, respectively; the predicted failure envelopes are plotted with solid lines. Tests with one or both stresses in tension were unsuccessful due to the failure of the adhesive before yielding of the foam.

Elastic-Brittle Material

15 biaxial compression tests were performed on cubic reticulated vitreous carbon foams with loading in the X-Y plane. Figures 6.20a and 6.20b illustrate 2 representative load-deformation curves. The complete set of data is given in Fig. 6.21 along with typical stress paths followed. Note that the definition of failure (Figs 6.20a and 6.20b) is consistent with that given in the case of uniaxial compressive loading. The analytical failure envelope is plotted in Fig. 6.21 with the solid line.

(c) Triaxial (Axisymmetric) Loading

Elastomeric Material

A total of 12 tests were performed on 28 kg/m^3 density flexible polyurethane specimens with radial pressure and axial stress acting simultaneously. The axial stress acted parallel to the strong material direction (X), while the radial pressure was normal to this. Failure of the specimens occured by elastic buckling of the cell walls. A typical axial load-deformation curve is given in Fig. 6.22. Failure was defined at the elastic collapse plateau, as for the uniaxial loading case. The results are plotted in Fig. 6.23; the dashed line in this figure corresponds to the analytical prediction of the elastic buckling envelope proposed by Zhang (1987).

Elastic-Plastic Materials

The rigid polyurethane foam specimens were subjected to simultaneous radial compression and axial compression or tension. The axial stress was parallel to the X material direction (strong direction), while the radial pressure was normal to this. Figure 6.24 shows typical axial load-deformation curves from axisymmetric testing of the (a) 64 kg/m^3 (12 tests), (b) 96 kg/m^3 (11 tests), and (c) 192 kg/m^3 (18 tests) density specimens, with axial and radial compression. As in the uniaxial loading case, failure was defined at the stress plateau. 10, 8, and 9 tests were also performed on the 64 kg/m^3, 96 kg/m^3, and 192 kg/m^3 density specimens, respectively, with axial tension and

radial compression. Typical axial load-deformation curves for all three densities are given in Fig. 6.25; failure in this case is defined at the termination of the linear elastic behavior. All the data obtained are summarized in Figs 6.26, 6.27, and 6.28. In the quadrant of radial compression-axial tension, all three foams failed by yielding and the data follow the yield envelope given by the model developed earlier (solid line). In the radial compression-axial compression quadrant the behavior is more complex with the yield envelope truncated by elastic buckling (dashed line). As the relative density of the material increases, the uniaxial elastic buckling strength (which varies as (relative density)^2) increases more rapidly than the uniaxial plastic collapse strength (which only increases as (relative density)$^{3/2}$). As a result, as the density of the material increases, the intercept of the elastic buckling surface on the axial stress axis is shifted away from that of the yield surface, requiring a greater compressive stress to induce failure by buckling rather than by yielding. This behavior is observed in Figs 6.26, 6.27, and 6.28.

The open-cell aluminum foam was loaded axisymmetrically with radial tension and axial compression (6 tests) or tension (5 tests) to characterize the remaining two quadrants of the axisymmetric yield envelope. All of the specimens were observed to fail by yielding. Typical axial load-deformation curves are given in Fig. 6.29. For axial compression-radial tension, an almost trilinear behavior was recorded: it is believed that the first stiffness degradation regime corresponds to failure (yielding) of the central part of the specimens, which, according to the finite element calculations described in Chapter 5, was the most highly stressed one; failure was defined at the termination of the initial linear elastic response, and the results of the finite element analyses (see Fig. 5.26) were used to calculate the associated stresses. When the axial stress was tensile, failure was defined at the yield plateau (Fig. 6.29b), consistent with the uniaxial case. The data obtained are in good agreement with the predictions given by the yield criterion (Fig. 6.30, solid line), except for one point.

Elastic-Brittle Material

The following tests were performed on reticulated vitreous carbon foam

specimens under axisymmetric loading conditions: 20 tests with radial and axial compression; 9 tests with radial tension and axial compression; 6 tests with radial compression and axial tension and 3 tests under the same conditions but using circumferentially notched specimens; and finally, 8 tests with radial and axial tension, using circumferentially notched specimens. In all cases, the axial load was aligned with the strong material direction (X), while the radial stresses acted normal to this. Typical axial load-deflection curves are given in Figs 6.31-6.33. Failure was defined in analogy to the uniaxial case: at the first crushing plateau when the axial stress was compressive, and at the fracture point when it was tensile. As Figs 6.32 and 6.33 indicate, the tensile behavior was linear elastic; the specimens failed by brittle fracture. The data obtained are plotted in Fig. 6.34. The fracture envelope is truncated by the elastic buckling envelope (dashed line) in the radial compression-axial compression quadrant. Moreover, the fast-brittle fracture cutoff is in a rather good agreement with the experimental results performed on notched specimens with the same fracture toughness (dotted line). The solid line in the figure corresponds to the theoretical prediction for the fracture surface. Even though there is a considerable scatter in the data, the overall agreement is good. The results are discussed further next.

6.5 Discussion

(a) Uniaxial Behavior

The uniaxial behavior of the materials in compression is the expected one. A linear regime is followed by a plateau associated with elastic buckling in elastomeric materials (flexible polyurethane foam, silicone rubber honeycomb), with yielding in elastic-plastic materials (rigid polyurethane and aluminum foams), and with brittle crushing in elastic-brittle materials (reticulated vitreous carbon).

The uniaxial tensile behavior is different. The linear part in the load-deformation curves of the closed-cell rigid polyurethane foams is followed by a hardening regime which is terminated by fracture (Figs 6.9-6.11). The initial yield (first deviation from

linearity in the load-deformation curves) corresponds to the formation of plastic hinges in the cell edges; at higher loads the cell faces resist tensile deformation by axial stretching; finally, when the load reaches a critical value, the material fails by the sudden propagation of a critical crack. In the open-cell aluminum foam, the linear regime is followed by a short yield plateau and then by a *tension softening* regime (Fig. 6.12); the cell walls first yield and undergo a plastic hinge collapse mechanism, and eventually rupture progressively. The reticulated vitreous carbon behaves in a brittle manner: linear elasticity is followed by brittle fracture due to the propagation of the critical crack existing in the material.

The compressive and tensile yield stresses associated with a certain material direction are about the same in the two lowest densities rigid polyurethane foams and the aluminum foam. However, the tensile yield stress of the highest density rigid polyurethane foam is 65-75% of the compressive strength; no reason for this is apparent. Note that the model for the multiaxial plastic collapse of 3D cellular solids developed earlier assumes equal compressive and tensile strengths.

Finally, the experimental results suggest that the anisotropy in mechanical properties reflects that of the microstructure of the materials (Table 6.1): the stiffness and strength of the foams loaded parallel to the rise direction (X direction) is higher than that obtained for loading in the plane normal to this (Figs 6.5-6.12).

(b) Elastic Buckling Surface

The data obtained in this study for the elastic buckling surface of elastomeric materials under biaxial and axisymmetric loads are repeated in Fig. 6.35. The failure envelope for both stress states proposed by Zhang (1987) lies well outside of the data; the maximum difference between the model and the test results is about 50%. It appears that the data lie between Zhang's envelope and the nearly linear buckling envelope proposed by Gibson and Ashby (1988); the latter is based on the results obtained by Timoshenko and Gere (1961) from the elastic stability analysis of a rectangular frame subject to loads in two orthogonal directions. Additional data for the buckling surface for axisymmetric loading on flexible polyethylene are available from Zhang (1989); they are shown in Fig.

6.36. Here, the agreement is better but there is still a difference of about 25%. Moreover, Shercliff (1988) measured the uniaxial buckling stresses and the hydrostatic pressures required to cause buckling for five different flexible polyester foams ranging in relative density from 0.01 to 0.05. The ratio of the two was more or less constant with an average value 0.83, which is in a perfect agreement with Zhang's (1987) prediction. By normalizing the axes of Figs 6.35 and 6.36 with respect to the uniaxial strengths, all of the data for the buckling of foams can be combined; they are compared with the model of Zhang (1987) and of Gibson and Ashby (1988) in Fig. 6.37.

Zhang's (1987) elastic buckling surface is fully described when the uniaxial elastic buckling strengths of the foam are known. For elastomeric materials, these strengths can be measured by performing simple uniaxial compression tests. But for elastic-plastic or elastic-brittle foams, the uniaxial buckling strengths are higher than the corresponding plastic or brittle collapse stresses. In this case, the uniaxial elastic buckling strengths can be estimated by extrapolating the data associated with the buckling cutoff until they intercept the principal stress axes. This is illustrated in Figs 6.41 and 6.43; the data for the buckling cutoffs are used for the estimation of the uniaxial buckling strength in the X direction, and of the biaxial (with equal stresses) buckling strength in the Y-Z plane.

Because of the difficulty in estimating the mode of buckling, this is the least well understood failure mode. The biaxial compression tests on rubber honeycomb models revealed two elastic buckling modes. The modeling and data for both modes indicate that the mode can have a significant effect on the elastic buckling surface (see Fig. 6.4). These observations suggest that the mode of buckling for foams may be different from that assumed in the analysis by Zhang (1987) and may itself depend on stress state; that may explain the discrepancy between the model and test results.

(c) Plastic Yield Surface

The plastic yield surface (eqn. (4.21)) was characterized in this study by biaxial and axisymmetric tests on closed-cell rigid polyurethane and open-cell aluminum foams.

Note that the failure surface is completely described by four material parameters: the uniaxial compressive strengths parallel to the three principal material directions and the relative density ratio.

The data for biaxial stress states follow the roughly elliptical yield envelope given by the model developed here (see Fig. 6.38). No interaction between failure modes was observed. In the compression-compression and tension-tension quadrants, the failure envelopes can be approximated by box-like envelopes corresponding to a maximum principal stress failure criterion. However, the data clearly indicate that a maximum principal stress criterion is invalid for combined compression-tension. The biaxial test results of Shaw and Sata (1966) and Patel (1969) are compared with the model in Fig. 6.39. In the compression-compression quadrant there is good agreement with the roughly elliptical yield envelope developed in Chapter 4; the maximum difference between our failure criterion and the maximum principal stress criterion is approximately 10%. In the tension-tension quadrant, the maximum principal stress fracture criterion holds. In the compression-tension quadrants, however, there is some discrepancy between Patel's limited data and the model suggested here. The discrepancy for the two data points corresponding to fracture (Fig. 6.39b, open symbols) may be due to the different definitions of failure used by Patel and in this thesis: Patel has taken final fracture as the failure point in tension, while we have used the initial yield point to define failure of the material. Our definition aims to characterize yielding failure of materials.

All of the plastic yield biaxial data from our tests and from Shaw and Sata (1966) and Patel (1969) are combined in Fig. 6.40 by normalizing the axes with respect to the uniaxial plastic collapse stresses. In general, the agreement is good with the exceptions of two data points obtained by Patel (1969) and of the data points in the tension-tension quadrant associated with materials which are characterized by different uniaxial strengths in tension and compression. Figure 6.40 confirms that the maximum principal stress criterion for the failure of elastic-plastic foams under biaxial loads is inadequate; it is in good agreement with both the data and our model only when the applied stresses are of the same sign.

The plastic collapse criterion developed in this study assumes that the materials

have equal strengths in both tension and compression. While this is typically the case in open-cell cellular materials, it is not so in closed cell materials, even if they show open-cell behavior. To account for a possible difference in the two strengths, the failure criterion (eqns (4.21), (4.23)) could be modified by normalizing the stresses with the average value of the two uniaxial strengths, instead of the uniaxial compressive strength. This modification would give a better agreement between the theoretical failure envelope and the data shown in Fig. 6.38. Alternatively, the normalization should be done with respect to the lowest or the highest of the two strengths in each direction when conservative or unconservative predictions of the material's strength are of interest, correspondingly. The first is typically the case in the design of structural sandwich panels and the second in packaging applications.

The results of the axisymmetric load tests on the rigid polyurethane and aluminum foams were shown in Figs 6.26-6.28 and 6.30; they are summarized in Fig. 6.41. The data for the rigid polyurethane loaded in radial compression are well described by the model for yielding. As expected, the yield envelope is truncated by elastic buckling in the compressive octant. The data follow Zhang's (1987) elastic buckling cutoff fairly closely, although the model overpredicts the elastic buckling stress for hydrostatic compression. As the density of the material increases, the intercept of the elastic buckling envelope on the axial stress axis is shifted away from that of the yield surface, confirming the fact that the dependence on density of the uniaxial buckling stress is stronger than that of the uniaxial plastic collapse strength. Tha data for tha aluminum foam loaded in radial tension are also well described by the model with the exception of one data point at the highest radial stress; this point represents failure at an axial stress of about 20% below that predicted by the model.

All of the data for axisymmetric loading are combined in Fig. 6.42 using normalized axes. Note that there is some variation in the yield envelopes for the different material densities: as the relative density ratio decreases, the failure envelope becomes increasingly elongated. Figure 6.42 also illustrates the buckling cutoff in the compressive octant. In general, the agreement between the data and the model is good. Figures 6.41 and 6.42 clearly show that the maximum principal stress criterion for the

plastic collapse of foams is not valid.

(d) Brittle Failure Surface

The brittle failure surface (eqn. (4.41)) was characterized by biaxial and axisymmetric tests on open-cell reticulated vitreous carbon foam; the data are repeated in Fig. 6.43. A larger scatter than for the other foams tested was observed in the tests with the reticulated vitreous carbon. This was due to the susceptibility of the crushing or the fracture strength of brittle materials to the microcracks inherent in their microstructure. The biaxial data are well described by the model for failure by tensile rupture of the bent cell walls. The axisymmetric data are well described by the same model truncated by elastic buckling in the compressive octant and by brittle fracture in the tensile octant. The model is completely defined by five parameters: the uniaxial compressive strengths of the foam parallel to the three principal material directions, the relative density ratio, and the ratio of the modulus of rupture of the cell wall material to its tensile strength. Although the scatter in the results is considerable, the overall agreement between the data and the model is good. The maximum principal stress criterion does not describe the data well; it approximates the behavior for biaxial compression-compression, and it is satisfactory in predicting the tensile cutoff shown in Fig. 6.43b.

6.6 Summary and Conclusions

In this chapter we have presented the experimental results obtained for the failure of 2D cellular materials by elastic buckling, and 3D cellular materials by elastic buckling, plastic yielding, and brittle collapse. The results indicate that the models obtained earlier in Chapters 3 and 4 describe the main features of failure under multiaxial stress states well. They support the fact that the most difficult feature to model accurately is the mode of buckling in elastomeric foams; the data indicate that the buckling surface is approximately described by a spherical surface in the compressive octant in stress space. The results confirm that the maximum principal stress criterion proposed in earlier papers (Shaw and Sata, 1966; Patel and Finnie, 1969; Zaslawsky, 1973) is inadequate although,

for plastic and brittle foams loaded biaxially, it approximates the observed behavior when the stresses are of the same sign. The models developed in this study give a better description of the data and are more general in the sense that they are valid under general stress states, they account for material anisotropy, and they describe all three failure modes observed in cellular materials: elastic buckling, plastic yielding, and brittle fracture. Finally, it must be emphasized that the models presented in this work were fully developed on a sound theoretical basis; no attempt was made here to fit models in test results.

References

Broek, D. (1986) *Elementary Engineering Fracture Mechanics*, 4th edn., Martinus Nijhoff Publishers, Dordrecht.

Gibson, L. J. and Ashby, M. F. (1982) The Mechanics of Three-Dimensional Cellular Materials, *Proc. Roy. Soc.*, **A382**, 43.

Gibson, L. J. and Ashby, M. F. (1988) *Cellular Solids: Structure and Properties*, Pergamon, Oxford.

Huber, A. T. (1987) Anisotropy in Cellular Materials, S.M. Thesis, Civil Engineering Department, Massachusetts Institute of Technology, Cambridge.

Huber, A. T. and Gibson, L. J. (1988) Anisotropy of Foams, *J. Mater. Sci.*, **23**, 3031.

Patel, M. R. (1969) The Deformation and Fracture of Rigid Cellular Plastics Under Multiaxial Stress, Ph.D. Thesis, University of California at Berkeley, U.S.A.

Patel, M. R. and Finnie, I. (1970) Structural Features and Mechanical Properties of Rigid Cellular Plastics, *J. Materials*, **5**, 909.

Shaw, M. C. and Sata, T. (1966) The Plastic Behavior of Cellular Materials, *Int. J. Mech. Sci.*, **8**, 469.

Shercliff, T. (1988) Response of Cellular Solids to Multiaxial Loading, Cambridge University Engineering Department Report, Cambridge, U.K.

Timoshenko, S. P. and Gere, J. M. (1961) *Theory of Elastic Stability*, 2nd edn., McGraw-Hill.

Zaslawsky, M. (1973) Multiaxial-Stress Studies on Rigid Polyurethane Foam, *Exp. Mech.*, **2**, 70.

Zhang, J. (1987) Mechanics of Cellular Materials, CPGS Thesis, Cambridge University Engineering Department, Cambridge, U.K.

Zhang, J. (1989) Ph.D. Thesis, Cambridge University Engineering Department, Cambridge, U.K.

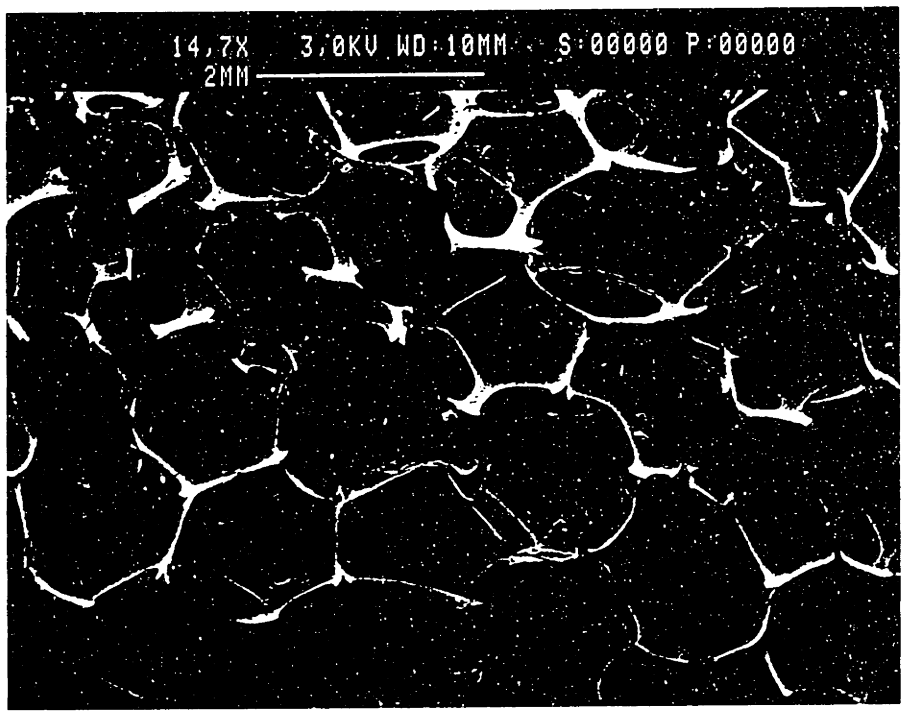

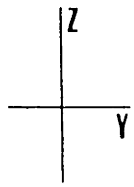

(a)

Fig. 6.1 Micrographs showing the microstructure of the materials tested: (a) open-cell flexible polyurethane, ρ^*=28 kg/m^3; (b) and (c) closed-cell rigid polyurethane, ρ^*=64 kg/m^3; (d) and (e) closed-cell rigid polyurethane, ρ^*=96 kg/m^3; (f) and (g) closed-cell rigid polyurethane, ρ^*=192 kg/m^3; (h) and (i) open-cell aluminum, ρ^*=135 kg/m^3; (j) and (k) open-cell reticulated vitreous carbon, ρ^*=48 kg/m^3. The material principal directions are marked next to the micrographs; X is the rise direction.

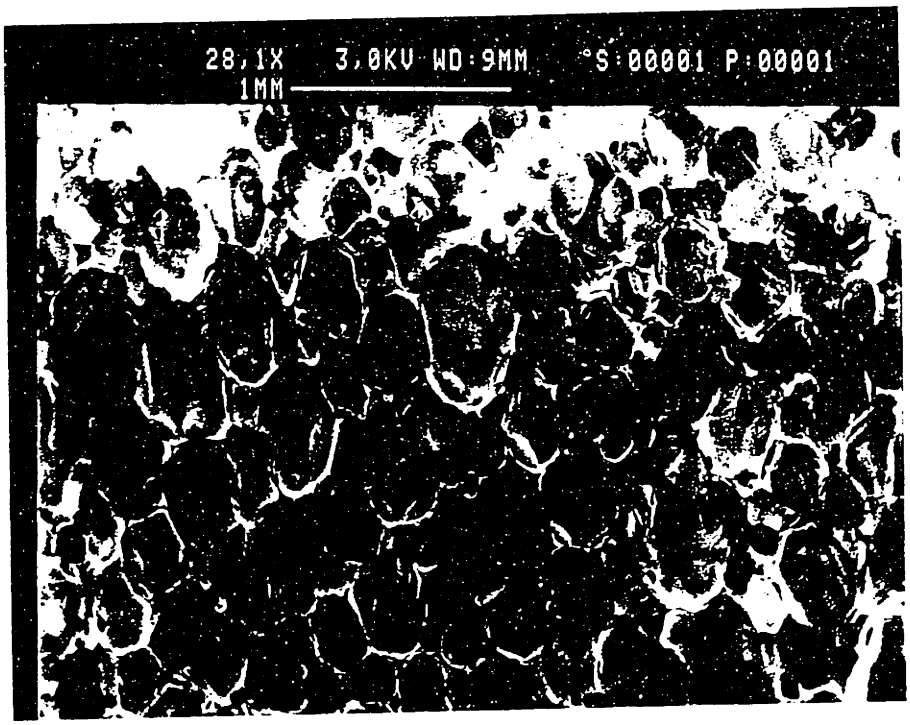

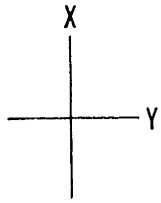

(b)

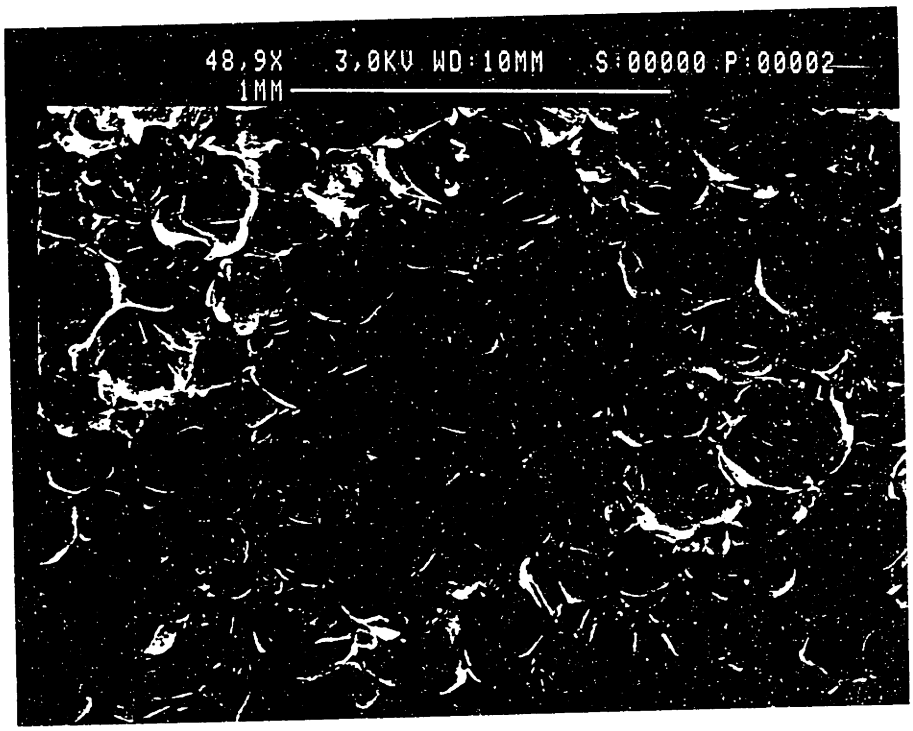

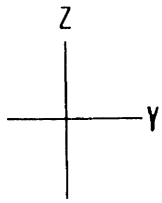

(c)

Fig. 6.1 cont'd.

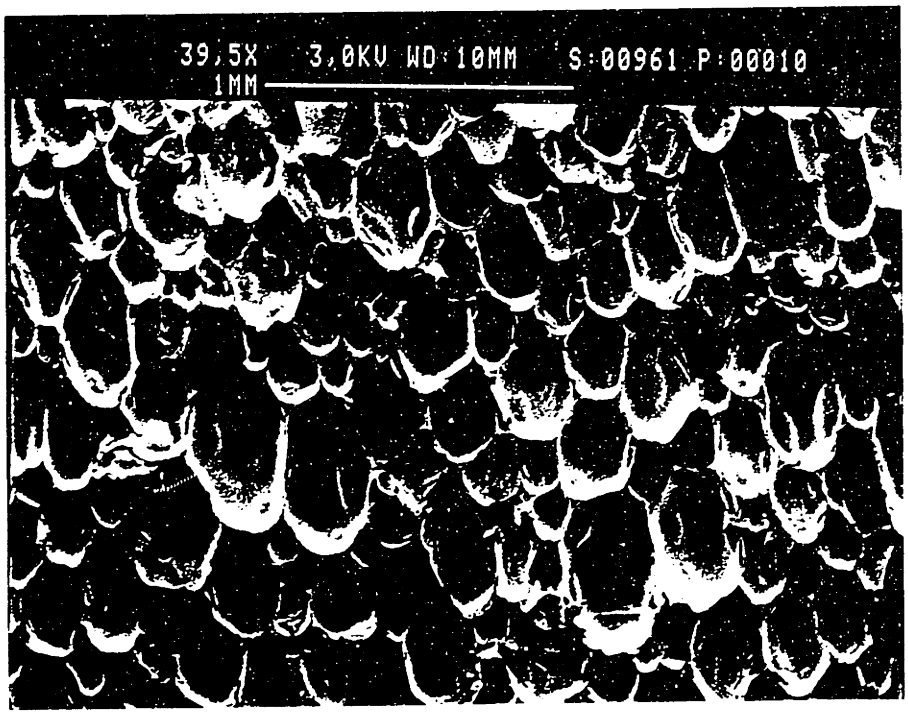

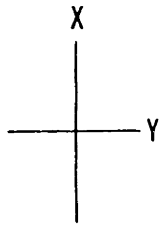

(d)

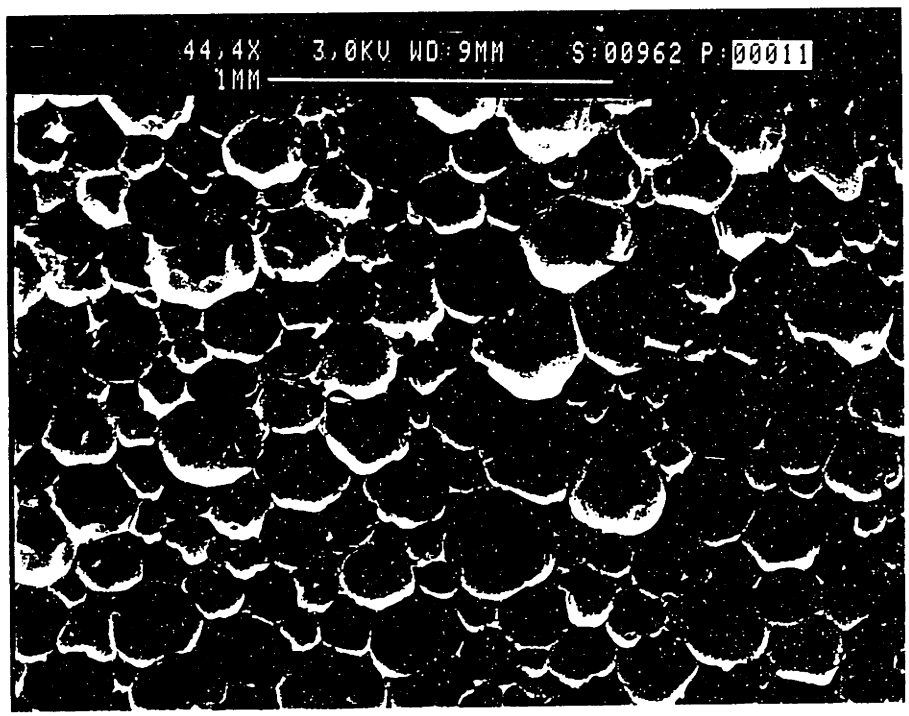

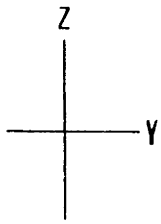

(e)

Fig. 6.1 cont'd.

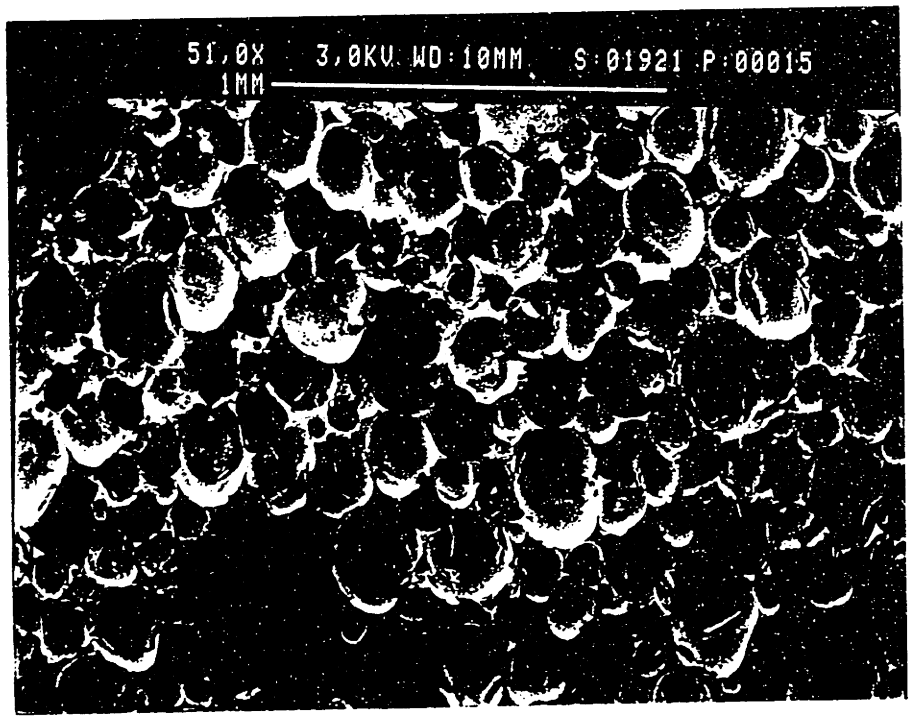

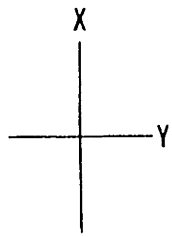

(f)

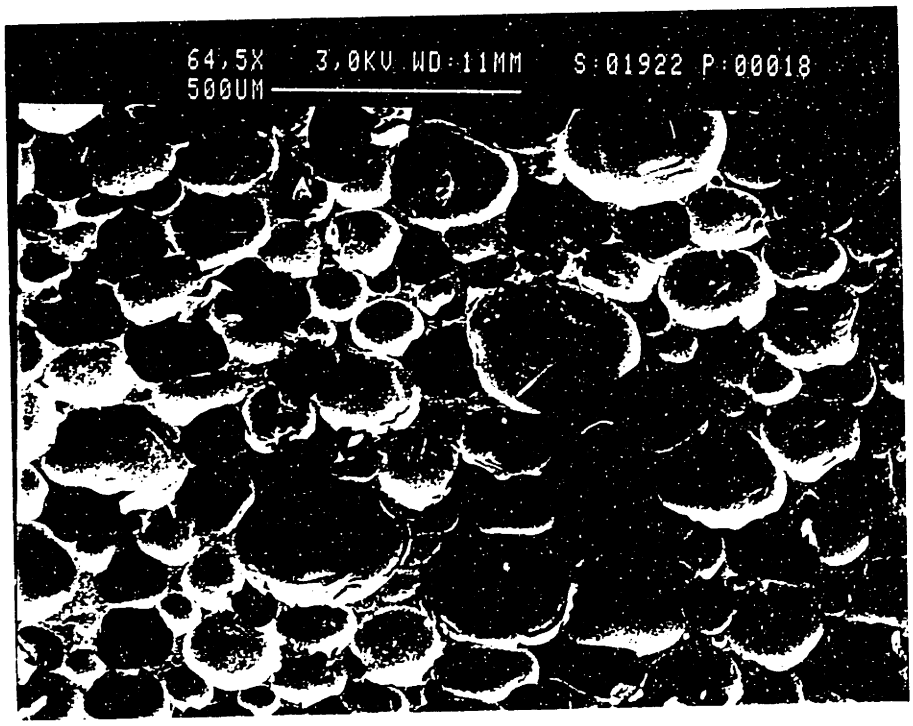

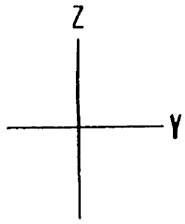

(g)

Fig. 6.1 cont'd.

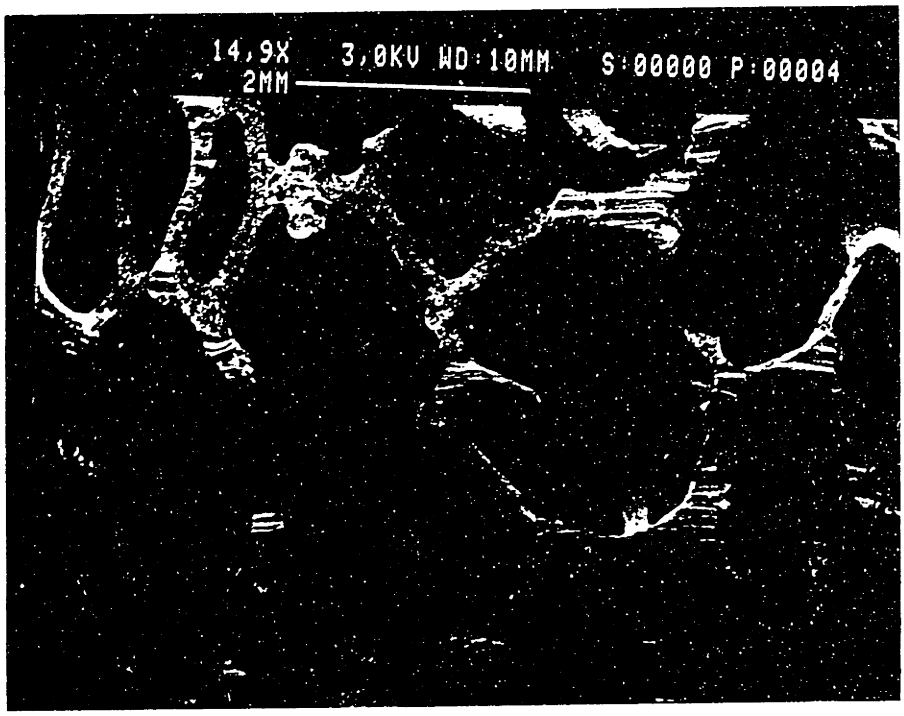

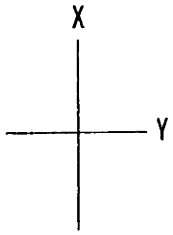

(h)

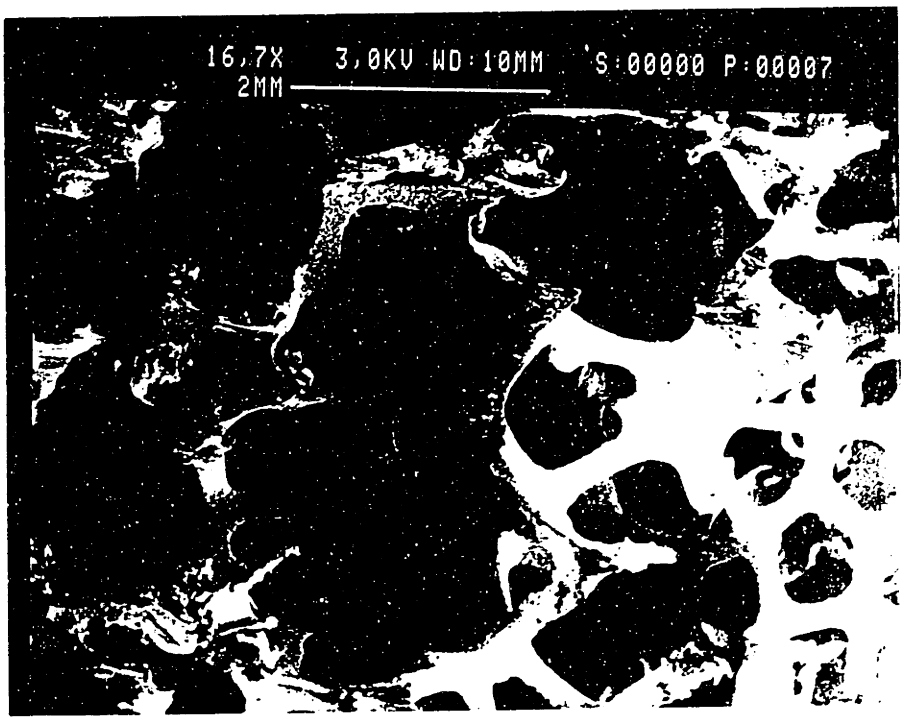

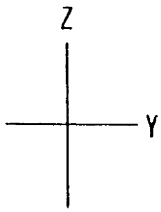

(i)

Fig. 6.1 cont'd.

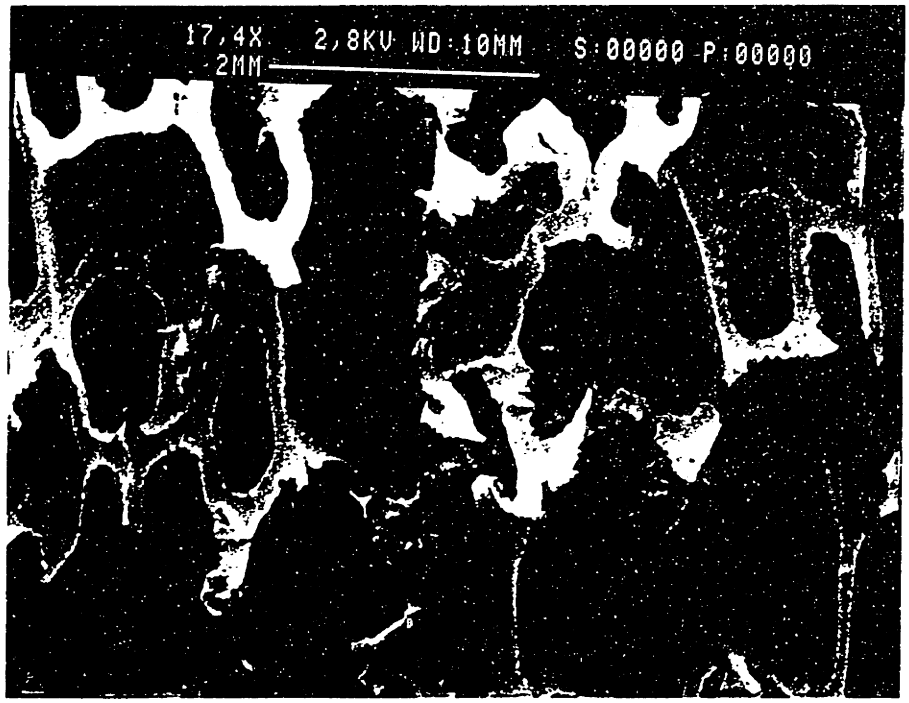

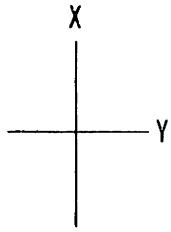

(j)

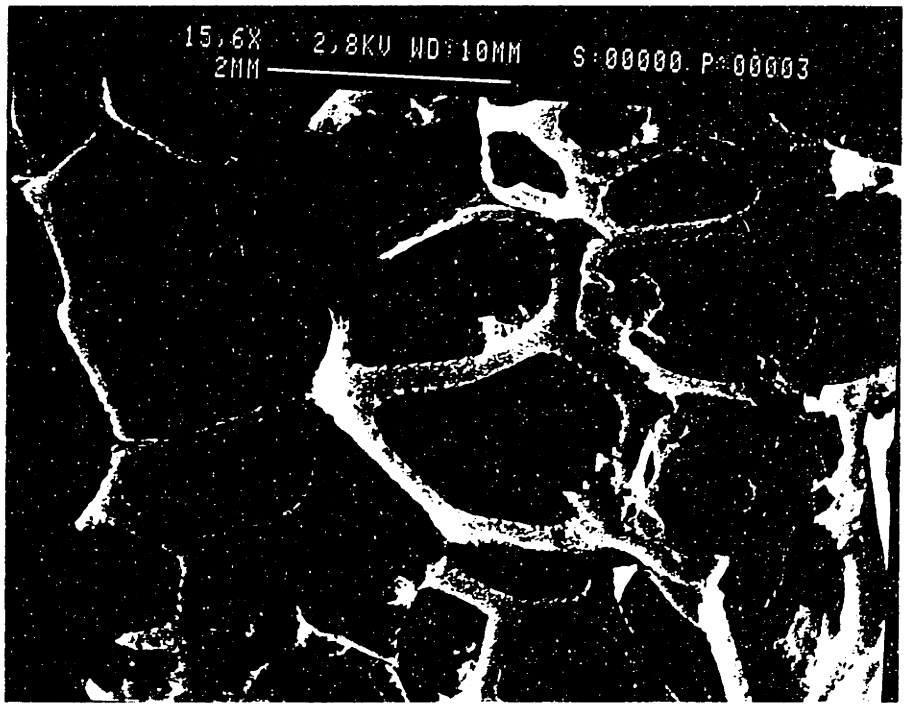

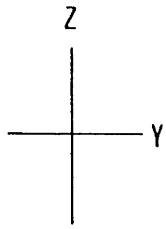

(k)

Fig. 6.1 cont'd.

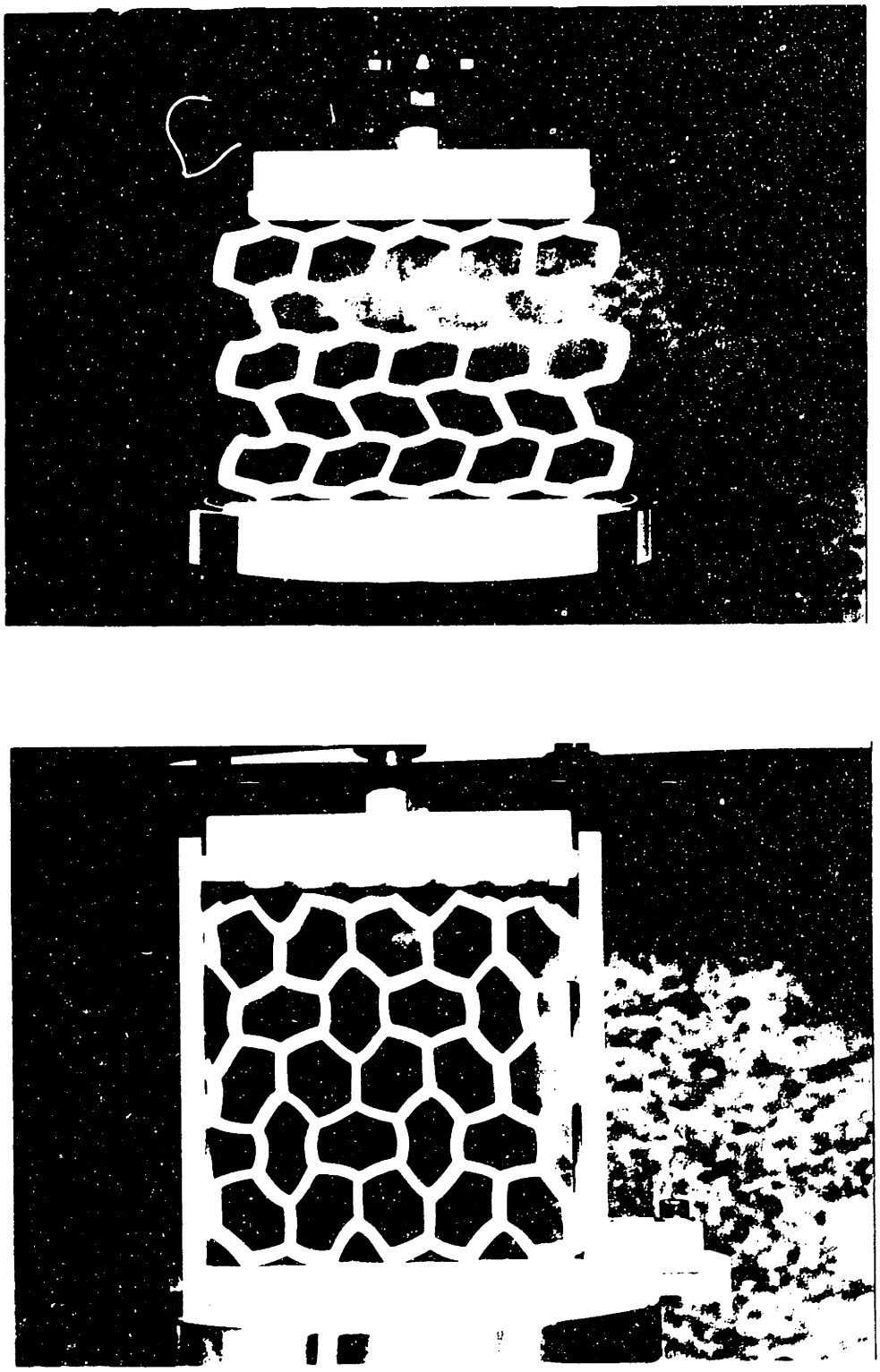

Fig. 6.2 Elastic buckling of flexible honeycomb structures. (a) Mode 1. (b) Mode 2.

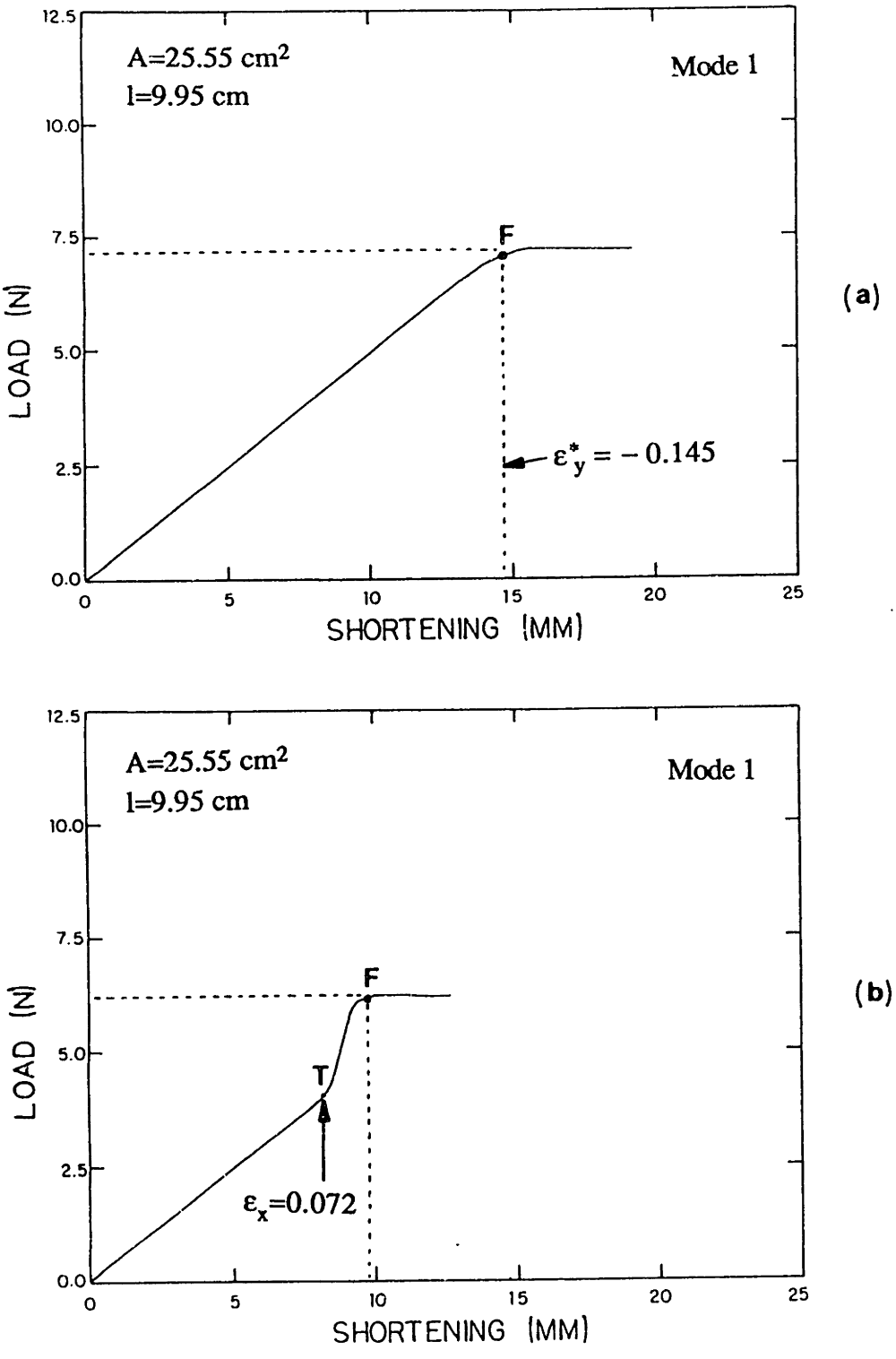

Fig. 6.3 Typical load-deflection curves for elastomeric honeycombs. (a) Uniaxial loading parallel to the Y direction. (b), (c), and (d) Biaxial loading.

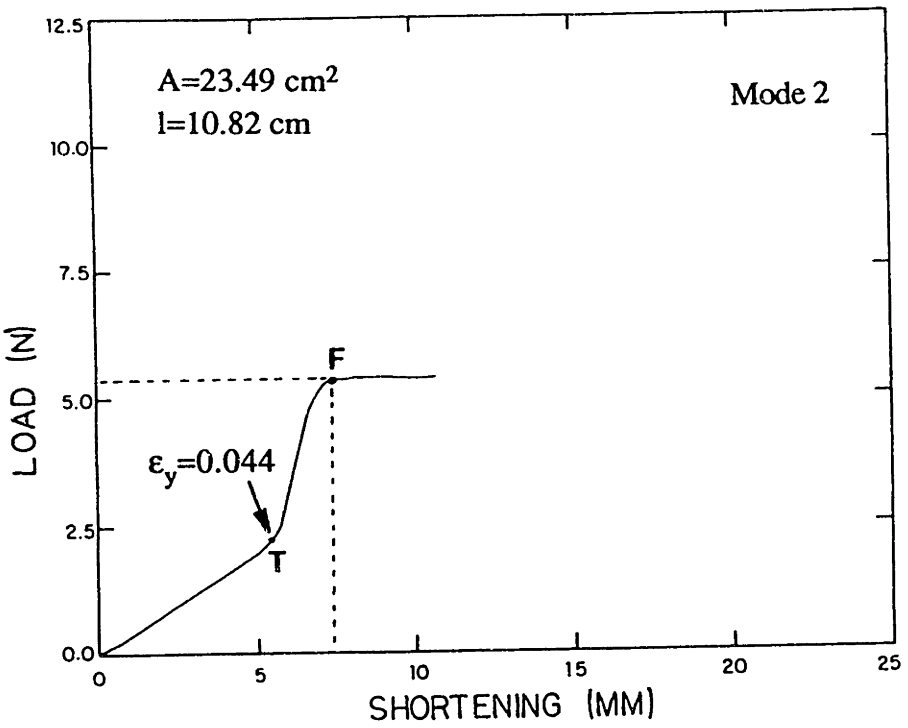

(c)

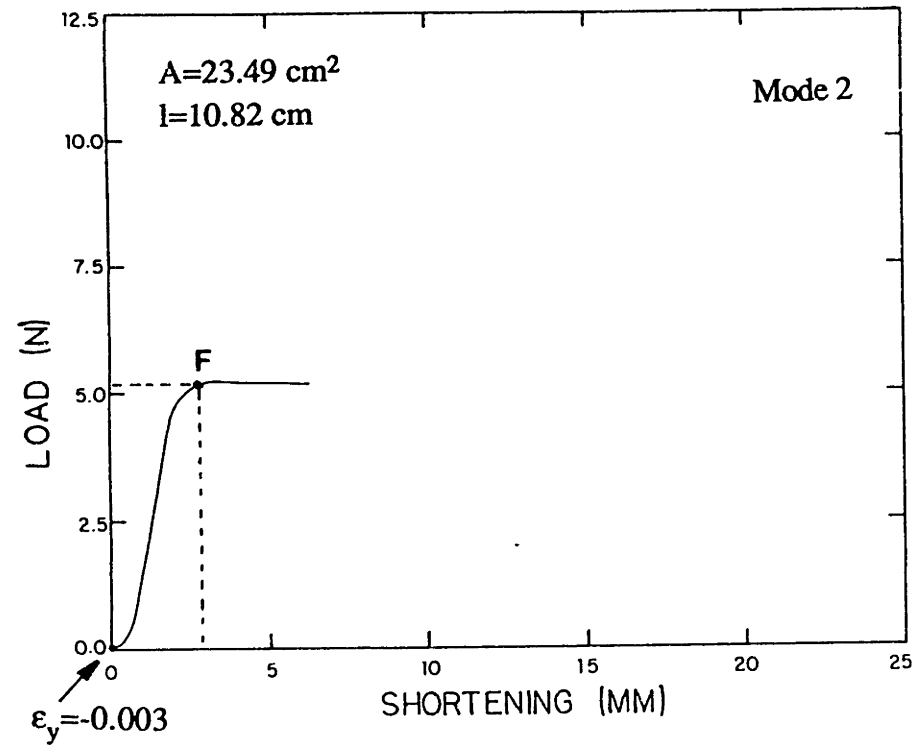

(d)

Fig. 6.3 cont'd.

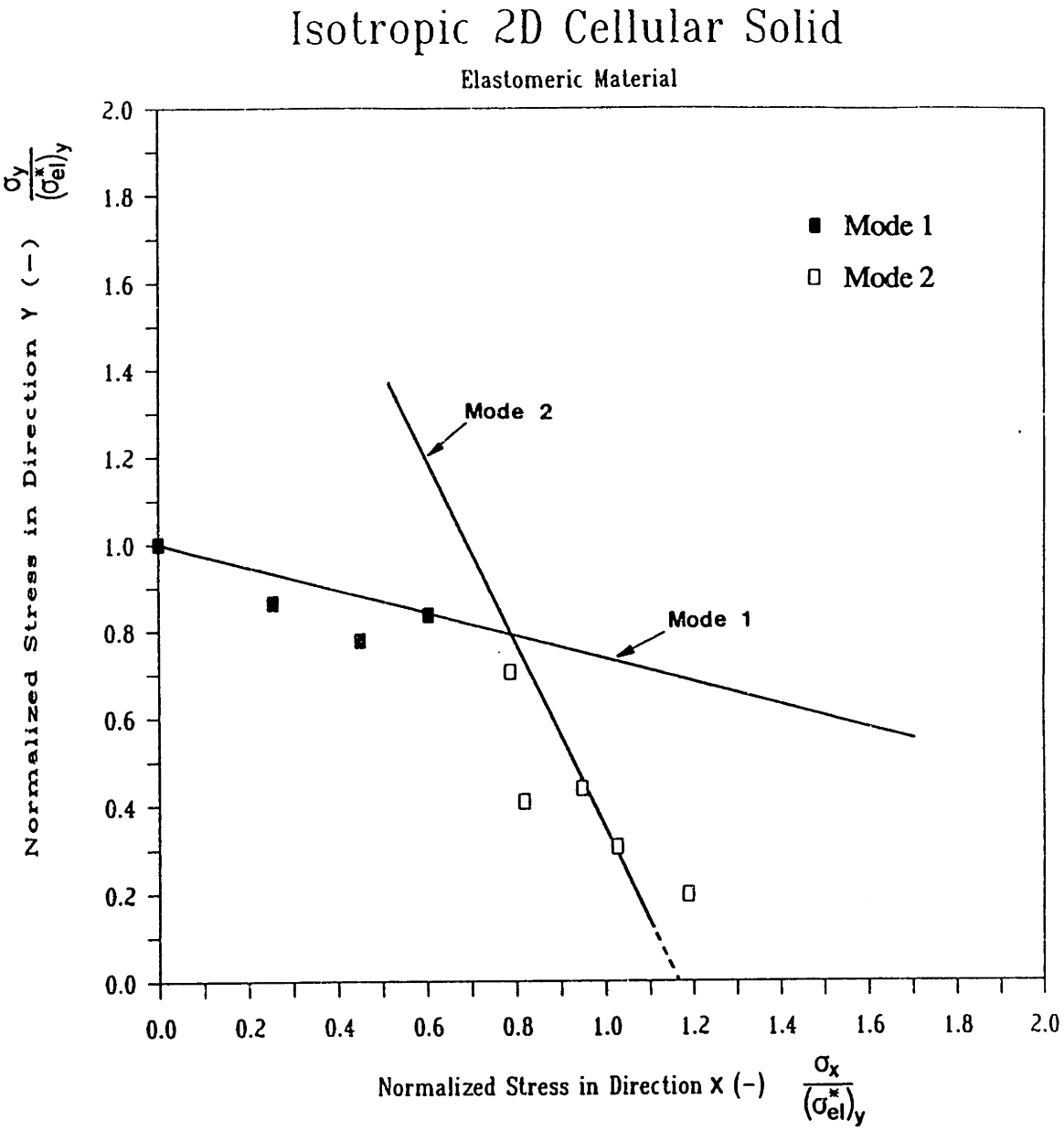

Fig. 6.4 The experimental results for the biaxial elastic buckling of isotropic honeycombs; the solid lines correspond to the analytical predictions.

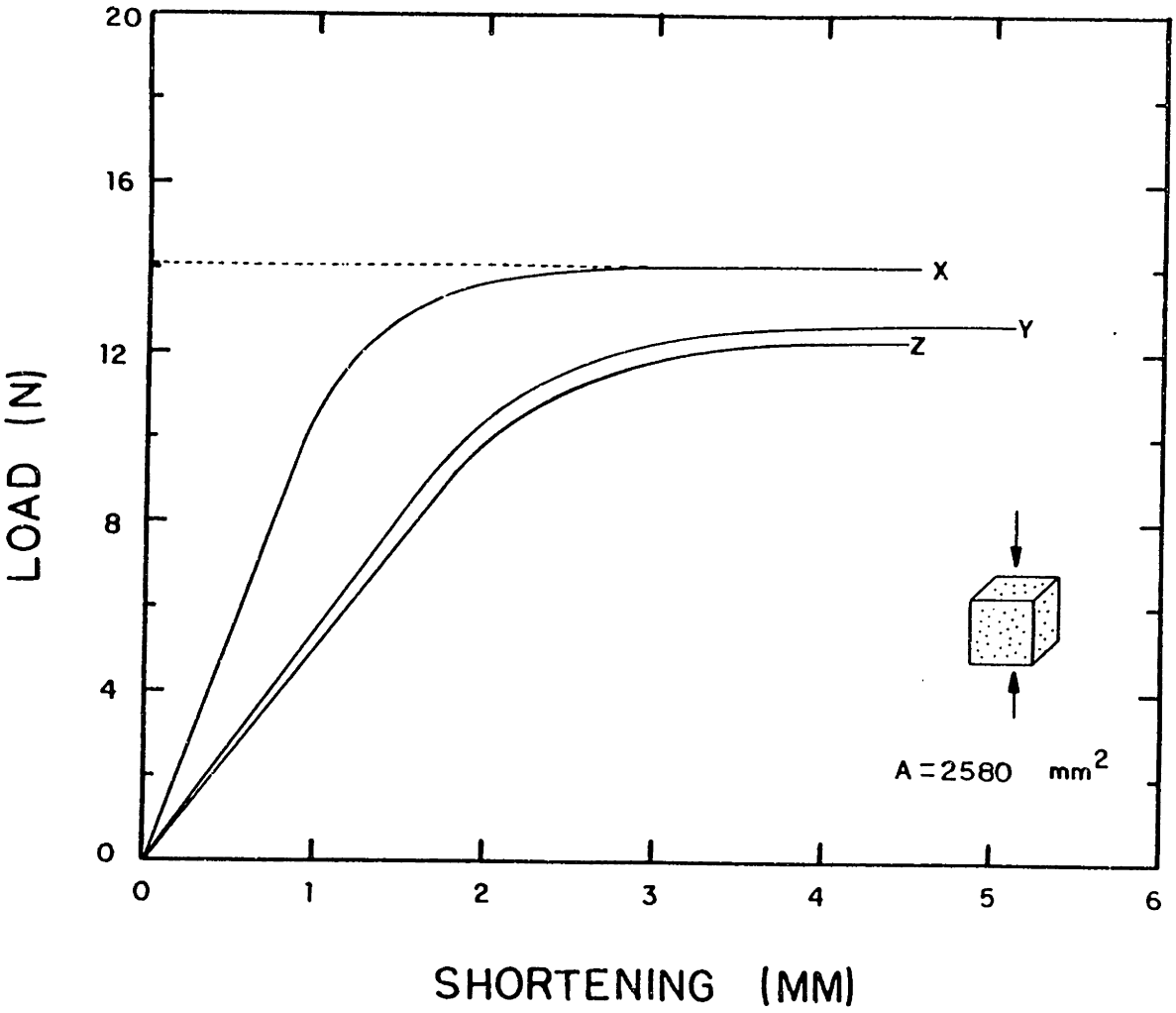

Fig. 6.5 Typical uniaxial compression results for flexible polyurethane loaded parallel to the three principal material directions.

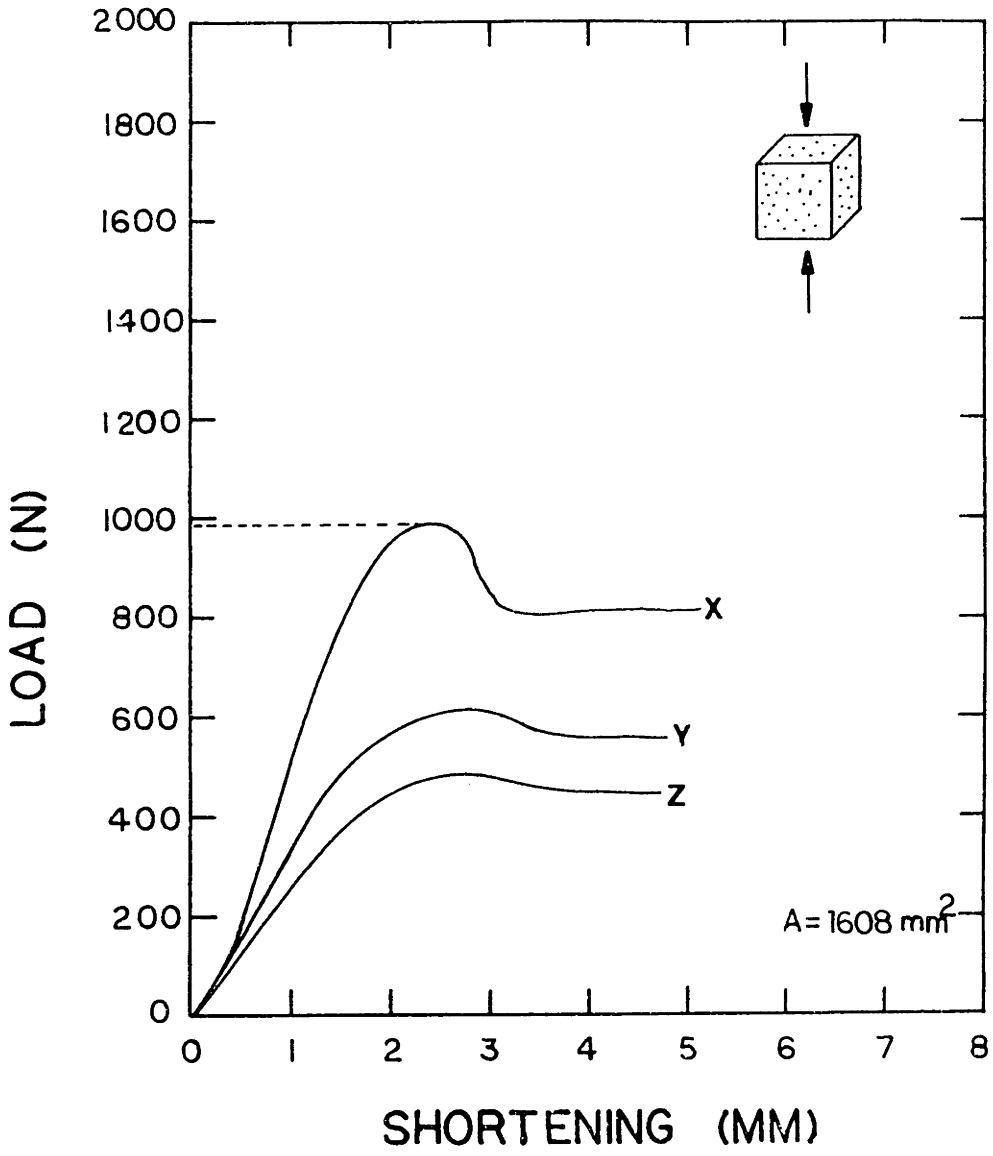

Fig. 6.6 Typical uniaxial compression results for rigid polyurethane loaded parallel to the three principal material directions. (a) ρ^*=64 kg/m^3; (b) ρ^*=96 kg/m^3; (c) ρ^*=192 kg/m^3.

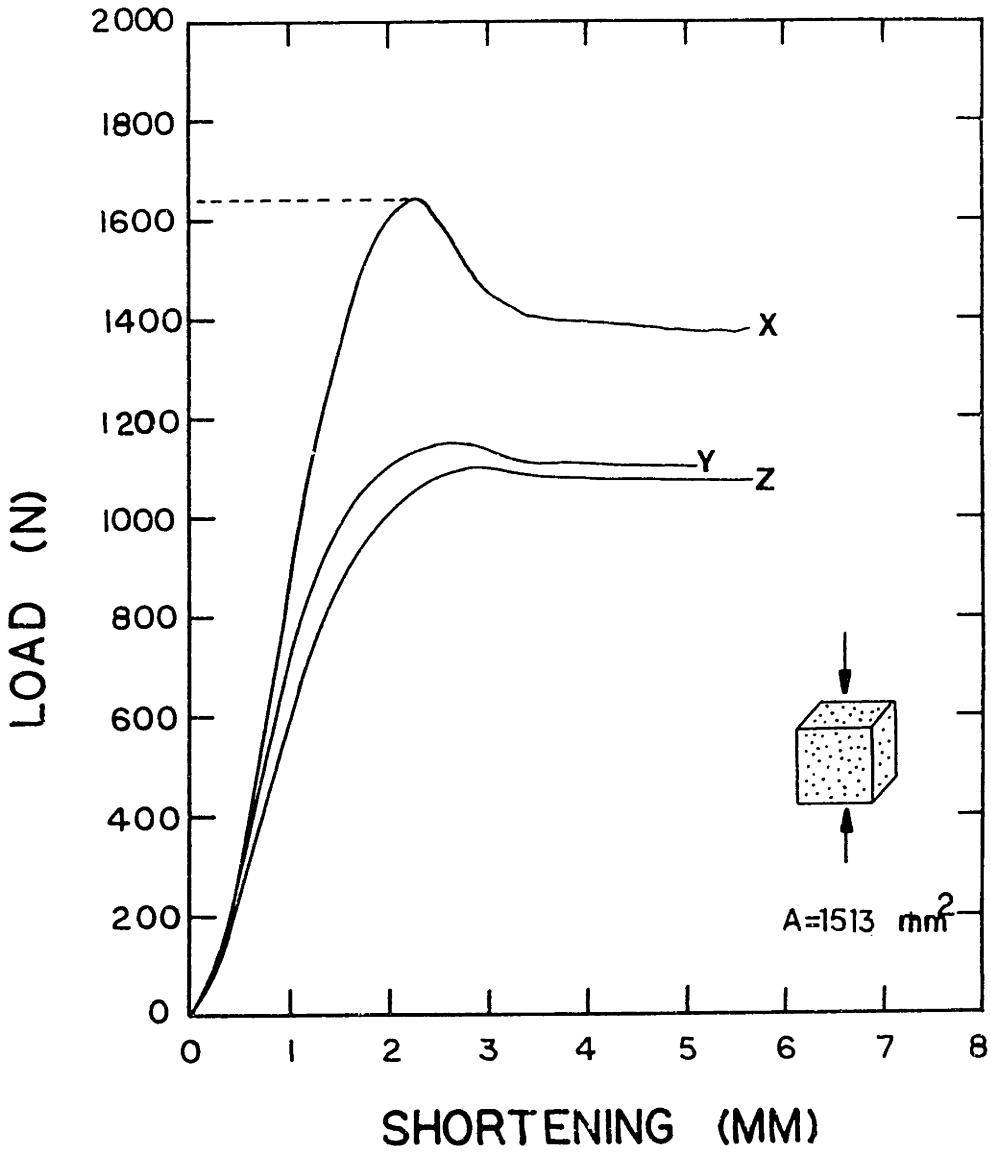

(b)

Fig. 6.6 cont'd.

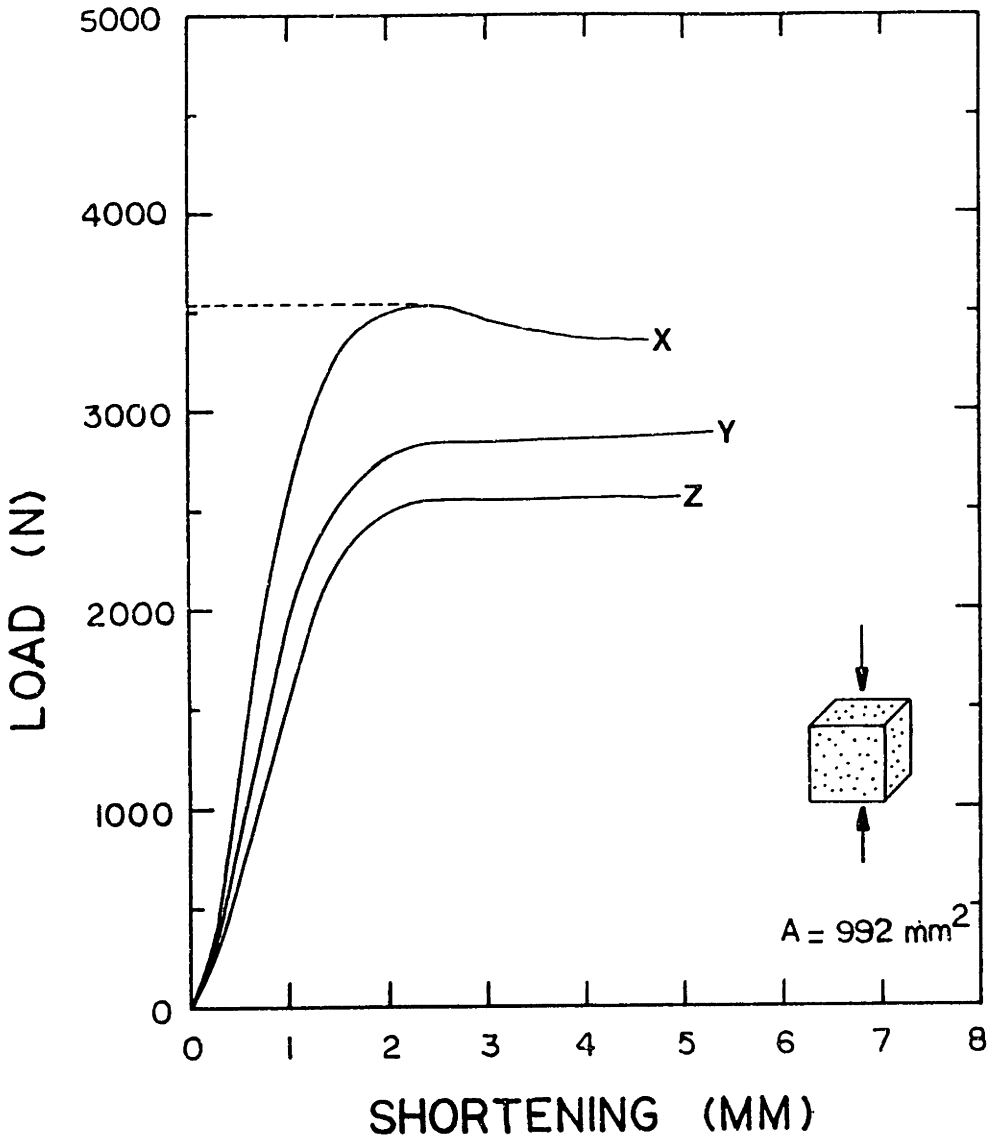

(c)

Fig. 6.6 cont'd.

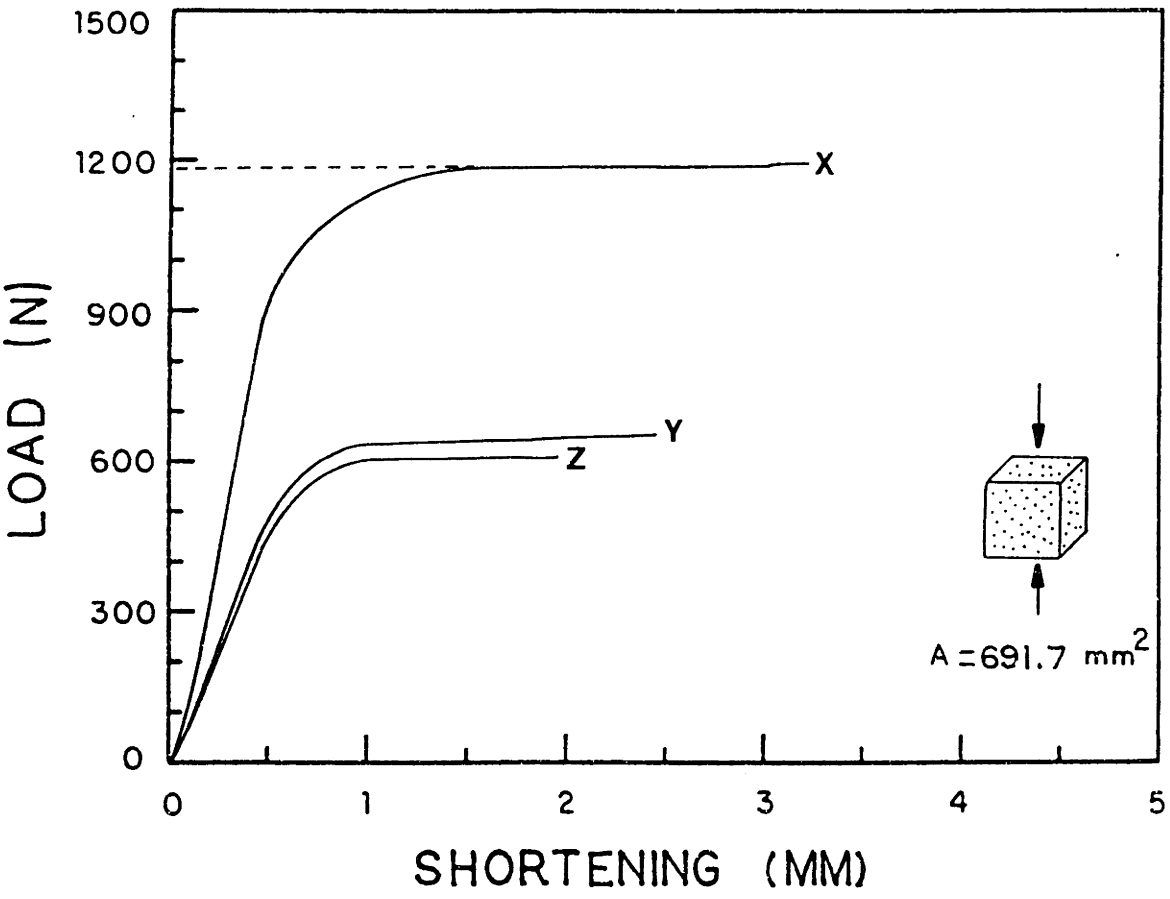

Fig. 6.7 Typical uniaxial compression results for aluminum foam loaded parallel to the three principal material directions.

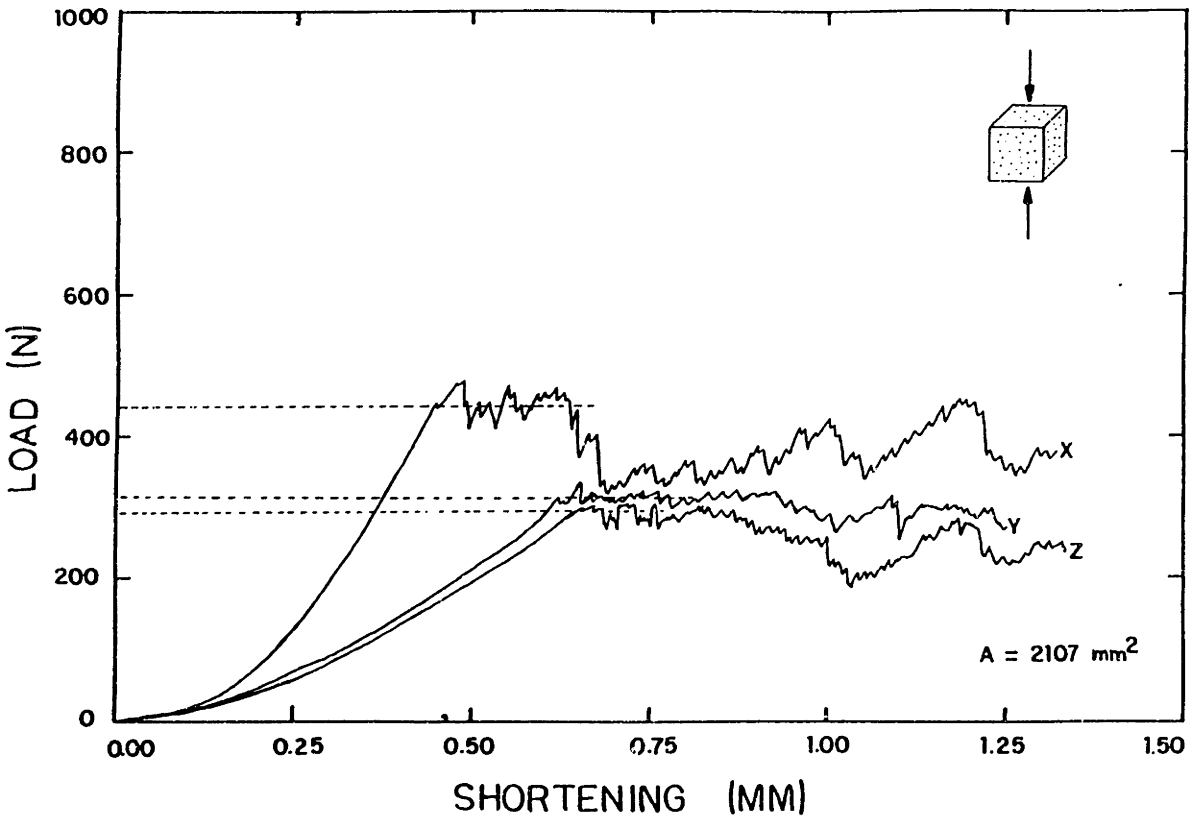

Fig. 6.8 Typical uniaxial compression results for reticulated vitreous carbon loaded parallel to the three principal material directions.

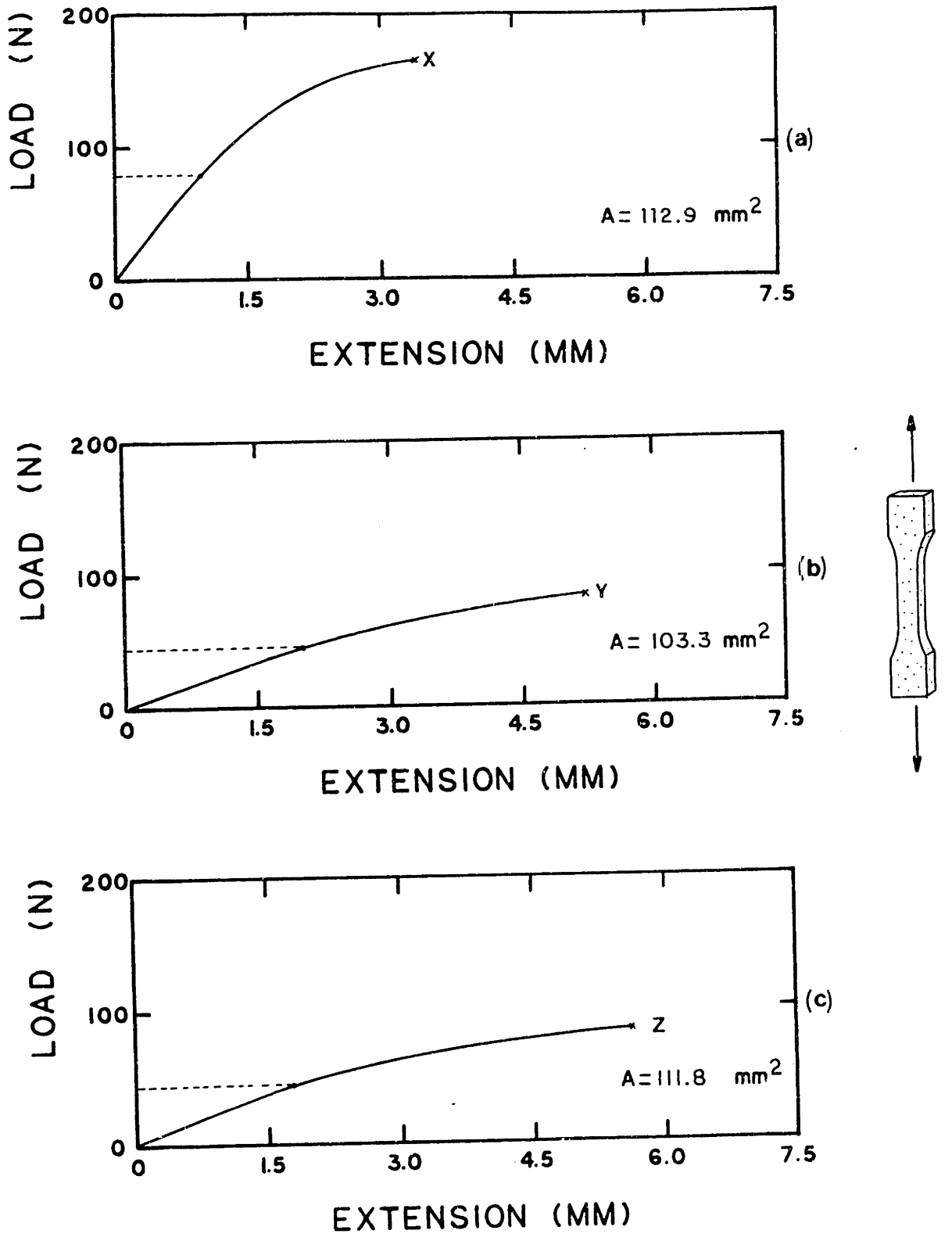

Fig. 6.9 Typical uniaxial tension curves for rigid polyurethane foam, ρ^*=64 kg/m^3; loading is parallel to the material directions (a) X, (b) Y, and (c) Z.

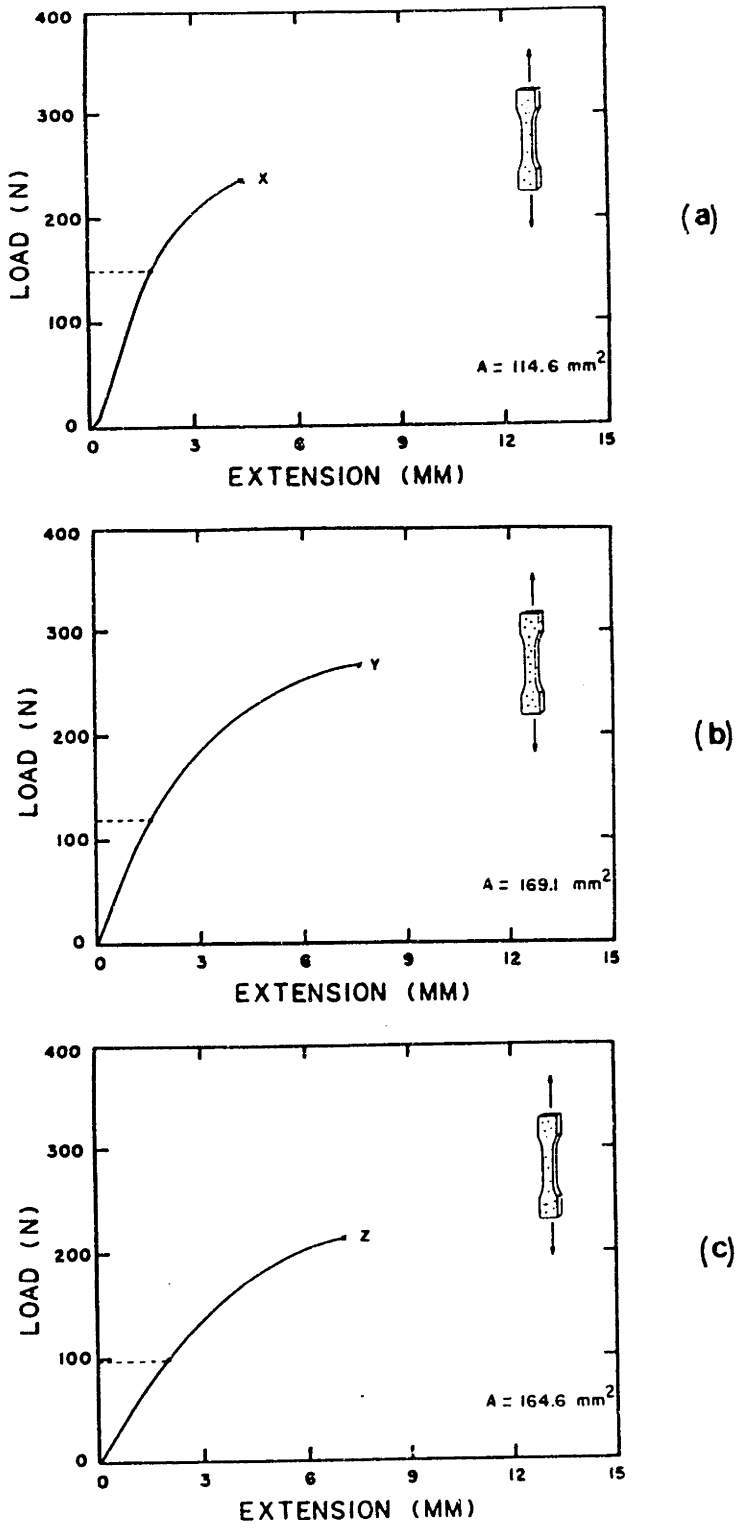

Fig. 6.10 Typical uniaxial tension curves for rigid polyurethane foam, ρ^*=96 kg/m^3; loading is parallel to the material directions (a) X, (b) Y, and (c) Z.

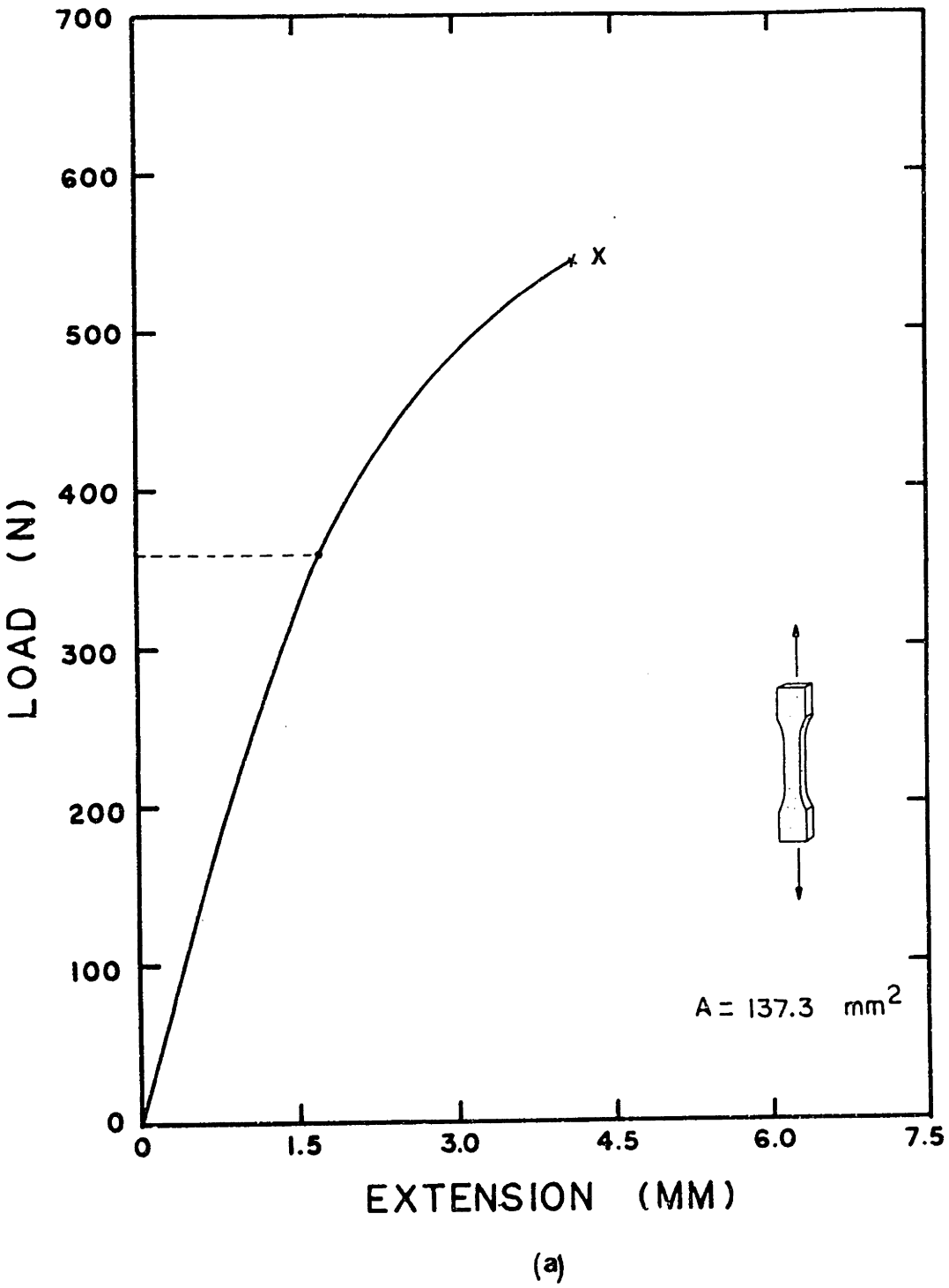

Fig. 6.11 Typical uniaxial tension curves for rigid polyurethane foam, ρ^*=192 kg/m^3; loading is parallel to the material directions (a) X, (b) Y, and (c) Z.

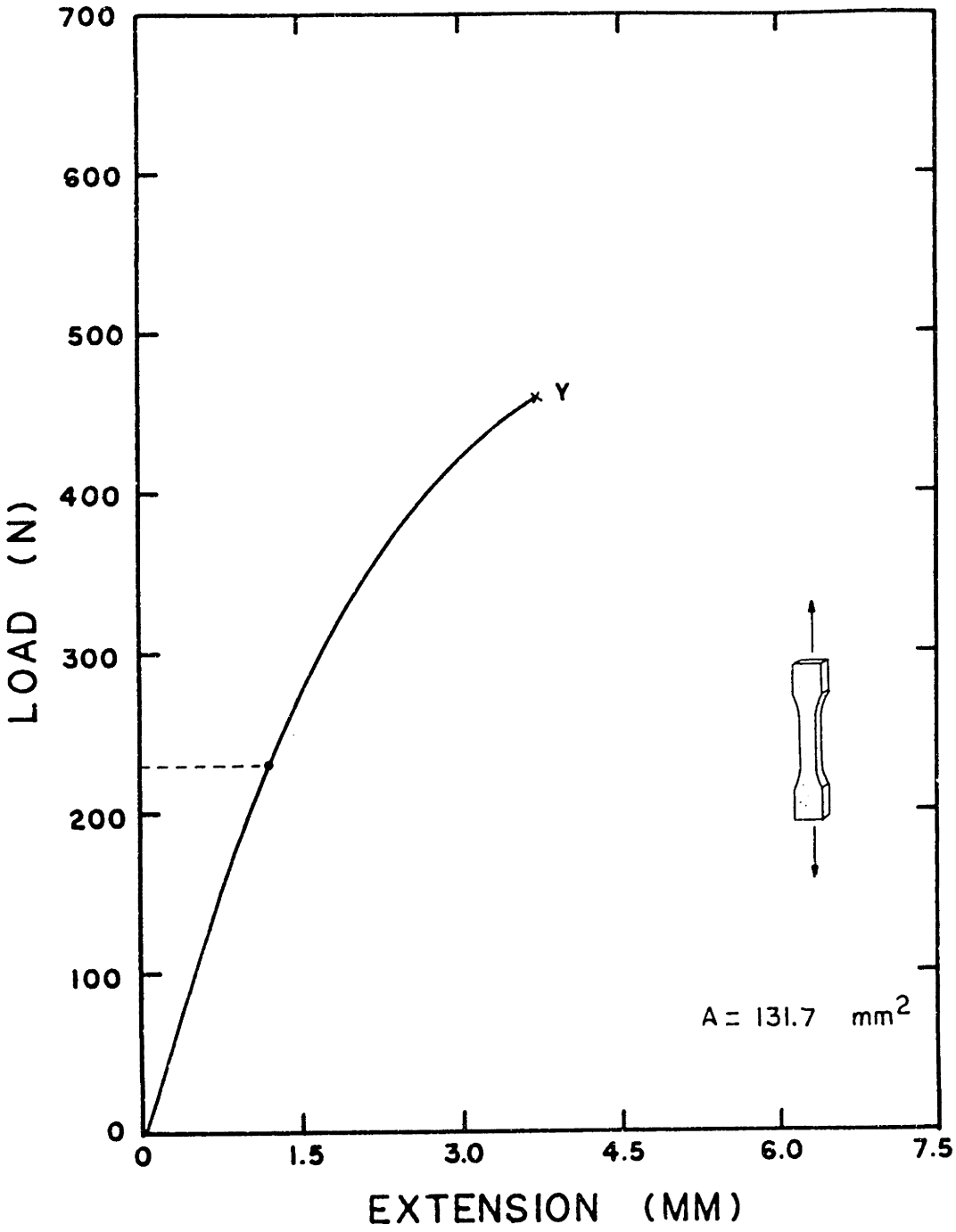

(b)

Fig. 6.11 cont'd.

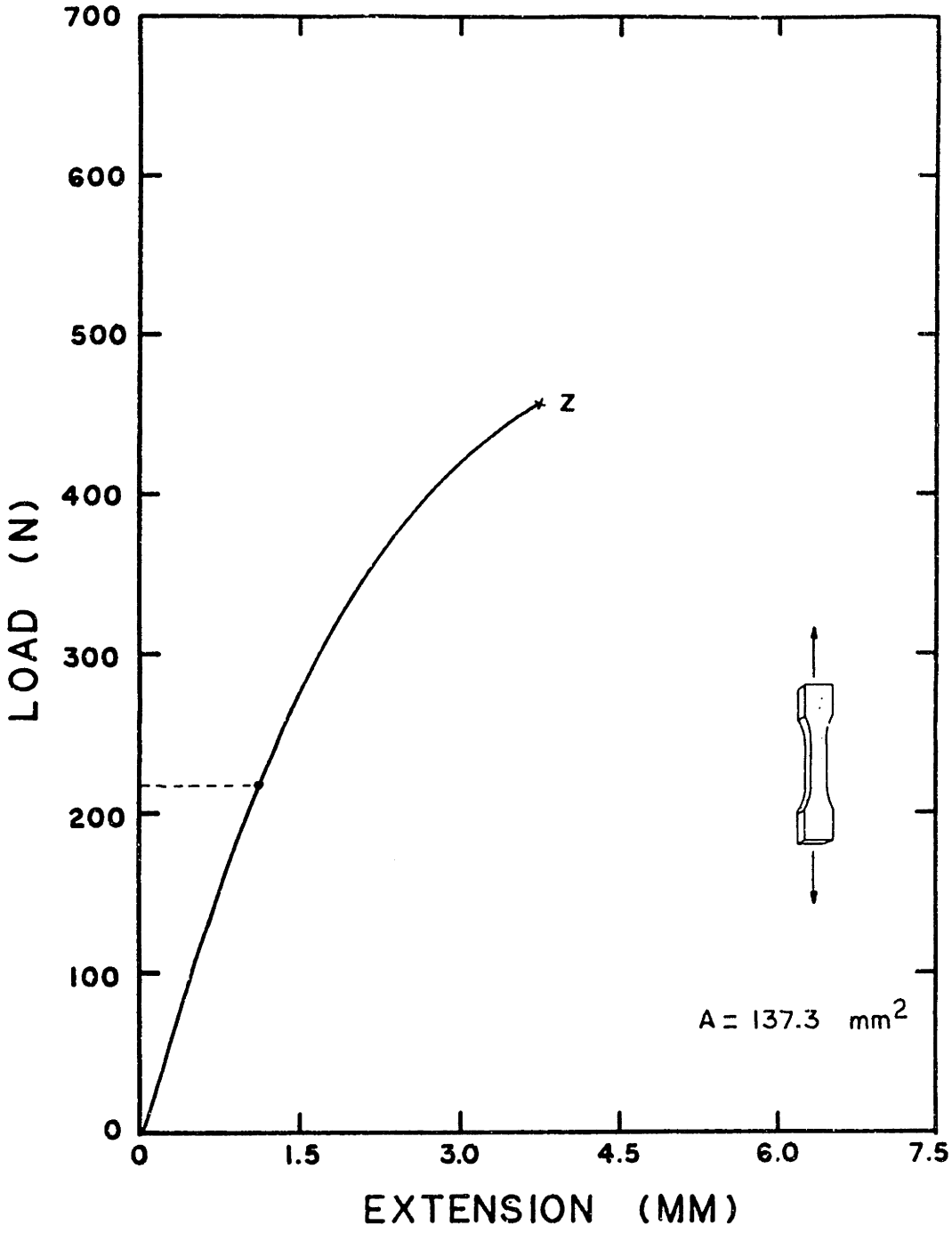

(c)

Fig. 6.11 cont'd.

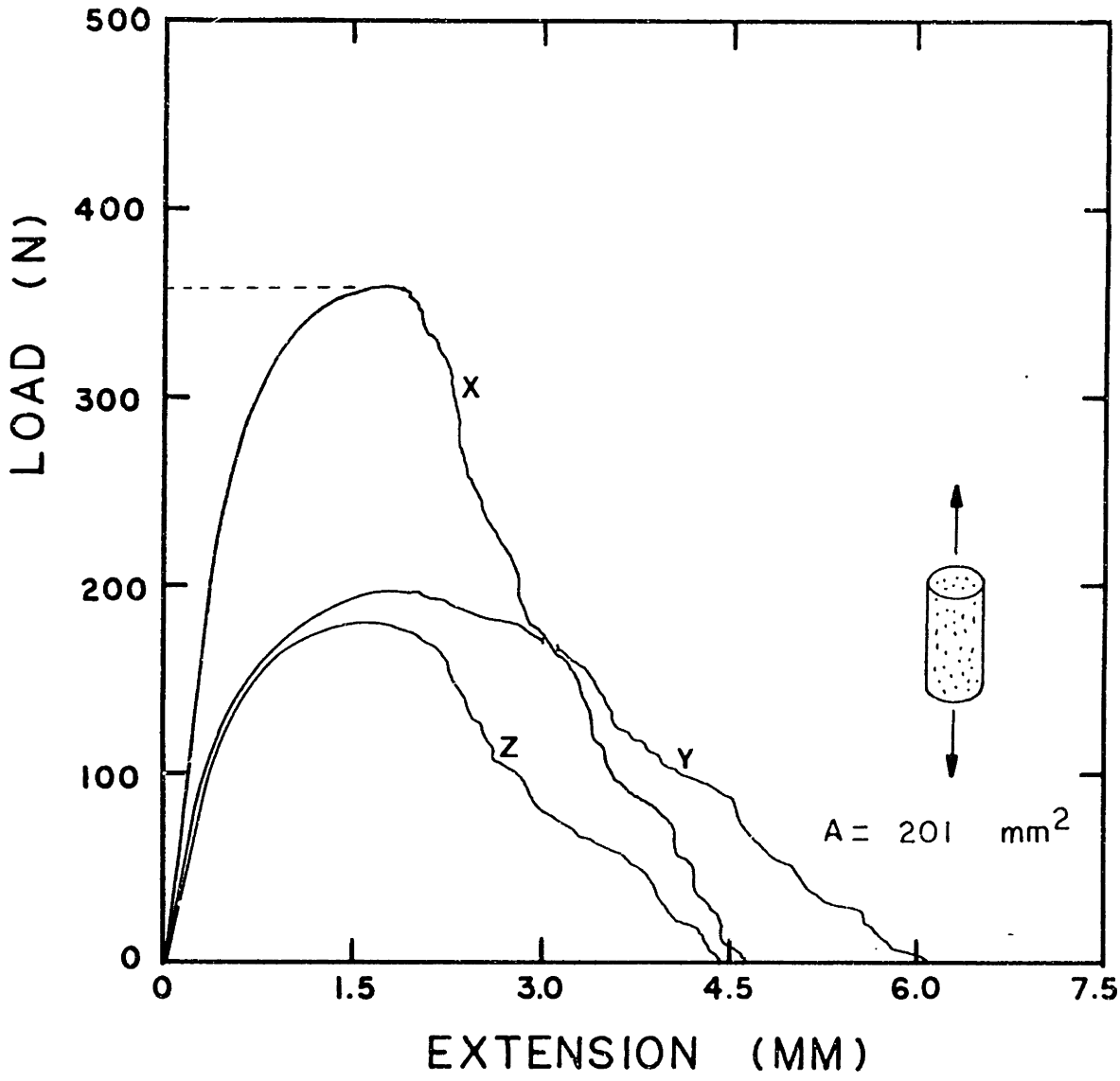

Fig. 6.12 Typical uniaxial tension curves for aluminum foam loaded parallel to the three principal material directions.

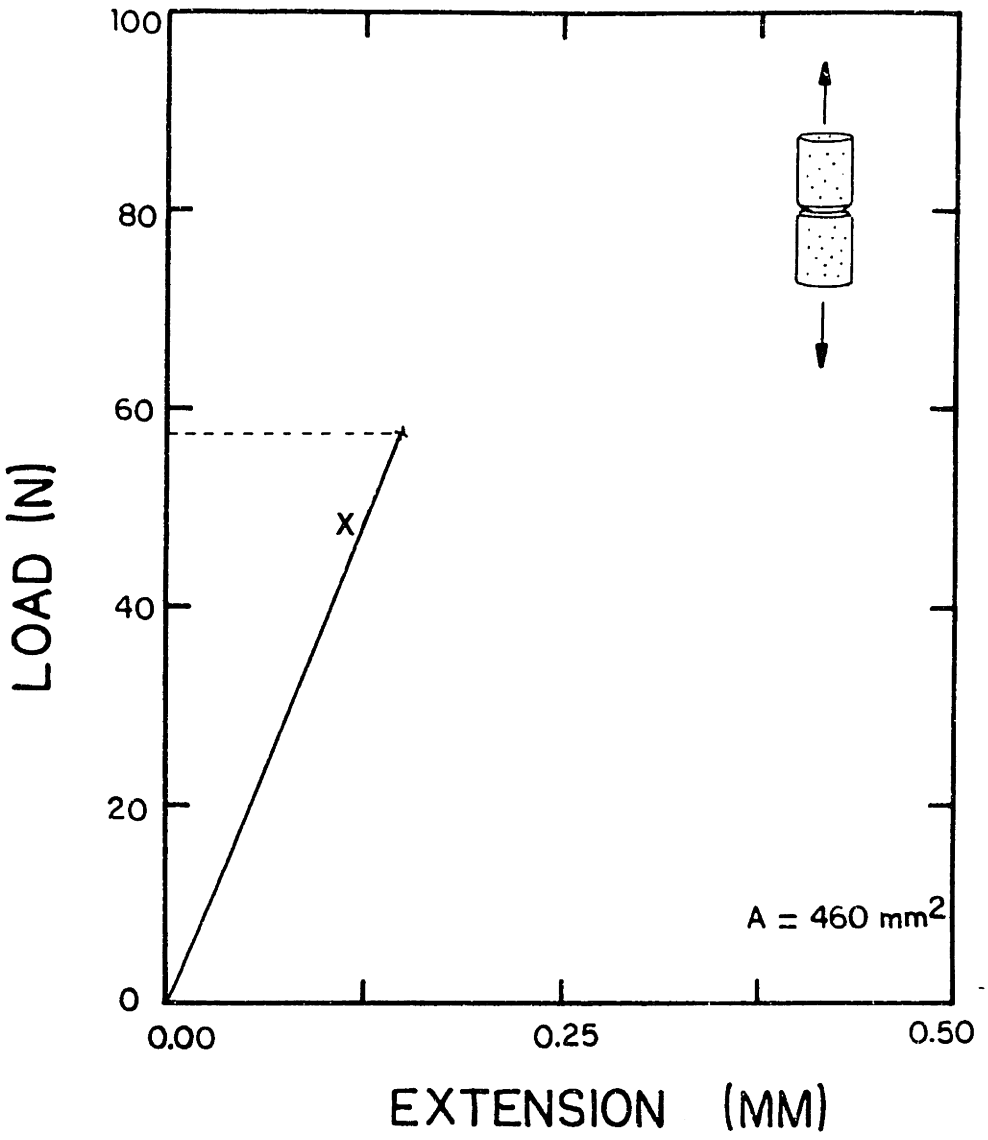

Fig. 6.13 A typical uniaxial tension curve for notched reticulated vitreous carbon specimens loaded parallel to the direction X.

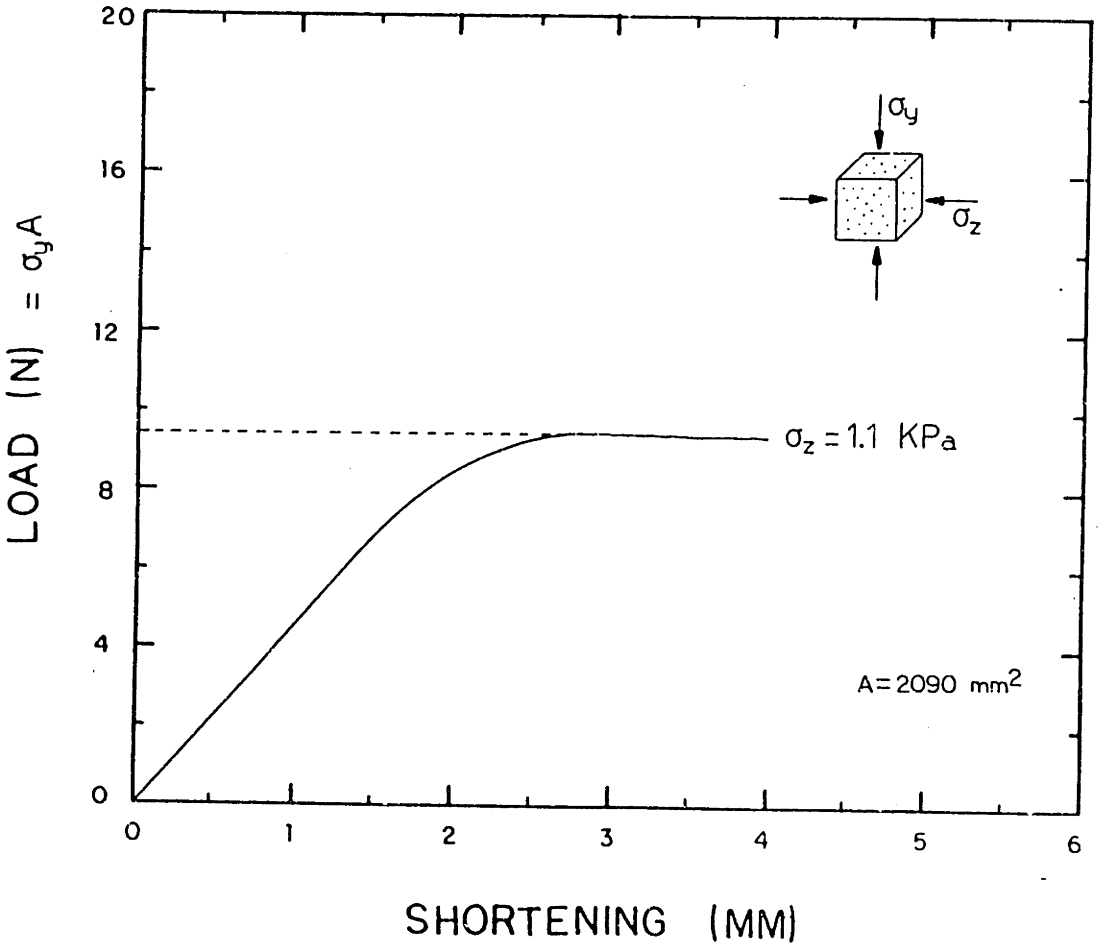

Fig. 6.14 A typical crosshead load-deformation curve for flexible polyurethane under biaxial compressive stresses.

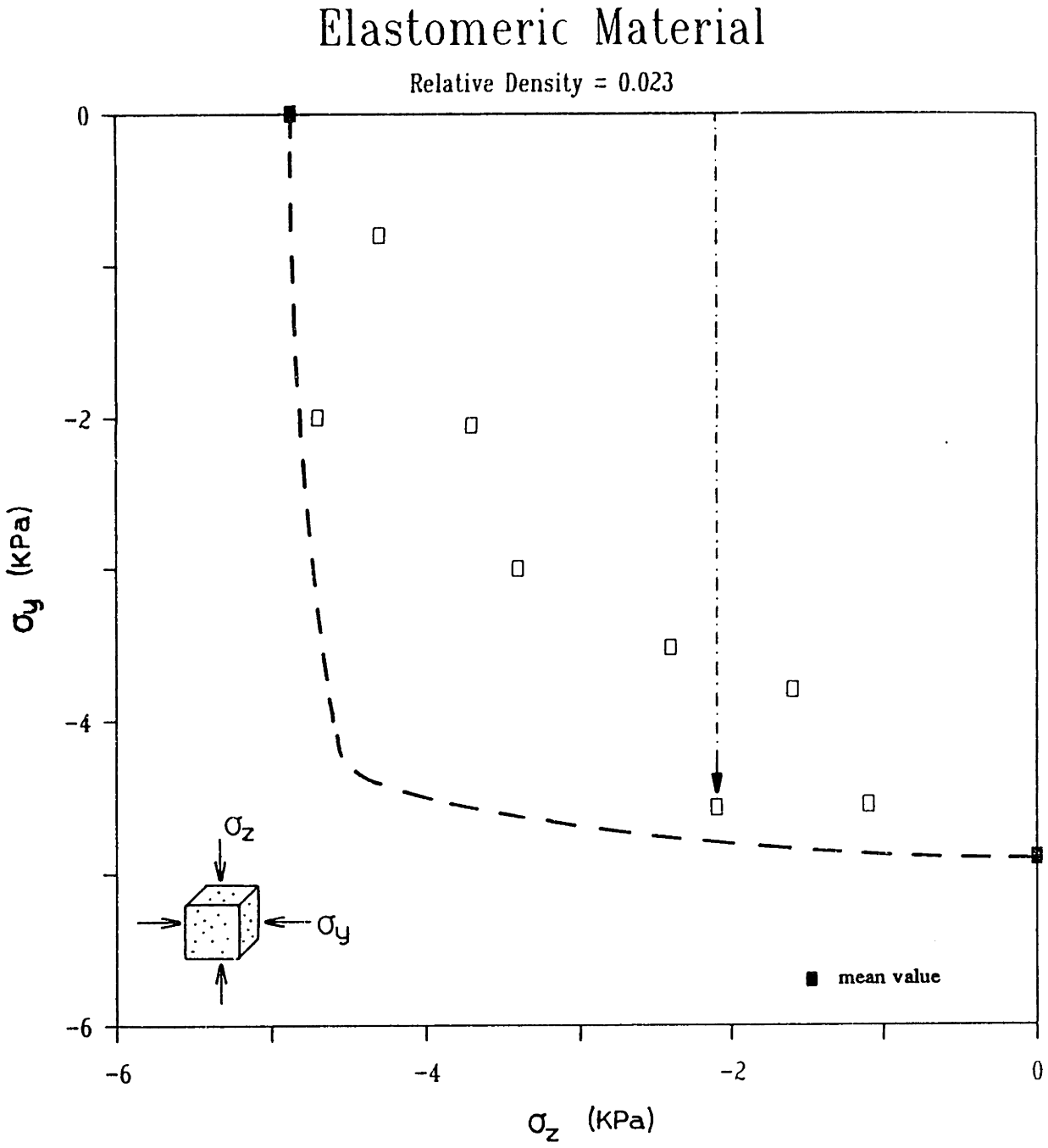

Fig. 6.15 Data for the failure of flexible polyurethane foam (ρ^*=28 kg/m^3) in biaxial compression in the Y-Z plane; the solid rectangles represent the mean uniaxial strengths. The elastic buckling envelope given by Zhang (1987) is indicated by the dashed line. The figure illustrates also a typical stress path.

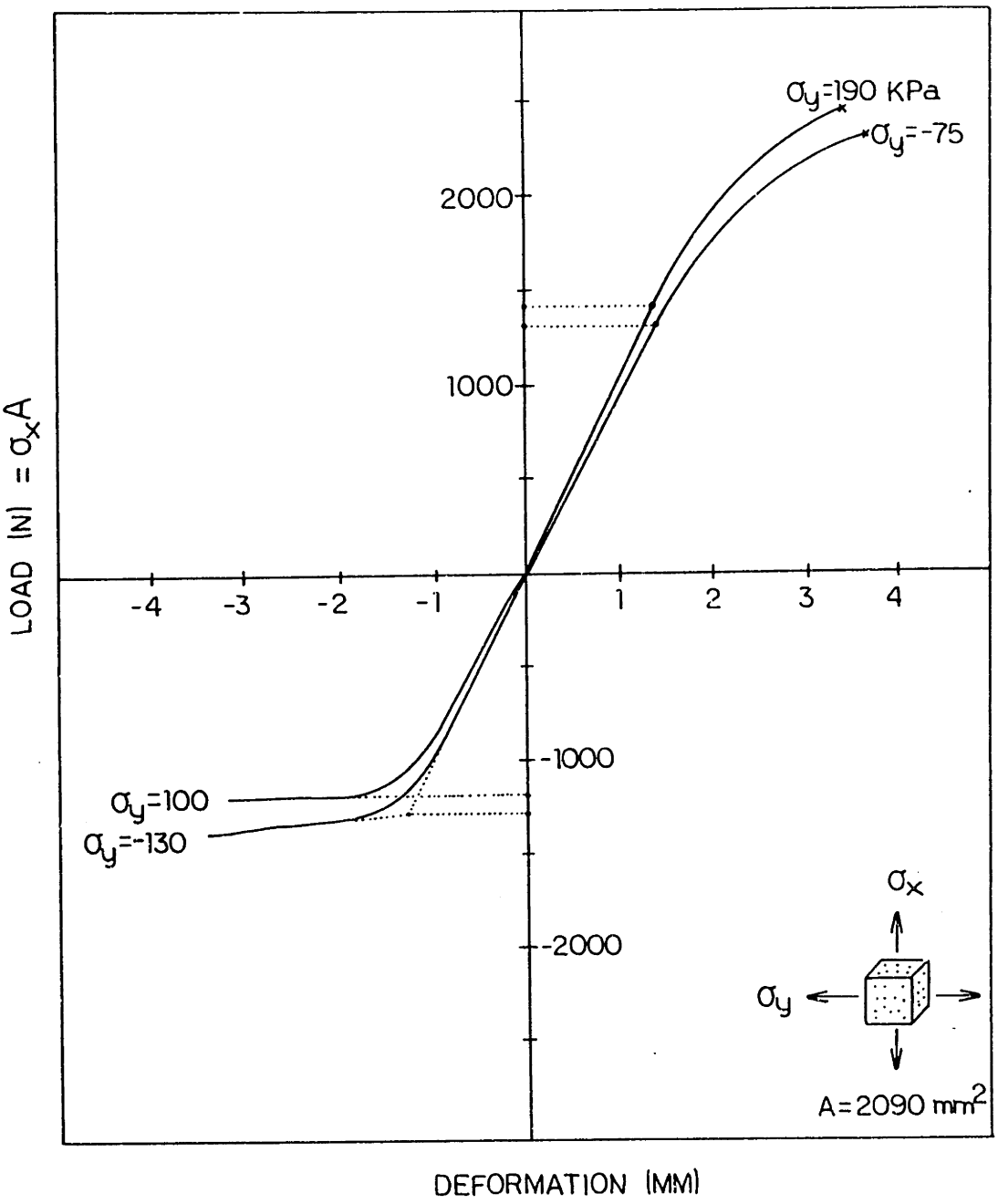

Fig. 6.16 Typical crosshead load-deformation curves for rigid polyurethane foam (ρ^*=64 kg/m^3) loaded biaxially (a), (b) in the X-Y plane, and (c), (d) in the Y-Z plane.

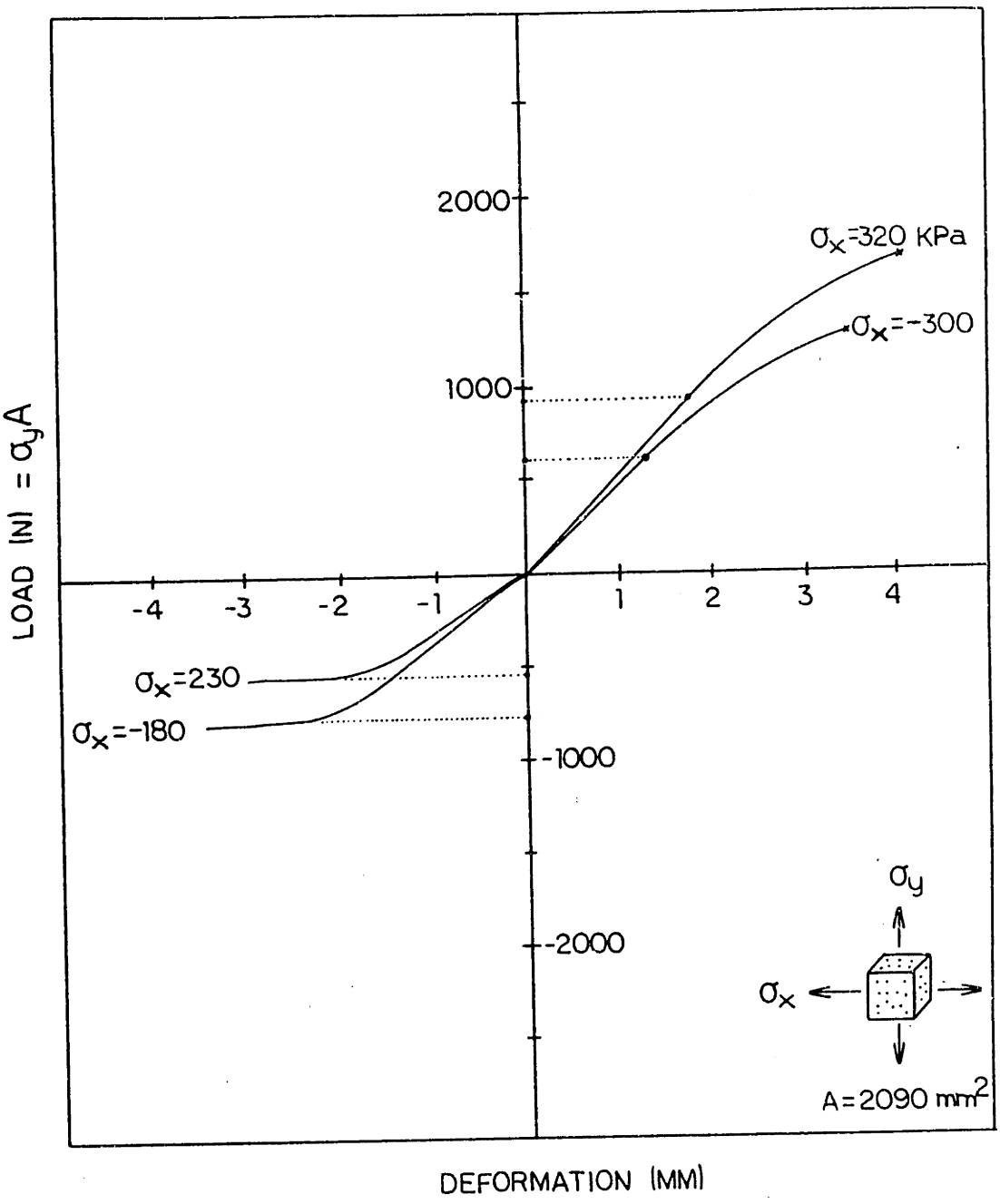

(b)

Fig. 6.16 cont'd.

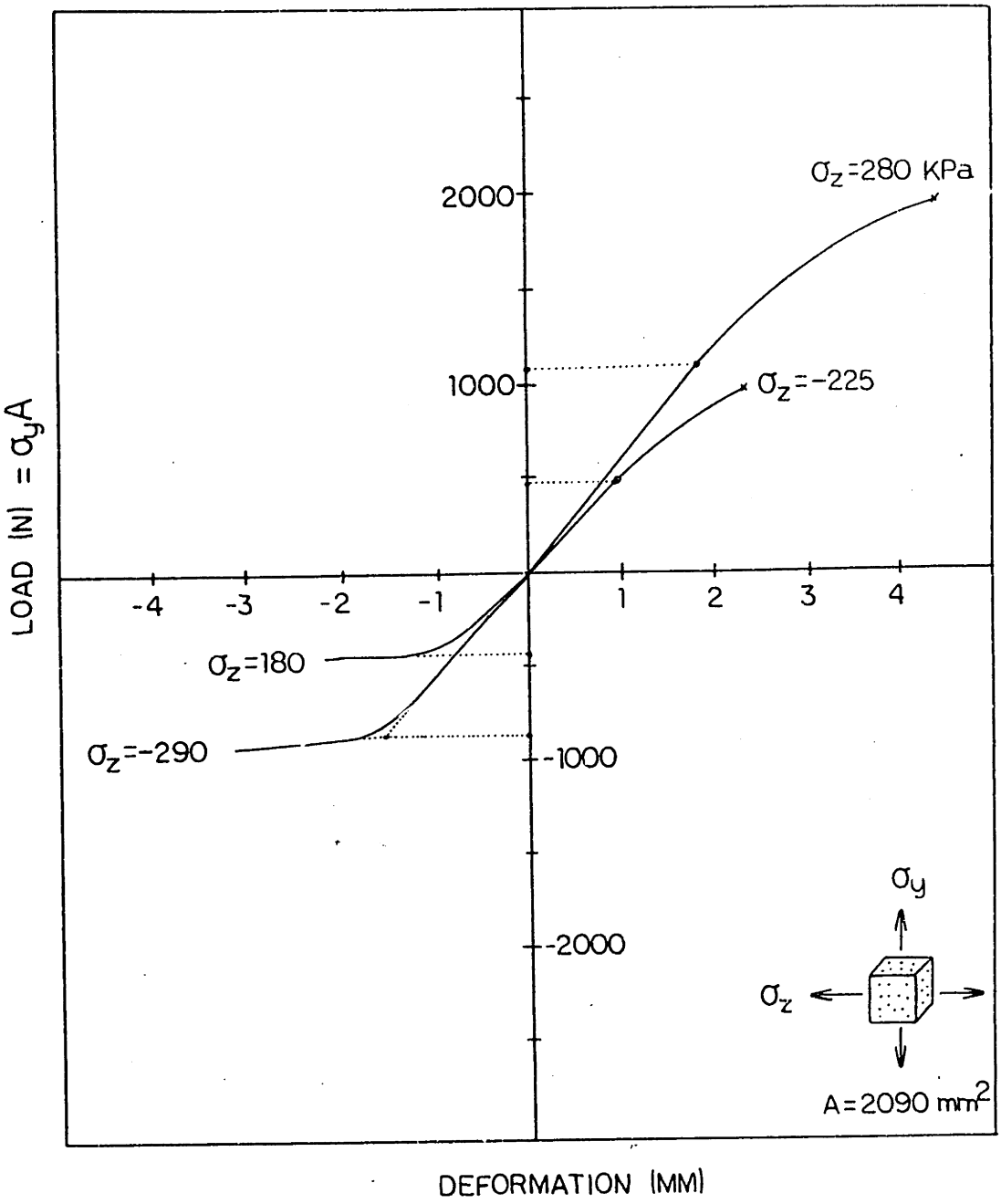

(c)

Fig. 6.16 cont'd.

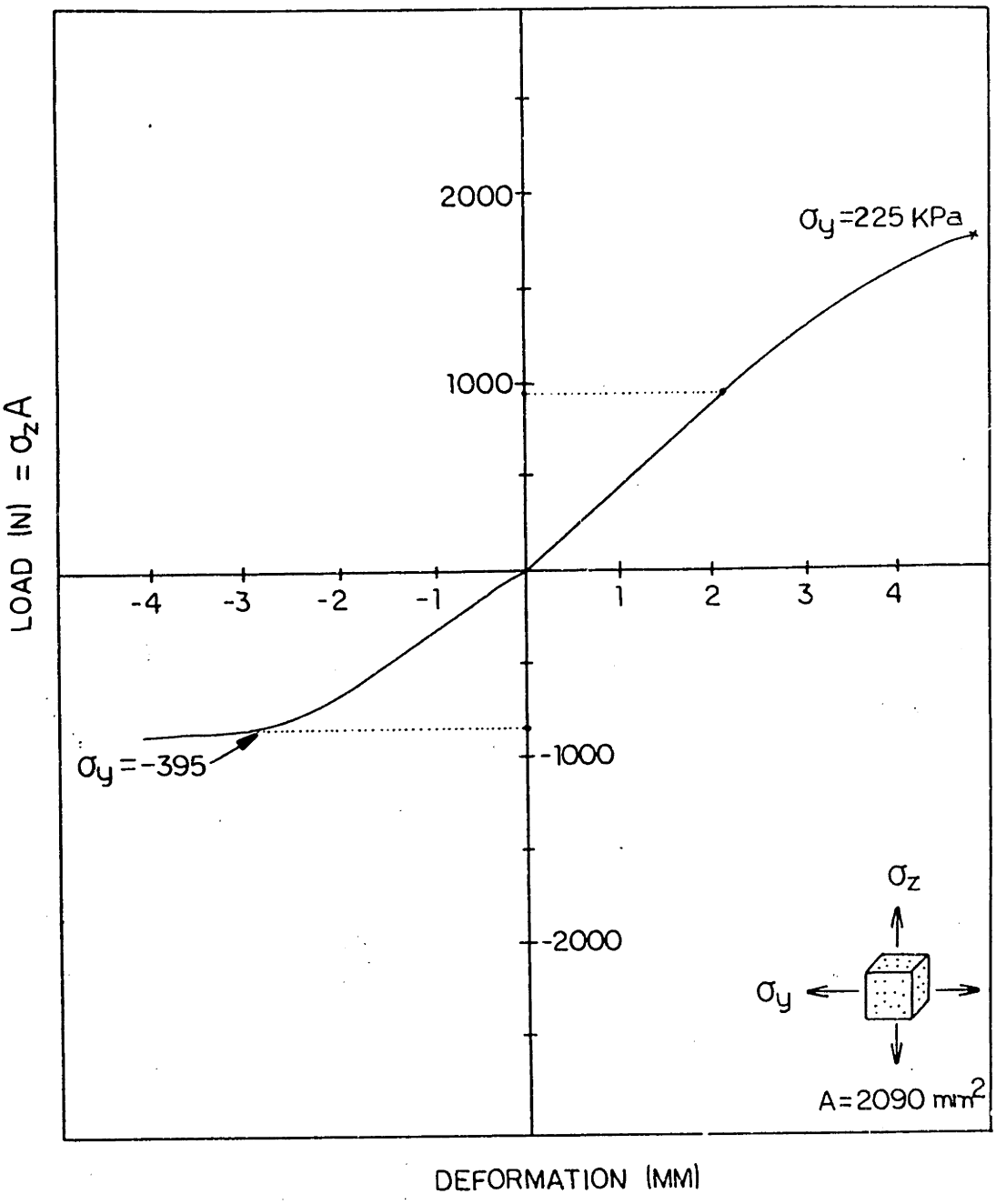

(d)

Fig. 6.16 cont'd.

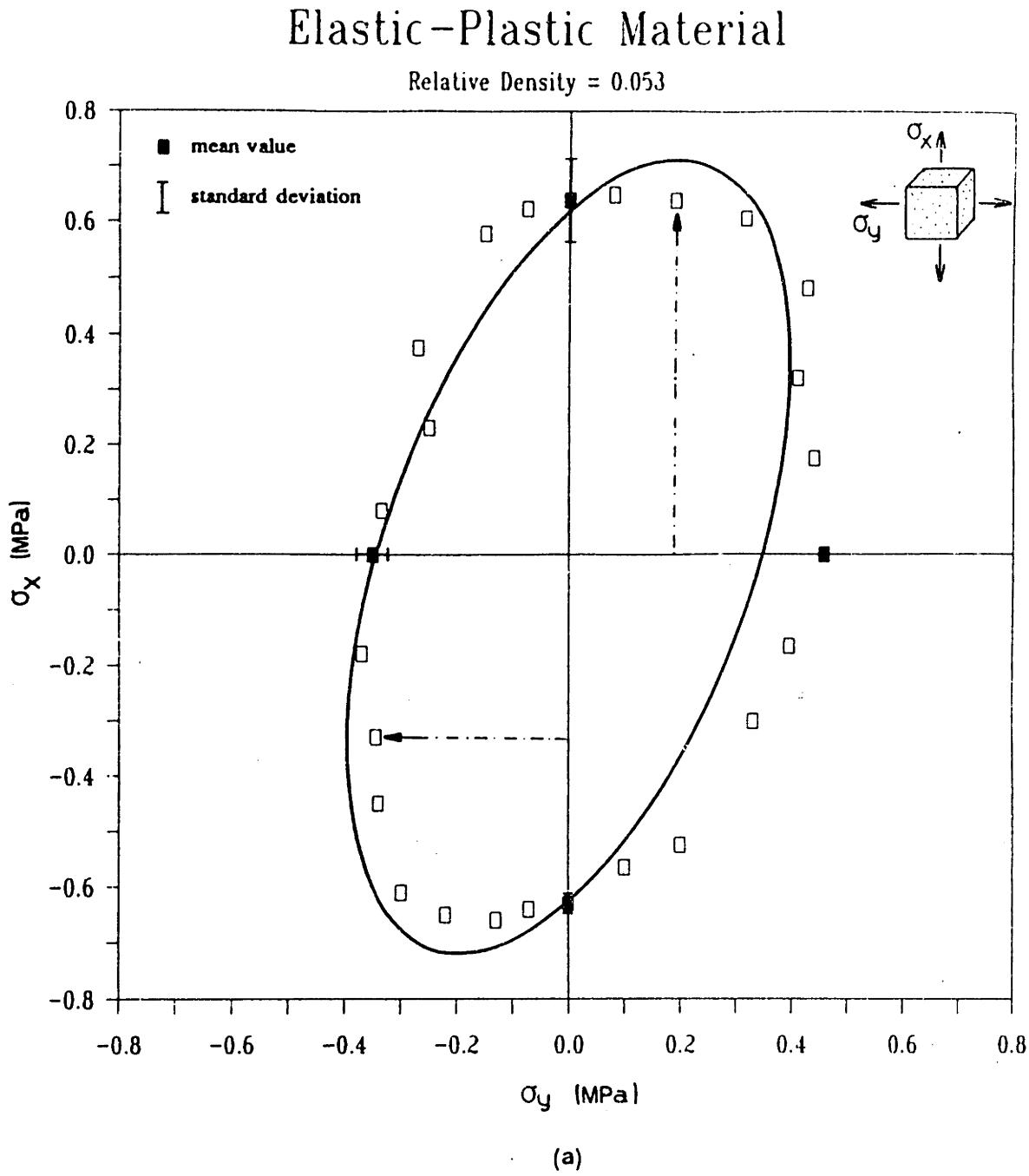

Fig. 6.17 Data for the failure of rigid polyurethane foam (ρ^*=64 kg/m^3) in biaxial loading in the (a) X-Y plane, and (b) in the Y-Z plane. The figures illustrate also typical stress paths. The yield envelope given by the model is indicated by the solid lines.

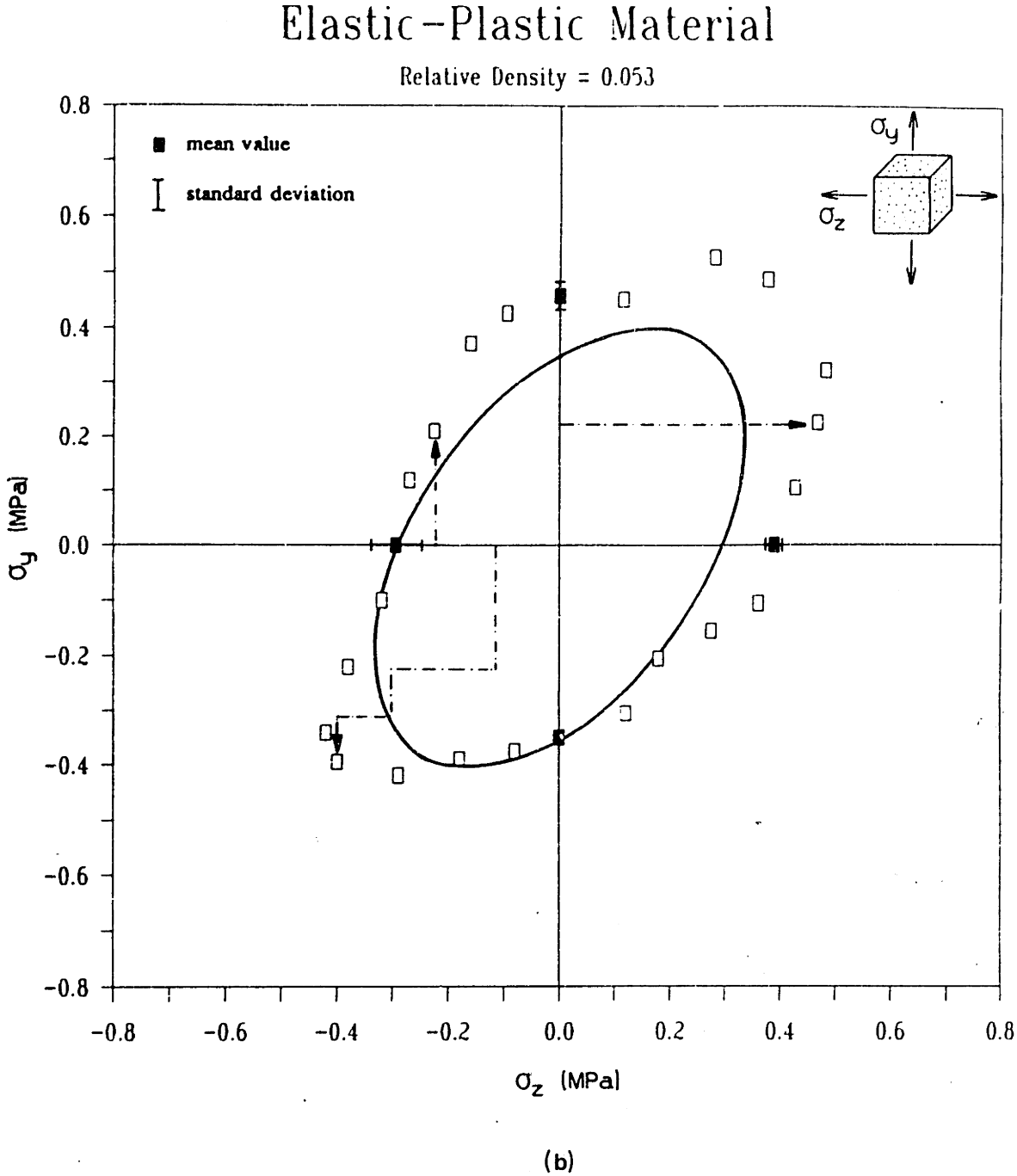

(b)

Fig. 6.17 cont'd.

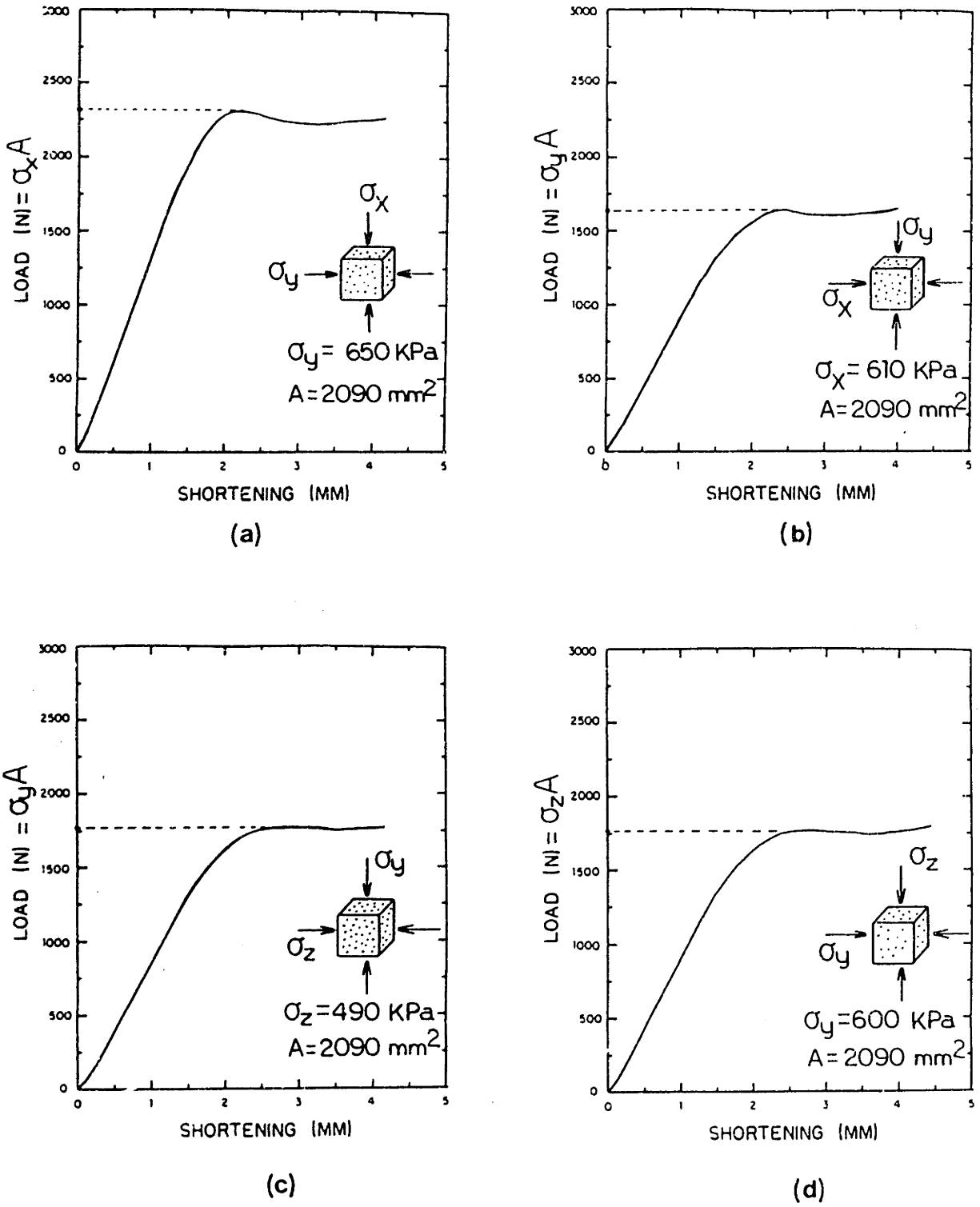

Fig. 6.18 Typical crosshead load-deformation curves for rigid polyurethane foam (ρ^*=96 kg/m^3) loaded in biaxial compression (a), (b) in the X-Y plane, and (c), (d) in the Y-Z plane.

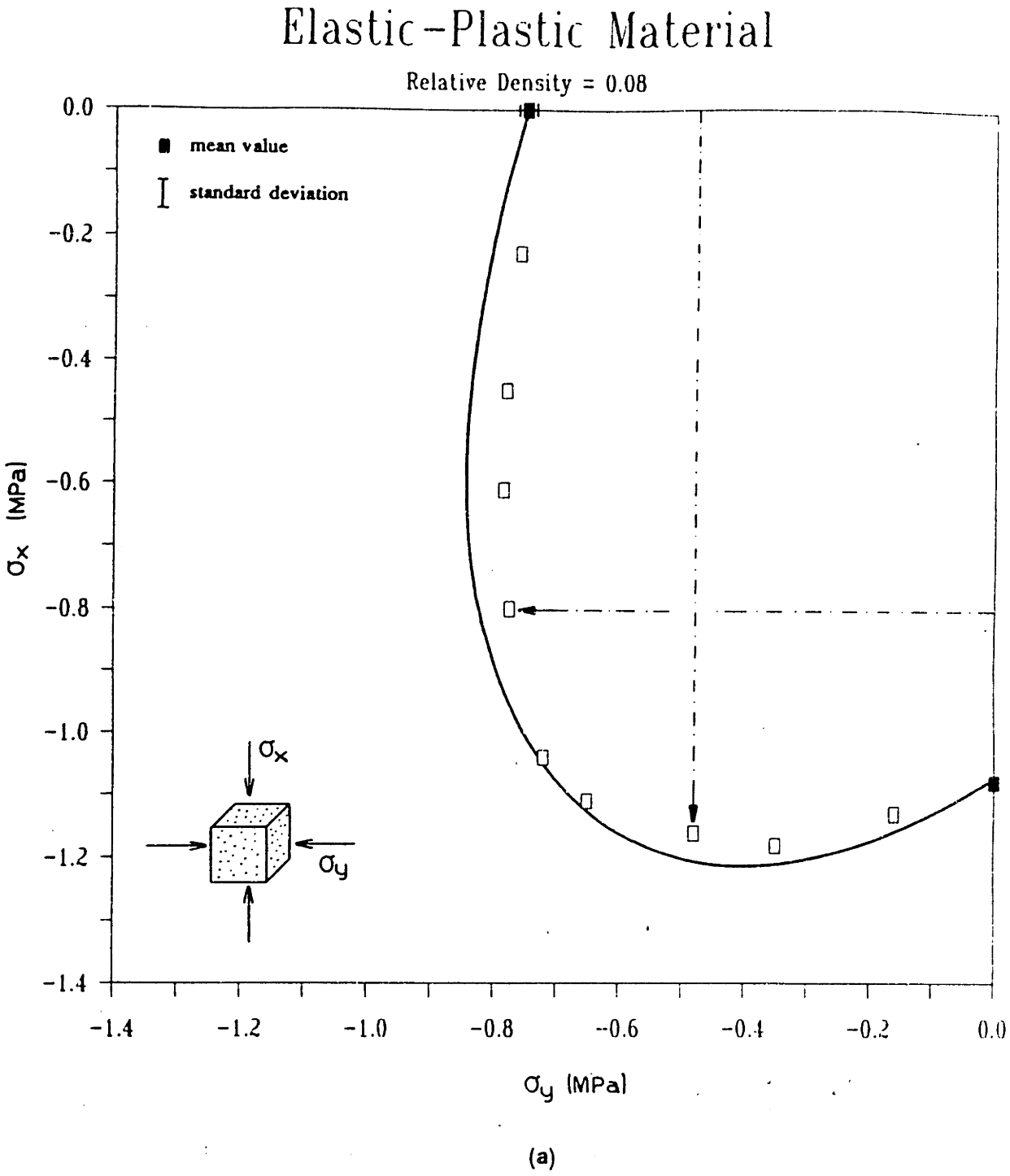

Fig. 6.19 Data for the failure of rigid polyurethane foam (ρ^*=96 kg/m^3) in biaxial compression in the (a) X-Y plane, and (b) in the Y-Z plane. The figures illustrate also typical stress paths. The yield envelope given by the model is indicated by the solid lines.

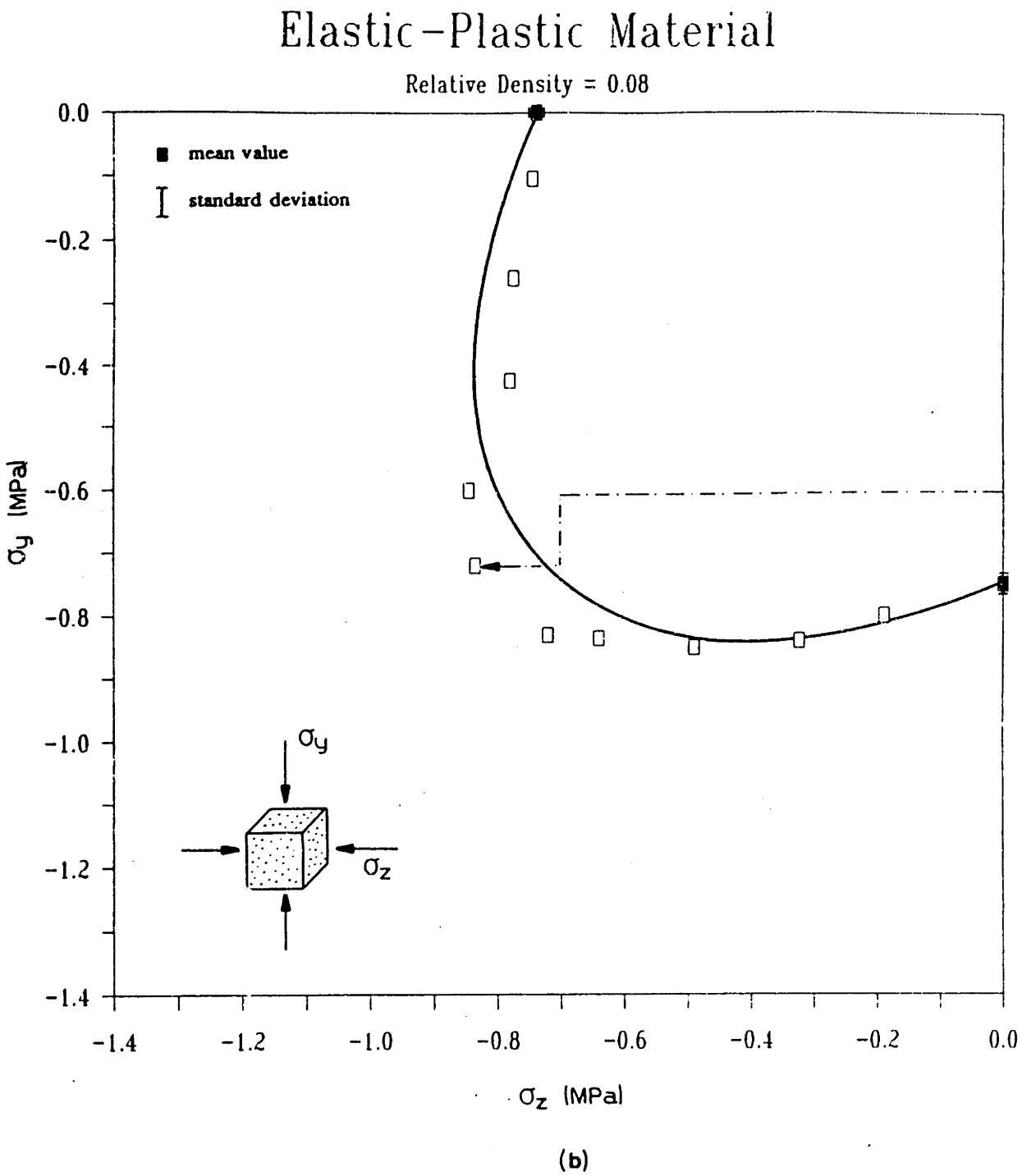

Fig. 6.19 cont'd.

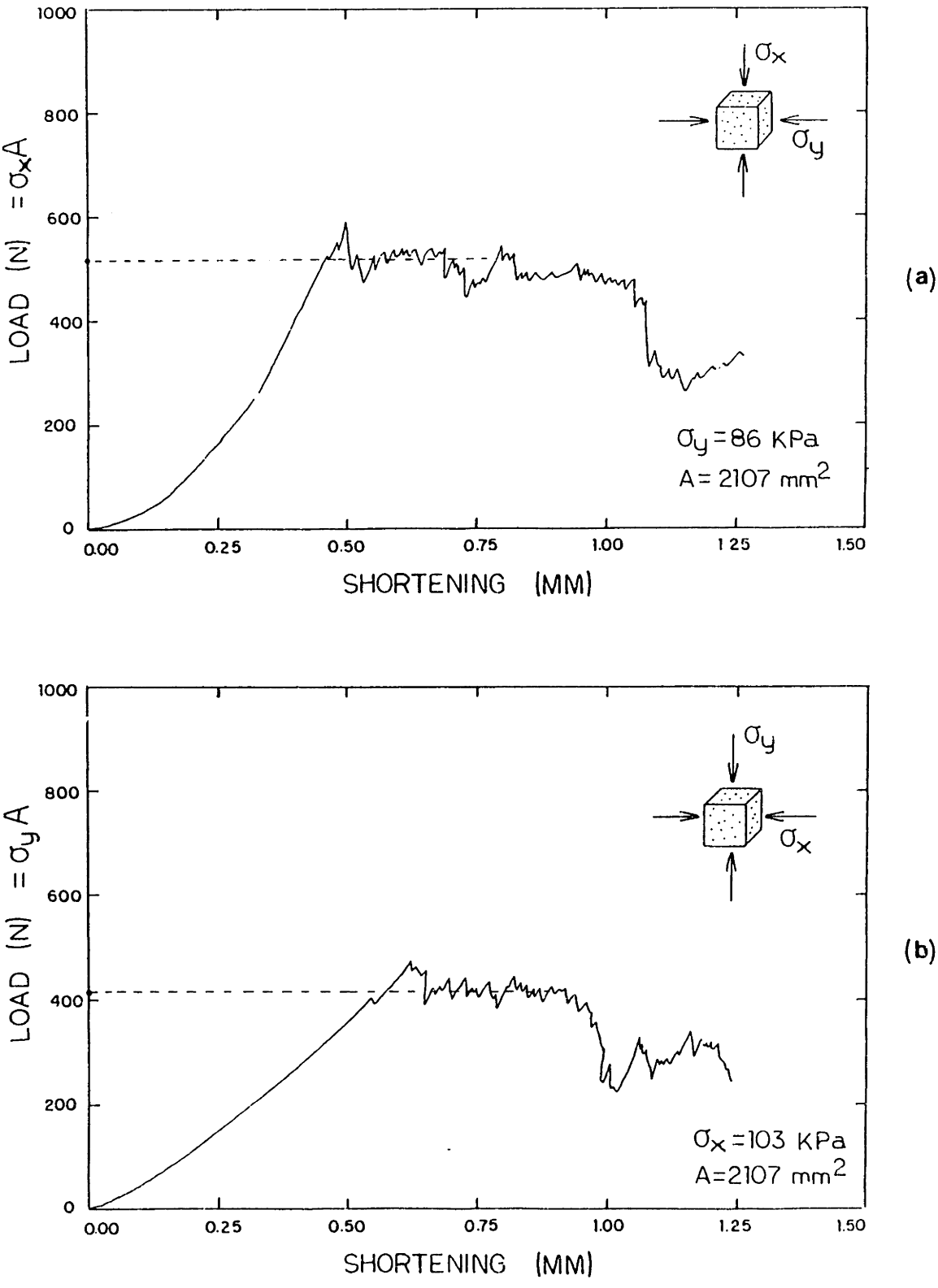

Fig. 6.20 (a) and (b) Typical crosshead load-deformation curves for reticulated vitreous carbon (ρ^*=48 kg/m^3) loaded in biaxial compression in the X-Y plane.

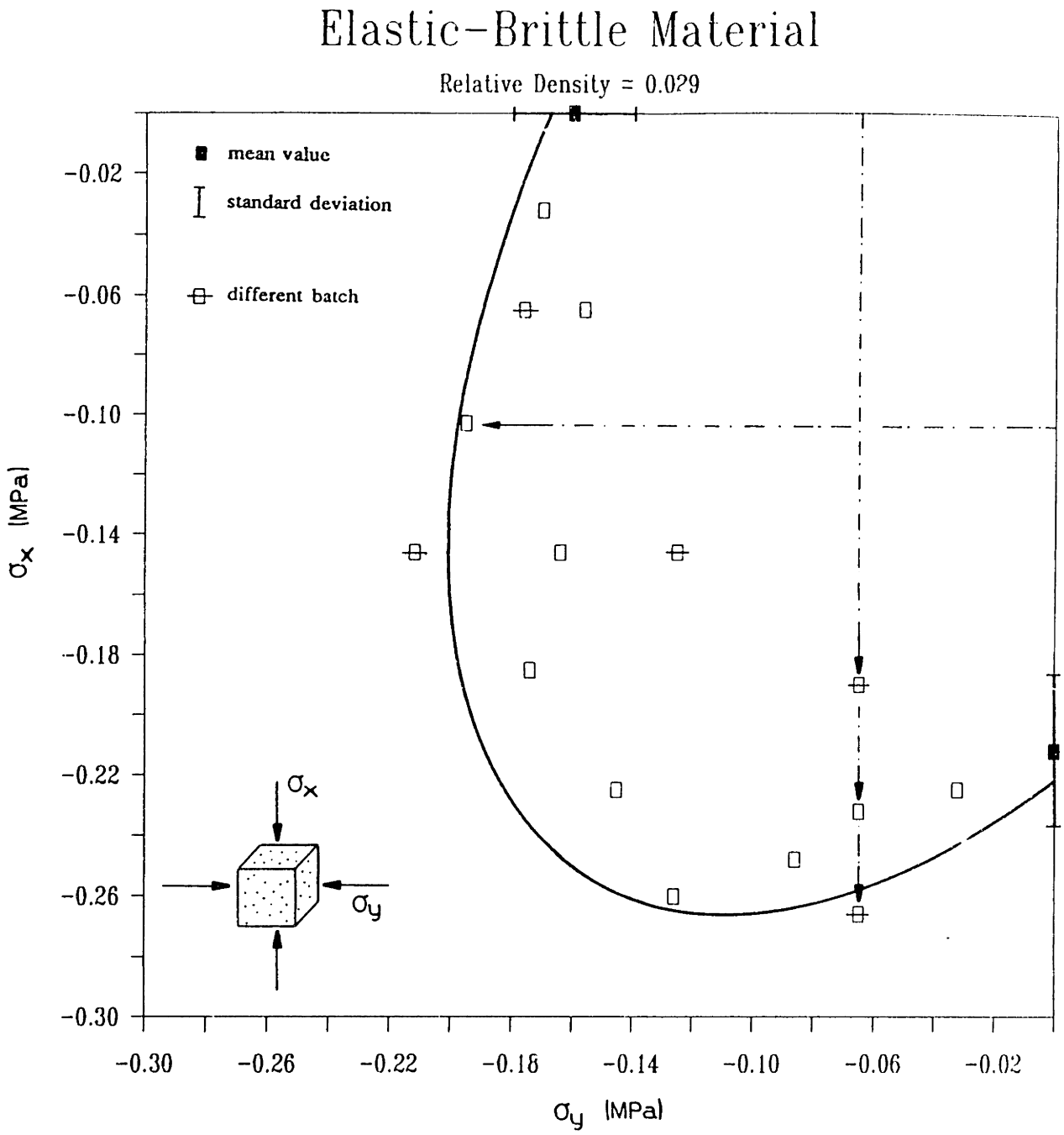

Fig. 6.21 Data for the failure of reticulated vitreous carbon (ρ^*=48 kg/m^3) in biaxial compression in the X-Y plane. The figure illustrates also typical stress paths. The crushing envelope given by the model is indicated by the solid line.

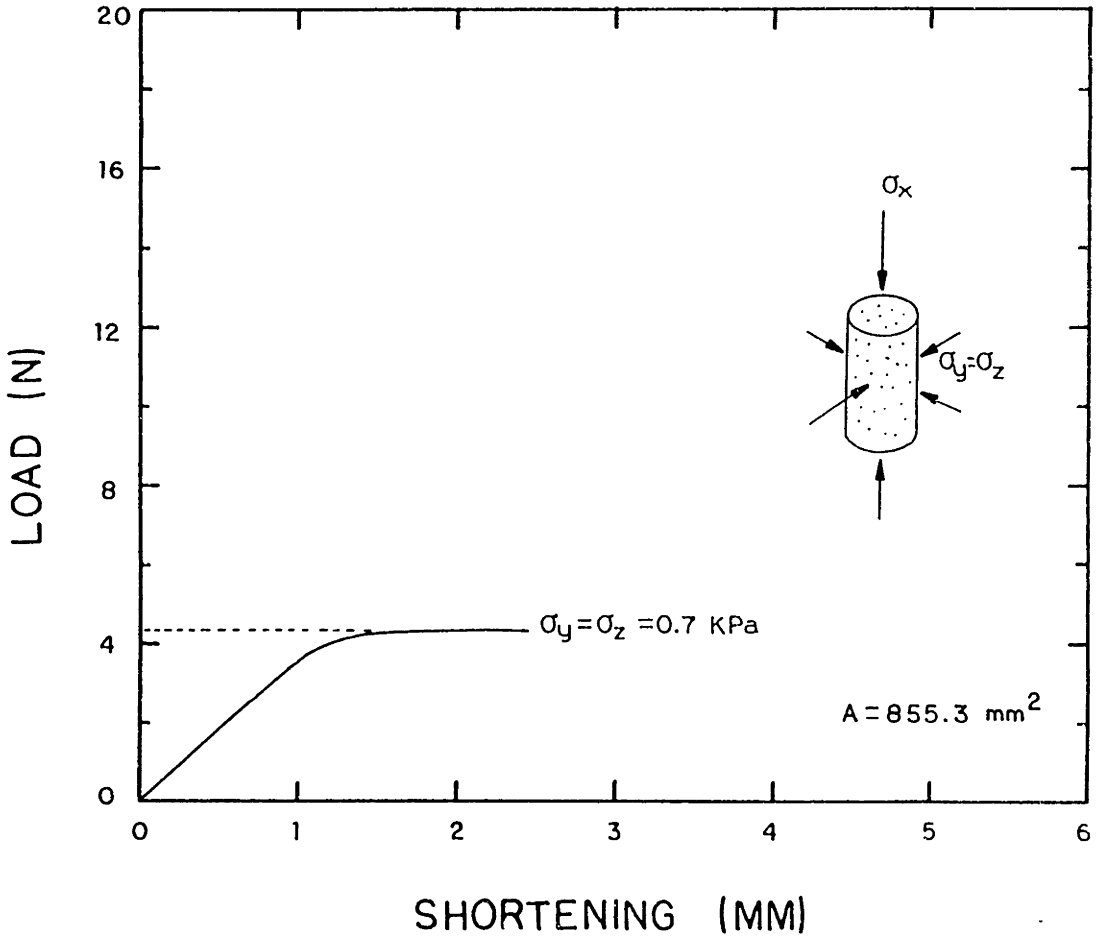

Fig. 6.22 A typical axial load-deformation curve for flexible polyurethane foam (ρ^*=28 kg/m^3) under axial and radial compression.

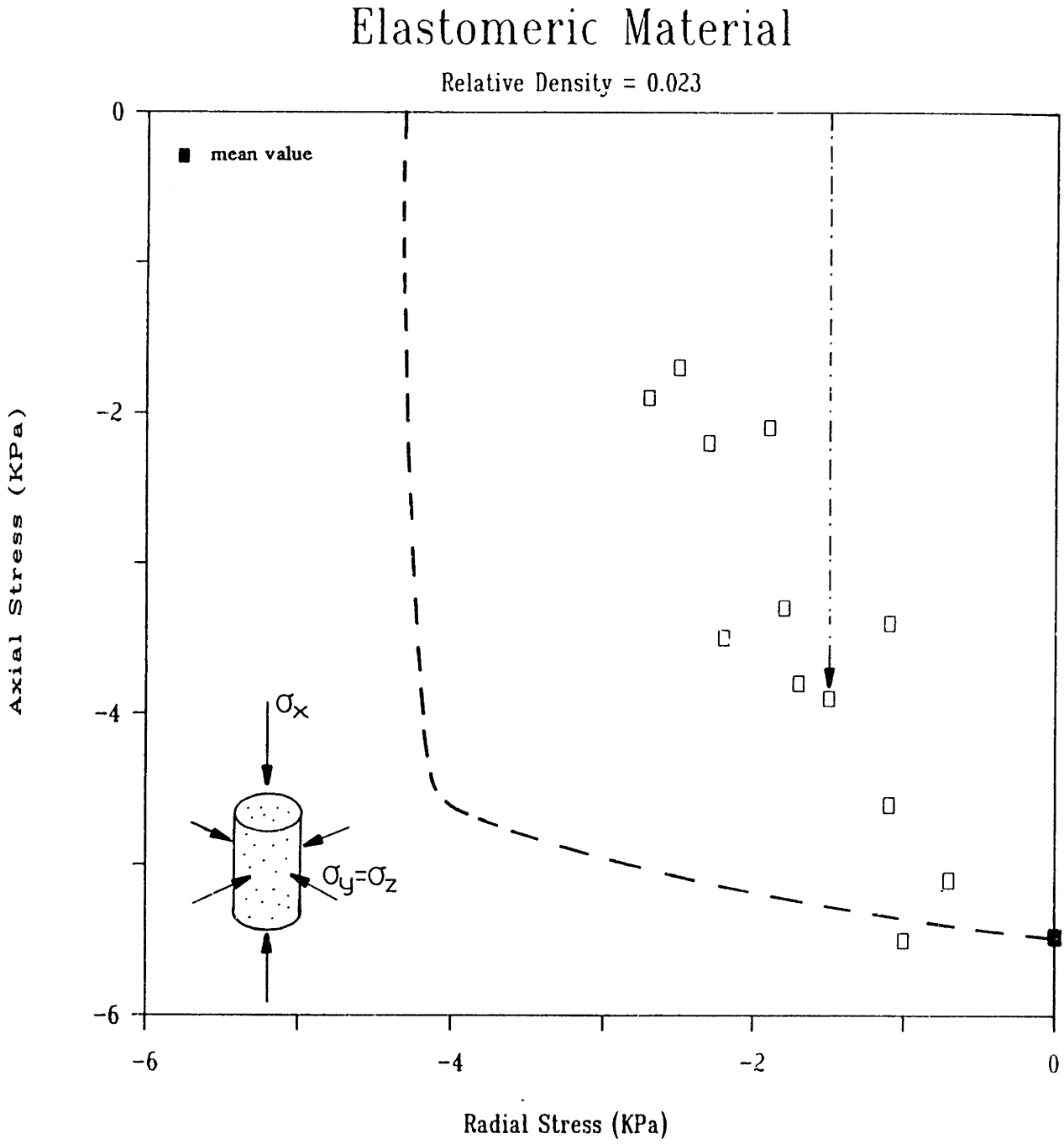

Fig. 6.23 Data for the failure of flexible polyurethane foam (ρ^*=28 kg/m^3) in axisymmetric compression. The elastic buckling envelope given by Zhang (1987) is indicated by the dashed line. A typical stress path is also illustrated.

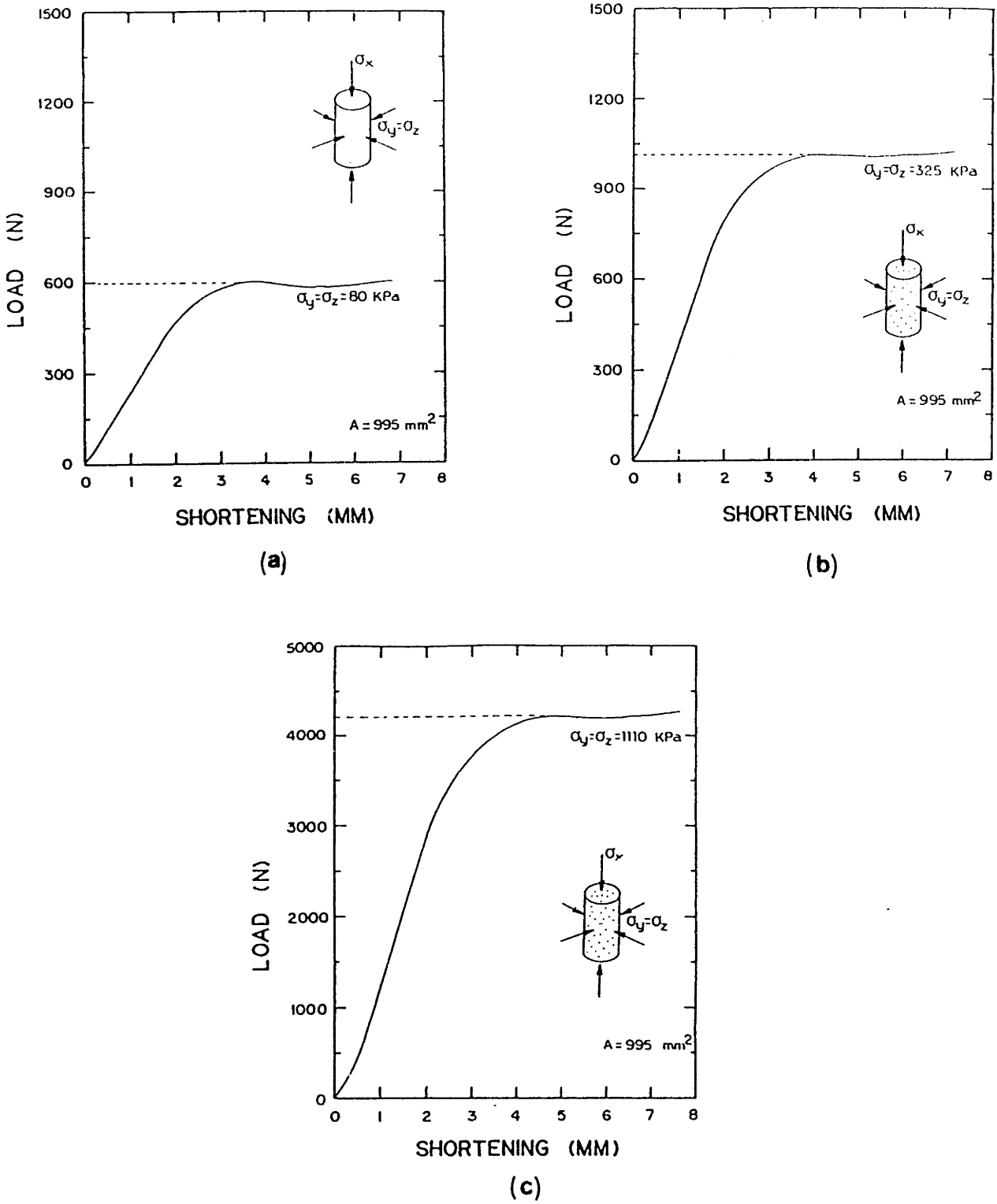

Fig. 6.24 Typical axial load-deformation curves for rigid polyurethane foam under axial compression parallel to the X material direction and radial compression normal to this. (a) ρ^*=64 kg/m^3; (b) ρ^*=96 kg/m^3; (c) ρ^*=192 kg/m^3.

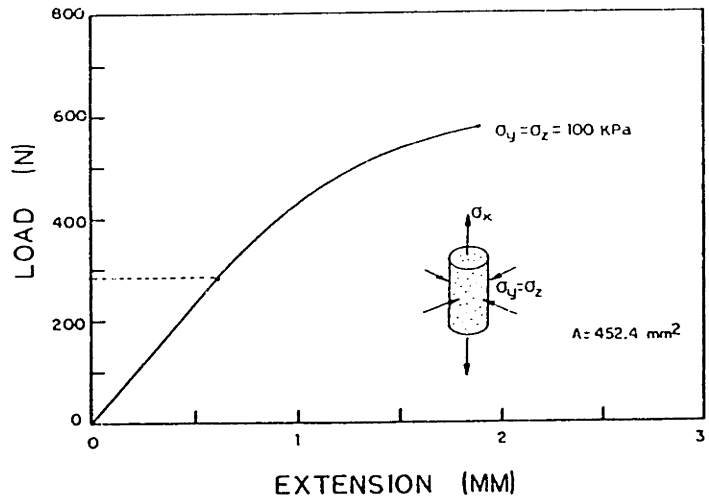

(a)

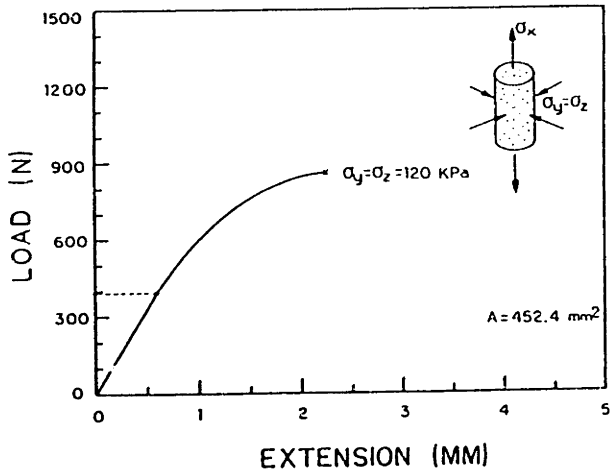

(b)

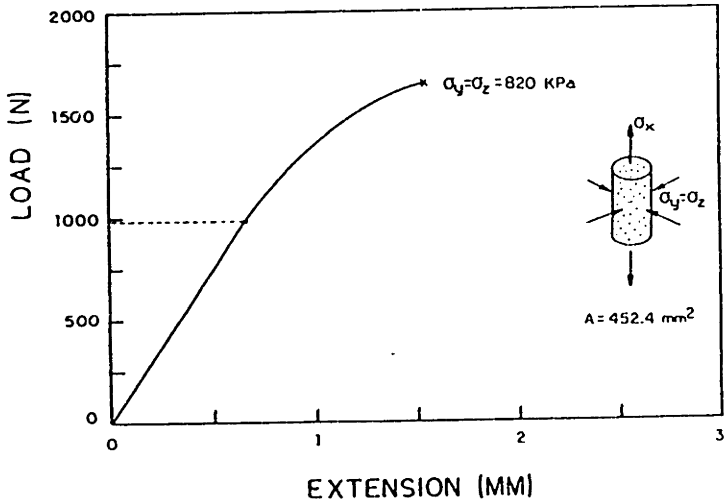

(c)

Fig. 6.25 Typical axial load-deformation curves for rigid polyurethane foam under axial tension parallel to the X material direction and radial compression normal to this. (a) ρ^*=64 kg/m^3; (b) ρ^*=96 kg/m^3; (c) ρ^*=192 kg/m^3.

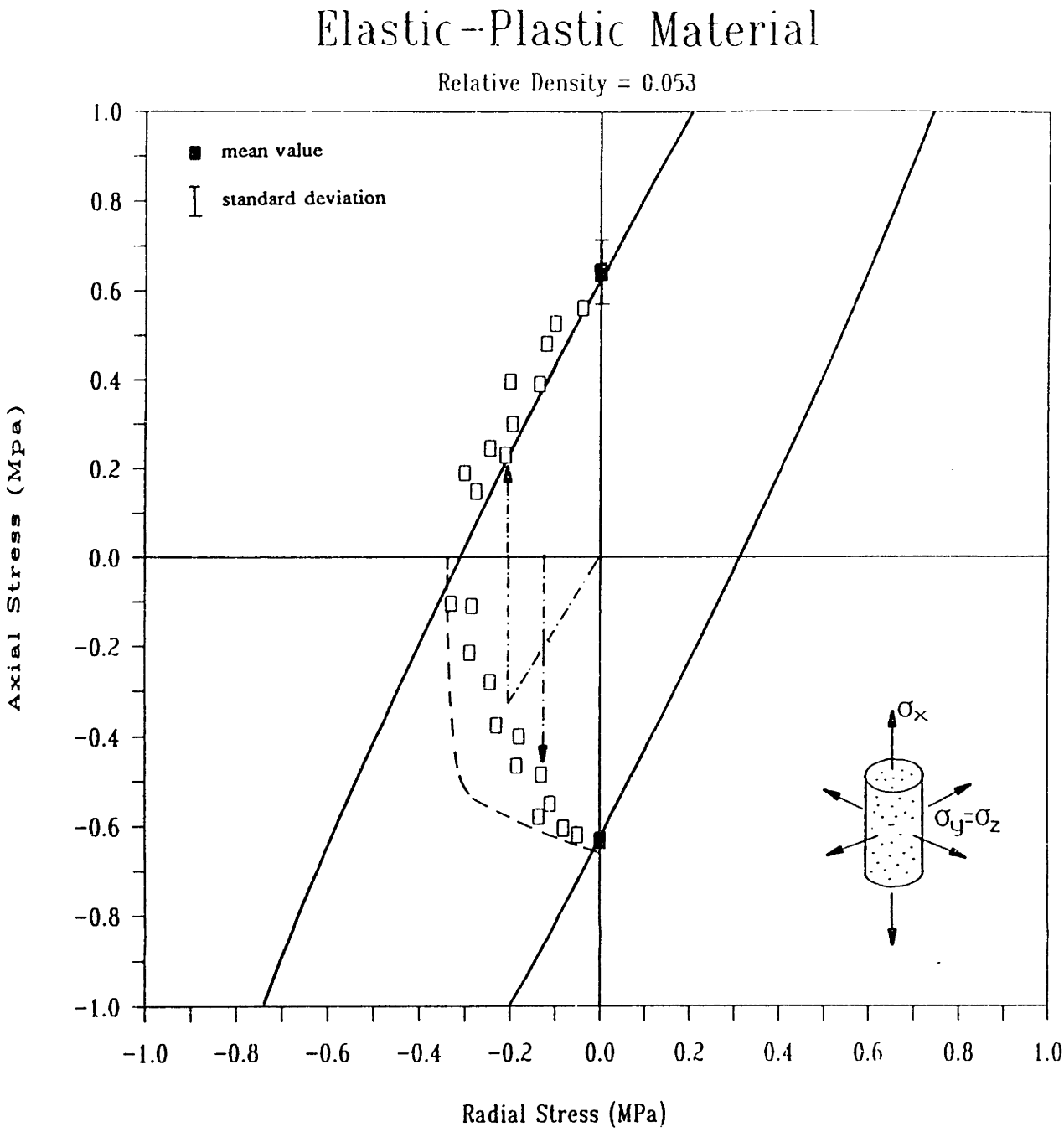

Fig. 6.26 Data for the failure of rigid polyurethane foam (ρ^*=64 kg/m^3) under radial compression and axial tension or compression. The yield envelope given by the model is indicated by the solid line. The elastic buckling envelope given by Zhang (1987) is indicated by the dashed line. Typical stress paths are also illustrated.

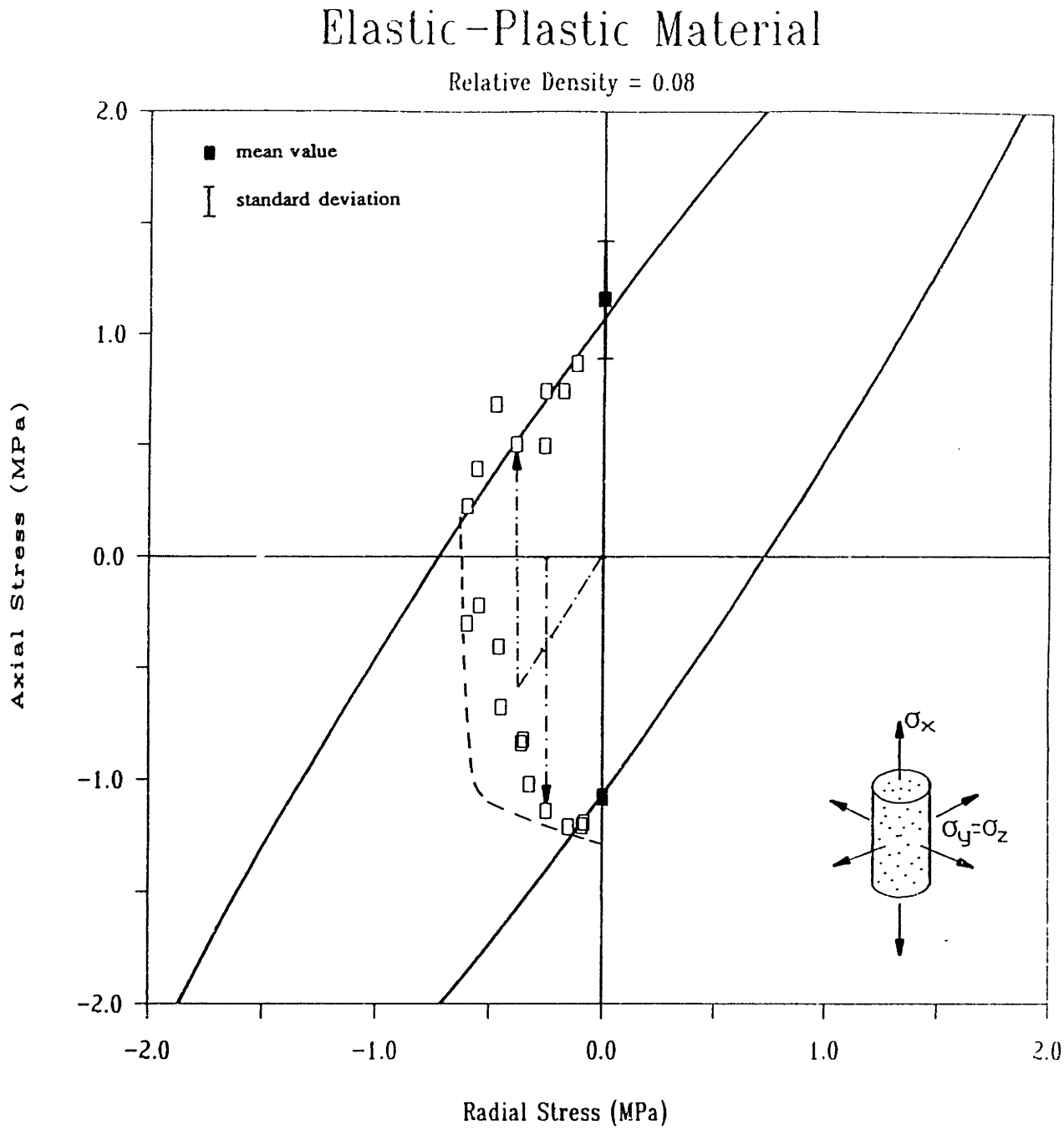

Fig. 6.27 Data for the failure of rigid polyurethane foam (ρ^*=96 kg/m^3) under radial compression and axial tension or compression. The yield envelope given by the model is indicated by the solid line. The elastic buckling envelope given by Zhang (1987) is indicated by the dashed line. Typical stress paths are also illustrated.

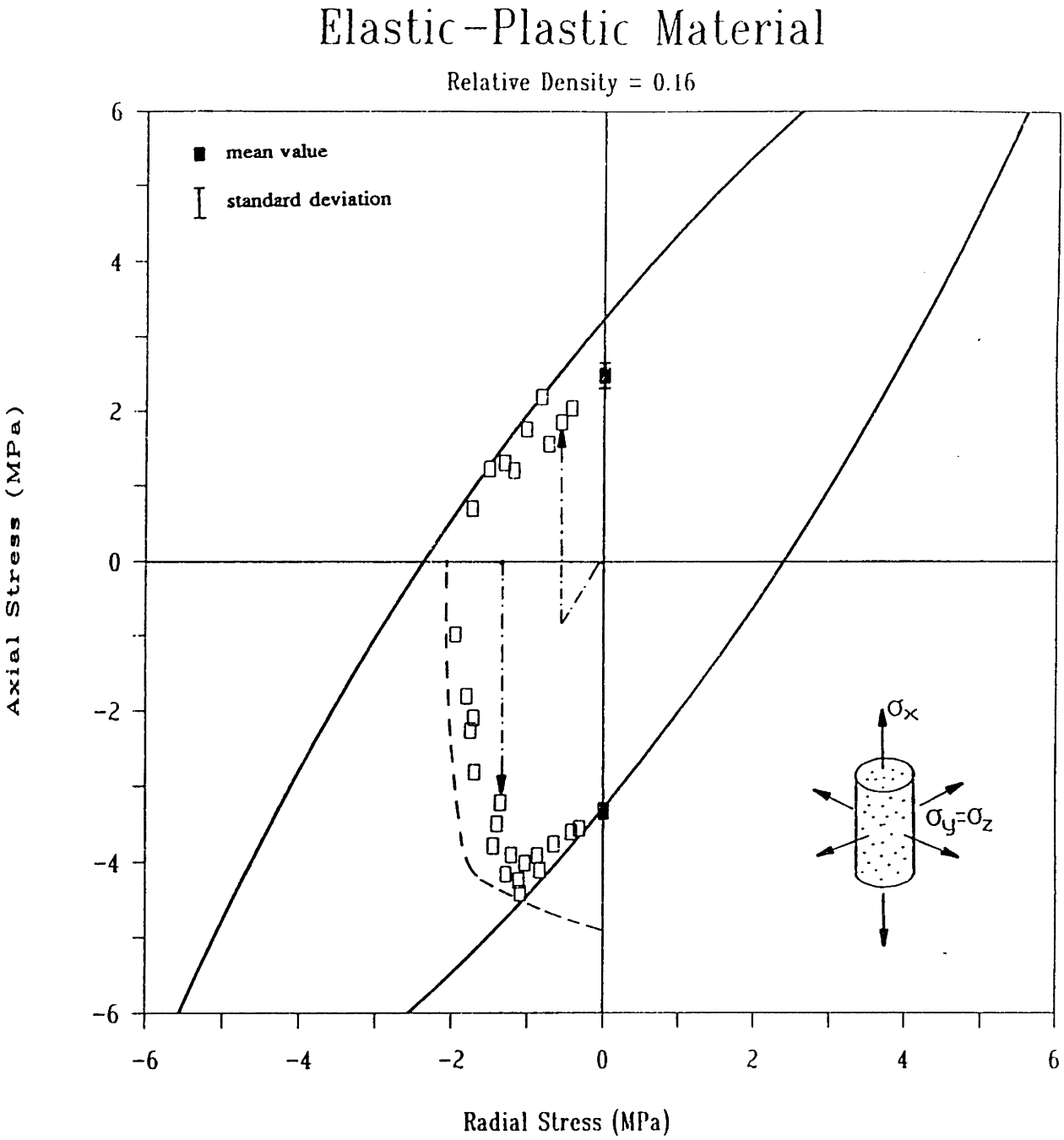

Fig. 6.28 Data for the failure of rigid polyurethane foam (ρ^*=192 kg/m^3) under radial compression and axial tension or compression. The yield envelope given by the model is indicated by the solid line. The elastic buckling envelope given by Zhang (1987) is indicated by the dashed line. Typical stress paths are also illustrated.

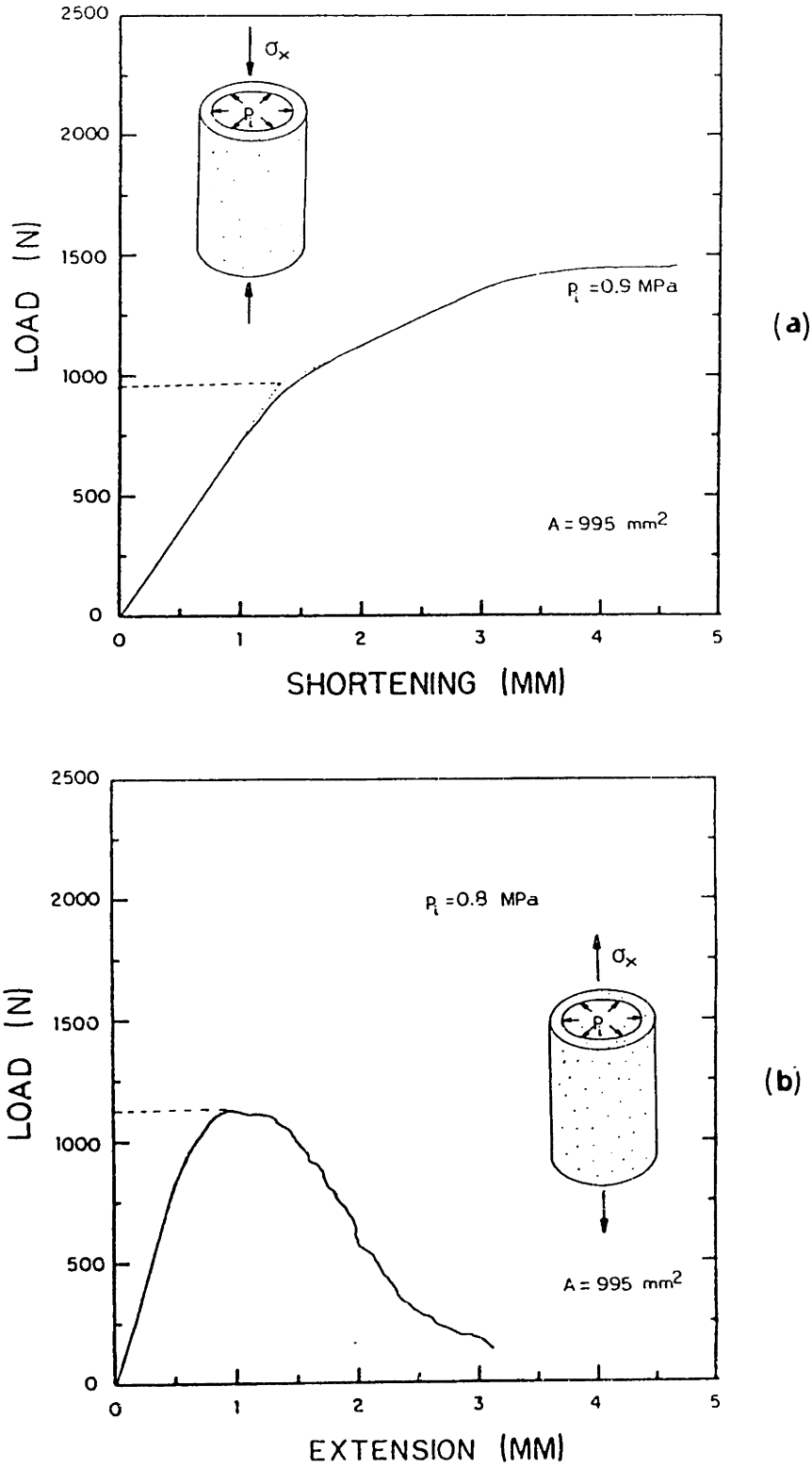

Fig. 6.29 Typical axial load-deformation curves for aluminum foam (ρ^*=135 kg/m^3) under radial tension and axial (a) compression or (b) tension. The axial load acts parallel to the X material direction.

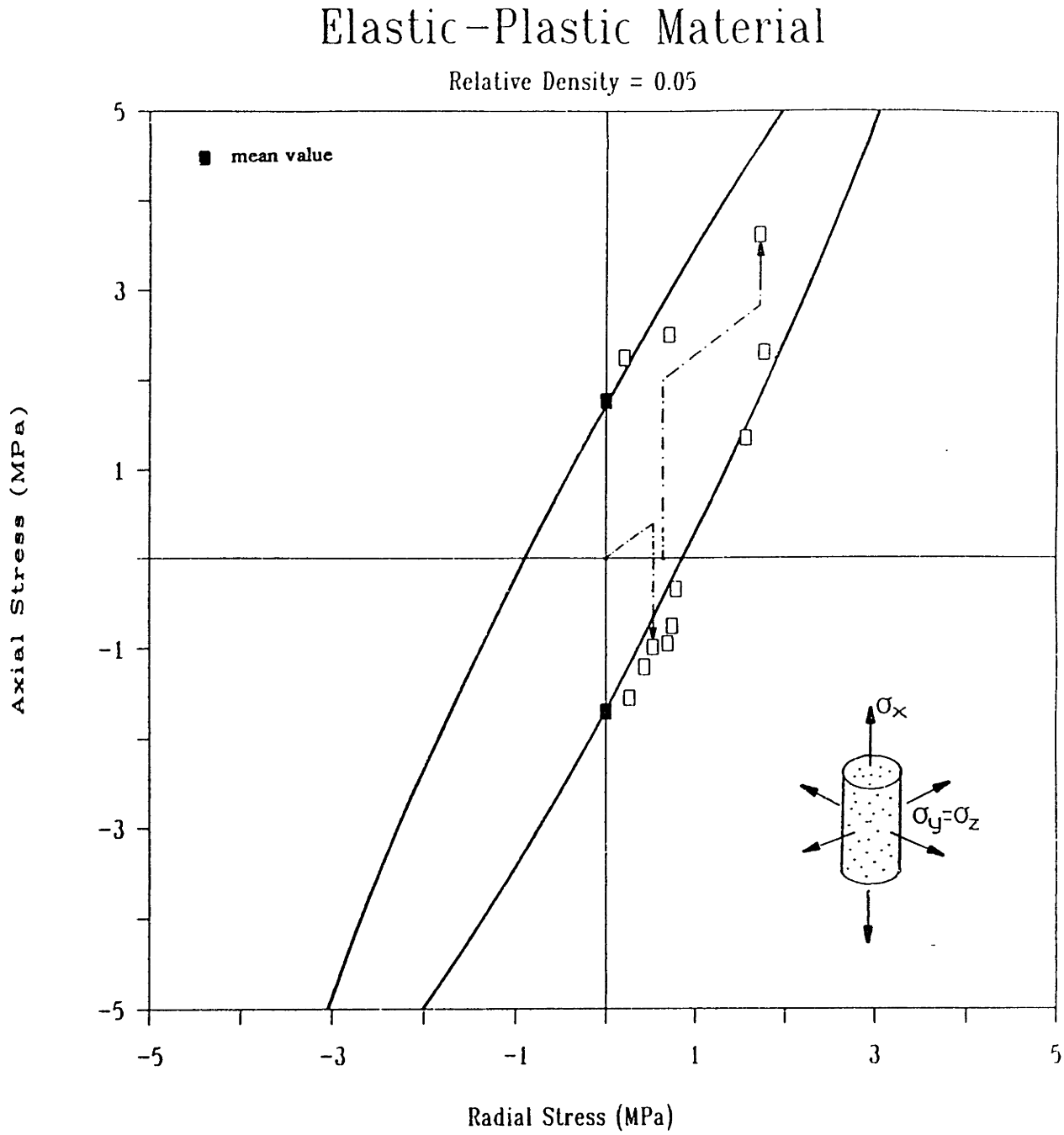

Fig. 6.30 Data for the failure of aluminum foam (ρ^*=135 kg/m^3) under radial tension and axial tension or compression. The yield envelope given by the model is indicated by the solid line. Typical stress paths are also illustrated.

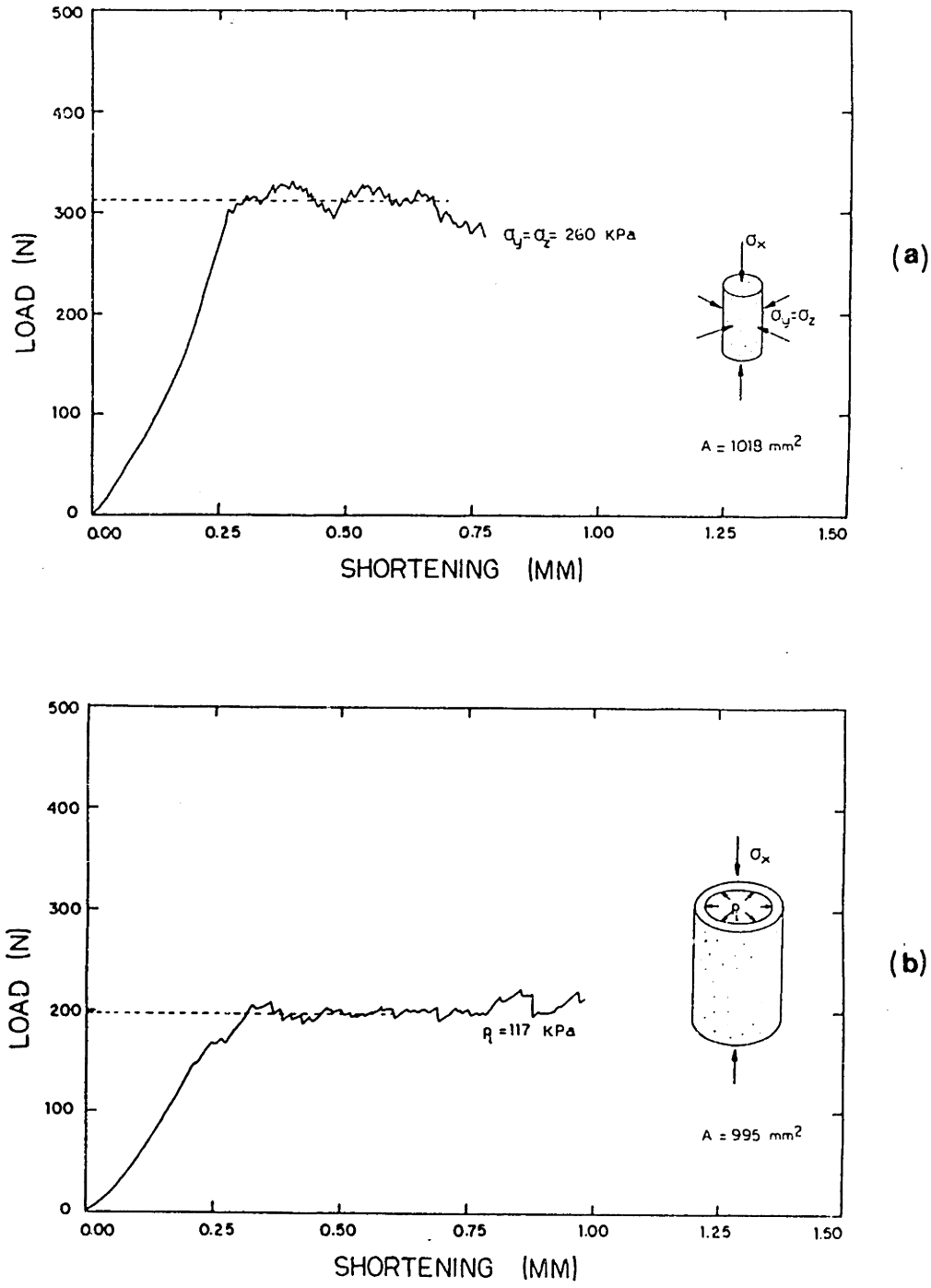

Fig. 6.31 Typical axial compressive load-deformation curves for reticulated vitreous carbon under axial compression and radial (a) compression or (b) tension. The axial load acts parallel to the X material direction.

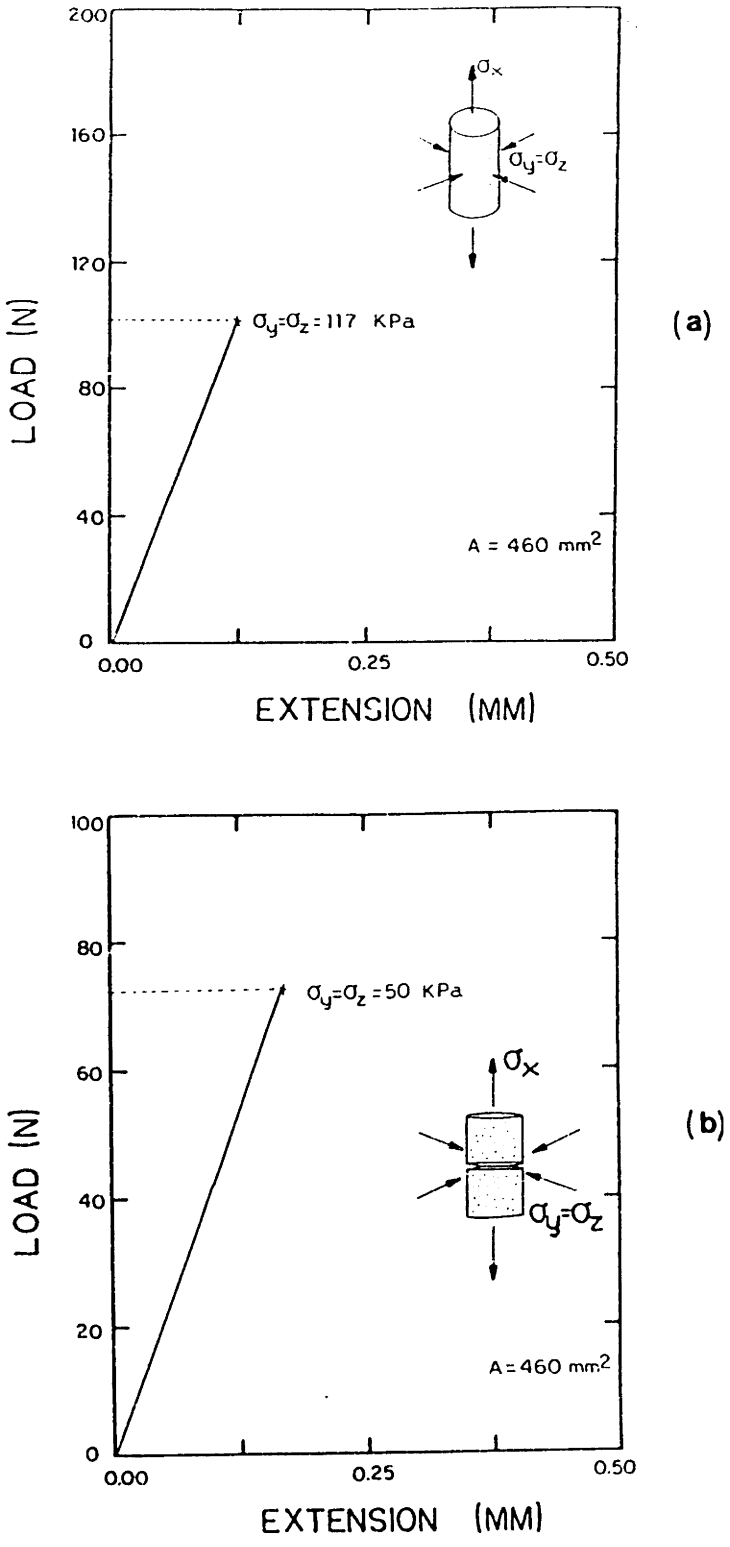

Fig. 6.32 Typical axial tensile load-deformation curves for reticulated vitreous carbon under axial tension and radial compression. The axial load acts parallel to the X material direction. (a) "Uncracked" specimens; (b) notched specimens.

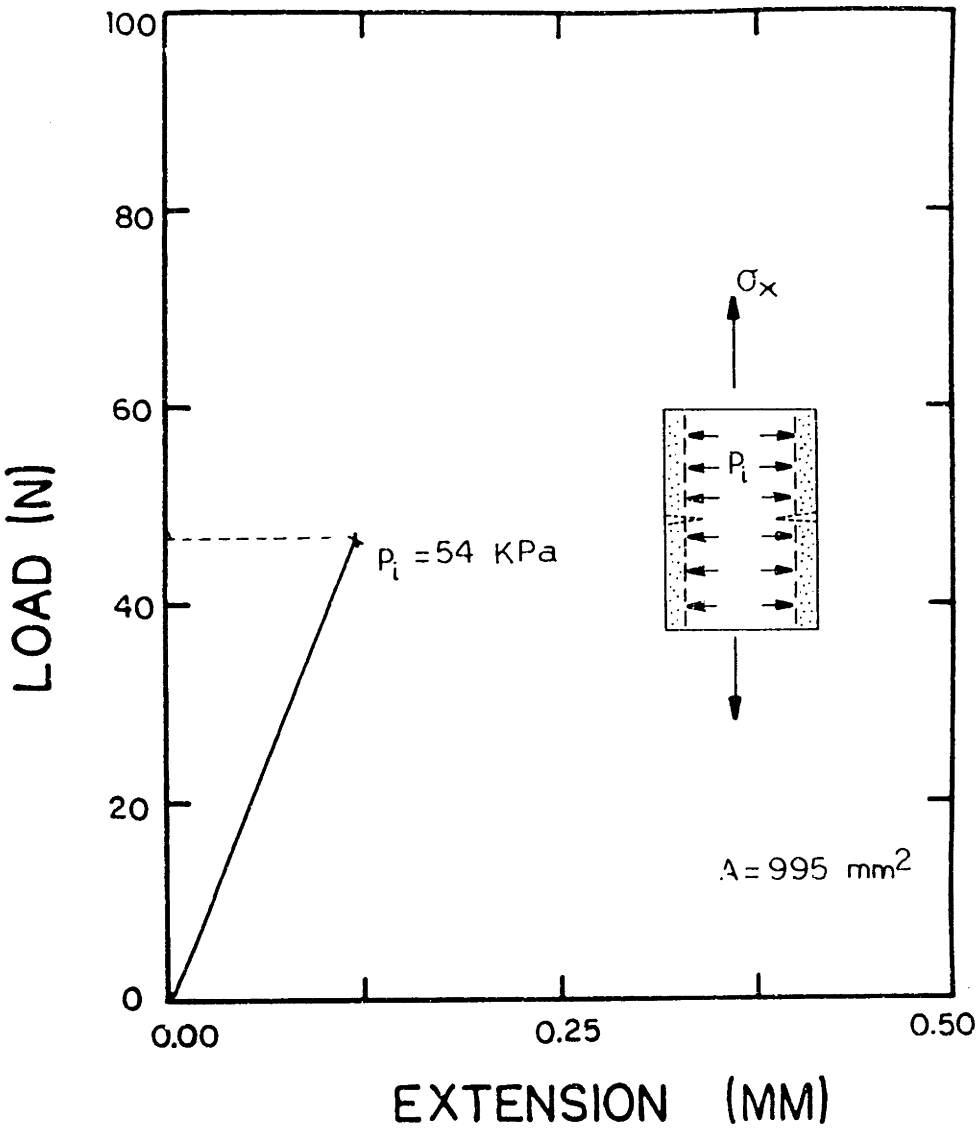

Fig. 6.33 A typical axial tensile load-deformation curve for notched reticulated vitreous carbon specimens under axial and radial tension. The axial load acts parallel to the X material direction.

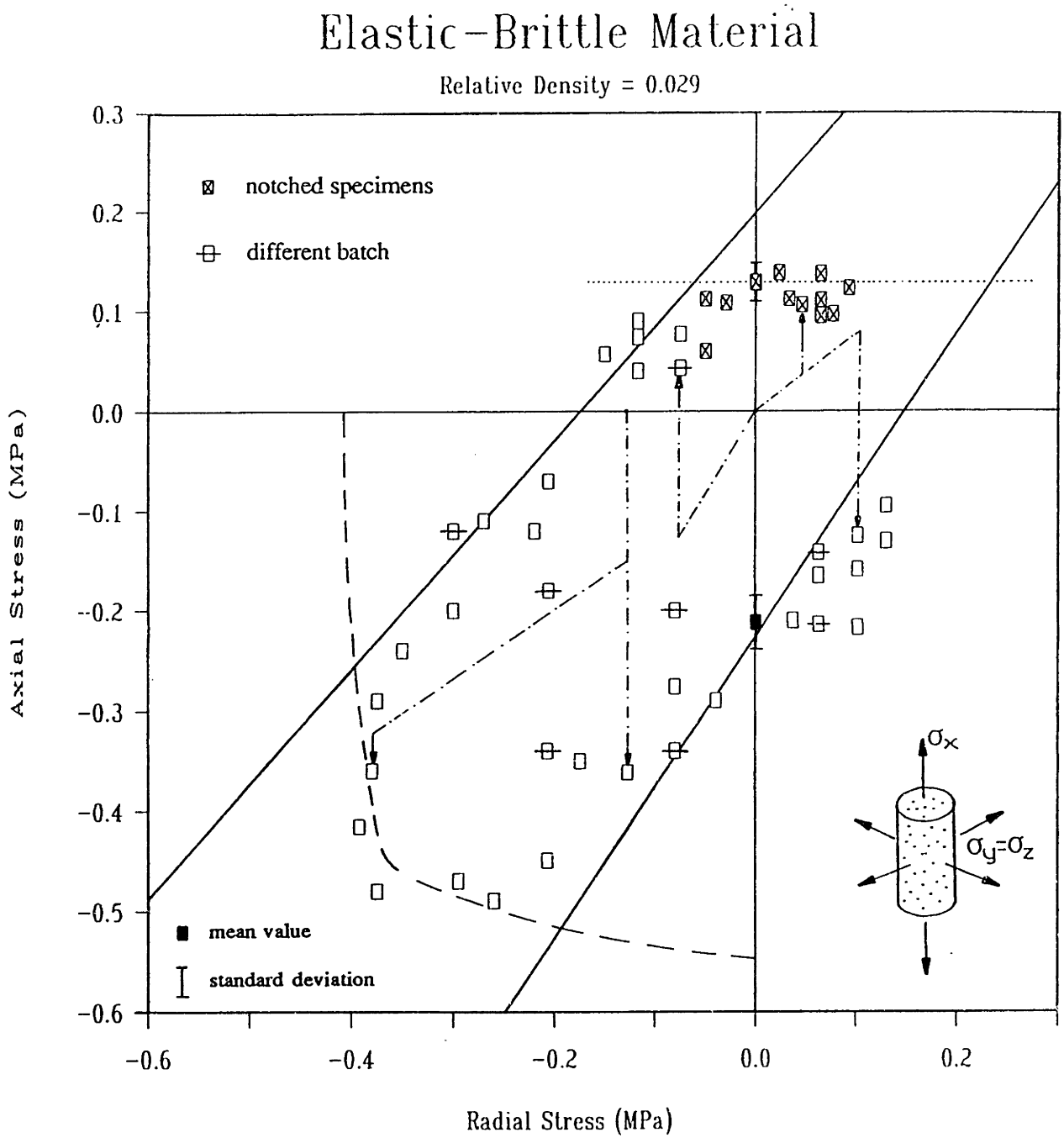

Fig. 6.34 Data for the failure of reticulated vitreous carbon (ρ^*=48 kg/m^3) under axisymmetric loading. The fracture envelope given by the model is indicated by the solid line; the tensile fracture cutoff is indicated by the dotted line; the elastic buckling cutoff is indicated by the dashed line. Typical stress paths are also illustrated.

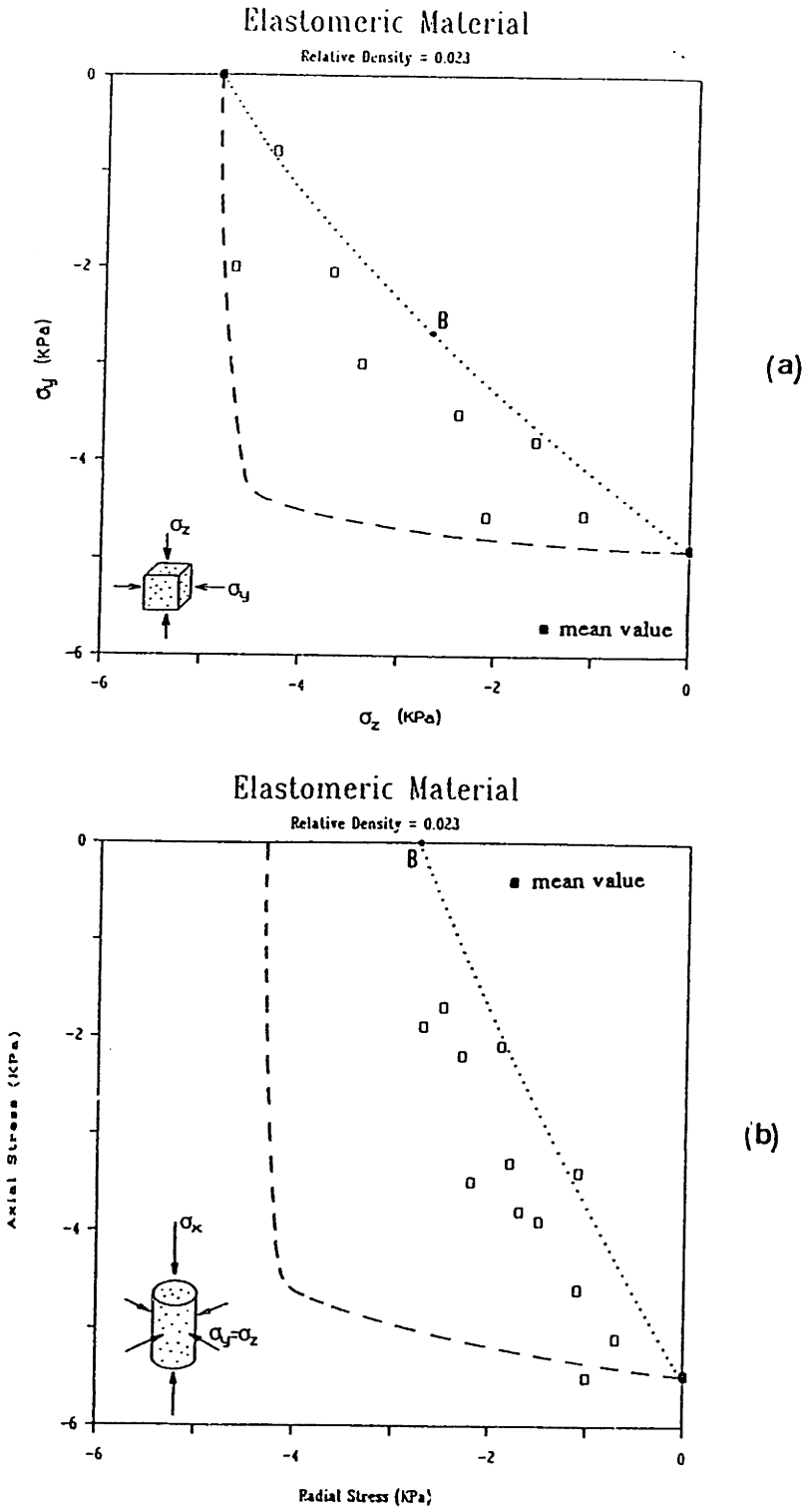

Fig. 6.35 Data for the failure of flexible polyurethane foam. The elastic buckling envelope given by Zhang (1987) is indicated by the dashed lines. The elastic buckling envelope proposed by Gibson and Ashby (1988) is indicated by the dotted lines (point B corresponds to equal biaxial compression). (a) Biaxial compression; (b) axisymmetric compression.

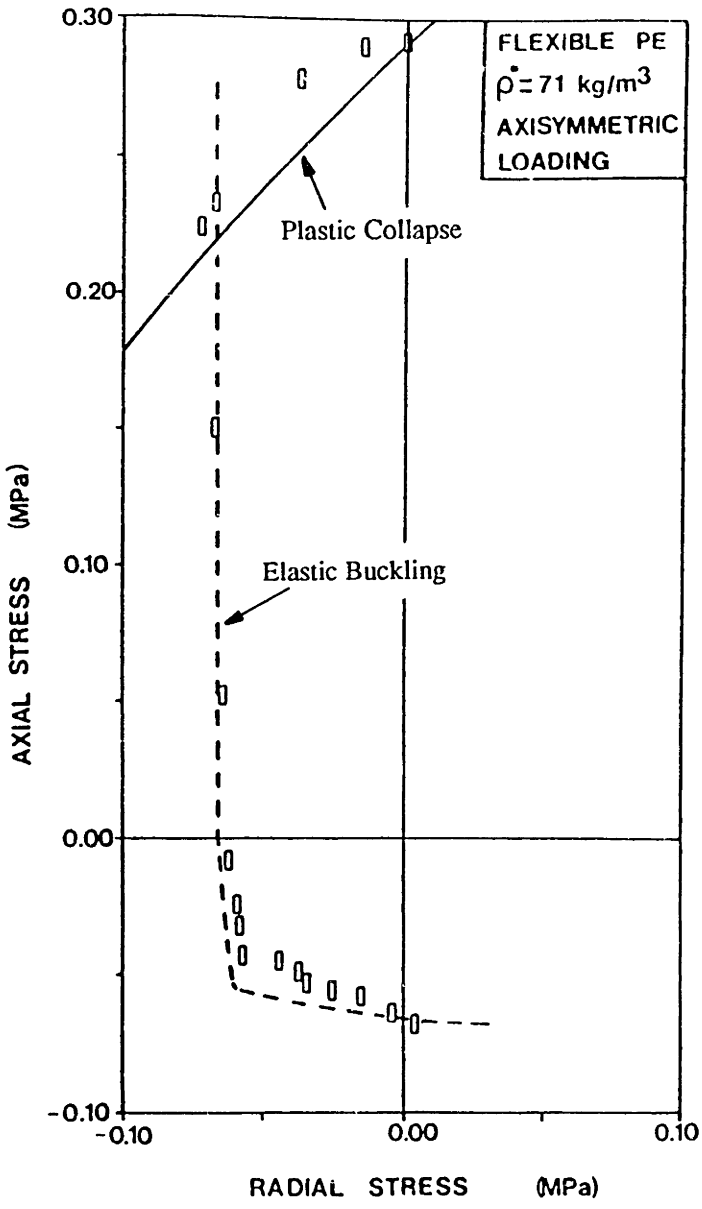

Fig. 6.36 Comparison of the proposed plastic collapse envelope and Zhang's (1987) elastic buckling envelope with his results from axisymmetric tests on flexible polyethylene.

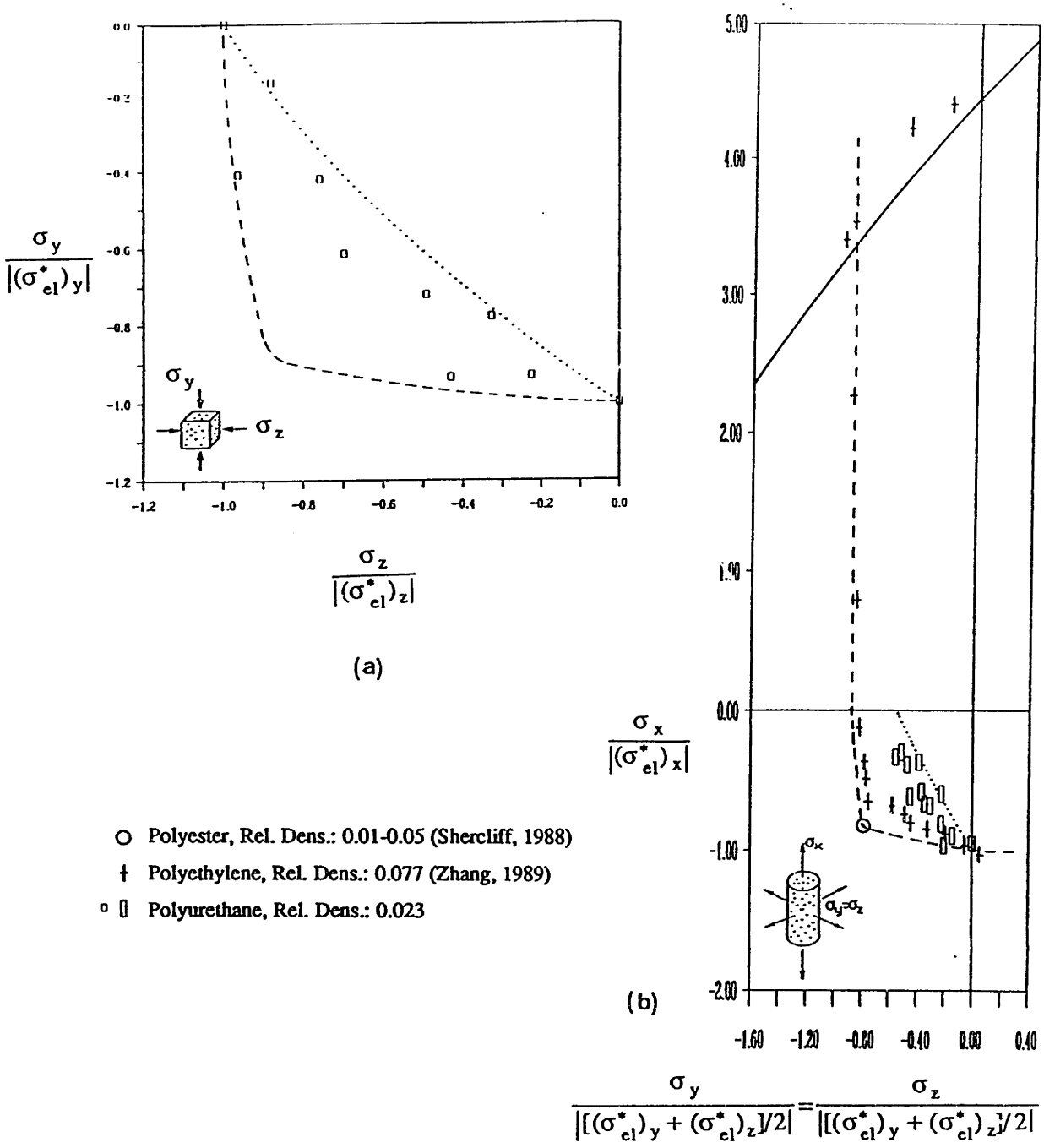

Fig. 6.37 Data for the failure of elastomeric foams, plotted in strength-normalized axes. The dashed lines indicate Zhang's (1987) elastic-buckling envelopes. The dotted lines indicate Gibson and Ashby's (1988) elastic buckling envelopes. The solid line indicates the proposed plastic collapse envelope. (a) Biaxial compression; (b) axisymmetric compression.

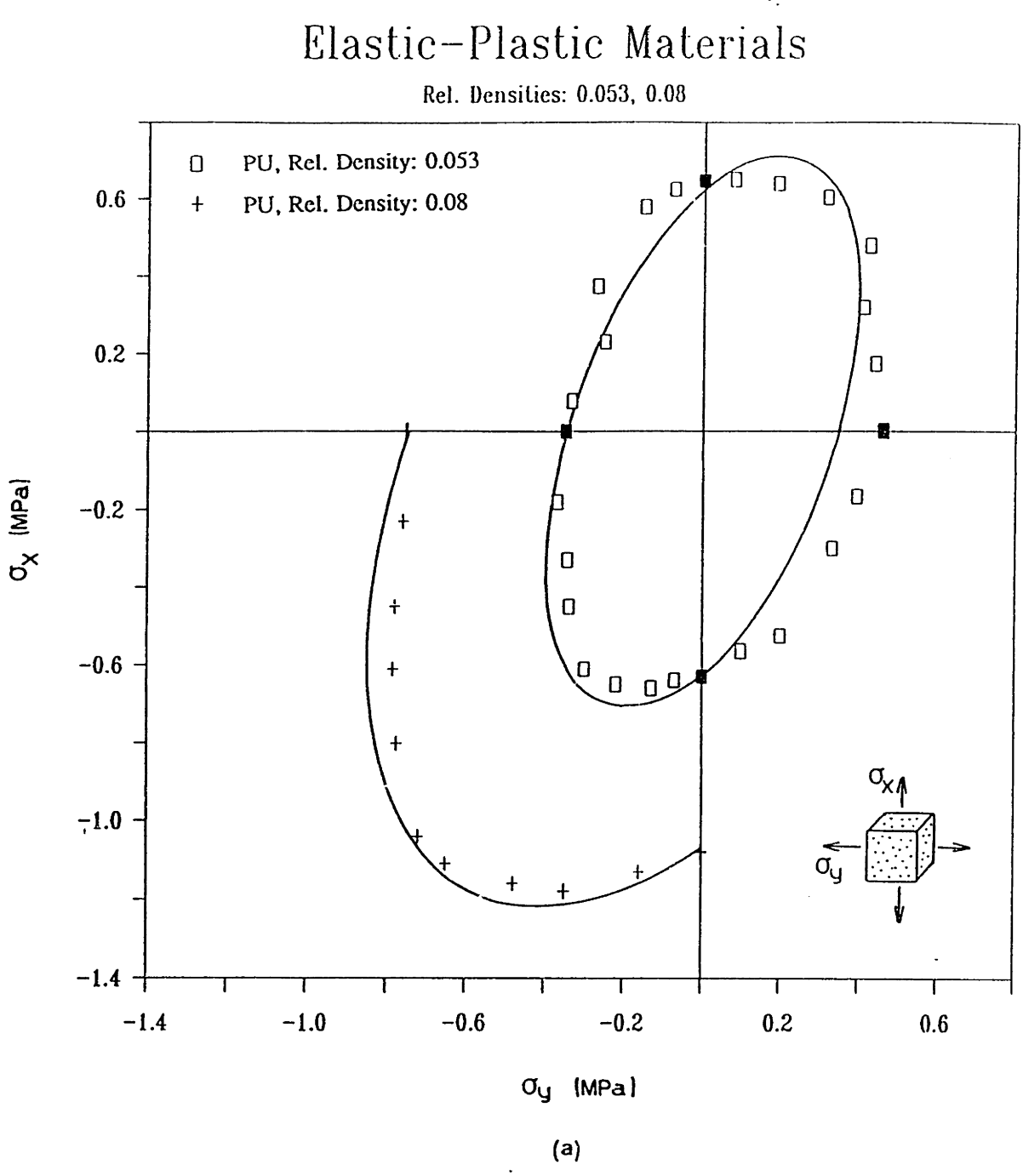

Fig. 6.38 Comparison of the proposed yield envelope with data for the failure of rigid polyurethane foams under biaxial stress conditions. (a) Stresses act in the X-Y plane; (b) stresses act in the Y-Z plane.

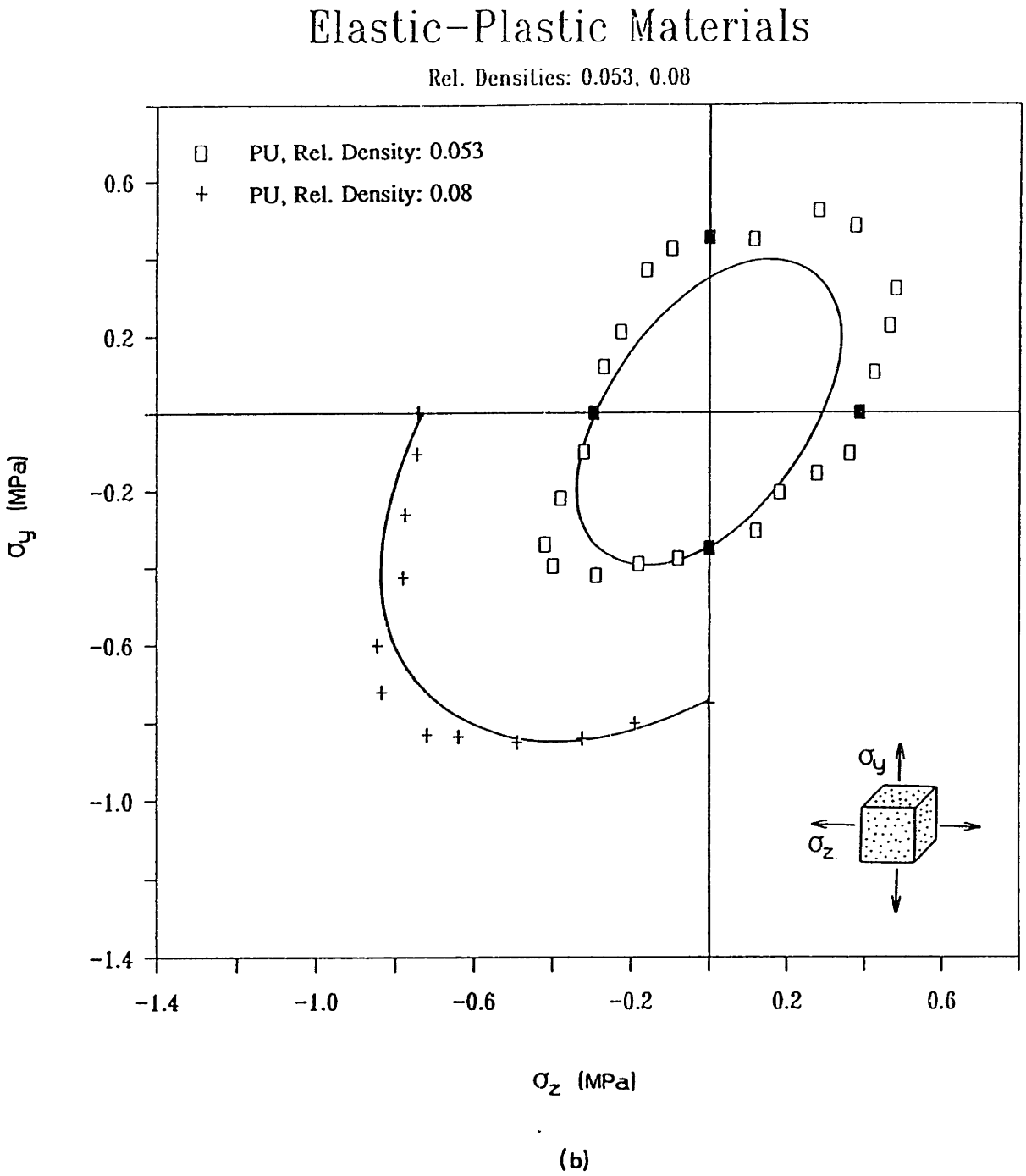

(b)

Fig. 6.38 cont'd.

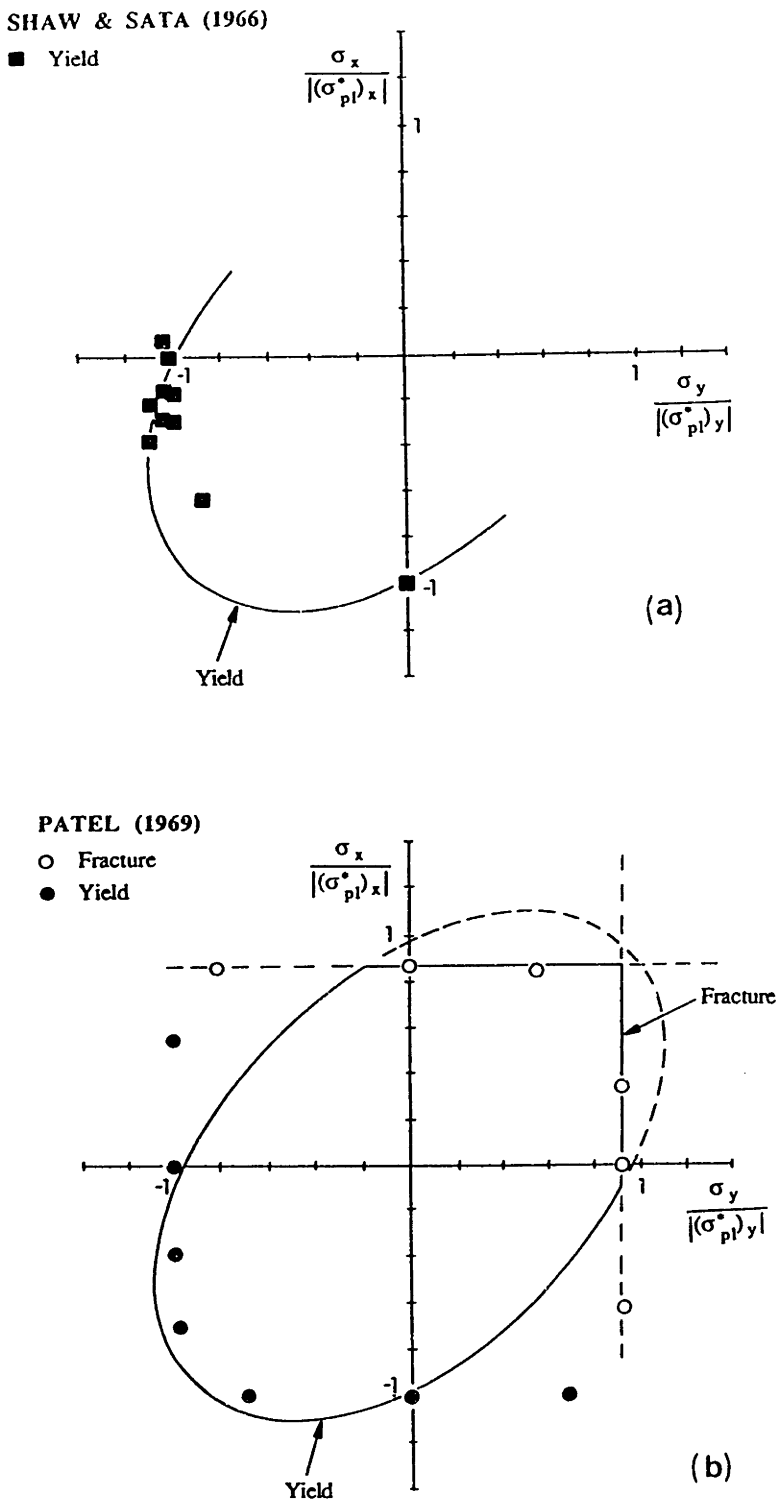

Fig. 6.39 Comparison of the proposed failure envelopes with biaxial test results from previous studies: (a) foamed polystyrene, Shaw and Sata (1966); (b) rigid polyurethane foam, Patel (1969).

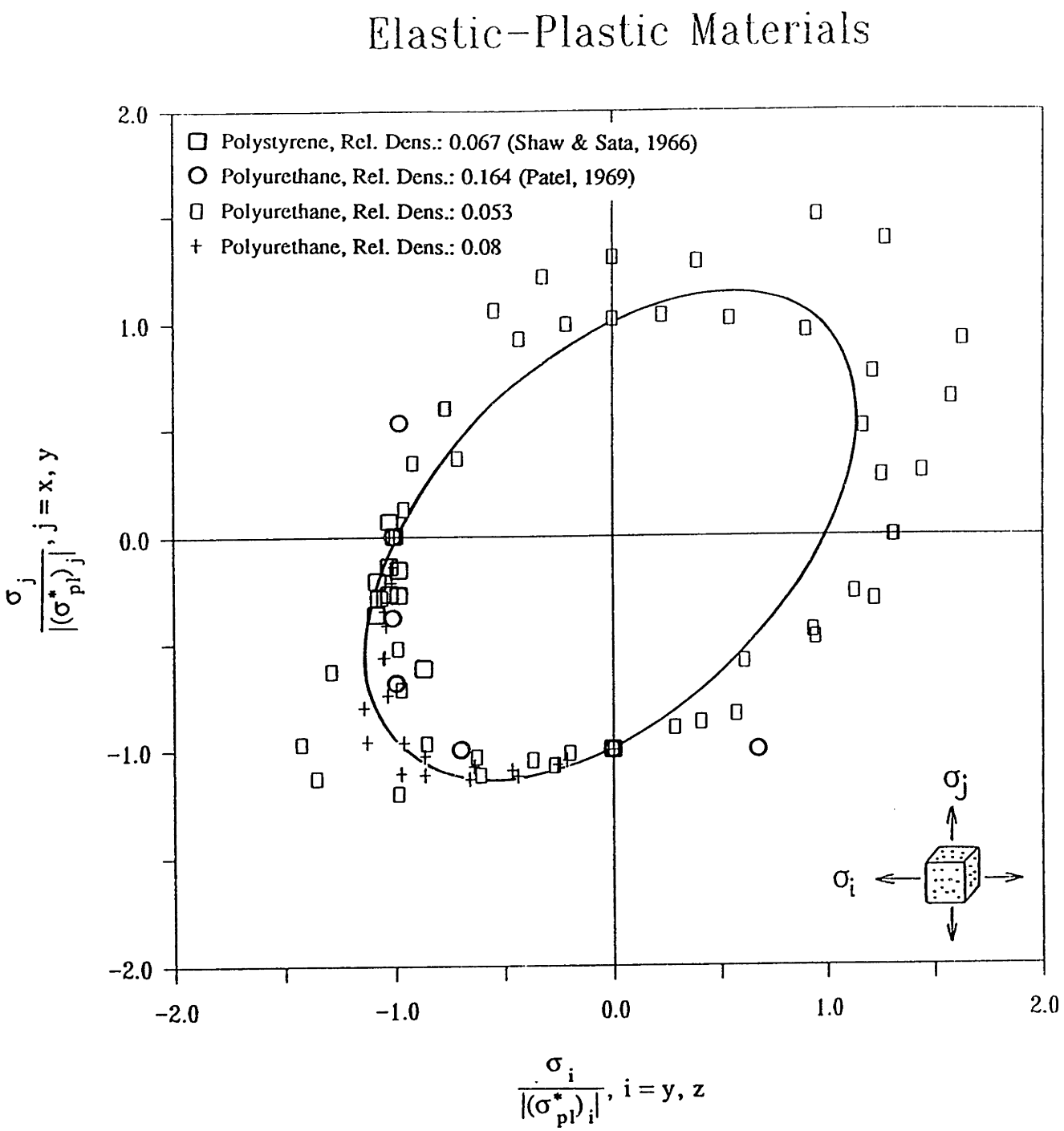

Fig. 6.40 Data for the plastic collapse of foams under biaxial stresses. The data are plotted in strength-normalized axes. The solid line indicates the proposed envelope.

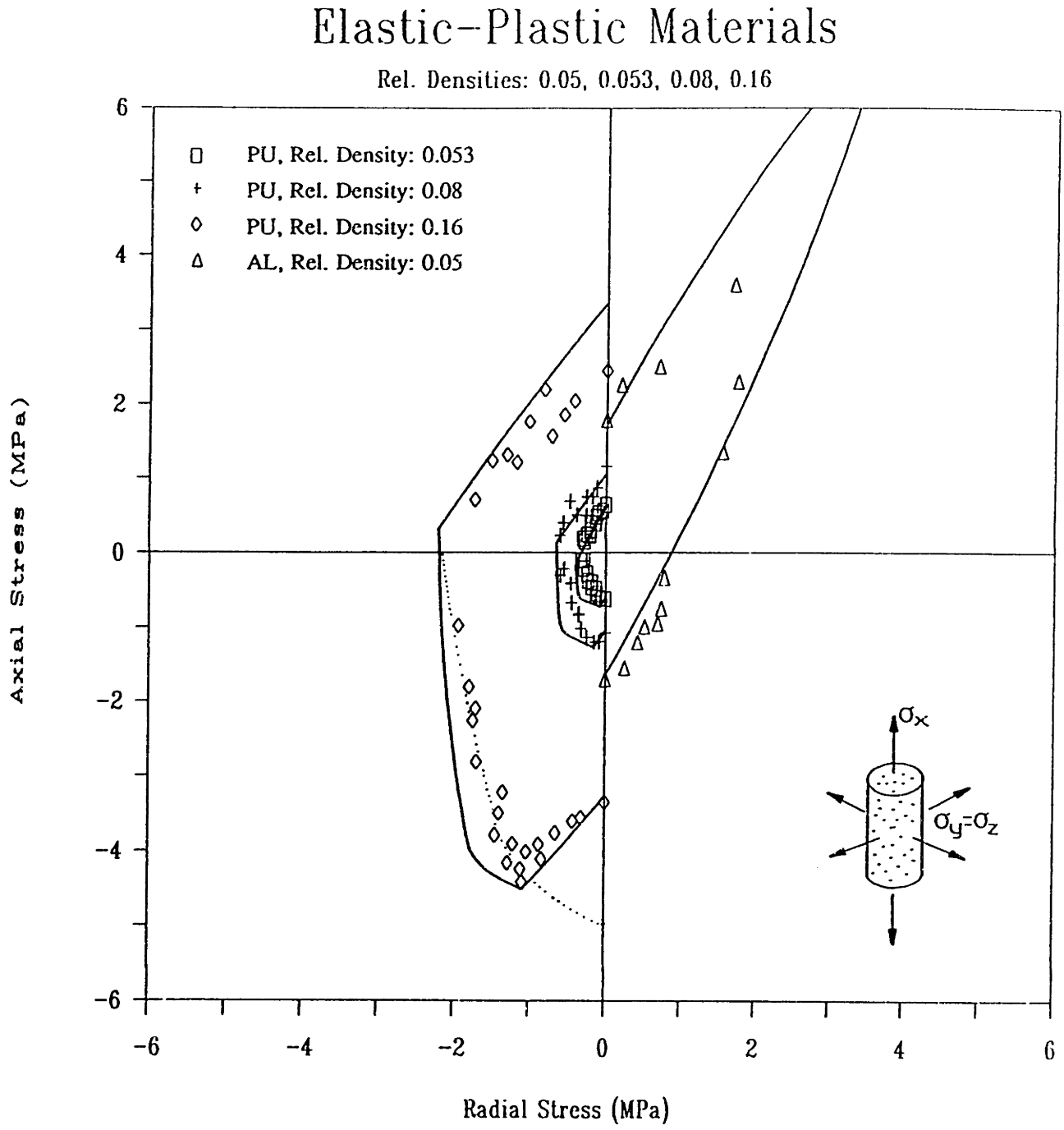

Fig. 6.41 Comparison of the data for the failure of elastic-plastic foams under axisymmetric stress conditions, with the proposed yield envelopes and the elastic buckling cutoff in the compression octant given by Zhang (1987). The dotted line indicates extrapolation of the data to estimate the uniaxial and biaxial (with equal stresses) elastic buckling strengths.

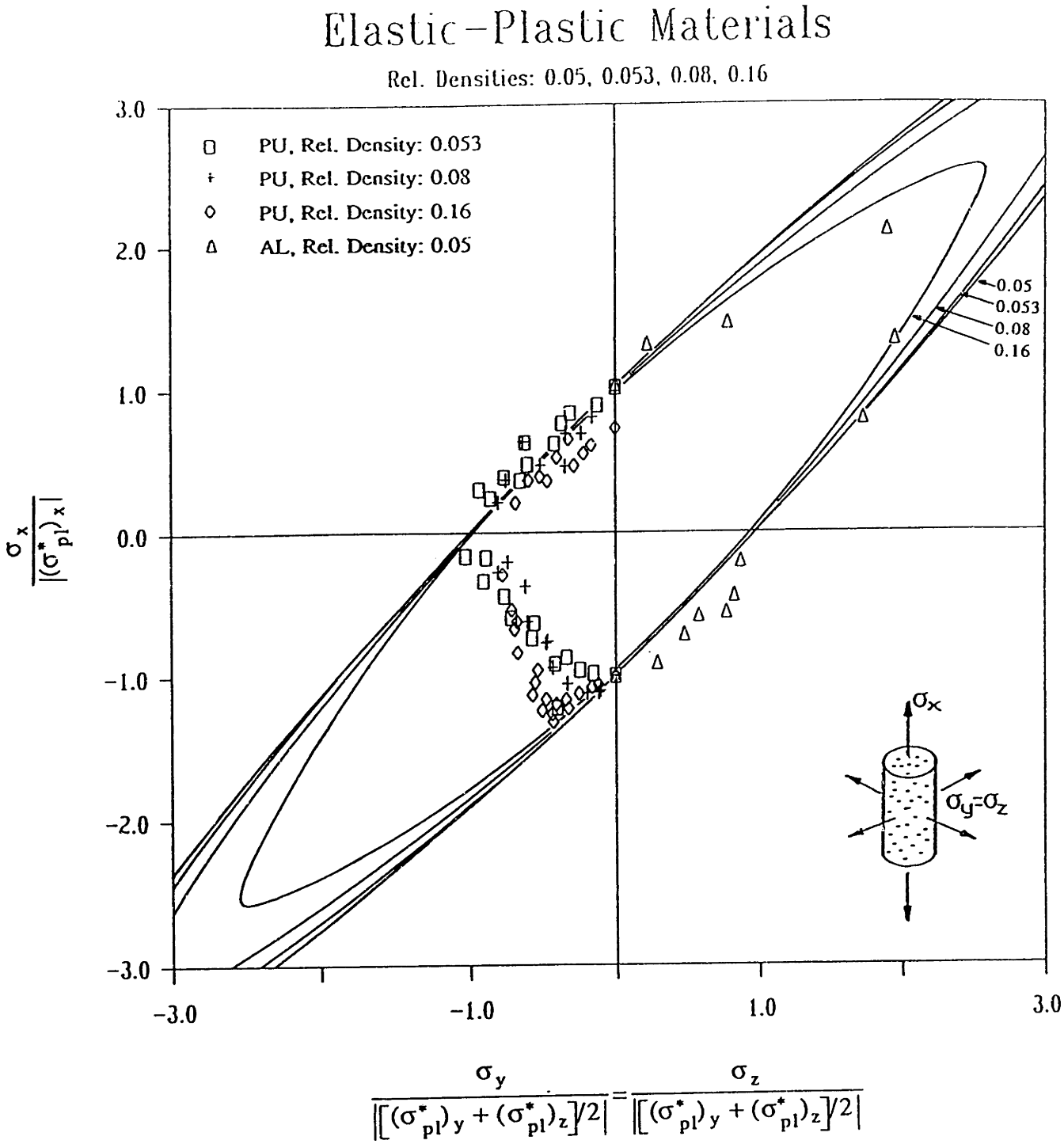

Fig. 6.42 Comparison of the data for axisymmetric loading of elastic-plastic foams with the proposed yield envelopes. Both the data and the failure envelopes are normalized with respect to the uniaxial plastic collapse stresses.

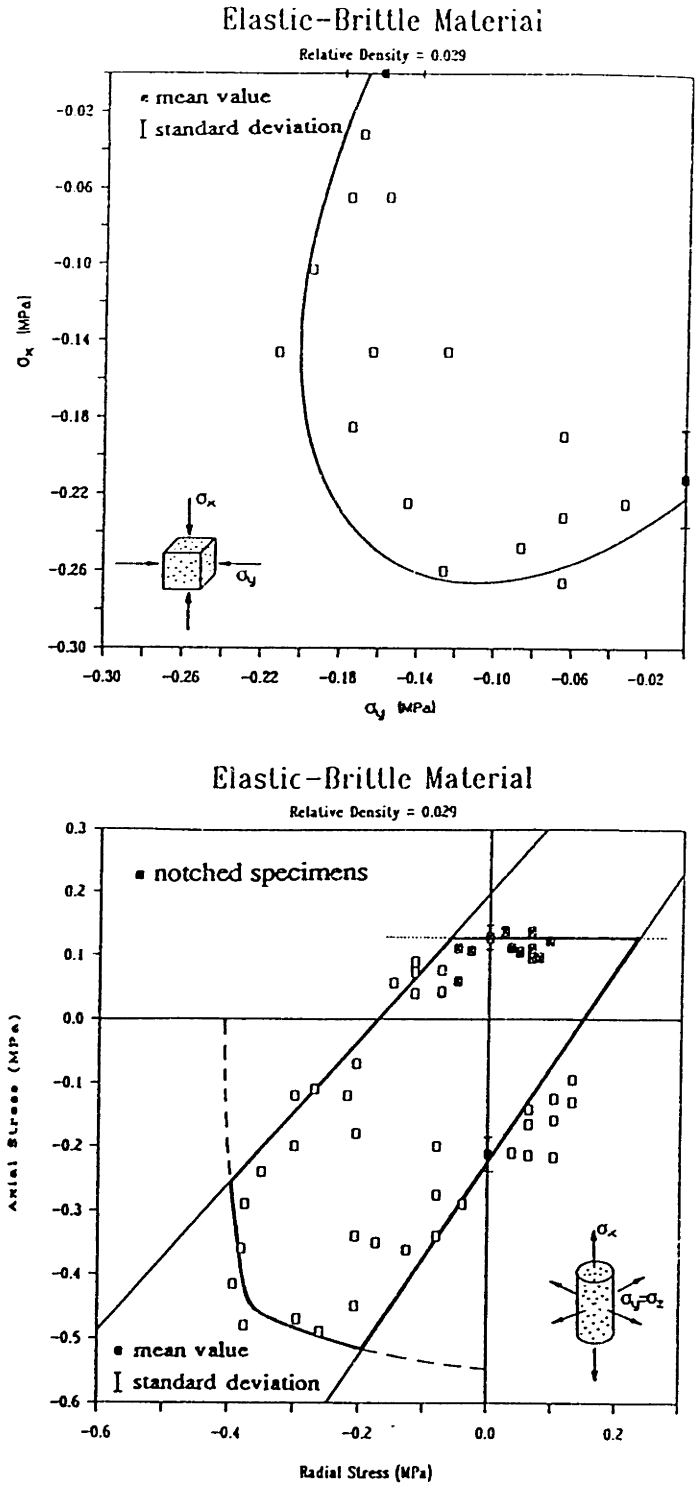

Fig. 6.43 Comparison of the data for the failure of reticulated vitreous carbon foam with the proposed failure envelopes. The fracture envelope given by the model is indicated by the solid line; the tensile fracture cutoff is indicated by the dotted line; Zhang's (1987) elastic buckling cutoff is indicated by the dashed line. (a) Biaxial compression; (b) axisymmetric loading.

CHAPTER VII

CONSTITUTIVE MODELING AND MULTIAXIAL FAILURE CRITERIA FOR ELASTIC-PLASTIC CELLULAR MATERIALS: IMPLICATIONS IN ENGINEERING DESIGN

7.1 Introduction

Engineering design problems involving the use of foams sometimes call for the finite element method of analysis; this chapter describes the implementation of FEM analysis using the complete constitutive equations for the foam. Foams are widely used as the cores of structural sandwich panels and as packaging to provide protection from accidental impacts. In both applications, the material may be subjected to multiaxial loads; this chapter also describes the use of the multiaxial failure criteria developed earlier to select foams with the appropriate properties. Elastic-plastic foams are most commonly used in the above applications; our discussion will be limited to them.

The finite element method can only be applied if the constitutive model of the material to be analyzed is available. The complete constitutive equations for elastic-plastic foams are described in this chapter, along with their use in FEM analysis.

Sandwich panels can fail in several ways: the faces or the core can yield plastically or fracture depending on the nature of the materials from which they are made; the compressive face can buckle locally or "wrinkle"; and the bond between the faces and core can fracture, causing delamination (Triantafillou and Gibson, 1987a). Our focus in this chapter is on the failure of the core. Existing failure criteria will be compared with the predictions given by the models developed in this work.

An effective package must absorb the energy of impacts or of forces generated by deceleration without subjecting the contents to damaging stresses. A description of the steps to be followed in packaging design is presented at the end of the chapter.

7.2 Constitutive Modeling and Finite Element Analysis

Problems involving complicated structural sandwich plates and shells under multiple loading conditions are difficult to solve analytically. Analytical solutions very often resort to series expansions of the displacement field and use of the energy theorems of structural analysis (e.g., Allen, 1969). The analysis is carried out more easily when numerical methods are employed. The *finite strip* and the *finite prism* methods are especially efficient in analyzing prismatic members such as building sandwich beams, for which it would be prohibitive in cost and time to apply the finite element method. The pioneering papers on the finite strip method were written by Cheung on plate bending problems (1968a and b); they were applied by the same author in the analysis of flat-faced sandwich plates (Cheung, 1976). The finite prism method was described by Cheung et al., (1976). The various applications of the finite strip method, the finite prism method, and, in addition, of the *finite layer* method are discussed comprehensively in Cheung (1981). The finite element method offers two advantages: it is of more general applicability, and it is already implemented in many commercial programs.

A nonlinear analysis using the finite element method requires a complete constitutive model in addition to the failure criterion for the material. A simple flow chart for a typical nonlinear finite element program is illustrated in Fig. 7.1. The discussion that follows describes a complete constitutive model for cellular materials idealized as isotropic elastic-perfectly plastic. The assumption of elastic-perfectly plastic behavior is in agreement with experimental evidence (see Figs 6.6, 6.7).

The elastic behavior is described by the following equation (Chen and Saleeb, 1982):

$$\sigma_{ij}=K\varepsilon_{kk}\delta_{ij}+2Ge_{ij} \tag{7.1}$$

where K=bulk modulus

G=shear modulus

e_{ij}=deviatoric strain

The shear modulus of the foam is given by Gibson and Ashby (1982) as

$$G^* = \frac{3}{8}\left(\frac{\rho^*}{\rho_s}\right)^2 E_s \tag{7.2}$$

In the above equation, ρ^* is the bulk material density, and ρ_s and E_s are the density and elastic modulus of the cell wall material, respectively. Since the bulk modulus of the foam, K^*, is associated with axial stretching of the cell walls only, we can write:

$$K^* = \frac{1}{3}\left(\frac{\rho^*}{\rho_s}\right)E_s \tag{7.3}$$

Combining eqns (7.1)-(7.3), the elastic behavior is described as follows:

$$\sigma_{ij} = \frac{1}{3}\left(\frac{\rho^*}{\rho_s}\right)E_s\varepsilon_{kk}\delta_{ij} + \frac{3}{4}\left(\frac{\rho^*}{\rho_s}\right)^2 E_s e_{ij} \tag{7.4}$$

or, in matrix form:

$$\{\sigma\}=[C^e]\{\varepsilon\} \tag{7.5}$$

$$\{\sigma\}^T=\{\sigma_x\ \sigma_y\ \sigma_z\ \tau_{xy}\ \tau_{yz}\ \tau_{zx}\}$$

$$\{\varepsilon\}^T=\{\varepsilon_x\ \varepsilon_y\ \varepsilon_z\ \gamma_{xy}\ \gamma_{yz}\ \gamma_{zx}\}$$

$$[C^e] = \begin{bmatrix} C_{11} & C_{12} & C_{12} & 0 & 0 & 0 \\ & C_{11} & C_{12} & 0 & 0 & 0 \\ & & C_{11} & 0 & 0 & 0 \\ & & & C_{44} & 0 & 0 \\ & \text{sym.} & & & C_{44} & 0 \\ & & & & & C_{44} \end{bmatrix}$$

$$C_{11} = E_s\left(\frac{\rho^*}{\rho_s}\right)\left[\frac{1}{3} + \frac{1}{2}\left(\frac{\rho^*}{\rho_s}\right)\right]$$

$$C_{12} = E_s\left(\frac{\rho^*}{\rho_s}\right)\left[\frac{1}{3} - \frac{1}{4}\left(\frac{\rho^*}{\rho_s}\right)\right]$$

$$C_{44} = \frac{3}{8}E_s\left(\frac{\rho^*}{\rho_s}\right)^2$$

The post-yield behavior was developed in Appendix 4B assuming associated plasticity (see eqns (4B.19) and (4B.20)). Note that the failure criterion is that described by eqn. (4.17). The applicability of the post-yield constitutive model is limited by the fact that the stress-strain curve in compression rises steeply at high strains, when the material densifies (see Fig. 4.1). The densification strain, ε_D, is approximately equal to $1-1.4(\rho^*/\rho_s)$ for uniaxial loading (Gibson and Ashby, 1988), and it is expected that a similar value is reached by the maximum principal strain when the material starts to densify under multiaxial loading conditions. The above expression gives strains of the order of 70%-90%, which are very unlikely to occur in practical applications.

Next, we briefly present a general numerical procedure for incorporating the

elastic-plastic constitutive models into computer programs (Zienkiewicz et al., 1969; Bathe, 1982; Chen, 1982). The input quantities in the present discussion are the stress components $\{\sigma\}_n$ and the strain components $\{\varepsilon\}_n$ obtained at the end of the nth loading increment, and the components of the new strains $\{\varepsilon\}_{n+1}$. The procedure to calculate the stresses $\{\sigma\}_{n+1}$ at the end of the (n+1)th loading increment is illustrated below:

1) Calculate the strain increment $\{\Delta\varepsilon\}_{n+1}=\{\varepsilon\}_{n+1}-\{\varepsilon\}_n$

2) Calculate the stress increment $\{\Delta\sigma\}$, assuming elastic behavior:

$$\{\Delta\sigma\}_{n+1}=[C^e]\{\Delta\varepsilon\}_{n+1}$$

3) Calculate the trial stress $\{\sigma\}'_{n+1}=\{\sigma\}_n+\{\Delta\sigma\}_{n+1}$

4) With $\{\sigma\}'_{n+1}$ as the state of stress, determine the value of the yield function f_1 (see eqn. (4.17)).

5) If $f_1(\{\sigma\}'_{n+1})\leq 0$, elastic behavior assumption holds. Hence $\{\sigma\}_{n+1}=\{\sigma\}'_{n+1}$ and *we return.*

   If $f_1(\{\sigma\}'_{n+1})>0$, *we continue.*

6) If the previous state of stress was plastic, we set r=0 and go to step 7). Otherwise, there is a transition from elastic to plastic behavior, and r, which is the portion of incremental strain taken elastically has to be determined; it is determined from the equation

$$f_1(\{\sigma\}_n+r\{\Delta\sigma\}_{n+1})=0$$

   since at the stress $\{\sigma\}_n+r\{\Delta\sigma\}_{n+1}$ the yield function f_1 becomes equal to zero and yielding is initiated.

7) Redefine $\{\sigma\}'_{n+1}$ as the stress at start of yield

$$\{\sigma\}'_{n+1}=\{\sigma\}_n+r\{\Delta\sigma\}_{n+1}$$

   and calculate the elastic-plastic strain increment

$$\{\Delta\varepsilon^{ep}\}_{n+1}=(1-r)\{\Delta\varepsilon\}_{n+1}$$

8) To obtain the final stresses, which include the effect of the complete strain increment

$\{\Delta\varepsilon\}_{n+1}$ we need to add to $\{\sigma\}'_{n+1}$ the stress corresponding to the elastic-plastic strain increment $\{\Delta\varepsilon^{ep}\}_{n+1}$. Since the material law is dependent on the current stress, $\{\Delta\varepsilon^{ep}\}_{n+1}$ is divided into subincrements $\{\Delta\varepsilon^{ep}_{sub}\}_{n+1}$ and $\{\sigma\}'_{n+1}$ is updated for each interval by the increments in stress corresponding to the increments in elastic-plastic strains in that interval. In the calculations, the stress-strain matrix corresponding to the latest available stress conditions is used; i.e., we calculate

$$\{\sigma\}'_{n+1} \leftarrow \{\sigma\}'_{n+1} + [C^{ep}]\{\Delta\varepsilon^{ep}_{sub}\}_{n+1}$$

for all elastic-plastic strain subincrements $\{\Delta\varepsilon^{ep}_{sub}\}_{n+1}$.

7.3 Design of Structural Sandwich Panels with Foam Cores

One way to test the validity of the failure condition for isotropic elastic-plastic foams obtained in Chapter 4 is to compare its predictions for the failure of the core in sandwich beams with data. The failure modes of a sandwich beam in bending are shown in Fig. 7.2. It may fail by the yielding of the faces (Kuenzi, 1965; Ueng and Liu, 1979; Froud, 1980; Ciba-Geigy, 1980; Triantafillou and Gibson, 1987a, b). The compression face may wrinkle-a local buckling of the skin into the core (Kuenzi, 1965; Allen, 1969; Chong and Hartsock, 1972 and 1974). The core, too, can fail, usually in shear (Ciba-Geigy, 1980; Hall and Robson, 1984) though compressive or tensile failure is also possible. Then, there is the bond between the face and core: it can fail; and since resin adhesives are usually brittle, debonding is by brittle fracture (Hong and Jeong, 1985; Zenkert, 1988; Triantafillou and Gibson, 1989). Finally, there is the possibility of indentation of the faces and core at the loading point; this can be avoided if the loads are distributed over a sufficiently large area. In a comprehensive study, Triantafillou and Gibson (1987a) developed equations describing the failure load for each mode of failure; they also produced failure mode maps showing the beam designs for which each failure mode is dominant, and gave the results of experiments confirming the failure equations and the failure mode maps.

Consider the sandwich beam shown in Fig. 7.3. The normal and shear stress distributions are illustrated in Fig. 7.4. The distributions shown in Figs 7.4e and 7.4f

approximate very closely the exact distributions in sandwich beams with *thin faces* and *compliant cores* (Allen, 1969); this is typical in most sandwich structures. In their study, Triantafillou and Gibson (1987a) assume that the core material fails when either the maximum principal stress, σ_1, equals the uniaxial yield strength, σ^*_{pl}, or the maximum shear stress, τ_{max}, equals the shear yield strength, τ^*_{pl}. The two failure conditions are written as follows:

$$\pm\frac{\sigma_x}{2}\pm\sqrt{\frac{\sigma_x^2}{4}+\tau_{xy}^2}=\sigma^*_{pl} \tag{7.6}$$

$$\sqrt{\frac{\sigma_x^2}{4}+\tau_{xy}^2}=\tau^*_{pl} \tag{7.7}$$

Equations (7.6) and (7.7) are now written in a more convenient form,

$$\pm\frac{\sigma_x}{\sigma^*_{pl}}+\frac{\tau_{xy}^2}{(\sigma^*_{pl})^2}=1 \tag{7.8}$$

$$\frac{\sigma_x^2}{4(\tau^*_{pl})^2}+\frac{\tau_{xy}^2}{(\tau^*_{pl})^2}=1 \tag{7.9}$$

The failure criterion obtained earlier for isotropic elastic-plastic foams (see eqn. (4.17)), when applied to plane stress conditions with a normal stress, σ_x, and a shear stress, τ_{xy}, yields the following:

$$\pm\left[\frac{\sigma_x^2}{(\sigma^*_{pl})^2}+\frac{3\tau_{xy}^2}{(\sigma^*_{pl})^2}+\right]^{1/2}+0.09\left(\frac{\rho^*}{\rho_s}\right)\frac{\sigma_x^2}{(\sigma^*_{pl})^2}=1 \tag{7.10}$$

Now, we wish to compare the inner envelope of eqns (7.8) and (7.9) plotted in the σ_x-τ_{xy} plane, with that given by eqn. (7.10). To do this, a relationship between σ^*_{pl} and τ^*_{pl} must be established. This relationship is obtained as follows: the general failure criterion (eqn. (4.17)) is applied to the case of plane stress biaxial tension-compression with $\sigma_1=-\sigma_2=\sigma$, and gives that $\sigma=(\sqrt{3}/3)\sigma^*_{pl}$; noting that this state of stress is equivalent to that of pure shear with $\tau=\sigma$, we conclude that

$$\tau^*_{pl} = \frac{\sqrt{3}}{3}\sigma^*_{pl} \tag{7.11}$$

Combining eqns (7.8) and (7.9) with (7.11) we obtain:

$$\pm \frac{\sigma_x}{\sigma^*_{pl}} + \frac{\tau^2_{xy}}{3(\tau^*_{pl})^2} = 1 \tag{7.12}$$

$$\frac{3\sigma^2_x}{4(\sigma^*_{pl})^2} + \frac{\tau^2_{xy}}{(\tau^*_{pl})^2} = 1 \tag{7.13}$$

Equations (7.12) and (7.13) describe the maximum principal stress and maximum shear stress criteria for the failure of the core material in structural sandwich beams. These criteria were used by Triantafillou and Gibson (1987a) in their earlier study (in the form given by eqns (7.12) and (7.13)); they are plotted in Fig. 7.5 with solid lines, along with their test results. The envelope described by the failure criterion obtained in this study (eqn. (7.10)) is plotted on the same figure with dashed lines, for a relative density ratio, ρ^*/ρ_s, equal to 0.1 (typical value in sandwich constructions); it is in close agreement with the inner envelope of eqns (7.12) and (7.13). The test results reported by Triantafillou and Gibson (1987a) correspond to almost pure shear conditions and do not help support either eqn. (7.10) or (7.13). Note that eqn. (7.10) gives a plot in the σ_x-τ_{xy} plane which

is practically insensitive to changes in the value of the relative density ratio, as long as this ratio is kept low (say $\rho^*/\rho_s<0.15$).

7.4 Material Selection in Packaging

Most things we buy are surrounded by packaging. The costs involved are considerable (Morton, 1978) and the potential for minimizing them is large. Very often, the packaging industry neglects the mechanics of the problem it faces; a lack of analysis is typical of much packaging. The reason for this lies in the complexity of the packaging process; the package must protect against drop, impact, puncture, crushing, and contamination by air, water, or other chemicals (Gibson, 1981).

The essence of protective packaging is the ability to absorb energy while keeping the peak force on the packaged object below the limit which will cause damage or injury. Foams are characterized by a tremendous energy absorption capacity, arising from the collapse of the cells as the cell walls buckle, bend plastically, or fracture. The peak stress generated is limited by the collapse stress, corresponding to a long, flat plateau of the stress-strain curve (see Fig. 4.1). By choosing the right cell wall material and relative density, the best foam can be selected for a given package.

An approach which has attractive generality as a way of optimizing the choice of foam, is offered by *energy absorption diagrams* (Maiti et al., 1984). The concept is briefly described next; note that the method is applicable only when the material is subjected to uniaxial stresses.

Consider Fig. 7.6a. It shows compression stress-strain curves for a given foam with a range of densities, at a fixed strain rate, $\dot{\varepsilon}_1$, and temperature, T_1. The area under each curve up to stress σ_p is the energy absorbed per unit volume, W. The value of W is plotted against σ_p for each curve, normalizing both by the modulus of the solid, E_s, in Fig. 7.6b. The best foam for a given package is the one that absorbs the most energy up to the maximum permitted package stress σ_p. Each foam density has a σ_p for which it is the best choice. It is given by the shoulder on the energy curve in Fig. 7.6b, because here the curve for that foam lies above that for any other.

Energy absorption diagrams give a systematic way of analysing the performance of foams in packaging. Given a foam of known material and density, the diagram immediately identifies the peak stress σ_p/E_s and the energy absorbed per unit volume, W/E_s, at which it is best used. The area of contact, A, between the foam and the packaged object can then be chosen to give a peak force ($F_p=\sigma_p A$) which is non-damaging, and the thickness, t, of the package can be adjusted so that the kinetic energy of the accidentally dropped object, U, is completely absorbed (U=WAt).

In some applications the packaging material resists complex multiaxial stress conditions. For instance, a multiaxial stress state arises in a protective helmet during an impact due to the complex geometry of the head and the helmet. The foam material in this case protects the head against impact by maintaining the stresses developed in the foam material (which are equal to the stresses applied onto the head) below a critical value. No analytical solution to the problem is possible. Instead, one has to perform a dynamic finite element analysis. The foam structure, considered as a continuum, is discretized in a fine mesh, and the multiaxial stresses developed are evaluated using the constitutive equations and the multiaxial failure criterion for the foam, as discussed in Section 7.2 for elastic-plastic foams.

To account for the effects of high strain rates, both the constitutive equations and the multiaxial failure criterion have to be modified. A logical modification for the second should be on the following basis: since the only parameters needed to describe the failure criterion are the relative density of the material and its uniaxial strength, a modified uniaxial strength must be considered, namely, the one that is obtained at the same strain rate as that of the impact.

The maximum stresses reached due to the impact will be obtained for a given foam from the time-history analysis. If they are above the required limits, the properties of the foam (relative density, yield strength of cell wall material) need to be changed and the analysis has to be performed again. The procedure is iterative in nature: it must be repeated until the maximum stresses developed are well below the specified "safe" values.

7.5 Conclusions

The evaluation of the response of foams under complex stress states very often requires the use of the finite element method. To facilitate the implementation of the method, the complete constitutive equations for isotropic elastic-plastic foams were described in this chapter.

The predictions of the newly developed multiaxial failure criterion for isotropic elastic-plastic 3D cellular solids were compared with analytical results obtained by previous theories with experimental support limited to nearly pure shear conditions. Comparisons were made in terms of the failure of the core material in structural sandwich panels. A remarkably close agreement was shown, adding confidence to the new failure criterion.

To properly evaluate the surface stresses suffered by a packaged component subjected to an impact (as a result of a drop, for instance), a dynamic finite element analysis is necessary, especially when the stress state developed is a complex multiaxial one. For elastic-plastic cellular materials, such an analysis should incorporate the constitutive model and the multiaxial failure criterion developed earlier in this study. This procedure should help in the optimum choice of packaging materials in applications with a complex package geometry.

References

Allen, H. G. (1969) *Analysis and Design of Structural Sandwich Panels*, Pergamon, Oxford.

Bathe, K.-J. (1982) *Finite Element Procedures in Engineering Analysis*, Prentice-Hall, Inc., New Jersey.

Chen, W. F. (1982) *Plasticity in Reinforced Concrete*, McGraw-Hill, New York.

Chen, W. F. and Saleeb, A. F. (1982) *Constitutive Equations for Engineering Materials, Vol. 1: Elasticity and Modeling*, John Wiley & Sons, Inc., New York.

Cheung, Y. K. (1968a) Finite Strip Method in the Analysis of Elastic Plates with Two Opposite Simply Supported Ends, *Proc. Inst. Civil Eng.*, **40**, 1.

Cheung, Y. K. (1968b) Finite Strip Method Analysis of Elastic Slabs, *J. Eng. Mech. Div.*, **94**(EM6), 1365.

Cheung, Y. K. (1976) *Finite Strip Method in Structural Analysis*, Pergamon.

Cheung, Y. K., Yeo, M. F. and Cumming, D. A. (1976) Three-Dimensional Analysis of Flexible Pavements with Special Reference to Edge Loads, *Proc. 1st Conf. of the Road Eng. Assoc. of Asia and Australia*, Bangkok.

Cheung, Y. K. (1981) Finite Strip Method in Structural and Continuum Mechanics, *Int'l. J. Structures*, **1**(1), 19.

Chong, K. P. and Hartsock, J. A. (1972) Flexural Wrinkling Mode of Elastic Buckling in Sandwich Panels, *Proc. ASCE Specialty Conf. on Composite Materials*, Pittsburgh, PA.

Chong, K. P. and Hartsock, J. A. (1974) Flexural Wrinkling in Foam-Filled Sandwich Panels, *J. Eng. Mech. Div.*, **100**(EM1), ASCE, 95-110, 1974.

Ciba-Geigy (1980) Aeroweb Honeycomb Sandwich Design, *Instr. Sheet AGC.33a, Part 2*, Bonded Structures Division, Duxford, Cambridge, U.K.

Froud, G. R. (1980) Your Sandwich Order, Sir?, *Composites*, **11**, 133.

Gibson, L. J. (1981) The Elastic and Plastic Behaviour of Cellular Materials, Ph.D. Thesis, Cambridge University Engineering Department, Cambridge, U.K.

Gibson, L. J. and Ashby, M. F. (1982) The Mechanics of Three-Dimensional Cellular Materials, *Proc. Roy. Soc.*, **A382**, 43.

Gibson, L. J. and Ashby, M. F. (1988) *Cellular Solids: Structure and Properties*,

Pergamon, Oxford.

Hall, D. J. and Robson, B. L. (1984) A Review of the Design and Materials Evaluation Programme for the GRP/Foam Sandwich Composite Hull of the RAN Minehunter, *Composites*, **15**, 266.

Hong, C. S. and Jeong, K. Y. (1985) Stress Intensity Factors in Anisotropic Sandwich Plate with a Part-Through Crack Under Mixed Mode Deformation, *Eng. Fract. Mech.*, **21**(2), 285.

Kuenzi, E. W. (1965) Minimum Weight Structural Sandwich, *U.S. Forest Service Res. Note FPL-086*, Forest Products Laboratory, Madison, WI.

Maiti, S. K., Gibson, L. J. and Ashby, M. F. (1984) Deformation and Energy Absorption Diagrams for Cellular Materials, *Acta Metal.*, **32**, 1963.

Morton, D. H. (1978) The Use of Materials in Packaging Systems, *Int. J. of Materials in Engineering Applications*, **1**, 66.

Triantafillou, T. and Gibson, L. J. (1987a) Failure Mode Maps for Foam Core Sandwich Beams, *Mat. Sci. Eng.*, **95**, 37.

Triantafillou, T. and Gibson, L. J. (1987b) Minimum Weight Design of Foam Core Sandwich Panels for a Given Strength, *Mat. Sci. Eng.*, **95**, 55.

Triantafillou, T. and Gibson, L. J. (1989) Debonding in Foam-Core Sandwich Panels, to appear in *Materials and Structures.*

Ueng, C. E. S. and Liu, T. L. (1979) Least Weight of a Sandwich Panel, in R. R. Craig (ed.), *Proc. ASCE Engineering Mechanics 3rd Specialty Conf., University of Texas at Austin, Sept. 17-19*, ASCE, N.Y., 41.

Zenkert, D. (1988) Sandwich Constructions: Development of a New Structural Element and Fracture of Core Materials, Report No. 88-20, The Royal Institute of Technology, Stockholm, Sweden.

Zienkiewicz, O. C., Valliapan, S. and King, I. P. (1969) Elasto-Plastic Solutions of Engineering Problems. Initial-Stress, Finite Element Approach, *Int. J. Num. Meth. Eng.*, **1**, 75.

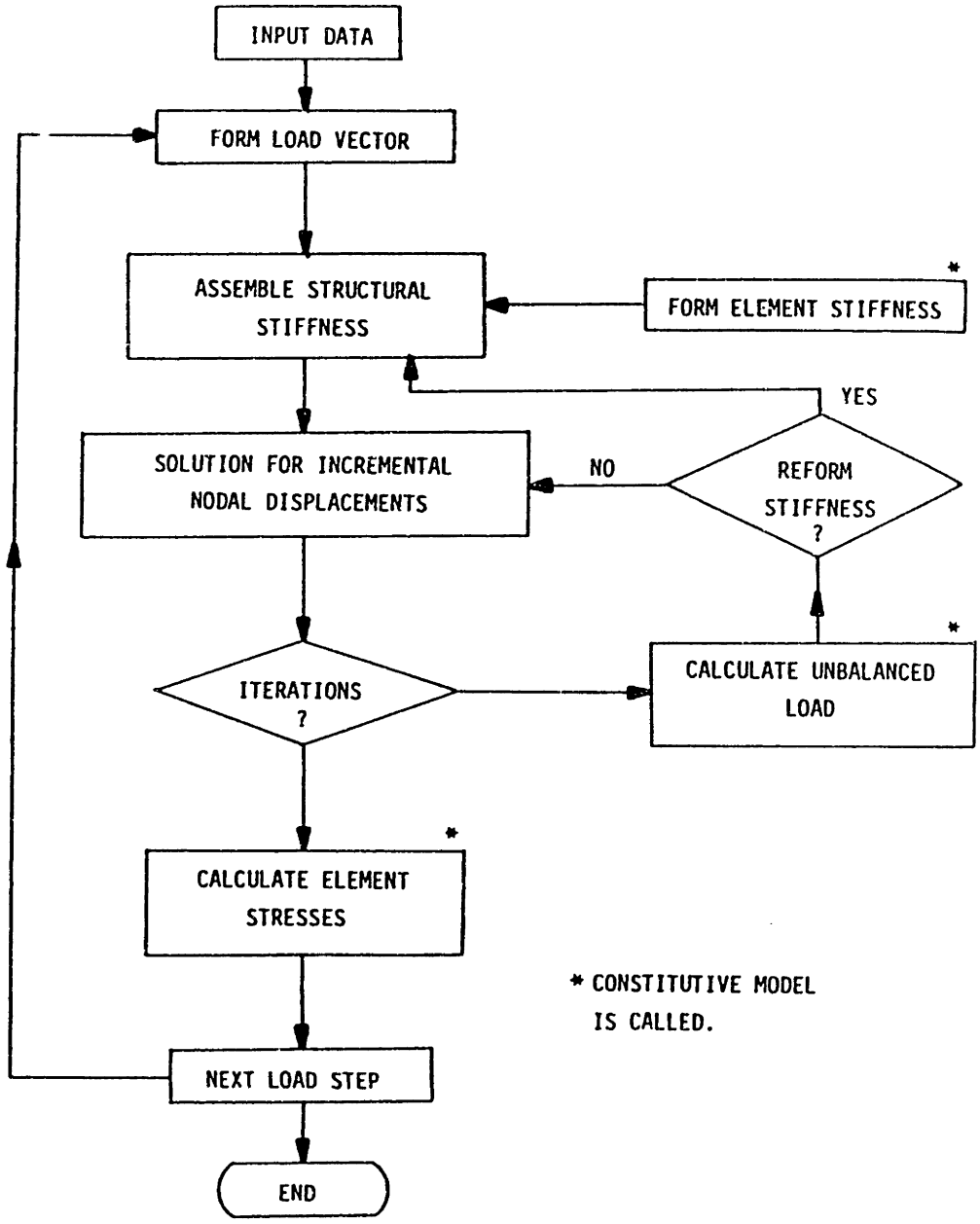

Fig. 7.1 A simple flow chart for a typical nonlinear finite element program.

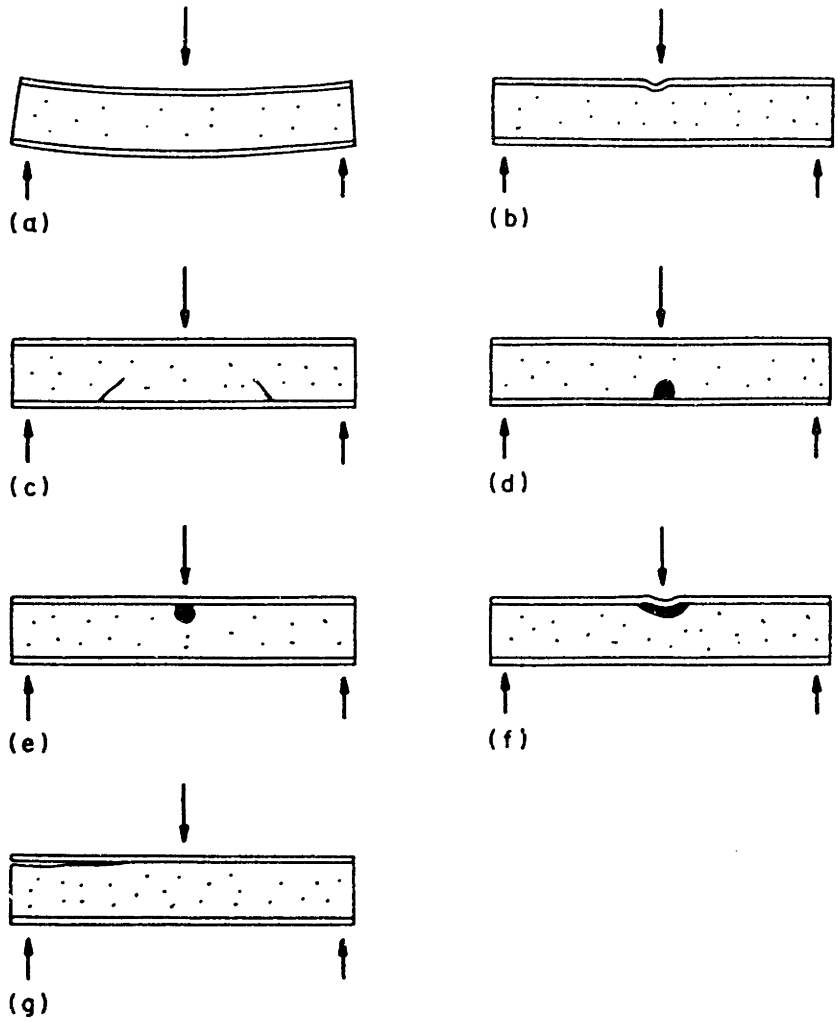

Fig. 7.2 The failure modes in a sandwich beam with face and core materials that yield: (a) face yielding; (b) face wrinkling; (c) core shear; (d) core tensile yield; (e) core compressive yield; (f) core indentation; (g) debonding (after Triantafillou and Gibson, 1987a).

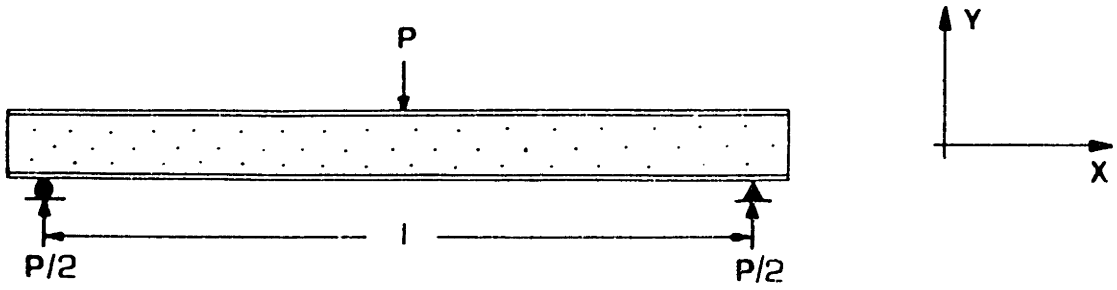

Fig. 7.3 A sandwich beam of span l loaded in bending.

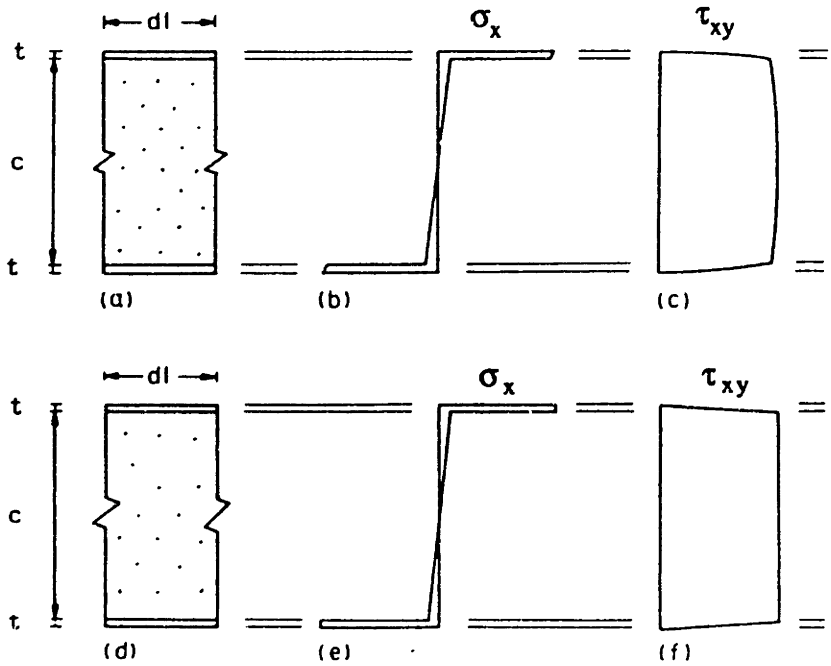

Fig. 7.4 The stress distribution in a sandwich beam: (a) a segment dl of the length of the beam; (b) the exact normal stress distribution; (c) the exact shear stress distribution; (d) the segment dl of the length of the beam; (e) the approximate normal stress distribution; (f) the approximate shear stress distribution (after Triantafillou and Gibson, 1987a).

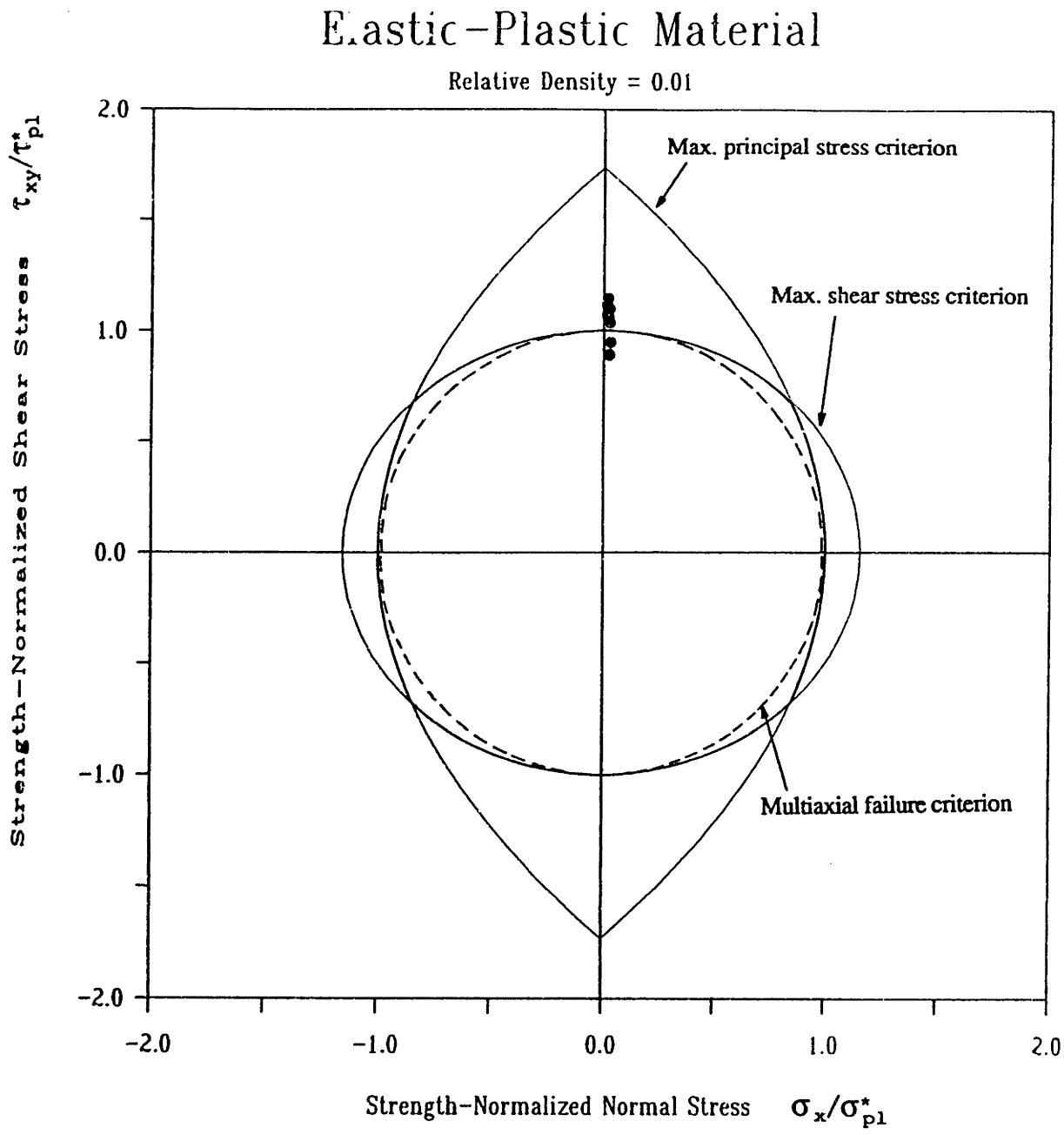

Fig. 7.5 The envelopes corresponding to failure of the core material in a sandwich beam loaded in bending, and comparison with data.

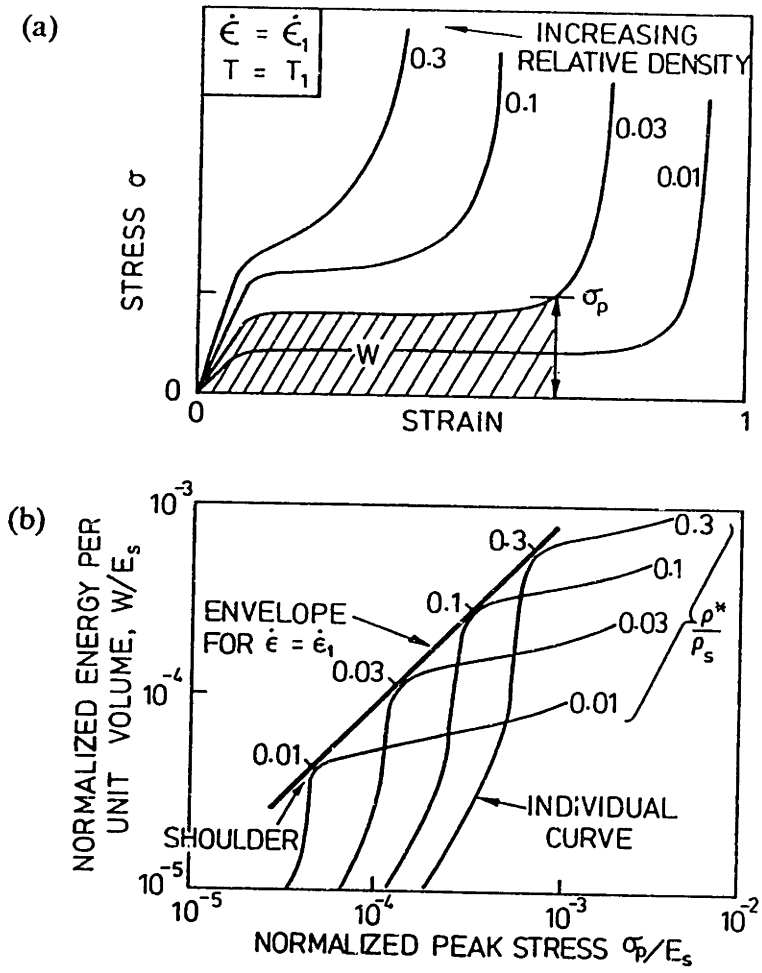

Fig. 7.6 The construction of energy absorption diagrams. (a) Stress-strain curves are measured at a single strain rate and temperature. (b) The area W under each curve up to the stress σ_p is plotted against σ_p, both normalized by the solid modulus E_p. The envelope which just touches each curve defines the optimum choice of foam at the given strain rate and temperature (after Gibson and Ashby, 1988).

CHAPTER VIII

SUMMARY-CONCLUSIONS-RECOMMENDATIONS

8.1 Summary

This study represents a contribution towards (a) the development of criteria to describe the failure of cellular materials under multiaxial loads, (b) the experimental validation of the proposed failure criteria, and (c) the use of multiaxial failure criteria for cellular materials in engineering applications.

Previous work in this area is limited. While some modeling of the multiaxial behavior of two-dimensional honeycombs has been done, there is no analytical model for that of three-dimensional foams. Earlier studies proposed an empirical maximum principal stress failure criterion for foams, primarily based on the results of biaxial tests. The current research was motivated by the practical problems of predicting the performance of structural sandwich panels and packaging materials under multiaxial loading conditions. In both cases, the cellular solid under consideration may be under a complex stress state, for which multiaxial failure criteria are required to predict its behavior. The major focus of the research has been on the development and verification of such failure criteria.

The contents of the thesis include the following:

(1) A review of the existing contributions towards understanding and modeling the behavior of cellular solids under uniaxial and multiaxial loading conditions.

(2) The development of criteria for the elastic buckling, plastic yield, and brittle failure of honeycombs under in-plane stresses.

(3) The development of multiaxial failure criteria for the plastic and brittle failure of foams accounting for anisotropy. The model for brittle failure is extended to

describe materials with porous cell walls such as cellular ceramics made from a polymeric foam precursor.

(4) The development of a constitutive model for isotropic elastic-plastic foams based on the concepts of "associated plasticity".

(5) Data for the elastic buckling and plastic and brittle failure of orthotropic foams under uniaxial, biaxial, and axisymmetric loading conditions. A novel experimental technique was developed for testing cylindrical specimens of materials with a continuous porosity under radially applied tensile stresses and axially applied compressive or tensile stresses. Data for the elastic buckling failure envelope of honeycombs were obtained to assist in the interpretation of the elastic buckling data for foams.

(6) A study of the application of the failure criteria to the design of structural sandwich panels, and to the design of protective packaging.

The materials analyzed in this study were hexagonal honeycombs and foams with open cells, or with closed cells but showing an open-cell behavior. Some of the key elements of the analysis are summarized below:

(1) Elastomeric materials fail in compression by elastic buckling. Elastic-plastic materials fail by the formation of plastic hinges in the cell walls or, under certain compressive stress states, by elastic buckling. Elastic-brittle materials fail when the extreme fiber stress developed in the cell struts reaches the modulus of rupture or the compressive strength of the cell wall material; the brittle failure surface is truncated in tension by fast brittle fracture and in compression by elastic buckling.

(2) When isotropic cellular solids are loaded in hydrostatic tension or compression, they respond by axial stretching of the cell struts; any deviation from this uniform stress state causes cell wall bending, which, in the case of foams, is attributed to the second invariant of the deviatoric stress tensor.

(3) Small strains were assumed throughout the analysis. Furthermore, the relative densities of the materials were assumed to be low (less than 0.3 for instance), justifying the assumption that the shear deformations of the cell walls are negligible compared to the bending deformations.

8.2 Conclusions

The important conclusions drawn from this study are the following:

(1) The elastic buckling envelope of biaxially compressed honeycombs is constructed by two approximately straight lines and is almost box-like; for isotropic honeycombs, the ratio of the equal biaxial stresses required to cause buckling to the uniaxial buckling stress is 0.83. Each of the straight portions of the failure envelope is associated with a specific buckling mode.

(2) Three modes of failure were identified for plastic or brittle honeycombs loaded in-plane, depending on the combination of stresses σ_x, σ_y, and τ_{xy}. In the absense of shear stresses, the failure envelopes are elongated along the line of equal biaxial stress, reflecting the much higher strength of the materials when the cell walls are subjected to axial stresses only and bending is suppressed. In the case of elastic-plastic honeycombs, the failure envelope is the intersection of two ellipses, while in the case of brittle honeycombs it is a rhombic shape with two pairs of straight lines: one corresponding to tensile rupture and the other, to compressive crushing of the cell wall material. A maximum principal tensile stress criterion is employed for the tensile fracture of brittle honeycombs, resulting in a box-like cutoff in the tension-tension quadrant. The elastic buckling failure envelope acts as a cutoff in the compressive quadrant.

(3) The failure criteria for isotropic foams developed in this study are functions of the first invariant of the stress tensor and the second invariant of the deviatoric stress tensor. The failure surfaces follow the results obtained for honeycombs: they are extremely elongated along the hydrostatic axis. For plastic materials, the failure surface resembles an ellipsoid with two vertices. For brittle materials, the surface consists of two cones associated with tensile and compressive bending failure of the cell struts. The surfaces are truncated by an almost box-like elastic buckling surface in the compressive octant of the principal stress space; for brittle materials, it is also truncated by a box-like cutoff in the tensile octant corresponding to a maximum principal tensile stress criterion for fracture.

(4) The failure criteria for foams were extended to account for material anisotropy (axisymmetry, orthotropy). This was achieved by distorting the failure surfaces so that they intersect the stress axes at the points corresponding to the uniaxial

strengths of the material in different directions.

(5) The failure criteria obtained in this study require a very limited number of parameters: the uniaxial strengths in the principal material directions, the relative density ratio, and if the material is brittle, the ratios of the modulus of rupture of the cell wall material to its tensile and compressive strengths. Therefore, the calibration of the equations describing failure is an easy task.

(6) The linear elastic constitutive relationships for isotropic foams obtained in this study take into account both axial and bending deformations of the cell walls. The yield surface for isotropic foams possesses desirable characteristics: it is convex and smooth (except for the two points on the hydrostatic axis corresponding to uniform extension or shortening of the cell walls). The post-yield constitutive equations for these materials were obtained on the basis of the classical plasticity theory with an associated flow rule assuming no hardening, which is typically the case in open-cell foams.

(7) The experimental failure envelope for isotropic elastomeric honeycombs compressed biaxially is in close agreement with the analytical one. The proposed failure criteria for foams agree reasonably well with biaxial test results obtained in previous studies, except for a few data points obtained with nearly equal stresses of opposite signs, in which case the failure criteria appear to be too conservative. The overall agreement between the analysis for elastic-plastic and elastic-brittle foams and the test results obtained in this study is good. However, a few data points associated with axisymmetric loading conditions lie well inside the failure envelopes; possible experimental errors may be the reason for this.

(8) The response of the materials tested under a multiaxial stress state was found to be slightly stiffer than the uniaxial one, when the lateral (in biaxial loading) or radial (in axisymmetric loading) and axial stresses (produced by the crosshead) were of the same sign; the opposite was observed when they were of opposite signs.

(9) The results of the microstructural characterization of the materials tested in this work indicate that they can be idealized as orthotropic or axisymmetric without significant error. In general, the anisotropy of the microstructure is reflected by that in the mechanical properties (Young's moduli, uniaxial strengths).

(10) The novel experimental technique developed in this study for axisymmetric loading of cylindrical specimens with radial tension and axial compression or tension is expected to give good results only when the true stress distribution in the specimens can be estimated with sufficient accuracy. In this study, the evaluation of the stress state was based on the finite element method. This experimental procedure is applicable to materials containing a continuous pore system and high void ratios.

(11) The predictions of the failure criterion for the plastic collapse of the core material in structural sandwich beams show a close agreement with analytical results obtained by previous theories.

8.3 Recommendations for Future Research

Overall, a framework for understanding the multiaxial behavior of cellular materials has been established. The models obtained in this study are found to give good agreement with test results, and given the uncertainties involved in the materials microstructure the development of more sophisticated models is not considered necessary.

The mechanical behavior of cellular materials is not completely understood and analyzed. Future research towards a better understanding should include the following:

(1) Experimental measurement of post-yield plastic strains to confirm the assumption of normality in the constitutive equation developed.

(2) Development and verification of failure criteria accounting for high strain rate effects.

(3) Study of the behavior of the materials under stress reversals and development of realistic constitutive models to account for cyclic loading conditions.

(4) Constitutive modeling of anisotropic cellular solids.

(5) Comparison of elastic constitutive equations for foams with data.

(6) Development of failure criteria for natural cellular solids (e.g., cancellous bone, wood), accounting for the anisotropic nature of their cell walls.

(7) Development of multiaxial failure criteria for cellular (aerated) concrete by modeling it as a closed-cell cellular material.